Strangeness Photoproduction off the Proton at Threshold Energies

Thomas Jude

School of Physics and Astronomony

The University of Edinburgh

A thesis submitted for the degree of

Doctor of Philosophy

2010

For Mum and Dad

Acknowledgements

Firstly I would like to thank my supervisor, Dan Watts for his excellent guidance and support over the last three and a half years, and Derek Glazier for suggestions with the analysis of this work.

I would like to thank the entire Edinburgh Nuclear Physics Research Group for providing such a good environment to work in. A special thanks to Claire Tarbert and Klaus Föhl for the guidance when I began my PhD, and a thank you to all present and past PhD students for the numerous tea breaks and making the work that much more enjoyable.

I particularly want to thank the other photonuclear PhD students; Daria Sokhan, Mark Sikora, Jo McAndrew and Pauline Hall Barrientos, for company at experiments and conferences over the last few years.

I am also grateful to the colleagues at The University of Glasgow, notably John Annand for analysis advice, and Ken Livingston and David Hamilton. Thank you also to Jamie Robinson and the Burger for entertaining nights out in Mainz.

I would like to thank everyone at the Crystal Ball Collaboration for giving me the support and opportunity to do the experiment and present my work at collaboration meetings, in particular Sergey Prakhov at UCLA for invaluable analysis advice.

I would like to thank Jane Patterson for dealing with all of the administration and making the last three and a half years flow seamlessly.

Most importantly I would like to thank my family for their support and encouragement.

Abstract

$K^+\Lambda$ photoproduction provides the best possibility for a model independent extraction of the photoproduction process and contributing resonances. To do this, it is vital that cross section measurements are well understood.

This thesis presents $\gamma p \rightarrow K^+\Lambda$ differential cross sections from the reaction threshold, to an invariant centre of mass energy of 1.87 GeV. The data was taken at MAMI-C electron microtron facility in Mainz, Germany, during July 2007 and April 2009. The 1.5 GeV MAMI-C electron beam was used to produce an energy tagged bremsstrahlung photon beam with a maximum energy of 1.4 GeV and an intensity of 10^5 γ $s^{-1}MeV^{-1}$. The beam impinged upon a liquid hydrogen target, with reaction products detected in two segmented calorimeter arrays; the Crystal Ball detector and TAPS.

This work pioneers a new method of K^+ detection in segmented calorimeters, in which the K^+ was identified from the signature of its weak decay inside the crystals of the calorimeter. This proved to be an excellent method of isolating K^+ and accessing strangeness photoproduction channels, with good agreement between experimental and Geant4 simulated data. A novel method in seperating $K^+\Lambda$ and $K^+\Sigma^0$ final states was also developed by identifying the photon from the decay: $\Sigma^0 \rightarrow \Lambda\gamma$.

The intense photon beam at the MAMI-C facility enabled differential cross section data with greater invariant mass resolution than previous measurements. The new measurement near threshold imposes important constraints to effective field theories based on the approximate chiral symmetry of QCD. At higher centre of mass energies it

also addresses the current problem of discrepant data sets and will form an important constraint on partial wave analysis for the nucleon excitation spectrum. As such, this work contributes to a major world wide programme aiming to extract the excitation spectrum of the nucleon and to understand the dynamics and interactions of its constituents. The greater statistics near threshold, and particularly at backwards K^+ centre of mass angles will give new valuable constraints to contributions from meson and hyperonic resonances on the reaction mechanism. The high resolution of the photon beam (approximately 2 MeV) also allows the first search for narrow resonances coupling to $K\Lambda$ final states.

The differential cross sections give good agreement with Kaon-MAID partial wave solutions, apart from at backward angles close to threshold, where the data is lower. Near threshold, the data agrees with calculations from the chiral unitary framework of Borasoy *et al*, tending to be in better accordance with the model than previous data. No strong structure from potential narrow resonance states was observed over the centre of mass energy region of 1650-1700 MeV, where narrow structure has been observed in recent η photoproduction off the neutron.

Declaration

The data presented in this thesis was obtained in experiments carried out by the CB@MAMI collaboration in the A2 hall of the Institüt fur Kernphysik at the University of Mainz, Germany. I played a major role in the preparation and execution of the experiment and the data analysis and interpretation is entirely my own work. Any contributions from colleagues in the CB@MAMI collaboration such as diagrams or calibrations are explicitly referenced in the text. This thesis was written by myself and the work presented in it has not been submitted in support of another degree or qualification from this or any other university or institute of learning.

Thomas Jude

Contents

List of Figures

Chapter 1

Introduction

The nucleon is the building block of all matter, and its structure underpins all of nuclear physics. A realistic description of the nucleon's internal structure was not developed until the 1960s. The quark model, which was theorised by Murray Gell-Mann [1] to explain many new particles which were being discovered at the time (such as the Δ^- and Δ^{++}), described the nucleon as a three quark system, interacting via the exchange of gluons. The quarks and gluons were attributed a color charge which is the source of the strong nuclear force.

Quantum Chromodynamics (QCD) was subsequentially developed as the non-abelain gauge theory which describes the interactions of the quarks and gluons within the nucleon. Due to the non-analytical nature of QCD, perturbation theories are required to solve QCD Lagrangians. Although successfully applied in high energy reactions, for the lower energy interactions in the nucleon, the strength of the strong coupling precludes the use of perturbation theory. In this energy regime, the nature of the potential between quarks confines the quarks to the nucleon. Despite approximately 98% of the nucleon mass being generated by these non-perturbative aspects of QCD, the mechanisms of confinement is an unresolved problem.

In the absence of analytical solutions of QCD in the non-perturbative regime, QCD inspired constituent quark models have been used as a tool to attempt to describe the nucleon and provide constraints on the dynamics and interactions of the nucleon constituents. No single model has been able to correctly predict the excited states of the proton or the neutron. In fact, the very first excited state

of the proton is not predicted by any constituent quark model to be the lowest excited state.

Perturbation schemes based on the approximate chiral symmetry of QCD have enabled the prediction of experimental observables. These theories are only applicable near the threshold energy of reactions but are an important test to non-perturbative QCD.

The photoproduction of mesons from the nucleon, where the reaction proceeds via a resonance state, is the reaction of choice for advancing our knowledge of the nucleon excited states. The coupling of the photon to the electromagnetic current of the nucleon is well understood via quantum electrodynamics (QED), and there are no initial state interactions which complicate the analysis of the data as with hadronic probes. In recent decades, tagged photon beams have enabled high quality data for pion photoproduction.

With recent increases in photon beam intensities, the photoproduction of mesons and baryons with non-zero strangeness has been realised. The photoproduction of strange hadrons presents unique tests to perturbation theories based upon the chiral symmetry breaking of QCD due to the comparatively large strange quark mass. It also provides a test for poorly established nucleon resonances which have been predicted by constituent quark models, in particular many "missing resonances" which have not been observed experimentally but are predicted to couple more strongly to strange reaction channels.

This thesis presents cross section measurements for the reaction: $\gamma p \rightarrow K^+\Lambda$, from threshold energy of 0.9 GeV to 1.4 GeV. There is a paucity of data for this reaction channel, and the existing world data set has significant discrepancies which have led to serious uncertainties in the excited nucleon states contributing to the reaction. The lack of high statistics near the threshold region also prevents a detailed examination of models based on chiral perturbation theory.

The recently upgraded MAMI-C facility with the Crystal Ball detector provided a high intensity photon beam with high energy resolution and nearly 4π angular acceptance, making the apparatus ideal for strangeness measurements near threshold energies. A new method of K^+ identification was developed, in which K^+ were identified by the detection of their weak decay inside the detector

crystals. This technique proved successful in reconstruction of the reaction and enables new opportunities for K^+ identification at other hadron facilities.

This thesis proceeds with a description of the current understanding of the nucleon in chapter 2. Chapter 3 describes previous measurements in the field and theoretical models directly related to strangeness photoproduction. The Crystal Ball detector and apparatus at the MAMI-C facility are described in chapter 4. Chapter 5 discusses the detector calibrations and chapter 6 describes the new method of K^+ identification. The method of extracting cross section measurements is described in chapter 7, with the $\gamma(p, K^+)\Lambda$ cross section measurements presented and discussed in chapter 8.

Chapter 2

The current understanding of the nucleon

This chapter explains the current understanding of the nucleon, from the development of the appropriate quantum numbers used to categorise the hadronic spectrum (section 2.1), to the underlying symmetries of the Standard Model and Quantum Chromodynamics (section 2.2). Section 2.4 discusses the models used to give predictions of the excited nucleon spectrum. Section 2.5 presents the formalism of the photoproduction mechanism and methods of partial wave analysis used to extract resonance parameters from experimental data.

2.1 The development of hadron physics

Heisenberg postulated in 1932 that the proton and neutron could be considered as the same particle, the "nucleon", under different charge substates [2]. The two states were labelled with a new quantum number, isospin (**I**). As an analogy to spin, the isospin for a nucleon is 1/2, with the z-axis orientation (referred to as I_3) aligned as $I_3 = +\frac{1}{2}$ for the proton and $I_3 = -\frac{1}{2}$ for the neutron. The two states are defined as an isospin doublet. The electronic charge, Q, is then defined as:

$$\frac{Q}{e} = \frac{1}{2} + I_3 \tag{2.1}$$

Neglecting effects from Coulomb interactions, the forces between nucleons, namely $p-p$, $p-n$ and $n-n$ are equivalent and charge independent, leading to the conclusion that isospin is conserved in strong interactions.

The pion is the lightest of the meson particles, existing as three charged sub-states (plus, minus and neutral) with isospin, $\mathbf{I} = 1$. To accomodate this into the same framework as the nucleon, a new quantum number, Baryon number (B) is used:

$$\frac{Q}{e} = \frac{B}{2} + I_3 \tag{2.2}$$

where nucleons (and other baryons) have $B = 1$ and pions (and other mesons) have $B = 0$.

In 1947, G. D. Rochester and C. C. Butler published photographs of cloud chamber plates showing particles produced from the interaction of cosmic rays[1]. They observed a neutral particle decaying to two charged pions, and a charged particle decaying to one charged and one neutral pion. Both particles (dubbed "V particles" due to their decay tracks) were determined to have a mass approximately half that of a proton. In 1953, much more cosmic ray data was taken in the French Pyrenees. It was noted that whilst the production of these particles was fast, (of the order of 10^{-20} s), the decays were much slower (of the order of 10^{-10} s). The anomaly was first explained by Pais [4] who postulated a new "strangeness" quantum number, S. Particles of non-zero strangeness were created fast in pairs, but once seperated could not decay rapidly.

The charged "V" particle, was considered as two seperate particles due to the difference in parity of two observed decay modes: $\Theta^+ \rightarrow \pi^+\pi^0$ and $\tau^+ \rightarrow \pi^+\pi^+\pi^-$, where the multiplicative parity of the reaction products is positive and negative respectively. With extensive measurements of the masses and lifetimes of the Θ^+ and the τ^+ it was realised that they were the same particle, known today as K^+. This was one of the first tests of parity violation of the weak decay [5].

As Λ had no charged sub-state counter part, it was assigned $\mathbf{I} = 0$. Strange particles can only decay weakly, leading to their "strange" decay properties. Through the observation of the weak decay: $\Lambda \rightarrow p\pi^-$ it was apparent that isospin is not conserved in the weak interaction.

[1]For a review of the early discoveries of strangeness see reference [3].

When produced in strong and electromagnetic reactions where the initial state does not contain strange particles, the Λ must be produced in "associated production" with a meson of non-zero strangeness. The lightest strange meson is the K^+, with strangeness, $S = -1$ and isospin, $I_3 = +\frac{1}{2}$.

Gell-Mann and Nishijima [1] adapted the relation to electronic charge and isospin to accomodate strangeness and hypercharge, Y defined as $Y = B + S$:

$$\frac{Q}{e} = \frac{B}{2} + \frac{S}{2} + I_3 = \frac{Y}{2} + I_3 \tag{2.3}$$

During the 1960s a plethora of hadron states were observed using bubble chambers. These were classified according to the quantum numbers in eq. 2.3, and patterns in particle properties became apparent. Fig. 2.1 groups hadron states of equal spin-parity, J^π. The patterns observed in fig. 2.1 allowed the prediction of the Ω^- before its detection in 1964 [6]. It was noted that each isospin doublet had similar masses (in fig. 2.1, the isospin doublets are states which are symmetric about the y-axis where $I_3 = 0$), and particles of different strangeness quantum number had large differences in mass. The classification of hadrons into multiplets and the observed mass differences suggested there was some higher symmetry, called unitary symmetry at the time but seperceded now by the Constituent Quark Model (CQM).

Three flavours of quarks were postulated by Gell-Mann to account for the observed patterns. The u, d and s (up, down and strange), where u and d are members of an isospin doublet and s an isospin singlet. The observed mass difference of particles of different strangeness is accounted for by the larger mass of the s quark compared to the u and d quarks. Particles in the baryon decuplet of $J^\pi = \frac{3}{2}^+$ (Δ^{++} for instance) require the quarks to be symmetric under spin flavour and space. To avoid violating the Pauli Exclusion Principle, the quantum number "color" was introduced, with baryons containing quarks of three different colors: red, green and blue.

Quark-antiquark combinations give rise to mesons: color singlet quark-antiquark pairs where either the quark spins align antiparallel or parallel, corresponding to the pseudoscalar mesons ($J^\pi = 0^-$), or the vector mesons ($J^\pi = 1^-$) respectively.

This simple classification scheme of the hadrons was superceded by Quantum Chromodynamics (QCD). QCD describes the interactions of quarks and gluons

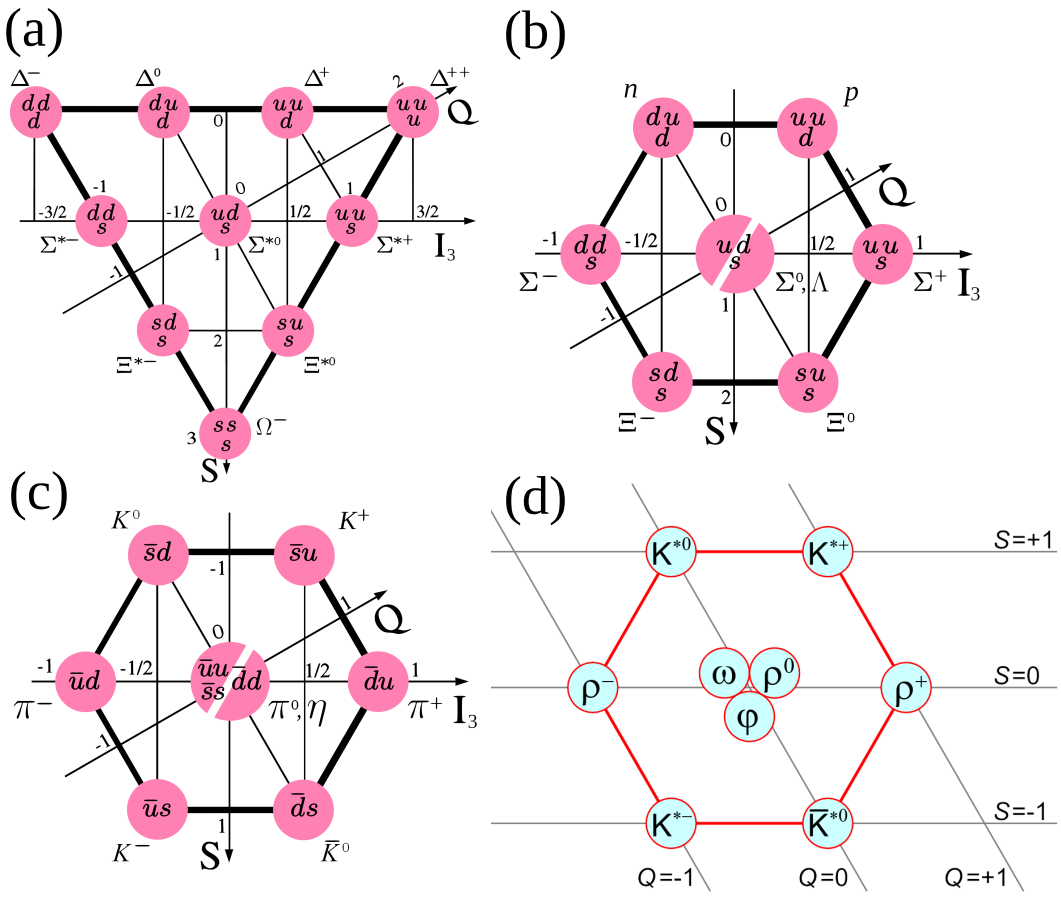

Figure 2.1: (a) The baryon decuplet ($J^\pi = \frac{3}{2}^+$). (b) The baryon octet ($J^\pi = \frac{1}{2}^+$). (c) The pseudoscaler mesons ($J^\pi = 0^-$). (d) The vector mesons ($J^\pi = 1^-$).

which give rise to the observed quantum numbers. QCD was in turn integrated into the Standard Model of particle physics. A brief overview of the Standard Model is described in the next section, with QCD and its applications described in more detail in section 2.3.

2.2 The Standard Model

The Standard Model is the theory of the electromagnetic, strong and weak interactions described via local gauge theories. Gauge theories are invariant under local transformations and are space-dependent. As an example, consider the Lagrangian for a free Dirac field:

$$\mathcal{L} = \overline{\psi}(i\gamma^{\mu}\delta_{\mu} - m)\psi \tag{2.4}$$

The fermion field, ψ and the complex conjugate can be transformed by phase rotations: $\psi \rightarrow e^{-i\omega(x)}$ and $\overline{\psi} \rightarrow e^{i\omega(x)}$, where $\omega(x)$ is a real constant and depends on the point in space-time (denoted as x). After the transformation, the Langrangian has changed and is therefore not invariant under local U(1) transformations. To restore gauge invariance, an interaction with a vector field, A_{μ} must be included in the Lagrangian. This ensures the Lagrangian does not change under the transformation. After defining a field strength as $F_{\mu\nu} = \delta_{\mu}A_{\nu} - \delta_{\nu}A_{\mu}$, the Lagrangian density becomes that of QED (eq. 2.5).

$$\mathcal{L} = -\frac{1}{4}F_{\mu\nu}F_{\nu\mu} + \overline{\psi}(i\gamma^{\mu}(\delta_{\mu} + ieA_{\mu} - m)\psi \tag{2.5}$$

From a starting point of insisting invariance under local U(1) symmetry, the same Lagrangian has been calculated as obtained from the quantisation of Maxwell's equations. The gauge invariance also ensures the photon is massless.

The U(1) group is a group of unitary 1×1 matrices, defined as abelian, as the members of the group commute with each other. This is not always the case however. Consider the group, SU(n) (SU is an abbreviation of Special Unitary, referring to the determinant of the matrix being equal to unity). This is a group of $n \times n$ matrices with $n^2 - 1$ parameters needed to completely define each matrix. Each matrix can be written as $e^{-i\omega^a \mathbf{T}^a}$ where ω^a are the real parameters and $\mathbf{T}^a$ are the generators of the group.

Eq. 2.6 is the gauge group for the Standard model. $U(1)_Y$, $SU(2)$, and $SU(3)$ are the gauge groups corresponding to hypercharge, isospin and the strong (color) force respectively. The n^2-1 number of generators for each group gives the family of leptons and fermions which describe all of nature[1] (at the time of writing) (table 2.1).

$$U(1)_Y \times SU(2) \times SU(3) \tag{2.6}$$

Leptons	e, ν_e
	μ, ν_μ
	τ, ν_τ
Quarks	d, u
	s, c
	b, t
Gauge Bosons	
γ, $W^\pm$, Z^0, g	

Table 2.1: Leptons, quarks and the gauge bosons which mediate interactions in the Standard Model. Antiparticles have been omitted.

2.3 Quantum Chromodynamics in the non-perturbative regime

Quantum Chromodynamics (QCD) is the theory of the strong interaction. Describing quarks as a fermion field, ψ_c, where c is the color quantum number, running from one to three, QCD is completely described by the non-abelian gauge group $SU(3)$. The eight generators of the group are the gluons which mediate the force between quarks. It is beyond the scope of this thesis to discuss the

[1]The generators for the SU(2) group are not the gauge bosons: γ, $W^\pm$ and Z^0, but it is their linear combinations which give the recognised particles.

intricacies of QCD, instead this section concentrates on some consequences of the theory and its application to hadron physics.

The coupling between gluons is equal to the coupling between gluons and quarks. This coupling is not constant, but varies as a function of energy or distance. Fig. 2.2 shows how the coupling, α_s, which is a measure of the interaction strength between quarks and gluons, varies with the momentum transfer, Q.

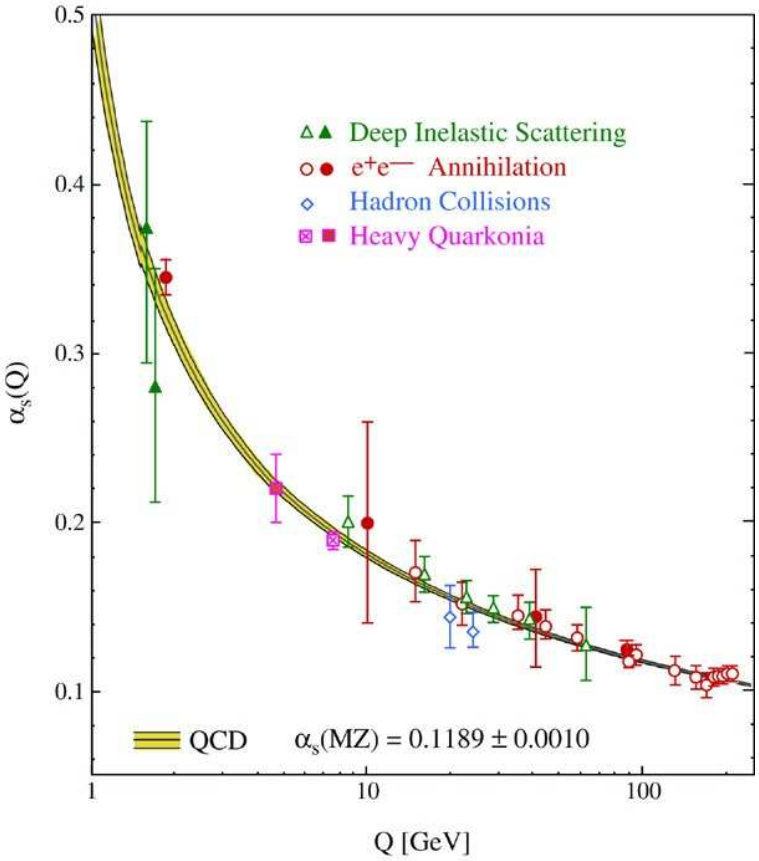

Figure 2.2: The QCD coupling as a function of momentum transfer.

The QCD Lagrangian which includes this coupling term, is thought to exactly describe all the properties and dynamics of the quark-gluon system. However, there is no analytical method of solving the Lagrangian to extract experimental observables due to the form of integrals which are generated. At high energies, where the coupling is small, perturbative methods can be used as an approxima-

tion. These involve power series expansion terms in the integrals, which converge very quickly in this energy regime.

At low energies (less than 2 GeV^2 in momentum transfer and at distances smaller than approximately 1.0 fm), a perturbative approximation does not work. Due to the strong interaction being much larger in magnitude, divergences appear in the power series expansion of the coupling term, making realistic approximations impossible. This is the non-pertubative regime which governs the physics of hadrons.

The nucleon can be considered as three valence quarks bound via the exchange of gluons in a QCD vacuum. The mass of valence quarks has been estimated from perturbative reactions to be 4-5 MeV/c^2. In this vacuum, there are also quark and anti-quark pairs continually being created and annihillated ("sea quarks"). The gluons interact with the valence quarks, the sea quarks and each other. The self-interaction of the gluons is a consequence of the non-abelian nature of QCD and the gauge invariance of the theory. Consequently, the mass of the nucleon is nearly entirely generated by the non-perturbative interactions of quarks and gluons (approximately 99%).

Increasing the distance between two valence quarks (equivalent to decreasing the energy) increases the coupling between them. The increase in binding energy prevents the isolation of a single quark or gluon. This is known as quark confinement (or hadronisation), only allowing observation of "color neutral" particles of baryons and mesons (three and two valence quarks respectively). The dynamics of the quark-gluon interaction can therefore only be gleaned via these hadronic degrees of freedom which are accessible with experimental methods. Measuring the properties of the hadrons therefore provides sensitive tests of non-perturbative QCD.

2.3.1 Lattice QCD

In 1974, K. G. Wilson [7] described a method to make ab initio calculations in low energy, non-perturbative QCD possible. The QCD Lagrangian was discretised into a space-time lattice with spacing a, with each lattice site containing the parameters of the local fermionic field. The local gauge invariance of QCD

was maintained using "gauge links", connecting fields at neighbouring lattice sites. The finite volume of each lattice site kept the Lagrangian well defined and analytically solvable, the calculated observables could then be extrapolated as $a \to 0$.

Despite the Lagrangrian being solvable, summing over the possible configurations of the system generated many terms. The number of terms was always finite, however this increased quickly with the size of the system. Monte Carlo techniques were developed as estimations [8] and allowed the accuracy of Lattice QCD (LQCD) calculations to rapidly improve with the increase in available computational power.

S. Durr *et. al.*[9] used LQCD to predict the ground state hadron mass spectrum up to the mass of the Ω, in agreement with experimental measurements (Fig. 2.3). The parameters required as an input were the light and strange quark masses and the QCD coupling strength. Systematic uncertainties were sufficiently small to conclude that the strong interaction at low energies is consistent with predictions of QCD[1].

Present LQCD calculations use large valence quark masses and extrapolate the measurements to the physical quark mass region. Calculations of nucleon form factors [10] (distributions of charge and mass in the nucleon), decay transitions and the nucleon excitation spectrum [11] have been made. Due to the extrapolation of the quark masses, many of these determinations are not precise, however with increased computational power in the next ten years, accurate calculations can be made close to the physical valence quark masses and reliable calculations of excited states of hadrons will become available. This will be an important milestone in hadron physics; when hadron properties will be a direct constraint on the validity of QCD in the non-perturbative regime.

2.3.2 Chiral perturbation theory

Effective field theories based on chiral perturbation use symmetries of QCD to provide predictions at low energy. First suggested in the 1960s, chiral pertur-

[1]Systematic uncertainties arose from the extrapolation of the quark mass to its physical mass, finite size effects of the lattice, and the extrapolation of the lattice spacing to zero.

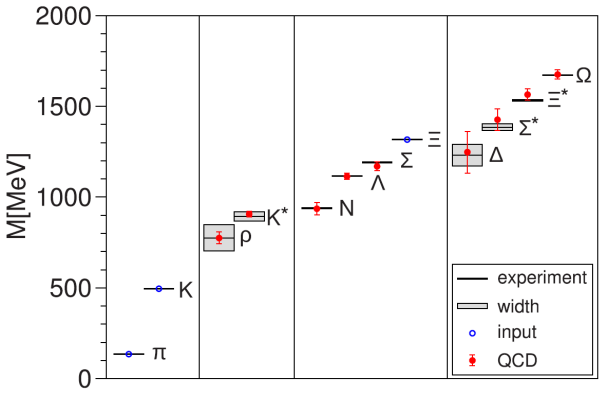

Figure 2.3: The light hadron spectrum. The widths in grey are the experimental measured particle widths. The error of the QCD data is the combined statistical and systematic error of the LQCD calculation. The π, K and Ξ masses were used in the LQCD calculations to set the light and strange quark masses. Taken from [9].

bation theory (χPT) was validated as a physical tool during the 1970s with the development of the Standard Model, and has been actively used from the 1980s. χPT is outlined below, but for an introduction to χPT, see references [12, 13], and for modern χPT theory see reference [14].

Considering quarks to be massless, the fermion (quark) field, ψ can be split into two helicities with spin parallel or anti-parallel to the momentum: $\psi = \psi_L + \psi_R$. The QCD interaction on both helicity states is identical. Massless quarks will never change helicity and a family of right handed and left handed particles would be generated, never to interact with the other via the strong interaction. The QCD Lagrangian can thus be considered chirally symmetric, denoted as $SU(3)_L \times SU(3)_R$, where a rotation to one helicity has no effect on the other (in this case for three quark flavours). For quarks with mass, helicity is not conserved as a Lorentz boost into a different inertial frame can change the quark spin projection. However, if the quark mass is small, $SU(3)_L \times SU(3)_R$ (referred to as chiral SU(3)) can be considered as an approximate symmetry, with the quark mass a perturbation.

For a more rigorous explanation, the QCD Lagrangian, $\mathcal{L}_{QCD}$ can be expanded

in terms of the handedness of the fermion field:

$$\begin{aligned} \mathcal{L}_{QCD} &= \overline{\psi}(i \not{D} - m)\psi \\ \mathcal{L}_{QCD} &= \overline{\psi}_L i \not{D}\psi_L + \overline{\psi}_R i \not{D}\psi_R + \overline{\psi}_R m\psi_L + \overline{\psi}_L m\psi_R \end{aligned} \tag{2.7}$$

where $\not{D}$ is the gauge covariant derivative, containing the gauge field and coupling terms, and m is the quark mass. The projection operators, P_L, P_R project the helicity of the quark field such that:

$$\begin{aligned} \psi_L &= P_L\psi \\ \psi_R &= P_R\psi \end{aligned} \tag{2.8}$$

It is apparent from eq. 2.8 that a projection operation on the Lagrangian renders the Lagrangian unchanged only when quarks are massless ($m = 0$). The Lagrangian decouples into left and right helicity terms, maintaining gauge invariance. The invariance is given as $SU(3)_L \times SU(3)_R$ (for a three quark flavour system), and the Lagrangian is chirally symmetric. If this symmetry was exact, for any hadron state, parity doublets would be observed in a similar manner to the isospin doublets. This is not the case, and $m \neq 0$ in eq. 2.8 removes the invariance.

A conceptually difficult aspect of χPT arises from how breaking the chiral invariance arrives at the prediction of scattering amplitudes and other phenomena. In the massless limit, there are many equivalent ground states in the vacua, with different combinations of left and right handed quarks (as the interactions are equal). In this limit, the massless Goldstone bosons π, K, η are generated. The breaking of the symmetry prevents the multiplet nature of a conserved symmetry (as in isospin), and the partner of the proton under rotational transformations is a proton plus a pion of zero energy. For a given state $|\beta\rangle$, the axial transformation gives $|\beta\rangle \rightarrow |\beta + \pi(P_\pi = 0)\rangle$. This was extended to the soft pion theorem of chiral symmetry [15] at the limit where the π momentum, $P_\pi \rightarrow 0$, and was able to relate hadronic processes of pion exchange, for example:

$$\pi\pi \rightarrow \pi\pi \tag{2.9}$$

$$K \rightarrow 3\pi \iff K \rightarrow 2\pi \tag{2.10}$$

$$\begin{aligned} K \to \pi\pi e\nu &\iff K \to \pi e\nu \\ \pi^0 \to 2\gamma &\iff \pi^0 \to 3\gamma \\ K \to \pi\pi e\nu &\iff \pi\pi \to \pi\pi \end{aligned}$$

The symmetries used in the soft pion theorem can be extended to an effective Lagrangian. The QCD Lagrangian is written as an effective Lagrangian in terms of the derivatives of a field, $U(x)$ describing the degrees of freedom of the hadrons:

$$\mathcal{L}_{QCD} \to \mathcal{L}_{eff}(U, \partial U, \partial^2 U, ...) = \mathcal{L}^2_{eff} + \mathcal{L}^4_{eff} + \mathcal{L}^6_{eff} + ... \tag{2.11}$$

where the superscript denotes the number of derivatives. The form of the effective Lagrangian is completely determined by symmetries from QCD, however magnitudes are required to be fixed from experimental data.

For the series to converge, the masses and momenta of the system must be small compared to the chiral symmetry breaking scale of the system, $\Lambda \approx 4\pi F_\pi \approx$ 1 GeV, where F_π is the pion decay constant ($\approx$ 92 MeV). This is expressed as the momentum fraction, q^2/Λ, where q is the momentum of the system. At sufficiently low energies, the expansion can be truncated to the order of one or two terms. Higher energies preclude this truncation as the q^2/Λ term does not decrease in higher order terms.

This is χPT at its most general. It is a theory developed from the symmetry breaking of QCD with no dynamical assumptions. Models based on chiral symmetry use these underlying symmetries and superimpose further dynamics to remove the limitations of χPT. These are used in extending χPT to higher energies, or including resonance structure in cross sections which have been measured experimentally. The framework presented in section 3.3.4 is an example, where chiral symmetries have been used to produce predictions of observables in strangeness photoproduction.

χPT for hadrons of non-zero strangeness provides a stringent test on the extent of chiral symmetry breaking. The constituent strange quark mass is of the order of 25 times that of the non-strange quarks. Therefore considering the quark mass as a perturbation to chiral SU(3) requires validation and is more challenging than the perturbation of non-strange quark masses in chiral SU(2).

2.4 Baryon Spectroscopy

The excited states of the nucleon have lifetimes of the order of $10^{-24}s$ with widths the order of 60 MeV to 500 MeV. The typical spacing of the resonant states (sometimes with masses within 10 MeV of each other) causes resonances to overlap and the production amplitudes to interfere. Most nucleon resonances decay via the emission of mesons back to the nucleon ground state and so experimental measurements of mesons in the final state provides a means of probing the nucleon excitation spectrum. It is clear however from fig. 2.4 that the overlapping of the resonances leaves large ambiguities to the spectrum.

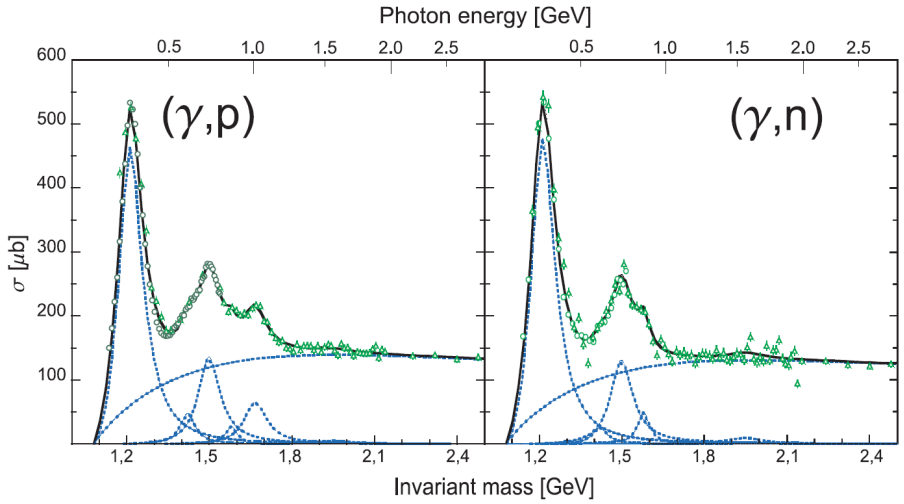

Figure 2.4: Cross section for the photo absorption on the proton and neutron (left and right respectively). Data points are from measured data with the resonance curves superimposed of $P_{33}(1232)$, $P_{11}(1440)$, $D_{13}(1520)$, $S_{11}(1535)$, $F_{15}(1680)$ (proton only), $F_{37}(1950)$ and a smooth background. Taken from [16].

The nucleon resonance spectrum is still far from satisfactorily understood. Table 2.5 lists the resonances recognised by the Particle Data Group (PDG) [17]. It is apparent from the star rating (described in table 2.5) that the existence of many states is dubious, and with the exception of the $N\pi$ channel, the contributing resonances to many reaction channels is very poorly understood.

The remainder of this section describes some of the theoretical quark models used to predict the masses, widths and other properties of nucleon resonances. The standard spectroscopic notation used to describe nucleon resonances is $L_{2I2J}(W)$, for a resonance state with angular momentum L (using spectroscopic notation S, P, D, ...), isospin I, angular momentum J and mass W, in MeV.

Table 2.6 lists the masses and widths of resonant states as extracted with different partial wave analyses (see section 2.5.3). It is clear that depending on the analysis, there are large discrepancies in the extracted widths and masses of resonances, even for some resonances where their existence is deemed as certain. Larger discrepancies exist for other properties, such as the electromagnetic coupling of the resonances (for more details see reference [17])

2.4.1 Quark models

At the relatively low energies of non-perturbative QCD, the complicated interactions between valence quarks, sea quarks and gluons does not provide a useful insight to understand nucleon properties. At present, there is no analytical method to proceed from the QCD Langrangian to describe the nucleon and the observed excited states, and so effective field theories are necessary to understand the strong interaction between nucleons and mesons. The relevant degrees-of-freedom must be recognised, whilst maintaining the underlying symmetries of QCD. This was achieved with constituent quark models.

Motivated by QCD, constituent quark models (CQM) describe the nucleon as three heavy constituent quarks, the sum of the effective masses of which account for the nucleon mass. The u and d quarks are typically attributed a mass between 200-350 MeV, with the strange quark 150-200 MeV heavier (although these masses vary depending on the model). A first attempt at describing the nucleon excitation spectrum with a CQM was done by Faiman and Hendry [19]. In this model, resonances were excitations of the three quark system confined in a three dimensional harmonic oscillator potential. The model was successful in reproducing the masses of low lying resonances which had been measured experimentally at the time. Koniuk and Isgur [20] extended this to include structure

Particle	$L_{2I\,2J}$	Overall status	Status as seen in — $N\pi$	$N\eta$	ΛK	ΣK	$\Delta\pi$	$N\rho$	$N\gamma$
$N(939)$	P_{11}	****							
$N(1440)$	P_{11}	****	****	*			***	*	***
$N(1520)$	D_{13}	****	****	***			****	****	****
$N(1535)$	S_{11}	****	****	****			*	**	***
$N(1650)$	S_{11}	****	****	*	***	**	***	**	***
$N(1675)$	D_{15}	****	****	*	*		****	*	****
$N(1680)$	F_{15}	****	****	*			****	****	****
$N(1700)$	D_{13}	***	***	*	**	*	**	*	**
$N(1710)$	P_{11}	***	***	**	**	*	**	*	***
$N(1720)$	P_{13}	****	****	*	**	*	*	**	**
$N(1900)$	P_{13}	**	**					*	
$N(1990)$	F_{17}	**	**	*	*	*			*
$N(2000)$	F_{15}	**	**	*	*	*	*	**	
$N(2080)$	D_{13}	**	**	*	*				*
$N(2090)$	S_{11}	*	*						
$N(2100)$	P_{11}	*	*	*					
$N(2190)$	G_{17}	****	****	*	*	*		*	*
$N(2200)$	D_{15}	**	**	*	*				
$N(2220)$	H_{19}	****	****	*					
$N(2250)$	G_{19}	****	****	*					
$N(2600)$	$I_{1\,11}$	***	***						
$N(2700)$	$K_{1\,13}$	**	**						
$\Delta(1232)$	P_{33}	****	****	F					****
$\Delta(1600)$	P_{33}	***	***	o			***	*	**
$\Delta(1620)$	S_{31}	****	****	r			****	****	***
$\Delta(1700)$	D_{33}	****	****	b		*	***	**	***
$\Delta(1750)$	P_{31}	*	*	i					
$\Delta(1900)$	S_{31}	**	**	d		*	*	**	*
$\Delta(1905)$	F_{35}	****	****	d		*	**	**	***
$\Delta(1910)$	P_{31}	****	****	e		*	*	*	*
$\Delta(1920)$	P_{33}	***	***	n		*	**		*
$\Delta(1930)$	D_{35}	***	***			*			**
$\Delta(1940)$	D_{33}	*	*	F					
$\Delta(1950)$	F_{37}	****	****	o		*	****	*	****
$\Delta(2000)$	F_{35}	**		r			**		
$\Delta(2150)$	S_{31}	*	*	b					
$\Delta(2200)$	G_{37}	*	*	i					
$\Delta(2300)$	H_{39}	**	**	d					
$\Delta(2350)$	D_{35}	*	*	d					
$\Delta(2390)$	F_{37}	*	*	e					
$\Delta(2400)$	G_{39}	**	**	n					
$\Delta(2420)$	$H_{3\,11}$	****	****						*
$\Delta(2750)$	$I_{3\,13}$	**	**						
$\Delta(2950)$	$K_{3\,15}$	**	**						

**** Existence is certain, and properties are at least fairly well explored.
*** Existence ranges from very likely to certain, but further confirmation is desirable and/or quantum numbers, branching fractions, *etc.* are not well determined.
** Evidence of existence is only fair.
* Evidence of existence is poor.

Figure 2.5: Experimental status of nucleon resonances. The star rating for each resonance is explained in the table caption. Taken from reference [17].

Resonance	Our estimate	Our rating	KH	CM	Kent	GWU	BnGa
$N_{1/2^+}(1440)$	1450±32; 300±100	****	1410±12; 135±10	1440±30; 340±70	1462±10; 391±34	1485 ± 1; 284±18	1440±12; 335±50
$N_{3/2^-}(1520)$	1522 ± 4; 115±10	****	1519 ± 4; 114 ± 7	1525±10; 120±15	1524 ± 4; 124 ± 8	1516± 1; 99± 3	1524 ± 4; 117 ± 6
$N_{1/2^-}(1535)$	1538±10; 175±45	****	1526 ± 7; 120±20	1550±40; 240±80	1534 ± 7; 151±27	1547 ± 1; 188± 4	1535±20; 170±35
$N_{1/2^-}(1650)$	1660±18; 165±25	****	1670 ± 8; 180±20	1650±30; 150±40	1659 ± 9; 170±12	1635 ± 1; 115 ± 3	1680±40; 170±45
$N_{5/2^-}(1675)$	1675 ± 5; 153±22	****	1679 ± 8; 120±15	1675±10; 160±20	1676 ± 2; 159± 7	1674 ± 1; 147 ± 1	1678 ± 5; 177±15
$N_{5/2^+}(1680)$	1683 ± 3; 126 ± 9	****	1684 ± 3; 128± 8	1680±10; 120±10	1684 ± 4; 139± 8	1680 ± 1; 128 ± 1	1685 ± 5; 117±12
$N_{3/2^-}(1700)$	1725±50; 190±110	***	1731±15; 110±30	1675±25; 90±40	1737±44; 250±230	-	1730±40; 310±60
$N_{1/2^+}(1710)$	1713±12;220±180	***	1723 ± 9; 120±15	1700±50; 90±30	1717±28; 480±330	-	1725±25;200±35
$N_{3/2^+}(1720)$	1730±30; 320±210	****	1710±20; 190±30	1700±50; 125±70	1717±31; 380±180	1750 ± 5; 256±22	1770±100; 650±120
$N_{3/2^-}(1860)$	1850±40; 260±170	**	-	1880±100; 180±60	1804±55; 450±185	-	1870±25;150±40
$N_{5/2^+}(1870)$	1880±40; 270±180	$\overline{**}$	1882±10; 95±20	-	1903±87; 490±310	1818; 118	1910±50; 360±80
$N_{1/2^+}(1880)$	1890±50; 210±100	*	-	-	1885±30; 113±44	-	1900±30; 300±40
$N_{3/2^+}(1900)$	1940±50; 340±150	*	-	-	1879±17; 498±78	-	1960±30; 185±40
$N_{1/2^-}(1905)$	1905±50; 250±150	*	1880±20; 95±30	-	1928±59; 414±157	-	-
$N_{7/2^+}(1990)$	2020±60; 410±110	**	2005±150; 350±100	1970±50; 350±120	2086±28; 535±120	-	-
$N_{3/2^-}(2080)$	2100±55; 310±110	$\overline{**}$	2080±20; 265±40	2060±80; 300±100	-	-	2160±35; 370±50
$N_{1/2^-}(2090)$				2180±80; 350±100	-	-	-
$N_{1/2^+}(2100)$	2090±100; 230±200	*	2050±20; 200±30	2125±75; 260±100	-	-	-
$N_{5/2^-}(2200)$	2160±85; 350±50	**	2228±30; 310±50	2180±80; 400±100	-	-	2065±25; 340±40
			KH	CM	Kent	GWU	Hendry
$N_{7/2^-}(2190)$	2150±30; 440±110	****	2140±12; 390±30	2200±70; 500±150	2127± 9; 550±50	2152±2; 484±13	2140± 40; 270± 50
$N_{9/2^+}(2220)$	2260±60; 490±115	****	2205±10; 365±30	2230±80; 500±150	-	2316±3; 633±17	2300±100; 450±150
$N_{9/2^-}(2250)$	2255±50; 420±150	****	2268±15; 300±40	2250±80; 400±120	-	2302±6; 628±28	2200±100; 350±100
$N_{11/2^-}(2600)$	2630±120; 650±250	**	2577±50;400±100	-	-	-	2700±100; 900±100
$N_{13/2^+}(2700)$	2800±160; 600±300	**	2612±45; 350±50	-	-	-	3000±100; 900±150
			KH	CM	Kent	GWU	BnGa
$\Delta_{3/2^+}(1232)$	1232 ± 1; 118 ± 2	****	1232 ± 3; 116 ± 5	1232 ± 2; 120 ± 5	1231 ± 1; 118 ± 4	1233 ± 1; 119 ± 1	1230 ± 2; 112 ± 4
$\Delta_{3/2^+}(1600)$	1615±80; 360±120	***	1522±15; 220±40	1600±50; 300±100	1706±10; 430±73	-	1640±40; 480±100
$\Delta_{1/2^-}(1620)$	1626±23; 130 ± 45	****	1610 ± 7; 139±18	1620±20; 140±20	1672 ± 7; 154±37	1614 ± 1; 71 ± 3	1625±10; 148±15
$\Delta_{3/2^-}(1700)$	1720±50; 370±200	****	1680±70; 230±80	1710±30; 280±80	1762±44; 600±250	1688 ± 3; 182 ± 8	1780±40; 580±120
$\Delta_{1/2^+}(1750)$			-	-	1744±36; 300±120	-	-
$\Delta_{1/2^-}(1900)$	1910±50; 190±100	**	1908±30; 140±40	1890±50; 170±50	1920±24; 263±39	-	-
$\Delta_{5/2^+}(1905)$	1885±25; 330 ± 50	****	1905±20; 260±20	1910±30; 400±100	1881±18; 327±51	1856 ± 2; 321± 9	1870±32; 340±32
$\Delta_{1/2^+}(1910)$	1935±90; 280±150	****	1888±20; 280±50	1910±40; 225±50	1882±10; 229±25	2068 ± 2; 543±10	-
$\Delta_{3/2^+}(1920)$	1950±70; 260±100	***	1868±10; 220±80	1920±80; 300±100	2014±16; 152±55	-	1995±40; 360±50
$\Delta_{5/2^-}(1930)$	1930±30; 350±170	$\overline{**}$	1901±15; 195±60	1940±30; 320±60	1956±22; 530±140	-	-
$\Delta_{3/2^-}(1940)$	1995±60; 340±130	$\overline{**}$	-	1940±100;200±100	2057±110; 460±320	-	1995±40; 360 ± 50
$\Delta_{7/2^+}(1950)$	1930±16; 285 ± 45	****	1913 ± 8; 224±10	1950±15; 340±50	1945 ± 2; 300 ± 7	1921± 1; 271 ± 1	1928±8; 290±14
$\Delta_{5/2^+}(2000)$			2200±125;400±125	-	1752±32; 251±93	-	-
$\Delta_{1/2^-}(2150)$			-	2200±100; 200±100	-	-	-
			KH	CM	Kent	GWU	Hendry
$\Delta_{7/2^-}(2200)$	2230 ± 50; 420±100	**	2215±10; 400±100	2200±80; 450±100	-	-	2280±80; 400±150
$\Delta_{9/2^+}(2300)$	2360±125; 420±200	**	2217±80; 300±100	2400±125; 425±150	-	-	2450±100; 500±200
$\Delta_{5/2^-}(2350)$	2310 ± 85; 490±250	***	2305±26; 300 ± 70	2400±125; 400±150	-	2233±53; 773±187	-
$\Delta_{7/2^+}(2390)$	2390±100; 300±200	*	2425 ± 60; 300 ± 80	2350±100; 300±100	-	-	-
$\Delta_{9/2^-}(2400)$	2400±190; 530±300	**	2468±50;480±100	2300±100; 330±100	-	2643±141; 895±432	2200±100; 450±200
$\Delta_{11/2^+}(2420)$	2462±120; 490±150	***	2416 ± 17; 340±28	2400±125; 450±150	-	2633±29; 692 ± 47	2400±60; 460±100
$\Delta_{13/2^-}(2750)$	2720±100; 420±200	**	2794±80; 350±100	-	-	-	2650±100; 500±100
$\Delta_{15/2^+}(2950)$	2920±100; 500±200	**	2990±100; 330±100	-	-	-	2850±100; 700±200

Figure 2.6: Breit-Wigner masses and widths (in MeV) of resonance states extracted with different partial wave analyses [18]. For a discription of the different partial wave analyses see reference [18].

based on ideas from QCD. A long range two-body potential between the constituent quarks was used to model quark confinement, with a one-gluon-exchange (OGE) approximation to model short-range interactions.

Other quark models include Goldstone-exchange models [21], where pions are exchanged between light quarks in the nucleon, bag models where massless quarks are confined to a deep potential well and cloudy bag models [22], which introduces a pion cloud to maintain chiral symmetry at the nucleon surface. For a review of quark models see reference [23].

2.4.2 Skyrme models

The Skyrme model [24] describes the nucleon as a soliton of the chiral field. The quantisation of the rotation of the soliton gives rise to the spin and parity of the excited states of the nucleon. The states can therefore be considered different rotational states of the same particle. The model was succesful in predicting the baryon octet and decuplet of states with spins 1/2 and 3/2 respectively. the mass differences between nucleons in these multiplets were calculated to within 1% of the accepted masses [25].

2.4.3 Missing and poorly understood resonances

Many nucleon resonances predicted by constituent quark models have not been observed in experimental measurements. One possibility is that the models are not adequately describing the dynamics of the nucleon system. As a general rule, the number of predicted resonances scales with the degrees of freedom in the model. As one possible explanation for the poor agreement between constituent quark models and experimental data, diquark models [26] were formulated in which two of the quarks were tightly bound inside the hadron. This was proposed as being due to completely anti-symmetric wavefunctions between u and d quarks.

Santopinto [27] used a diquark model to successfully predict low lying nucleon resonances. A signature of this model would be the production of a state with angular momentum 1 and positive parity, however this is hard to measure experimentally as it requires the strong interaction from a hadronic probe with spin transfer. Lattice QCD calculations [28] suggested that diquarks do not form and

partial wave analysis (decribed in section 2.5.3) [29], suggested that a diquark model would calculate unrealistically large widths to the resonances (albeit with limited experimental data in 1981).

Capstick and Roberts [30] suggested that resonances predicted by quark models which have not been observed experimentally may not couple to the extensively measured $N\pi$ channels. Adapting a previous quark model [31] which used a relativised model of the quarks and included spin dependent interaction terms, they demonstrated that many missing and poorly established resonances have substantial amplitudes to final states containing hadrons of non-zero strangeness (fig. 2.7). This is a major motivation for the study of strangeness production to improve our knowledge of baryon spectroscopy.

2.5 Photoproduction

This section presents the theoretical formalism used to describe the photoproduction process, and a discussion of the partial wave analysis techniques used to extract information on nucleon resonances from experimental data.

2.5.1 The production process formalism

The Mandelstam variables s, t and u are commonly used to describe the kinematics of a scattering or production process in a Lorentz invariant fashion. Consider the reaction in fig. 2.8. The Mandelstam variables are defined in terms of the particle four-momenta:

$$\begin{aligned} s &= (k + p_i)^2 = (q + p_f)^2 \\ t &= (p_i - p_f)^2 = (k - q)^2 \\ u &= (p_i - q)^2 = (k - p_f)^2 \end{aligned} \tag{2.12}$$

where the four-momentum of each particle is defined in terms of particle energy and three-momentum: $p = [E, \mathbf{p}]$. It is apparent that s gives you the square of the energy of the reaction: $s = W^2$, and t the square of the momentum transfer.

The scattering process can be represented by three different classes of Feynman diagrams; s-channel, u-channel and t-channel (fig. 2.9). For each process,

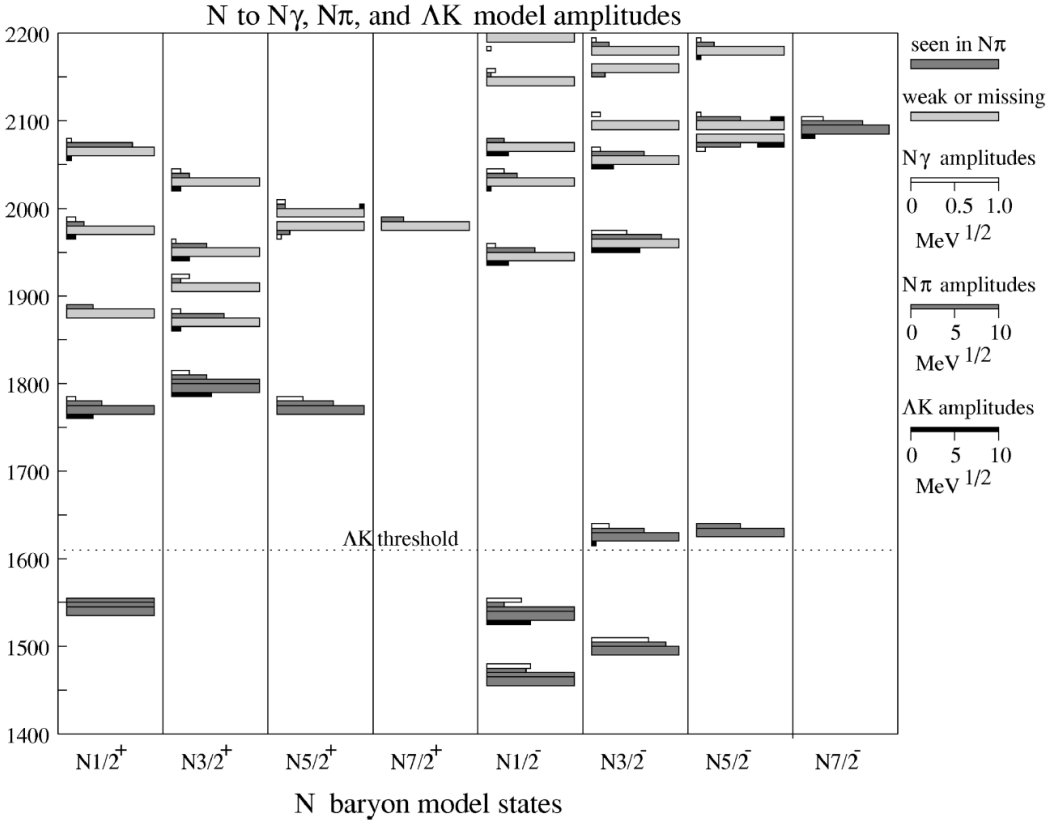

Figure 2.7: $N\gamma$, $N\pi$ and ΛK decay amplitude predictions for nucleon resonances using the CQM of Capstick and Roberts [30]. Whether the resonance is seen in $N\pi$ data or is missing, and the modelled strength of coupling to different final states is included as a legend on the right hand side. Taken from reference [30].

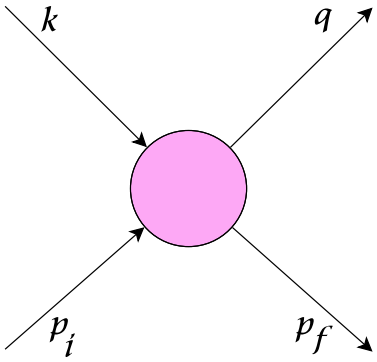

Figure 2.8: Schematic diagram of two incident particles with momenta k and p_i (the incident photon and target nucleon in photoproduction reactions) interacting, with two particles with momenta p_f and q left in the final state.

the square of the four-momentum of the intermediate particle is equal to the Mandelstam variable, s, t, or u respectively. Nucleon resonances contribute in the s-channel.

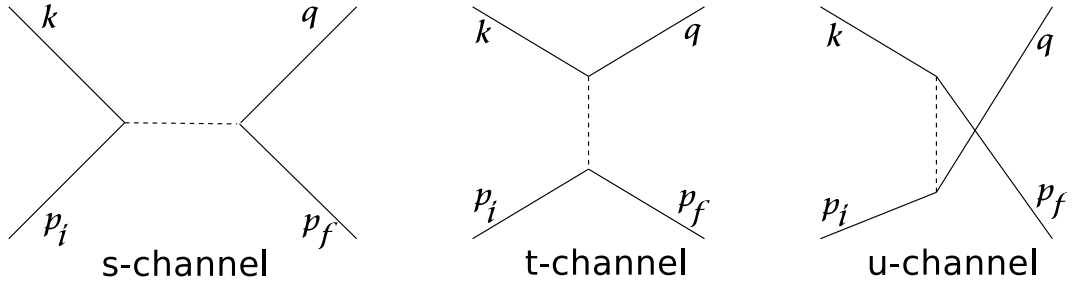

Figure 2.9: s, t and u-channel Feynman diagrams with intermediate states represented with a dotted line. Notation is of the particles momenta described in fig. 2.8.

2.5.2 Cross sections and polarisation observables

The photoproduction reaction is specified by the the momentum of the incident beam particle, k, the momentum of the target nuclei, p_i, and the momentum of

the outgoing meson, q. The independent variation of q and k allows the process to be explored over different spatial distributions and the entire process can be described by s and t. For a fixed value of s, t is a linear function of $\cos\theta$, where θ is the meson polar scattering angle in the centre of mass frame. The process can be described by a complex amplitude, $A(s, \cos\theta)$. The differential cross section for the reaction can then be described as:

$$\frac{d\sigma}{d\Omega} = |A_s(s, \cos\theta)|^2 \tag{2.13}$$

A scattering matrix, S is used to relate the initial and final states, the probability P_{fi} changing from initial state $\langle i|$ to final state $|f\rangle$ is given as:

$$P_{fi} = |\langle f|S|i\rangle|^2 \tag{2.14}$$

this is expressed in the Bjorken Drell notation [32] as:

$$P_{fi} = \delta_{fi} - \frac{i}{4\pi^2}\delta^4(P_f - P_i)(\frac{M^2}{4E_\gamma E_i E_q E_f})^{1/2}\langle f|T|i\rangle \tag{2.15}$$

where T is the transmission matrix; $T = \epsilon_\mu J_\mu$, where ϵ_μ is the photon polarisation vector and J_μ is the nucleon electromagnetic current. The differential cross section can be expressed in terms of the transmission matrix:

$$\frac{d\sigma}{d\Omega} = \frac{q}{k}\sum|\frac{M}{4\pi W}\langle f|T|i\rangle|^2 \tag{2.16}$$

where M is the mass of the nucleon and W is the invariant mass of the system.

For a given spin configuration, Chew, Goldberger, Low and Nambu [33] developed a parameterisation for the photoproduction of pseudoscalar mesons with nucleons, expressing the nucleon electromagnetic current in terms of the nucleon spin matrices σ and photon and meson unit vectors, $\hat{\mathbf{k}}$ and $\hat{\mathbf{q}}$:

$$\mathbf{J} = \frac{4\pi W}{M}(i\sigma F_1 + (\sigma\cdot\hat{\mathbf{k}})(\sigma\times\hat{\mathbf{q}})F_2 + i\tilde{\mathbf{k}}(\tilde{\sigma}\cdot\hat{\mathbf{q}})F_3 + i\tilde{\mathbf{k}}(\sigma\cdot\hat{\mathbf{k}})F_4 \tag{2.17}$$

where:

$$\tilde{\sigma} = \sigma - (\sigma\cdot\hat{\mathbf{q}})\hat{\mathbf{q}} \tag{2.18}$$

$$\tilde{\mathbf{k}} = \hat{\mathbf{k}} - (\hat{\mathbf{k}}\cdot\hat{\mathbf{q}})\hat{\mathbf{q}} \tag{2.19}$$

F_1, F_2, F_3 and F_4 are known as CGLN amplitudes and can be expressed in terms of angular momentum and electric and magnetic multipoles by a partial wave expansion:

$$\begin{aligned}
F_1(\theta) &= \sum_{l=0}^{\infty}(lM_{l+} + E_{l+})P'_{l-1}(\cos\theta) + ((l+1)M_{l-} + E_{l-})P'_{l-1}(\cos\theta) \\
F_2(\theta) &= \sum_{l=0}^{\infty}((l+1)M_{l+} + lM_{l-})P'_{l}(\cos\theta) \\
F_3(\theta) &= \sum_{l=0}^{\infty}(E_{l+} - M_{l+})P''_{l+1}(\cos\theta) + (E_{l-} + M_{l-})P''_{l-1}(\cos\theta) \\
F_4(\theta) &= \sum_{l=0}^{\infty}(M_{l+} - E_{l+} - M_{l-} - E_{l-})P''_{l}(\cos\theta)
\end{aligned} \tag{2.20}$$

where P'_l and P''_l are derivatives of Legendre polynomials, l is the relative orbital angular momentum of the meson and the $+$ or $-$ determines whether the spin of the baryon should be added or subtracted.

Fig. 2.10 depicts the photoproduction of a pseudoscalar meson, in this case a K^+ via the excitation of a nucleon resonance, N^*, with definite spin and parity. The expansion of the photon field into electric and magnetic multipoles with angular momentum L_γ and parity $\pi_\gamma = (-1)^{L_\gamma}$ or $\pi_\gamma = (-1)^{L_\gamma+1}$ for electric and magnetic multipoles respectively implies that the angular momentum of the resonance obeys the selection rule:

$$|L_\gamma - 1/2| \leq J_{N^*} \leq |L_\gamma + 1/2| \tag{2.21}$$

where the spin of the incident nucleon has magnitude $1/2$ and the total angular momentum of the photon, $L_\gamma = \ell + \mathbf{s}_\gamma$, where ℓ and $\mathbf{s}_\gamma$ are the angular momentum and spin of the photon.

When the resonance strongly decays to the pseudoscalar meson and baryon, the angular momentum and parity selection rules are given as:

$$|L_{K^+} - 1/2| \leq J_{N^*} \leq |L_{K^+} + 1/2| \tag{2.22}$$

$$\pi_{N^*} = \pi_N \pi_{K^+}(-1)^{L_{K^+}} = (-1)^{L_{K^+}+1} \tag{2.23}$$

The combination of these two sets of selection rules limits the spin and parity of the resonance to:

$$L_\gamma \pm 1/2 = J_{N^*} = L_{K^+} \pm 1/2 \tag{2.24}$$

$$\pi_{N^*} = \pi_\gamma = (-1)^{L_{K^+}+1} \tag{2.25}$$

By parity and conservation of angular momentum, two possibilities are allowed. The angular momentum of an electric multipole can be $L = L_{K^+} \pm 1$ and for a magnetic multipole can be only $L = L_{K^+}$.

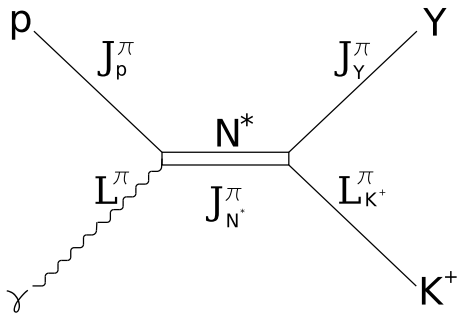

Figure 2.10: The photoproduction of a K^+ and hyperon (Y) in the s-channel via a resonance (N^*) state.

If a cross section is dominated by a single resonance, the quantum numbers are reflected in the angular distribution due to the dependance of the Legendre polynomials in the CGLN amplitudes. In π^0 photoproduction, for example, the $P_{33}(1232)$ (the Δ resonance) is derived from the M_{1+} multipole and the angular distribution follows a $5 - 3\cos^2\theta$ variation. It is not always this transparent; a $3/2^+$ resonance can be derived from an M1 or E2 multipole for instance, and most photoproduction mechanisms have more than one resonance contribution.

Isospin, which is conserved at the hadronic vertex but not at the electromagnetic vertex, provides a further constriant to the photoproduction process. The electromagnetic current consists of an isoscalar and an isovector component, where the isoscalar component conserves isospin and the isovector component allows isospin to change by one. The transmission matrix T can be split into

seperate isovector and isoscaler parts, producing three matrix elements following the notation $\langle I_f, I_{f3}|\hat{A}|I_i, I_{i3}\rangle$ [34] (eq. 2.26).

$$\begin{aligned} A^{IS} &= \langle\frac{1}{2},\pm\frac{1}{2}|\hat{S}|\frac{1}{2},\pm\frac{1}{2}\rangle \\ \mp A^{IV} &= \langle\frac{1}{2},\pm\frac{1}{2}|\hat{V}|\frac{1}{2},\pm\frac{1}{2}\rangle \\ A^{V3} &= \langle\frac{3}{2},\pm\frac{1}{2}|\hat{V}|\frac{1}{2},\pm\frac{1}{2}\rangle \end{aligned} \tag{2.26}$$

A complete characterisation of the amplitudes therefore also requires photoproduction measurements off the neutron and proton.

The isospin amplitudes can be expressed as four s-channel helicity amplitudes; $T^{\lambda_\gamma}_{\lambda_N\lambda_{N'}}$, where λ_γ is the photon helicity, and λ_N and $\lambda_{N'}$ the helicity of the initial and final nucleons. These can be expressed as a non-flip, two single flip and a double flip amplitude (N, S_1, S_2 and D respectively):

$$\begin{aligned} N \equiv T^1_{+-} = T^{-1}_{-+} \qquad S_1 \equiv T^1_{--} = T^{-1}_{++} \\ S_2 \equiv T^1_{++} = T^{-1}_{--} \qquad D \equiv T^1_{-+} = T^{-1}_{+-} \end{aligned} \tag{2.27}$$

The helicity amplitudes are normalised such that the sum of their squares determines the differential unpolarised cross section:

$$\frac{d\sigma}{d\Omega} = |N|^2 + |S_1|^2 + |S_2|^2 + |D|^2 \tag{2.28}$$

The amplitudes can also be writted in transversity form [35]:

$$\begin{aligned} b_1 &= \frac{1}{2}[(S_1+S_2)+i(N-D)] \quad b_3 = \frac{1}{2}[(S_1-S_2)-i(N+D)] \\ b_2 &= \frac{1}{2}[(S_1+S_2)-i(N-D)] \quad b_4 = \frac{1}{2}[(S_1-S_2)+i(N+D)] \end{aligned} \tag{2.29}$$

From either the helicity or transversity amplitudes, sixteen independent experimental polarisation observables can be measured. The differential cross section and polarisation observables require different combinations of beam polarisation (circular or linear), target polarisation (transverse or longitudinal) and recoil nucleon polarisations (tranverse or longitudinal). The single polarisation observables, Σ, T and P require the polarisation of the beam, the target, and the recoiling baryon respectively. There are three sets of double polarisation observables:

G, H, E and F, which are different combinations of beam target polarisation, O_X, O_Z, C_X and C_Z, which are combinations of beam recoil polarisation and T_X, T_Z, L_X and L_Z, which are combinations of target-recoil polarisation. How each of the polarisation observables are related to the amplitudes is tabulated in 2.2.

The single polarisation observables are only constructed from combinations of the magnitudes of the transversity amplitudes. Double polarisation observables are therefore required to obtain information on the phase difference of the amplitudes and provide a "complete measurement" in which the phase and magnitude can be unambiguously constrained. The polarisation observables required for a complete measurement was contested until Barker, Donnachie and Storrow [35] proved that all of the single polariation observables and a further five double polarisation with no more than three from the same set were required.

Useful information has been extracted from differential cross section measurements by fitting existing data sets with model dependent calculations. This of course is very sensitive on the model inputs, examples include isobar models [36], coupled channel analysis [37] and effective field Lagrangians based on chiral perturbation theory [38] which are all described in section 3.

2.5.3 Partial wave analysis

Partial wave analyses provide a tool for extracting the amplitudes, masses and widths of resonances from experimental data by decomposing the transmission matrix into a series of partial waves of definite angular momenta and multipoles. The majority of partial wave analyses begin with the separation of the transmission matrix into background and resonance terms. This procedure is presented in this section.

The Hamiltonian describing the meson baryon interaction can be described as:

$$H = H_0 + V_{BG} + V_R(E) \tag{2.30}$$

where H_0 is the free Hamiltonian describing the kinetic energy of the photon, meson and baryons, and V_{BG} and $V_R(E)$ are the potentials due to background

Usual symbols	Helicity representation	Transversity representation	Experiment required[a]
σ/t	$\|N\|^2+\|S_1\|^2+\|S_2\|^2+\|D\|^2$	$\|b_1\|^2+\|b_2\|^2+\|b_3\|^2+\|b_4\|^2$	$\{-;-;-\}$
Σ	$2\Re(S_1^*S_2 - ND^*)$	$\|b_1\|^2+\|b_2\|^2-\|b_3\|^2-\|b_4\|^2$	$\{L(\frac{\pi}{2},0);-;-\}$ $\{-;y;y\}$
T	$2\Im(S_1N^* - S_2D^*)$	$\|b_1\|^2-\|b_2\|^2-\|b_3\|^2+\|b_4\|^2$	$\{-;y;-\}$ $\{L(\frac{\pi}{2},0);0;y\}$
P	$2\Im(S_2N^* - S_1D^*)$	$\|b_1\|^2-\|b_2\|^2+\|b_3\|^2-\|b_4\|^2$	$\{-;-;y\}$ $\{L(\frac{\pi}{2},0);y;-\}$
G	$-2\Im(S_1S_2^* + ND^*)$	$2\Im(b_1b_3^* + b_2b_4^*)$	$\{L(\pm\frac{\pi}{4});z;-\}$
H	$-2\Im(S_1D^* + S_2N^*)$	$-2\Re(b_1b_3^* - b_2b_4^*)$	$\{L(\pm\frac{\pi}{4});x;-\}$
E	$\|S_2\|^2-\|S_1\|^2-\|D\|^2+\|N\|^2$	$-2\Re(b_1b_3^* + b_2b_4^*)$	$\{c;z;-\}$
F	$2\Re(S_2D^* + S_1N^*)$	$2\Im(b_1b_3^* - b_2b_4^*)$	$\{c;x;-\}$
O_x	$-2\Im(S_2D_2^* + S_1N^*)$	$-2\Re(b_1b_4^* - b_2b_3^*)$	$\{L(\pm\frac{\pi}{4});-;x'\}$
O_z	$-2\Im(S_2S_1^* + ND^*)$	$-2\Im(b_1b_4^* + b_2b_3^*)$	$\{L(\pm\frac{\pi}{4});-;z'\}$
C_x	$-2\Re(S_2N^* + S_1D^*)$	$2\Im(b_1b_4^* - b_2b_3^*)$	$\{c;-;x'\}$
C_z	$\|S_2\|^2-\|S_1\|^2-\|N\|^2+\|D\|^2$	$-2\Re(b_1b_4^* + b_2b_3^*)$	$\{c;-;z'\}$
T_x	$2\Re(S_1S_2^* + ND^*)$	$2\Re(b_1b_2^* - b_3b_4^*)$	$\{-;x;x'\}$
T_z	$2\Re(S_1N^* + S_2D^*)$	$2\Im(b_1b_2^* - b_3b_4^*)$	$\{-;x;z'\}$
L_x	$2\Re(S_2N^* - S_1D^*)$	$2\Im(b_1b_2^* + b_3b_4^*)$	$\{-;z;x'\}$
L_z	$\|S_1\|^2+\|S_2\|^2-\|N\|^2-\|D\|^2$	$2\Re(b_1b_2^* - b_3b_4^*)$	$\{-;z;z'\}$

[a] Notation is $\{P_\gamma; P_T; P_R\}$ where:
P_γ = polarisation of beam,
$L(\theta)$ = beam linearly polarised at angle θ to scattering plane,
C = circularly polarised beam;
P_T = direction of target polarisation;
P_R = component of recoil polarisation measured.

Table 2.2: Helicity and transversity representations of polarisation observables. [35].

(non-resonant) and resonant terms. The resonant potential is given as [39]:

$$V_R(E) = \sum_{a,b} \sum_{N_i^*} \frac{\Gamma_{i,a}^{\dagger} \Gamma_{i,b}}{E - M_i^0} \tag{2.31}$$

where E is the total energy of the system, $\Gamma_{i,a}$ is the decay of the ith N^* state to state a, and M_i^0 is related to the mass position of the resonance.

The transmission matrix going from state a to b via c (for example, $\gamma p \rightarrow P_{33}(1232) \rightarrow p\pi^0$), is given as [39]:

$$T_{a,b}(E) = V_{a,b} + \sum_c V_{a,c} g_c(E) T_{c,b}(E) \tag{2.32}$$

with the propagator of channel c:

$$\begin{aligned} g_c(E) &= \langle c|g(E)|c\rangle & (2.33)\\ g(E) &= \frac{1}{E - H_0 + i\epsilon} & (2.34)\\ &= g^P(E) - i\pi\delta(E - H_0) & (2.35) \end{aligned}$$

where:

$$g^P(E) = P\frac{1}{E - H_0} \tag{2.36}$$

The K-matrix can now be defined as:

$$K_{a,b}(E) = V_{a,b} + \sum_c V_{a,c} g_c^P(E) K_{c,b}(E) \tag{2.37}$$

The K-matrix and T-matrix are then be related as:

$$T_{a,b}(E) = K_{a,b}(E) - \sum_c T_{a,c}(E)[i\pi\delta(E - H_0)_c K_{c,b}(E) \tag{2.38}$$

The transmission matrix can be split into separate background and resonance terms:

$$T_{a,b}(E) = t_{a,b}^{bg}(E) + t_{a,b}^{R}(E) \tag{2.39}$$

where the sum over all states includes all possible angular momenta and isospin quantum numbers. Separating the transmission matrix in this way allows seperate calculations for the background and resonance contributions.

Two major partial wave models which use this as a starting point to describe photoproduction are MAID [36, 40, 41] and SAID [42, 43, 44].

The Kaon-MAID model, specific to strangeness photoproduction, describes the transmission-matrix in terms of a single channel, splitting this into separate background and resonance terms as described above. The resonant terms are expanded into a series of partial waves, with definite multipoles, angular momentum and parity. A Born approximation with single intermediate particle states is used to model the background terms.

The resonant T-matrix is parameterised into a Breit Wigner form and fitted to current experimentally verified states according to the PDG classification [17]. The current Kaon-Maid model includes the $S_{11}(1650)$, $P_{11}(1710)$, $P_{13}(1720)$ and $D_{13}(1900)$ resonances.

The SAID analysis [42, 43, 44] makes no assumptions on resonance contributions and channels to include in the partial wave analysis. The entire resonance coupling amplitudes are extracted from the determination of multipoles from data.

The SAID analysis uses three channels (γN, πN, and $\pi\Delta$) to describe all open channels. The T-matrix can then be described as:

$$T_{\gamma N,\pi M} = A_1(1 + iT_{\pi N,\pi N}) + A_R T_{\pi N,\pi N} \tag{2.40}$$

where A_I and A_R parameterise the background and resonance terms respectively. A_R is given as:

$$A_R = \frac{m_\pi}{k_0}(\frac{q_0}{k_0})^{l_\alpha} \sum_{n=0}^{N} p_n (\frac{E_\pi}{m_\pi})^n \tag{2.41}$$

where k_0 and q_0 are the on-shell momenta for the pion and photon and P_n is a free parameter.

The potential due to background interactions is calculated from partial wave analysis of Born terms and Legendre polynomials. This fixes the free parameter p_n. Resonance amplitudes are then extracted from multipoles close to resonance positions using Breit-Wigner parameterisations.

The development of the SAID framework for strangeness photoproduction is in progress.

Chapter 3

Current status of $K^+\Lambda$ photoproduction

Data from $\gamma(p, K^+)\Lambda$ and $\gamma(p, K^+)\Sigma^0$ measurements can be split into two categories: old data prior to 1980 and new data post 1990. A review of the old data sets can be found in reference [45]. The statistical accuracy of old data was poor and no resonance structure from cross section measurements could be extracted. There was a lack of data from the 1980s, and it was the construction of the accelerator facilities such as JLab, ELSA and SPring8, with higher statistics data which reignited theoretical interest in strangeness photoproduction. The measurements and fits from theoretical models discussed in the remainder of this chapter focus on the new data, predominantly from the SAPHIR detector (section 3.1.1) and the CLAS detector (section 3.1.2).

3.1 Cross section measurements

3.1.1 SAPHIR cross section measurement

K. H. Glander *et al.* [46], made the first detailed cross section measurements for photoproduction of $K^+\Lambda$ and $K^+\Sigma^0$. Data was taken from threshold to 2.6 GeV using the ELSA electron accelerating facility [47] and the SAPHIR (Spectrometer Arrangement for PHoto Induced Reactions) detector [48].

ELSA accelerated electrons to an energy of 3.5 GeV. These were incident upon a thin metal radiator producing energy tagged bremstrahlung radiation up to an energy of 2.6 GeV. Fig. 3.1 is a schematic of the SAPHIR detector. The detector was based around a central drift chamber[1] (CDC) in a volume between two magnetic pole pieces. At the front and sides of the CDC were three planar drift chambers, and surrounding these were scintillator hodoscopes for time of flight measurements. In the centre of the drift chamber was a liquid hydrogen target.

The drift chambers measured particle momenta through the curving of their trajectory in the magnetic field, and reconstructed the vertices of the reaction in the target and the vertex of the Λ decay in the drift chamber. The scintillator hodoscope measured the time of flight of reaction products from the target. Combining the measurements between the scintillator hodoscope and the drift chambers allowed the mass of the reaction products to be determined. The drift chambers completely surrounded the target to allow a large angular acceptance of detection. Consequently, the photon flux was kept low to avoid exceeding the maximum load of the cells in the drift chamber.

Events were reconstructed from the incident photon energy which was measured in the SAPHIR tagging system, and the charged particles identified in the drift chambers. The analysis required the identification of two positive tracks and one negative track in the drift chamber. These corresponded to the K^+, and the proton and π^- from the Λ decay. The vertices of the reactions were reconstructed from these tracks. Two separate detached vertices were required; the initial vertex where the K^+ and Λ were produced, and a second vertex from the decay: $\Lambda \rightarrow p\pi^-$. The momentum of the K^+ and Λ were reconstructed to determine the primary vertex in the target.

The missing mass, M of the incident photon and proton momentum (p_γ and

[1] A drift chamber is series of drift cells. Each cell has a perimeter of field shaping wires with a negative bias and a central sense wire with a positive bias. As a charged particle passes through the cell, electrons are liberated from the gas in the cell and detected on the sense wire. Tracks of charged particles can thus be reproduced with a fine mesh of drift cells. For a detailed description of drift chambers see reference [49, 50].

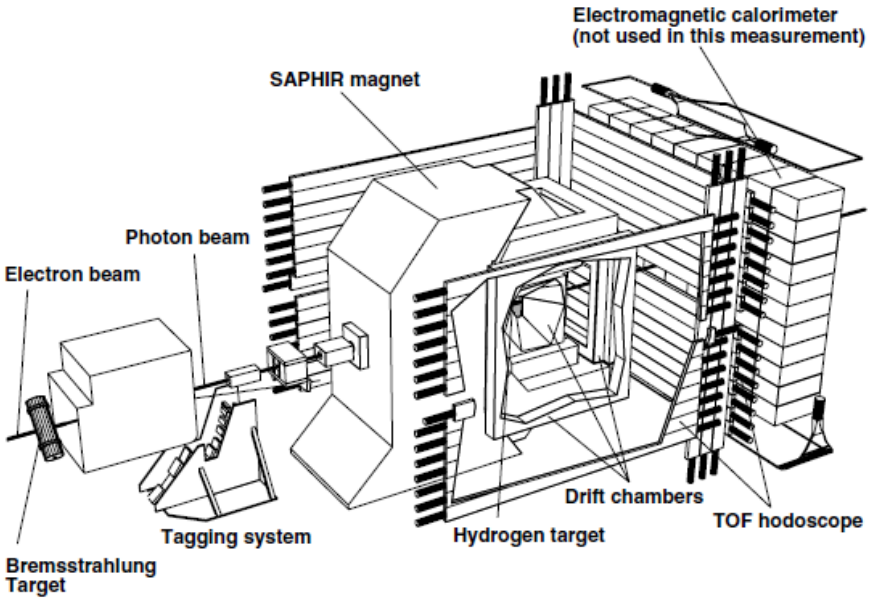

Figure 3.1: The SAPHIR detector [46].

p_p), minus the detected K^+ momentum (p_{K^+}) was calculated from eq. 3.1.

$$M = \sqrt{(p_\gamma + p_p - p_{K^+})^2} \tag{3.1}$$

The distribution of the missing mass showed expected peaks over the Λ and Σ^0 masses but with a large background (fig. 3.2(a)). A small peak could also be seen corresponding to the masses of the $\Lambda(1405)$ and $\Sigma^0(1385)$. To reduce the background from other reaction channels, a series of selection cuts were used:

1. The reconstructed vertex of the K^+ and Λ production had to be within the volume of the target.

2. The invariant mass reconstructed from the detected proton and π^- (the Λ decay products) had to be within 8 MeV of the Λ mass.

3. To select $\gamma(p, K^+)\Lambda$, the missing mass in eq. 3.1 had to be within 1000-1240 MeV and for $\gamma(p, K^+)\Sigma^0$, the missing mass had to be within 1050-1350 MeV.

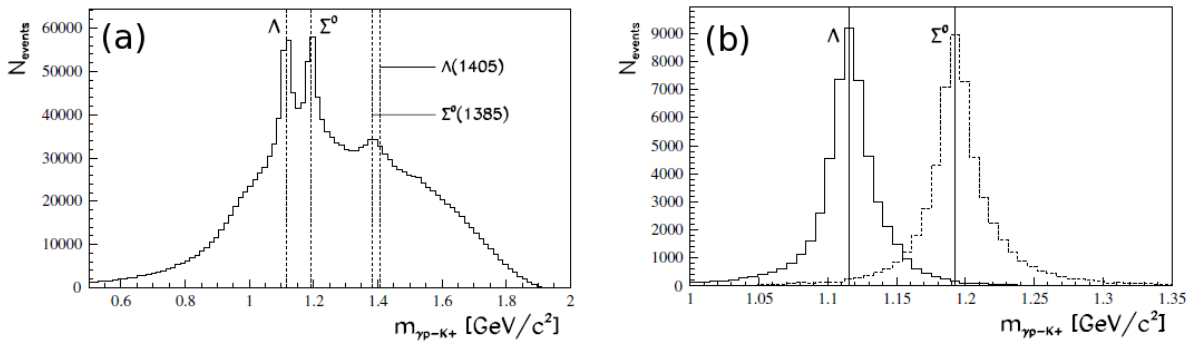

Figure 3.2: (a) Missing mass from the K^+ with two tracks required in the drift chamber and (b) after the selection cuts to reduce background from other reaction channels. Taken from [46].

After the selection cuts, nearly 52 thousand $K^+\Lambda$ and 54 thousand $K^+\Sigma^0$ remained (fig. 3.2(b)). To check other reaction channels were not significantly contaminating the data sample, the time difference between the vertex in the target and the second vertex from the Λ decay was fitted with an exponential function (fig. 3.3). Setting the decay time to the lifetime of Λ (approximately 26 ns) described the experimental data well. If other reaction channels (such as $\gamma p \rightarrow p\pi^+\pi^-$) were passing the selection cuts, a greater proportion of events would have a smaller decay time, spoiling the exponential fit.

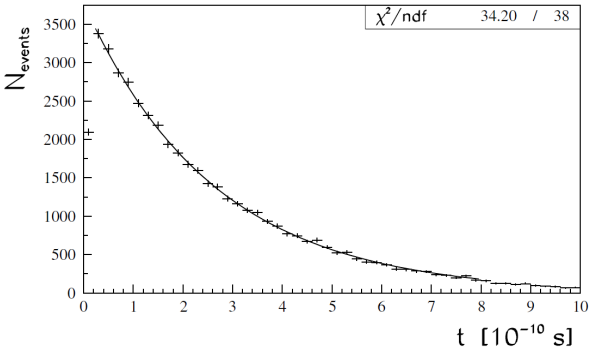

Figure 3.3: Time difference between the reaction vertex in the target and the reconstructed vertex of the Λ decay. Taken from [46]

A simulation of the photon tagger and scintillation hodoscopes was used to measure the detection efficiency. To correct for $K^+\Lambda$ events migrating into the events selected as $K^+\Sigma^0$ and vice-versa, a Monte Carlo generated sample of each reaction channel was input into the simulation. The yields were altered according to the fraction of events which had migrated into the incorrect event sample (of the order of 7% of $K^+\Lambda$ into $K^+\Sigma^0$ and 2% of $K^+\Sigma^0$ into $K^+\Lambda$).

3.1.2 Jefferson Lab cross section measurements

Bradford *et al.* [51] extracted differential cross sections for $\gamma p \rightarrow K^+\Lambda$ and $\gamma p \rightarrow K^+\Sigma^0$ from threshold to 2.95 GeV with the CLAS detector at Jefferson Lab in 2006.

The CLAS detector [52] is a magnetic toroidal spectrometer (fig. 3.4) split into six segments with superconducting coils providing the magnetic field. The trajectories of charged particles were measured in the drift chambers, with plastic scintillator detectors placed outside of the chambers to measure the time of flight of particles. At forward angles, gas cerenkov detectors identified electrons and electromagnetic calorimeters identified showering particles (photons and electrons). At the centre of CLAS was a 40 cm long liquid hydrogen target surrounded by a segmented ring of plastic scintillators which detected outgoing particles and provided a starting time for time of flight identification. CLAS provided the charge, momentum, and mass of particles of interest with nearly 4π steradian acceptance (although at certain angles there was zero acceptance due to the magnetic coils).

Similar to the SAPHIR detector, particles were identified by tracking their momenta in the magnetic field and by time of flight techniques (TOF). The event sample required the detection of a K^+ in coincidence with a proton from the decay: $\Lambda \rightarrow p\pi^-$. The kinetic energy of the K^+ and proton were corrected for the energy loss in the material of the detector, and the missing mass from the K^+ and the proton was reconstructed. Events were selected where the missing mass was consistent with the π^- mass.

From this event sample, the missing mass of the K^+ was reconstructed, with peaks at the Λ and Σ^0 masses. The yields of the $\gamma(p, K^+)\Lambda$ and $\gamma(p, K^+)\Sigma^0$ channels were extracted from fits to the misssing mass plots. The width of the

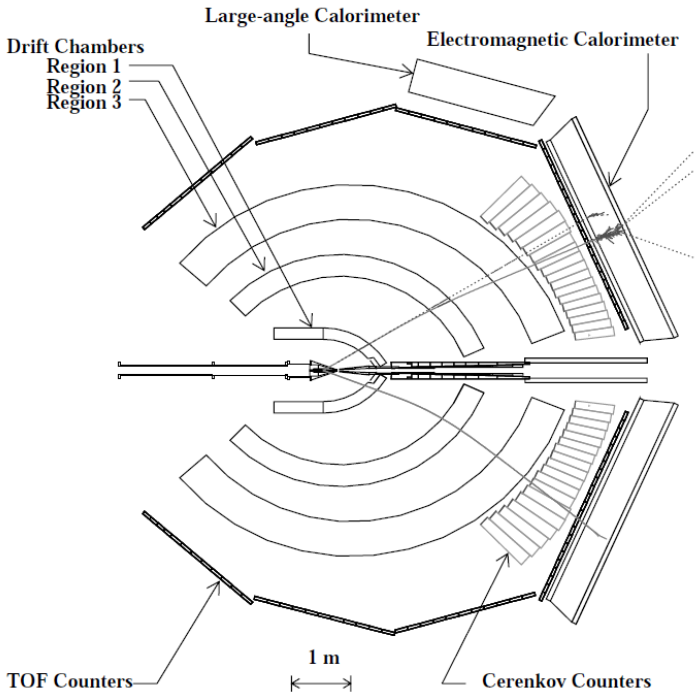

Figure 3.4: Cross section along the beam line of the CLAS detector [52].

mass peaks and the extent of background varied depending on the incident photon beam energy.

To constrain fits for ranges with few data points, the event sample was first fitted to 25 MeV beam energy ranges and all polar angles. Two Gaussian functions were used to describe the Λ and Σ^0 mass peaks, with the background described as a polynomial. Each energy range was split further into $\cos(\theta_{cm})$ ranges of 0.1 (where θ_{cm} is the centre of mass polar angle of K^+ detection). Each of these smaller ranges were fitted in the same manner to the previous sample (fig. 3.5), however the widths and centroids of the Gaussians and the shape of the background were constrained by the fits to the data over all angles.

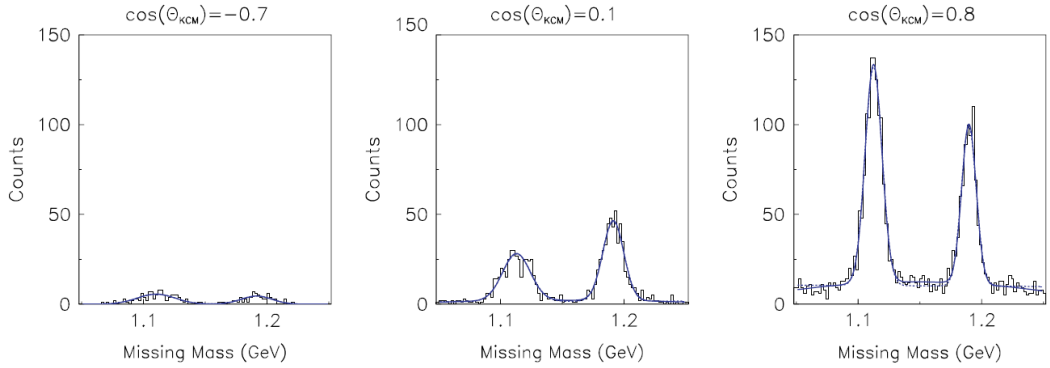

Figure 3.5: K^+ missing mass at an incident photon beam energy of 1.825 GeV for polar angles $\cos(\theta_{cm})$ = -0.7, 0.1, 0.8. The sum of two Gaussian functions (for the hyperon mass peaks) and a polynomial to the background has been fitted (blue line). Taken from [51].

Systematic uncertainties in the cross section were estimated from the measurement of the well known cross section $p(\gamma, \pi^+)n$ using as similar method of analysis as possible. This was compared to the SAID [53] parameterisation of the world data set, giving an estimated systematic uncertainty of less then 7%. Including additional systematic uncertainties from the yield extraction, the detector model and track reconstruction, gave an overall uncertainty of 8%.

Recent measurements with the CLAS detetector from a different data set by McCracken *et al* [54] have extracted cross sections broadly consistent with the

previous analysis by Bradford *et al.*

3.1.3 Discrepancies in the CLAS and SAPHIR data sets

Fig. 3.6 is the total $\gamma(p, K^+)\Lambda$ cross sections from the SAPHIR [46] and CLAS [51] data sets. Neither data sets had complete kinematic coverage and relied on the extrapolation into unmeasured kinematic regions. It is clear there are large discrepancies between the data sets.

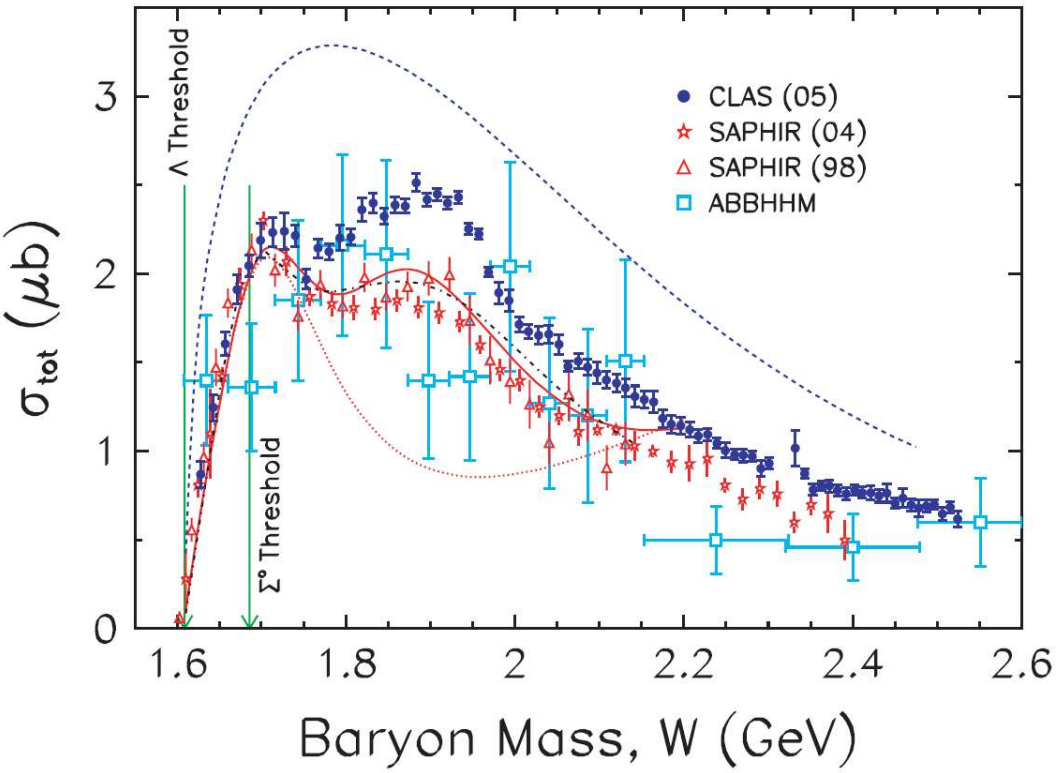

Figure 3.6: Total cross sections from SAPHIR [46] and CLAS [51] detectors. The red triangular points are from earlier measurements with the SAPHIR detector [55] and light blue squares from the ABBHHM collaboration in 1969 [45]. The dashed blue line is a Regge parameterisation [56, 57] (section 3.3.5), the dotted and solid red lines are Kaon-Maid predictions [41] with and without the D_{13} resonance and the dot-dashed black line is an isobar model [58] (section 3.3.2). Taken from [51].

The CLAS data is statistically more precise than the SAPHIR data, however the SAPHIR data has better coverage at more extreme forward and backward angles. The cross sections extracted from the CLAS data set are approximately 1.3 times that of the SAPHIR data above a centre of mass energy of 1.9 GeV. Section 3.3 describes theoretical models and fits to these data sets, and outlines how this discrepancy has serious consequences in interpreting the resonances contributing to the reaction.

3.1.4 The LEPS cross section measurements

The LEPS (Laser-Electron Photon) beam line at the SPRING8 facility was used to measure $K^+\Lambda$ cross sections at forward angles (centre of mass angles smaller than 60^0) for photon beam energies 1.5 to 2.4 GeV [59]. Whilst the energy regime does not overlap the beam energy at MAMI-C, the measurements provide a further constraint on the resonance spectrum and background contributions.

The photon beam was produced by compton scattering laser light off an 8 GeV electron beam at the SPring-8 facility in Japan. The photon beam was incident upon a liquid hydrogen target at the centre of the LEPS spectrometer.

The LEPS spectrometer was designed for the detection of charged hadrons at forward angles. The main features were a large dipole magnet and drift chambers for track reconstruction with a TOF wall at forward angles. The predominant method of $K^+\Lambda$ identification was from K^+ missing mass reconstruction.

The data were consistent with CLAS measurements [51] in the overlapping kinematic region.

3.2 Measurements of polarisation observables for $K^+\Lambda$ photoproduction

Although this thesis is concerned with the measurement of differential cross sections, measurements of polarisation observables are also important for models of strangeness photoproduction, and the technique of K^+ detection developed in this thesis will also allow such measurements in the future. Section 2.5.2 described how polarisation observables are of crucial importance to fully constrian partial

wave fits. This section presents the experimental status of the determination of these observables for $K^+\Lambda$ photoproduction.

The polarisation observables obtained to date correspond to measurements with a linearly polarised photon beam (Σ), with determination of the polarisation of the recoiling Λ (P), and with the transfer of polarisation from a circularly polarised photon beam to the recoiling Λ (C_X and C_Z).

3.2.1 Beam asymmetry, Σ, and recoil polarisation, P

The beam asymmetry, Σ is extracted using eq. 3.2, where $N_V(\phi)$ and $N_H(\phi)$ are the yields as a function of azimuthal angle of the reaction plane, for the case where the linear polarisation of the photon beam is aligned to the vertical or horizontal directions, and P_γ is the degree of incident photon beam polarisation.

$$P_\gamma \Sigma \cos(2\phi) = \frac{N_V(\phi) - N_H(\phi)}{N_V(\phi) + N_H(\phi)} \tag{3.2}$$

Extracting Σ using this ratio minimises systematic uncertainties from detection efficiencies and acceptances.

The GRAAL facility [60] used tagged cicularly and linearly polarised photons produced by Compton scattering laser photons, which were incident upon the LAγRANGE detector. This consisted of multi-wire proportional counters (MWPC) for charged particle identification with time of flight arrays at forward angles. The target was surrounded by the highly segmented BGO calorimeter for the detection of photons. Tracking detectors were used to identify the vertex of the Λ decay. Lleres *et al.* [61] used the GRAAL facility to extract the beam asymmetry, Σ and the recoil polarisation P for $K^+\Lambda$ photoproduction.

The observable, P, was extracted from the angular distribution of the Λ decay products. The weak decay of the Λ means that the polar angular distribution of the decay products reflects the polarisation of the Λ. This self analysing property of the Λ is unique; the polarisation of non-strange baryons which do not decay weakly cannot be measured in this manner[1]. Fig. 3.7 shows the extracted value

[1]Polarisation measurements of non-strange baryons require the measurement of subsequent baryon-nucleus scattering reactions, for example, the Edinburgh polarimeter with the Crystal Ball at MAMI-C [62].

of P compared to previous measurements from SAPHIR [46]. P has also been extracted with the CLAS detector [63].

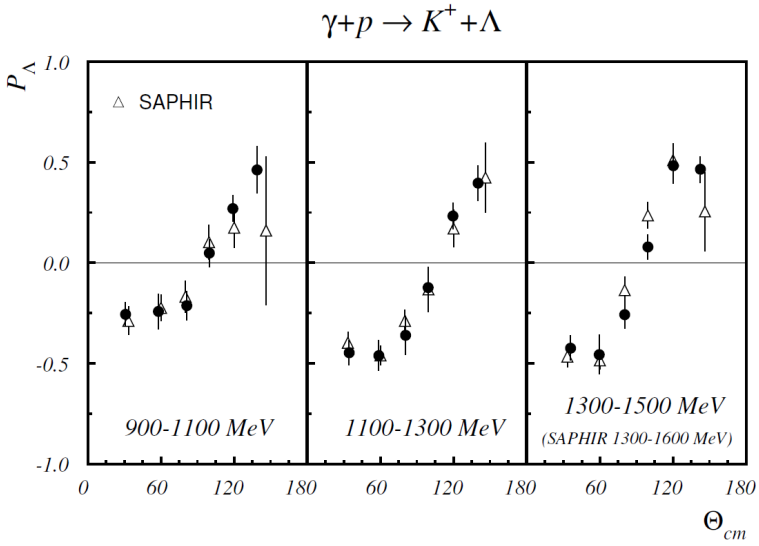

Figure 3.7: Recoil polarisation, P. GRAAL data [61] are black circles, SAPHIR [46] are white triangles. Taken from [61].

3.2.2 C_Z and C_X

The beam-recoil polarisation observables C_X and C_Z were extracted with CLAS using a circularly polarised beam [63]. "Flipping" the polarisation of the beam allowed an asymmetry to be constructed, a procedure which limits systematic errors from acceptances and detection effeciencies. C_X and C_Z were extracted from eq. 3.3, where θ is the polar angle to axis i, $N_\pm$ is the yield for that energy bin for $\pm$ beam helicity, α the weak decay constant (0.65 ± 0.04) [17] and $P_\odot$ the extent of circular polarisation.

$$A(\cos\theta_i) = \frac{N_+ - N_-}{N_+ + N_-} \alpha P_\odot C_i \cos\theta \tag{3.3}$$

It was found that the spin polarisation of the photons was almost entirely transferred to the Λ along the direction of the photon polarisation. This was reflected in the observable, C_Z being approximately unity for all angles and photon

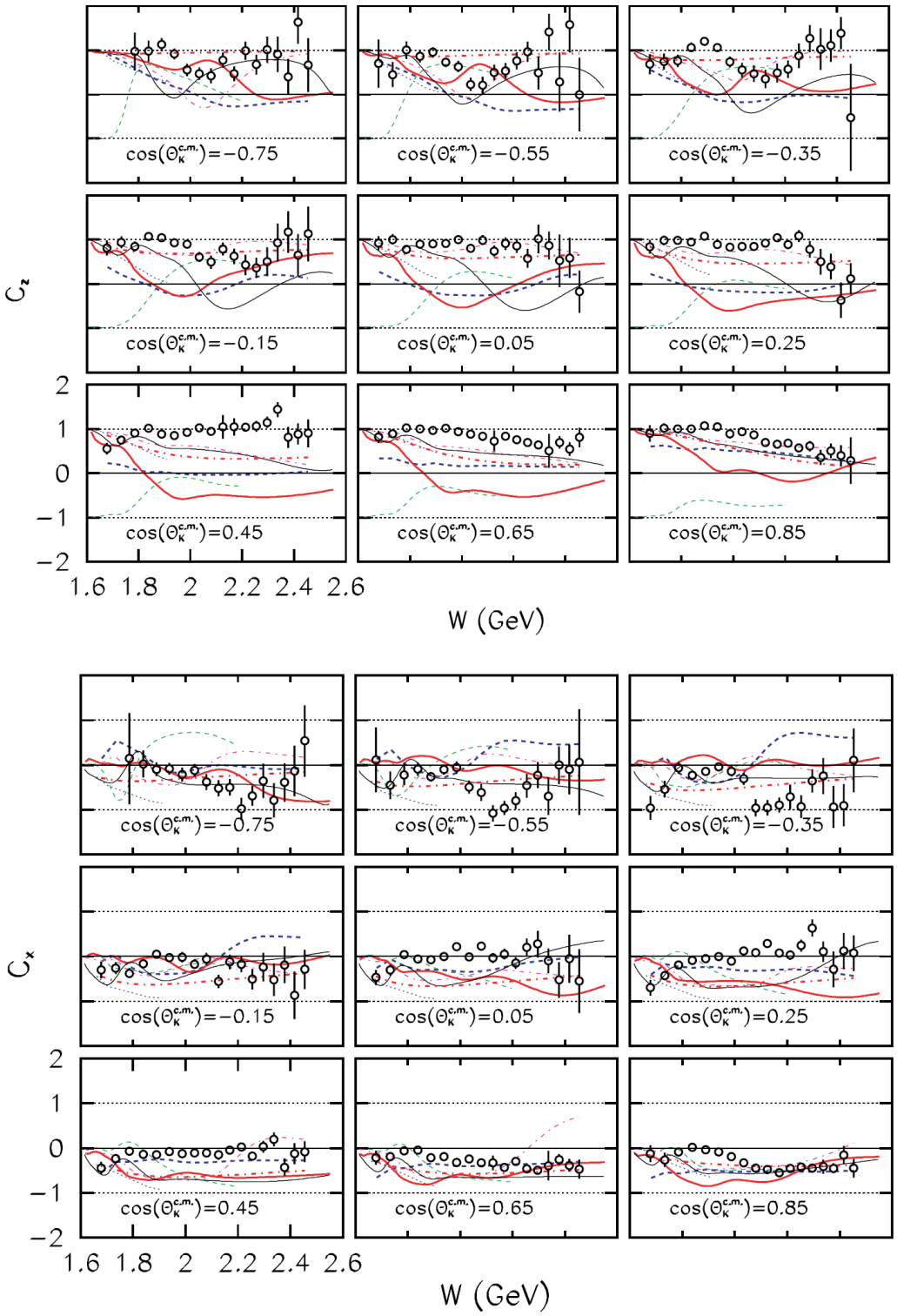

Figure 3.8: Top panel: The beam-recoil polarisation observable C_Z for $\gamma p \rightarrow K^+\Lambda$. Thin dash green line is a fit from Kaon-MAID [41] and other fits are models described in [63]. Bottom panel: equivalent graphs for C_X. Taken from [63].

beam energies (fig 3.8). Moreover, the total polarisation of the Λ, was found to be unity over all energies and angles:

$$R \equiv \sqrt{P^2 + C_X^2 + C_Z^2} \tag{3.4}$$

where R is the total magnitude of the hyperon polarisation vector. The measurements of C_Z, C_X and P could be fitted satisfactorily using a coupled channel resonance model by the Bonn-Gatchina group [64], however it was suggested [65] that the "simple" method of polarisation transfer suggests fundamental dynamics underlying the mechanism. Schumacher [65] postulated a toy model of the photoproduction process (fig. 3.9). In this model, the incoming photon fluctuates to a $s\bar{s}$ pair. The s which forms the Λ maintains the photon polarisation, resulting in a fully polarised Λ.

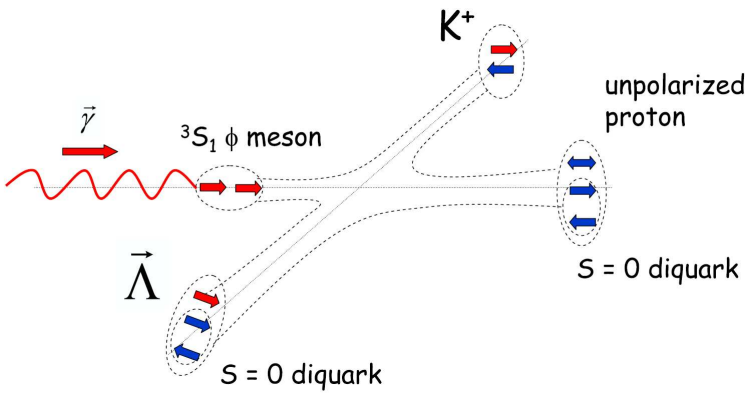

Figure 3.9: "Toy model" of the polarisation of the Λ. The photon fluctuates to a $s\bar{s}$ pair and the s quark retains its polarisation after the hadronisation process. Taken from [65].

The analysis of the transfer of linear polarisation to the recoil Λ is underway [66] (O_X and O_Z), however no published results are available at the time of writing. Data using polarised targets at Jefferson Lab and ELSA has been taken and will be available in the next two to three years. There is also a programme of experiments using a polarised target with the Crystal Ball at MAMI-C, where

the technique of K^+ identification described in this thesis (section 6) will be used. These experiments will allow the extraction of the observables, E, G, F, and T.

3.3 Theoretical models of strangeness photoproduction and comparison to current data

As outlined in section 2.5.3, the main motivation of the current programme of measurements is to provide sufficient data to allow an as model independent partial wave analysis of $\gamma(p, K^+)\Lambda$ as possible. Many model dependant approaches are also being developed however, and their agreement with current data and the physics interpretations are also described in this section.

3.3.1 Partial wave analysis

T. Mart and A. Sulaksono [67, 68] used a partial wave, multipole analysis approach to describe $K^+\Lambda$ photoproduction. The background was described by the Born terms and vector mesons in the t-channel and the resonant multipoles were assumed to have a Breit Wigner form. 15 PDG four-star resonances were included, the masses and widths were fixed to their PDG values to reduce the number of free parameters, and a χ^2 fit was performed from experimental data to constrain them.

The motive was to investigate the discrepancies between the SAPHIR [46] and CLAS [51] data sets and so two fits to the data were made. Fit 1 used SAPHIR and LEPS data set and Fit 2 used CLAS and LEPS data set (fig 3.10).

It was found that the discrepancies in the data lead to very different conclusions on resonance contributions. Fit 1 using the SAPHIR data suggests the dominant contributing resonances are $S_{11}(1650)$, $P_{13}(1720)$, $D_{13}(1700)$, $D_{13}(2080)$, $F_{13}(1680)$ and $F_{15}(2000)$, whereas Fit 2 with the CLAS data favours $P_{13}(1900)$, $D_{13}(2080)$, $D_{15}(1675)$, $F_{15}(1680)$ and $F_{17}(1990)$. The only common resonance between the fits is the $D_{13}(2010)$. It was noted that both fits suggested contributions from high spin F states ($L = 3$). These have not been included in models in the past.

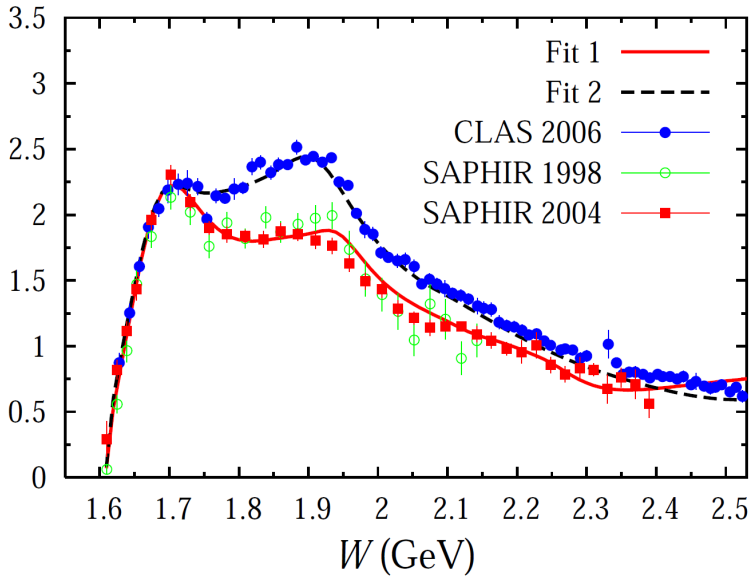

Figure 3.10: Total cross section for $K^+\Lambda$ photoproduction with the two multipole fits.

Nelson and Mart [69] extended the fitted data set to include new measurements of the polarisation observables C_X and C_Z from CLAS [63]. They defined a parameter, $\Delta\chi^2$ (eq. 3.5) to understand the importance of each resonance with and without the inclusion of the C_X and C_Z data from CLAS [63] (fig. 3.11):

$$\Delta\chi^2 = \frac{\chi^2_{All} - \chi^2_{All-N^*}}{\chi^2_{All}} \tag{3.5}$$

where χ^2_{All} is the chi squared of including all resonances and $\chi^2_{All-N^*}$ is the chi squared when not including the resonance in fig. 3.11.

From the comparison of the model fits with and without the C_X and C_Z data, it was found that the $P_{13}(1720)$ and the $S_{11}(1650)$ were always important, whereas the $P_{13}(1900)$ was only required in a data set without C_X and C_Z.

In conclusion, a partial wave, multipole analysis approach is still leaving large ambiguities to the important resonances depending on the data set used. These ambiguities are a major motive for further cross section measurements. It demonstrates the importance of the reliability of the cross section measurements upon the resonance parameters extracted.

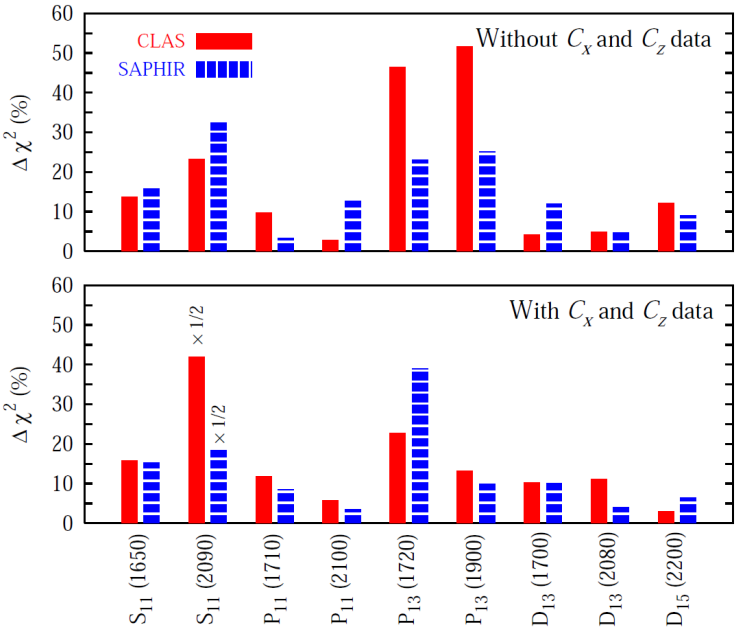

Figure 3.11: Multipole model of Mart and Nelson [69] to understand the significance of individual resonances in the CLAS and SAPHIR data(Upper panel). (Lower panel) As in the upper panel but including CLAS C_Z and C_X data [63]. Taken from [69].

3.3.2 Isobar models

Isobar models employ effective Lagrangians which describe the hadron interaction from a series of tree-level Feynman diagrams of resonant and non-resonant meson exchange. Each particle is described as an effective field with coupling amplitudes, mass and decay widths. No channel coupling effects or final state interactions are included (section 3.3.3), which reduces the complexity of the problem. The coupling constants for each resonance are treated as free parameters and are extracted by fits to the available data base.

Thom made the first serious effort at fitting the existing data to an isobar model in 1966 [70]. Fig. 3.12 shows the born terms and the vector meson exchange term K^*, the amplitudes of which give the non-resonant background. These were expanded into partial wave amplitudes to constrain their relative importance. Only two of the nine coupling constants in the Feynman diagrams were known accurately. The unknown terms were constrained by χ^2 fits to existing data. Resonances were added to the background by adding the resonant multipole to the non-resonant counterpart.

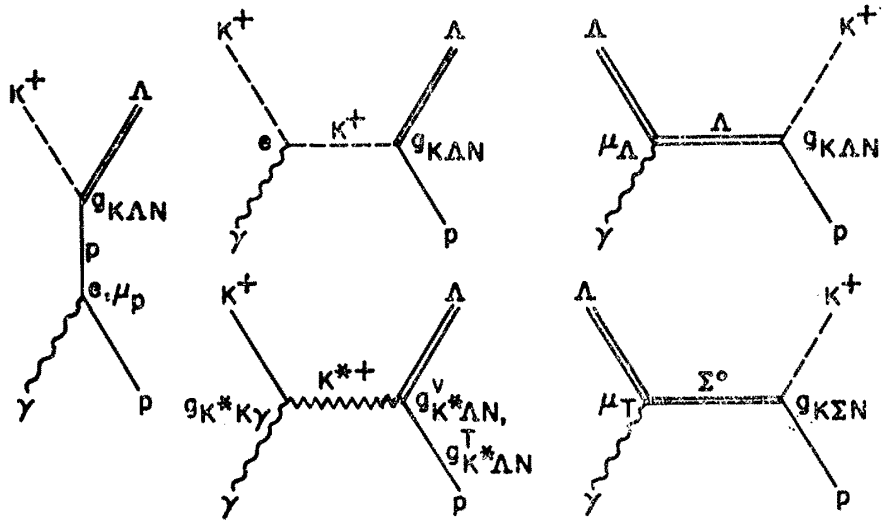

Figure 3.12: Feynam diagrams of the terms included in the isobar model of Thom [70] to describe strangeness photoproduction. Taken from [70].

In conclusion, it was judged that the inclusion of P and D states with angular momentum, $J = 1/2$ and $3/2$ respectively provided the best fits to data (lowest value of χ^2). There was large systematic uncertainty however by the limited knowledge of the coupling constants in the background terms and the paucity of data to constrain the model's parameters.

With the addition of new experimental data to constrain parameters from isobar models, Mart and Bennhold provided the first indication of a missing resonance in $K^+\Lambda$ photoproduction in 1999 [36]. The low energy resonance part of the model included the states: $S_{11}(1650)$, $P_{11}(1710)$ and $P_{13}(1720)$ which had been found to have significant decay widths into the $K^+\Lambda$ channel from coupled-channel analysis in [71] (section 3.3.3). The background was modelled with the born terms and the $K^*(892)$ and $K_1(1270)$ vector mesons in the t-channel.

This model did not reproduce the structure observed in the then most recent total cross section measurements from SAPHIR [55], where a peak over a centre of mass energy of 1900 MeV was observed. It was noted that a peak does not necessarily imply a new resonance. The broad overlapping resonances in the vicinity and the energy being close to the threshold of η', $K^*\Lambda$ and $K\Lambda^*$ could cause final state interactions to attribute to structure in the cross section. Nevertheless, the model exclusively studied the possibility of the structure arising from the inclusion of a poorly established resonance. The constituent quark model of Capstick and Roberts [31] suggested the states $S_{11}(1945), P_{11}(1975), P_{13}(1950)$ and $D_{13}(1960)$ could all have significant decay widths to $K^+\Lambda$.

The inclusion of the "missing" $D_{13}(1960)$ gave improved agreement with the cross section data from SAPHIR, with good agreement with the coupling parameters predicted from quark models [31] (fig. 3.13). It was concluded that a detailed partial wave analysis was required to determine that the structure was indeed due to this poorly established resonance.

Saghai [72] argued that the SAPHIR data could be fitted without the inclusion of the $D_{13}(1960)$, instead including two hyperonic resonances: $P_{01}(1810)$ and $P_{03}(1890)$ to the background. The model reproduced the SAPHIR data equally as well as the Mart-Bennhold model. This demonstrated that with the limited amount of experimental data to constrain the fits and the parameters in the

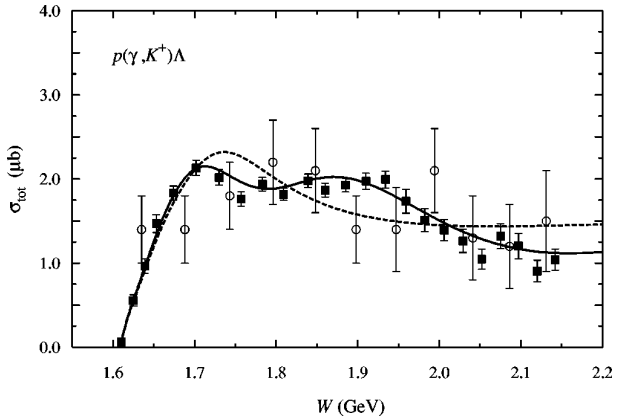

Figure 3.13: Total cross section for $K^+\Lambda$ photoproduction using the Mart and Bennhold isobar model [36]. The solid line is with the inclusion of the $D_{13}(1960)$ and the dashed line without. Solid squares are from [55] and older data in open circles (references in [55]). Taken from [36].

contributing resonances and background, it was premature to draw conclusions on poorly established resonances.

Janssen *et al.* [73] investigated the effect of the background terms on the structure of SAPHIR data using a field theoretic approach. Each intermediate particle in the reaction dynamics was considered an effective field, with mass, width and coupling amplitudes. For clarity, the resonant terms were defined as the established s-channel resonances: $S_{11}(1650)$, $P_{11}(1710)$, $P_{13}(1720)$ and $D_{13}(1895)$. The background was defined as the Born terms, t channel contributions from the vector meson $K^*(892)$ and the axial vector meson $K_1(1270)$.

It was judged that depending on the extent of SU(3) symmetry breaking, the Born terms can have far too much strength, creating models which exceed data on the total cross section. To counter this, three methods were implemented:

(a) Hadronic form factors were introduced to reduce the Born strength, with smaller cut off masses, Λ.

(b) Introducing hyperon resonances which interfere destructively with the Born terms.

(c) Ignoring the complete range of the coupling constants in the Born terms, resulting in strengths that are significantly smaller than what is expected from broken SU(3) symmetry.

Fig. 3.14 shows the results of the models from the three different methods. It is clear that the treatment of the background dramatically influences the parameters of the resonances, making the extraction of these resonances from cross section data alone extremely difficult.

Fig. 3.15 shows the SAPHIR data fitted with the "missing resonances", $D_{13}(1895)$ and $P_{13}(1720)$. It is clear that depending on the technique of modelling background contributions there is no preference to include either resonance over the other to reproduce the SAPHIR data.

This example gives further support that polarisation observables and improved accuracy in cross section data are required to constrain the reaction mechanism and contributing resonances.

3.3.3 Coupled channel analysis

Isobar models are limited as they do not include multistep processes of intermediate states ($\gamma N \rightarrow \pi N \rightarrow KY$) or final state interactions (FSI). As well as the interaction terms included in the isobar models, coupled channel analysis include these processes. For strangeness photoproduction this is important as the $\gamma N \rightarrow \pi N$ amplitudes are much larger than the direct $\gamma N \rightarrow KY$ amplitudes.

Chiang and Tabakin [74] used a coupled channel method to describe $K^+\Lambda$ photoproduction data. An existing isobar model of Williams, Ji and Cotanch [75] was used to describe the direct $\gamma p \rightarrow K^+\Lambda$ interaction, and the amplitudes associated with the πN channel were defined from the partial wave analysis of Arndt *et al.* [76, 77]. Fig. 3.16 shows the coupled channel approach for $\gamma(p, K^+)\Lambda$ cross section data. The inclusion of the πN channels made a significant effect upon the total cross section, contributing approximately 20%. This study was focussed on the effect of the coupled channel analysis rather than the accurate reproduction of data, and it was concluded that coupled-channel mechanisms must be included for proper calculations of kaon photoproduction reactions.

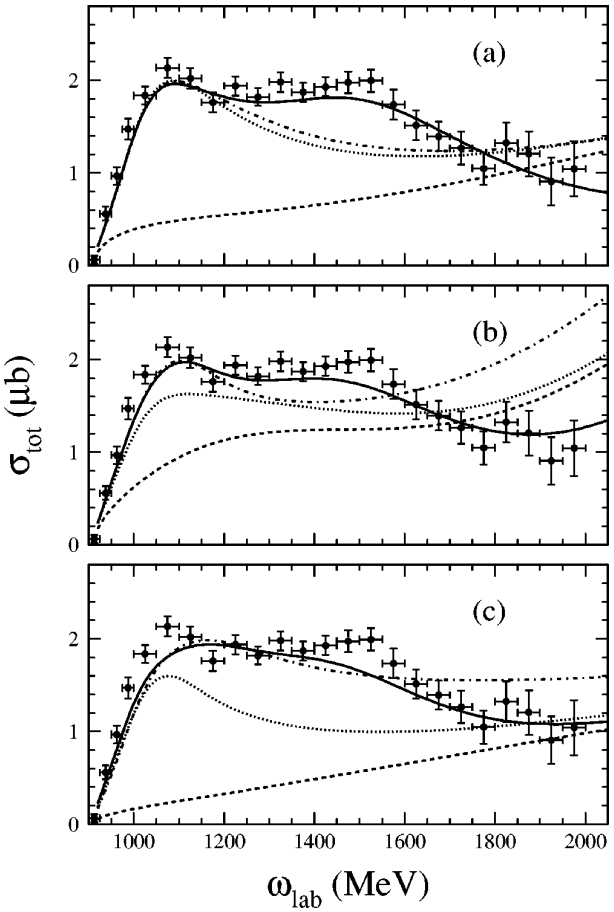

Figure 3.14: Total $\gamma(p, K^+)\Lambda$ cross section fits with the isobar model of Janssen *et al.* [73] using the three methods of treating the background contribution: (a,b,c). The dashed line includes the background terms only, the dotted line also includes the $S_{11}(1650)$ and the $P_{11}(1710)$ resonances. The dot dashed line adds the $P_{13}(1720)$ resonance. The solid line also includes the $D_{13}(1897)$. Data are from [55].

Usov and Scholton [78] extended the coupled-channel method to a K-matrix approach. The K-matrix formalism takes into account coupled channel effects, with an additional term required to the interaction kernel to account for the coupling to other channels (the K-matrix was introduced in section 2.5.3) . The advantage of this formalism is that it forces symmetries to be obeyed and main-

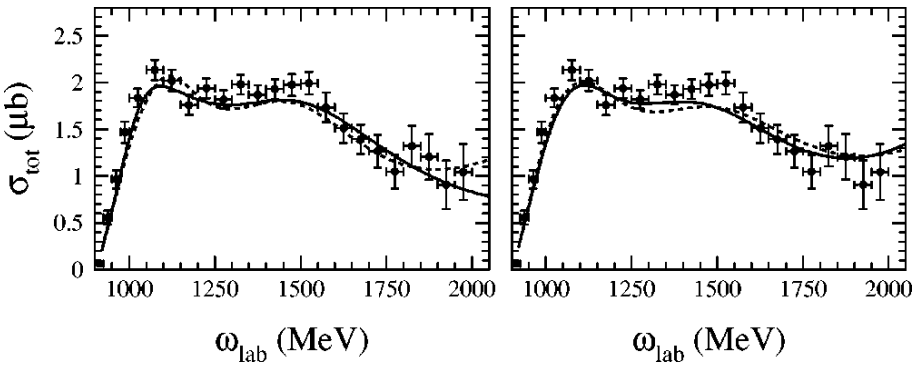

Figure 3.15: Total $\gamma(p, K^+)\Lambda$ cross sections for using model (a) on the left and model (b) on the right to describe background contributions. The solid line includes the D_{13} resonance and the dashed line includes the P_{13} resonance. Taken from [73].

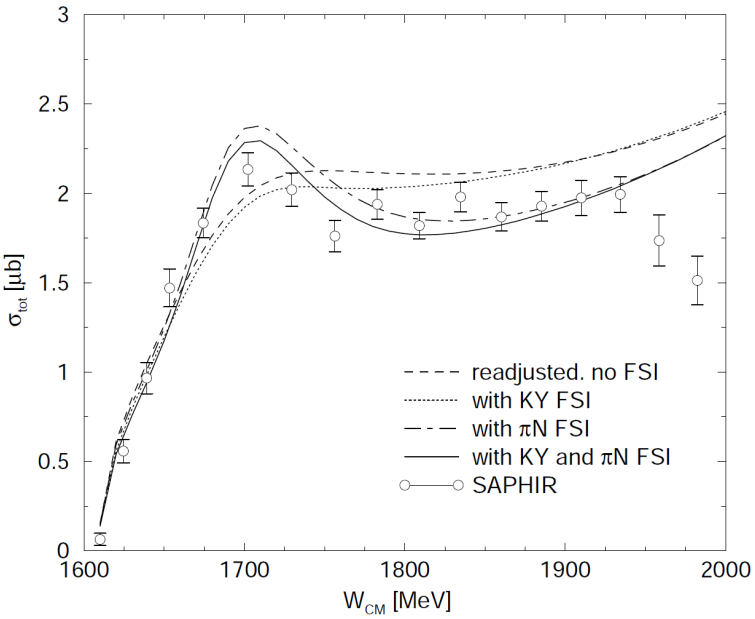

Figure 3.16: Total cross sections with the coupled channel model of Chiang and Tabakin [74] for $\gamma(p, K^+)\Lambda$ calculated with the coupled channel analysis method. The SAPHIR data is from [55]. Taken from [74].

tains gauge invariance. Fig. 3.17 show the model fits to the SAPHIR [46] and CLAS [79] data sets.

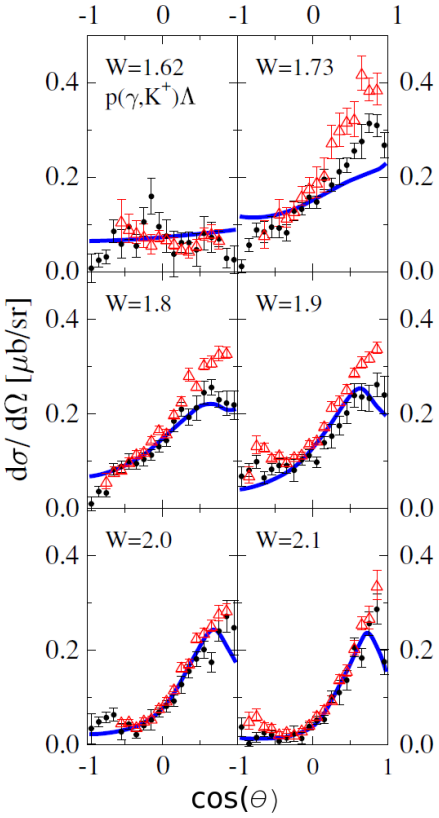

Figure 3.17: Differential cross sections for $\gamma(p, K^+)\Lambda$ (blue lines) using the Usov and Scholton [78] K-matrix approach of a coupled channel analysis. Black data from SAPHIR [46] and red data from CLAS [79]. Taken from [78].

The inconsistency between SAPHIR and CLAS data sets was noted. At backward angles where the CLAS data exhibits a more pronounced peak at 1.9 and 2.1 GeV, it was suggested this could be due to an additional P or D resonance.

Julia-Diaz *et al.* [37] extended the coupled channel approach to include a chiral constituent quark model [80, 81] to describe the direct KY photoproduction channel. This allowed the handling of all known resonances with a reasonable amount of parameters, unlike previous methods which employed isobar Lagrangians for

the direct channel. It was discussed that in principle, all significant reaction channels should be included in the coupled channel approach, for instance πN, ηN, ωN, KY, ϕN, $\pi\pi N$. This would include a vast number of interactions, and the corresponding data sets required to constrain coupling terms in the interactions have not all been studied sufficiently. For these reasons, the analysis was limited to using only πN as a coupled channel, whilst acknowledging that future analysis would benefit from the inclusion of other channels.

The model benefitted from new data being available to constrain $\pi N \rightarrow KY$ and $KY \rightarrow KY$ interactions and details from constituent quark models and Particle Data Group PDG [82] information. The model parameters were constrained by using three different constraints: (i) all SAPHIR data, (ii) recent CLAS differential cross section data and (iii) all available data (fig. 3.18). The two different fits to the data were constructed to account for the discrepancies in SAPHIR and CLAS data. It was noted that the SAPHIR data was more compatible with the fits, with a smaller χ^2 from the data set.

The results were extended in a search for poorly established resonances P_{13}, S_{11} and D_{13}, allowing parameters (mass, width, strength) from the resonances to be adjustable in the fitting procedure. Models with and without these resonances were fitted to CLAS [51] and SAPHIR [46] data (fig. 3.18). It was noted that the inclusion of the S_{11} has a significant destructive effect at backward angles and for centre of mass energies less than 1.9 GeV. Contributions from P_{13} are confined to an energy range 1.8-2.0 GeV, and D_{13} has a significant effect at 90° polar angles.

In summary, the model indicates that current world data supports strong contributions from known resonances $S_{11}(1535)$, $P_{13}(1900)$ and $D_{13}(1520)$ having significant contributions to the cross section. When the model is constrained by CLAS data alone, three more resonances were suggested: $S_{11}(1650)$, $F_{15}(1680)$ and $F_{15}(2000)$.

3.3.4 Chiral perturbation theory in an effect field Lagrangian

Borasoy, Bruns, Meissner and Nissler [38] presented a framework based upon a chiral effective Lagrangian to reproduce photo and electro-production of the kaon off the proton.

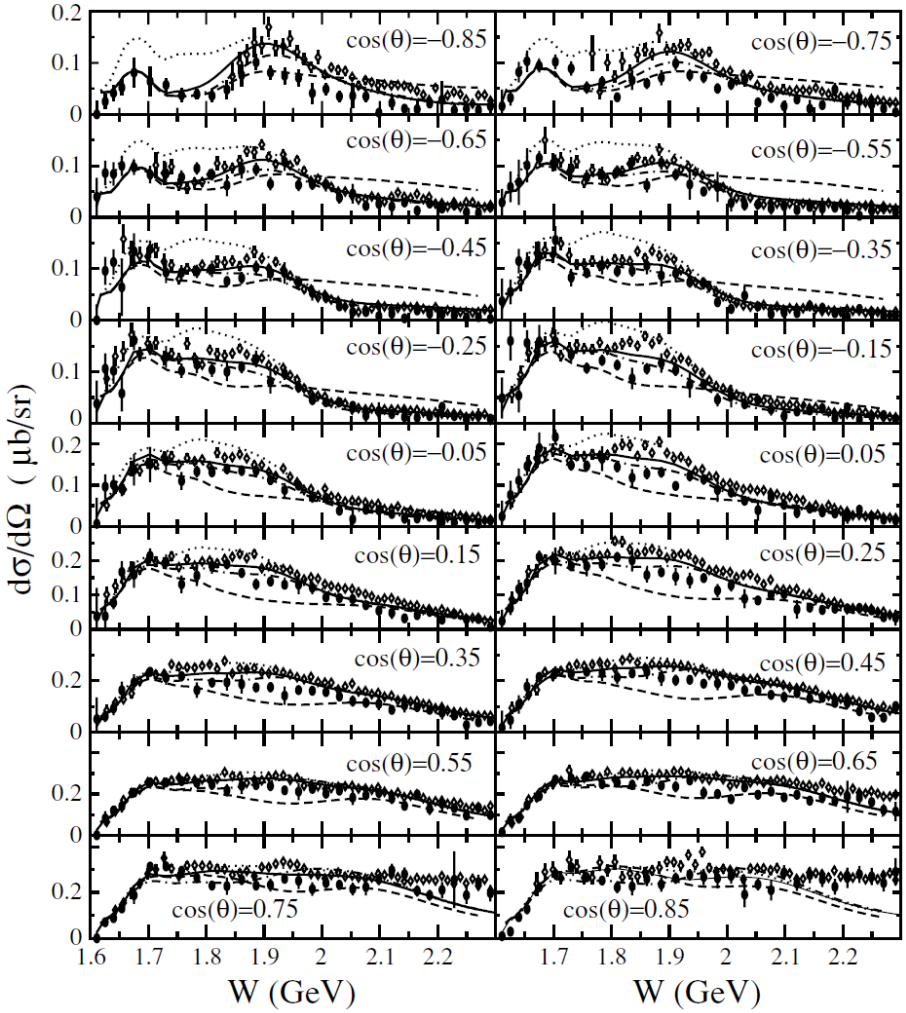

Figure 3.18: Differential cross sections for $\gamma(p, K^+)\Lambda$ (blue lines) using the Julia-Diaz *et al.* [37] coupled channel model. Solid line is the complete model, dotted, dot-dashed, and dashed curves correspond to the absence of the third S_{11}, third P_{13} and D_{13} respectively. Data points are from [51] (Open diamonds), [46] (solid circles) and [59] (open squares). Taken from [37].

A chiral effective Lagrangian was used as a basis to a Bethe-Salpeter equation (BSE) [83]. BSE describes the interactions between two bodies in a bound state. To overcome the infinite amount of Feynman diagrams needed to exactly describe the interaction, the interactions can be grouped as an external potential experienced by one body due to the other. In this model, BSE was used to iterate over the sum of meson-baryon interactions, including all rescattering to an infinite order. A benefit of the BSE approach is the dynamic generation of resonances. The importance of resonances can then be studied without their explicit inclusion.

The free parameters of the model were the meson decay constants: F_π, F_K and F_η. The symmetry breaking differences responsible for constraining these parameters were beyond the working precision of the model. Including higher order terms in the χPT expansion (section 2.3.2) would allow the extraction of these parameters, but it was considered that this is future work. χ^2 fits to available data of the photoproduction of $K^+\Lambda$, $K^+\Sigma^0$ and $K^0\Sigma^+$ and the reactions: $\pi^- p \rightarrow K^0\Lambda$, $K^0\Sigma^0$ were used to constrain the free parameters. The model improved on previous models using χPT which were not gauge invariant.

The analysis was only applicable at low energies due to the truncation of the momentum term, p^2/Λ, not providing a satisfactory approximation at higher energies. Higher order partial waves were not described realistically and so the analysis was constrained to the s-wave dominated region below centre of mass energies of approximately 1.80 GeV (corresponding to a photon beam energy of 1.25 GeV when incident upon a proton target).

This model attempted to construct the simplest possible amplitudes for kaon production whilst mainting gauge invariance, and not to demand perfect agreement with experimental data where it is recognised that higher order terms are required. Fig. 3.19 shows the differential cross sections for $\gamma(p, K^+)\Lambda$ compared to existing data [51, 46].

In conclusion, it was recognised that the model gave a reasonable agreement with available data near threshold but at higher energies higher order terms are needed. Inconsistencies between CLAS and SAPHIR data, particularly at forward angles could not be resolved within the current framework.

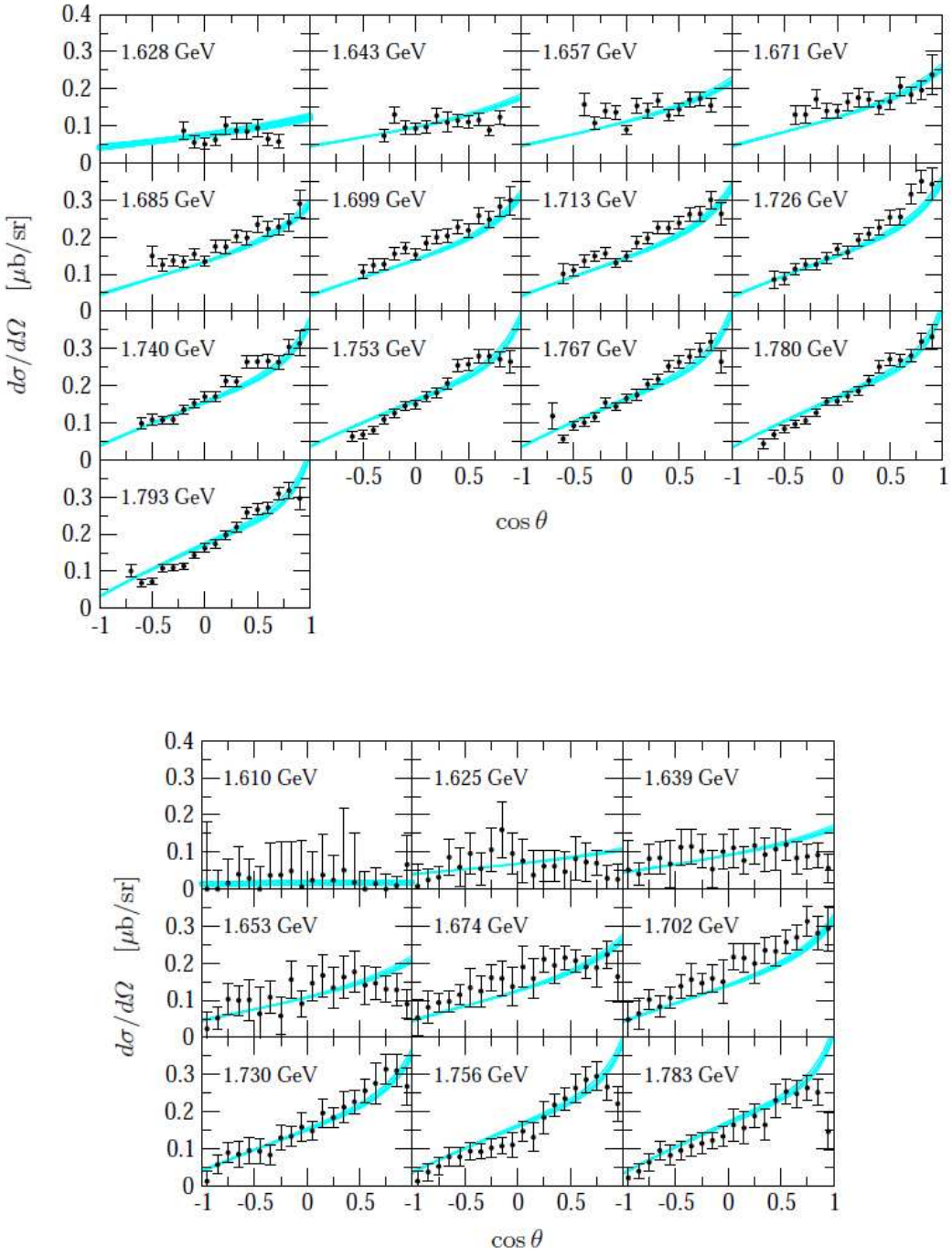

Figure 3.19: Differential cross sections fits from the model of Borasoy et al. [38] for $\gamma(p, K^+)\Lambda$ compared to CLAS [51] (top) and SAPHIR [46] data (bottom), with centre of mass energies labelled in each plot. Taken from [38].

3.3.5 Regge trajectories

Rather than exchanging individual particles as in iosbar models, Regge models group families of particles together with the same quantum numbers into Regge trajectories [84].

The t-channels of a reaction process can be decomposed into a series of partial waves. It was found that the orbital angular momentum could be expressed as continuous and complex whilst still solvable with the Schrödinger equation [84, 85]. The partial wave amplitudes, $A_l(t)$ could be considered as complex functions $A(l,t)$ for complex l. Singularities of the amplitude in the complex plane corresponded to poles (Regge poles) that trace out paths as the energy, t varies:

$$l = \alpha(t) \tag{3.6}$$

where $\alpha(t)$ is the Regge trajectory which corresponds to the exchange of families of particles (the squared mass of the particles lie on the Regge trajectories). Regge theory allowed the summation of the exchange of particles corresponding to each Regge trajectory. Regge theory predated and in some aspects was superceded by QCD; the theory required no knowledge of the internal structure of observed particles, however it is still used today in phenomenological models. The theory is particularly accurate at high energies (where t-channel exchanges dominate) and at forward angles. For a detailed description of Regge Theory see [86].

The Guidal-Laget-Vanderhaegen model [57, 56] employs Regge theory to describe $\gamma(p,K^+)\Lambda$ and $\gamma(p,K^+)\Sigma^0$. In this model, the dominant t-channel Regge trajectories of K and K^* were used, with the added inclusion of the s-channel nucleon pole to restore gauge invariance. Although giving general agreement with the magnitude of cross section data, structure in the beam energy dependance of the cross section evident in the world data set was not described by this model. It was considered these were due to resonances in the s-channel which were not included in the Regge model.

Corthals, Ryckebush and Van Cauteren [87] adopted a Regge-plus-resonance approach (RPR) to describe $\gamma(p,K^+)\Lambda$ in the resonance region. It was considered that whilst the Regge parameterisation remains physical in the resonance region,

the resonance structure cannot be reproduced by this background model. s-channel resonances were required to be superimposed onto the Regge, t-channel background. Similar to the Guidal-Laget-Vanderhaegen model, the dominant Feynman diagrams for $\gamma(p, K^+)\Lambda$ were identified (Fig. 3.20(a,b,c)), with the s-channel term (c) required to restore gauge invariance. Fig. 3.20(d) is a Chew-Frautschi plot which shows the meson trajectories that were used to describe the high-energy amplitude.

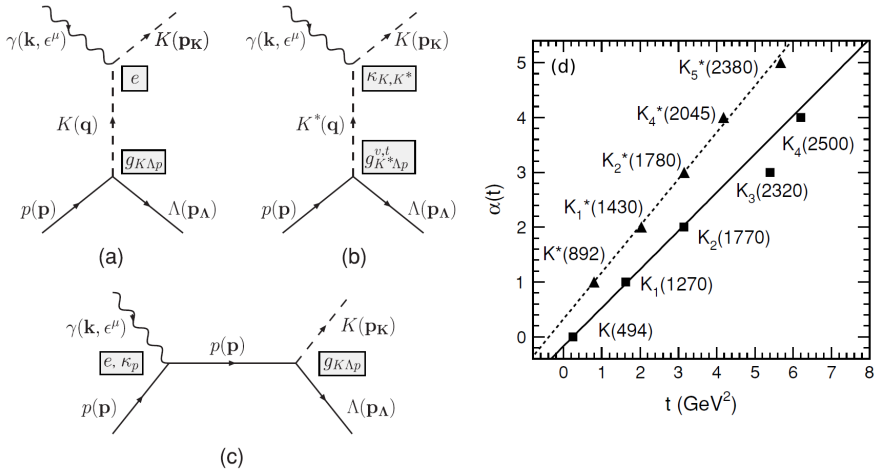

Figure 3.20: Feynman diagrams included in the RPR model of Corthals *et al.* [87] for the $\gamma(p, K^+)\Lambda$ amplitudes above 4 GeV for (a) K and (b) K^* Regge trajectories and (c) to restore gauge invariance. Taken from [87].

Variations in the parameterisation of the Regge trajectories were compared to experimental data above the resonance region, the χ^2 of the fits being used to select three of the variants. Resonance structures were superimposed such that they vanished in the high-energy limit. The selection of resonances used was non-trivial. The "core" resonances which have been used in many other studies were included which were the $S_{11}(1650)$, the $P_{11}(1710)$ and the $P_{13}(1720)$, and the effect of including a $D_{13}(1900)$ or a $P_{11}(1900)$ was investigated. Fig. 3.21 show the model calculations with cross section data set from CLAS [51].

It is apparent from all of the fits that the Regge trajectories alone do not describe the data well; s-channel resonances need to be superimposed to fit to ex-

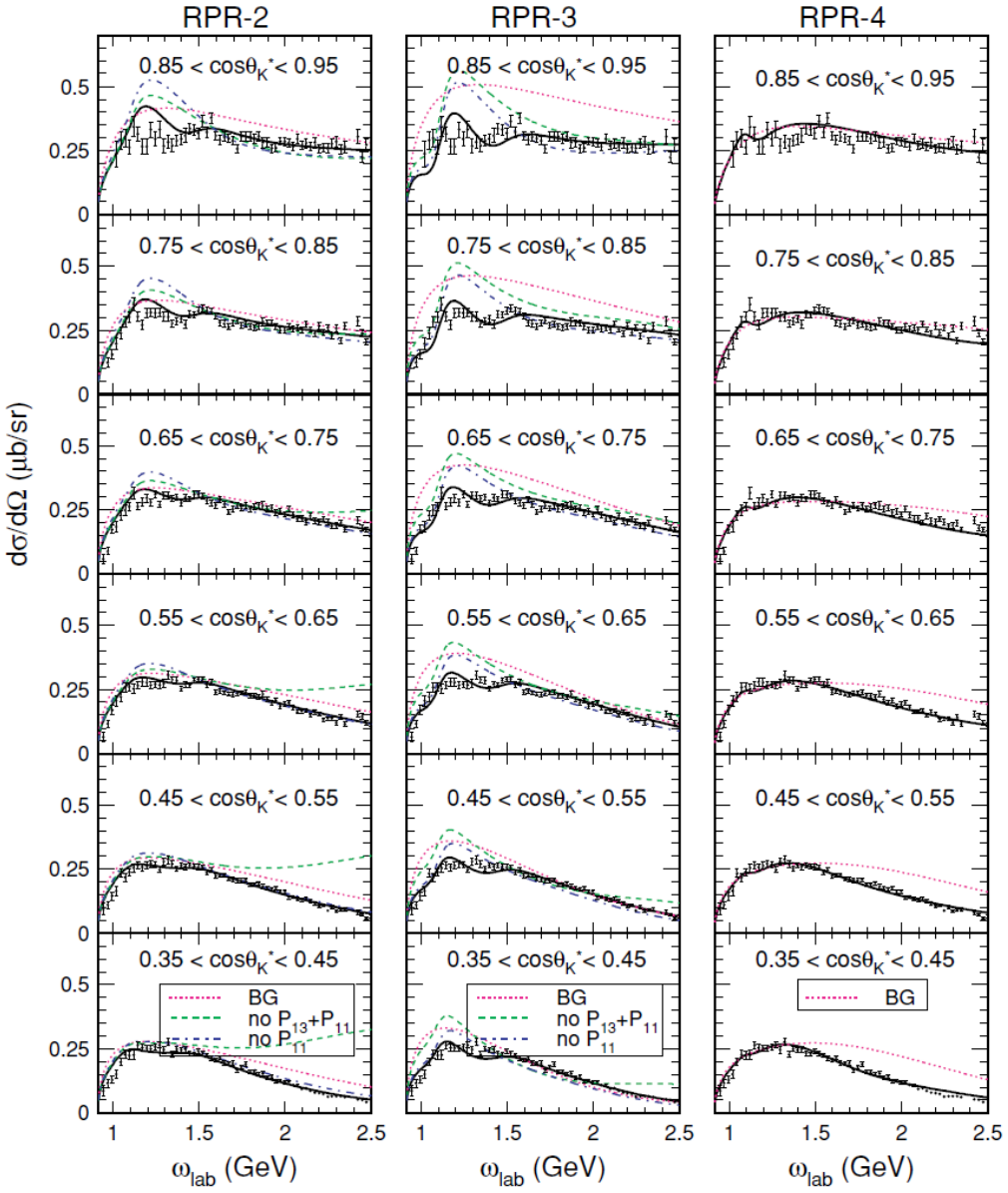

Figure 3.21: Differential cross sections with three variants on the Regge trajectory backgrounds (RPR 1, 2 and 3) from the RPR model of Corthals *et al.* [87]. RPR 2 and RPR 3 include the "core" resonances, the two star $P_{13}(1900)$ and the "missing" $P_{11}(1900)$, whilst RPR 3 only includes the "core" resonances.

isting data sets. Of the four variations of Regge parameterisation, variants RPR-2 and RPR-3 require the $P_{11}(1900)$ for accurate fits whereas variant RPR-4 can reproduce narrow structure at forward angles without needing the superposition of a resonance in the 1900 MeV region.

In conclusion, it was suggested that peaks and structure in the cross sections maybe explained in the tuning of the background without the introduction of another "missing resonance", and that more accurate data and a wider range of observables was required.

3.3.6 Constraining Strangness photoproduction with the Gerasimov-Drell-Hearn Sum Rule

The Gerasimov-Drell-Hearn Sum Rule (GDH) [88] relates the anomalous magnetic moment of the nucleon, κ_N with mass M and spin S, to the difference of polarised total absorption cross section (eq. 3.7).

$$I = \int_0^\infty \frac{\sigma_{3/2} - \sigma_{1/2}}{\nu} \mathrm{d}\nu = 4\pi^2\kappa^2 \frac{e^2}{M^2} S \tag{3.7}$$

where ν is the photon energy and $\sigma_{3/2}$ ($\sigma_{1/2}$) denotes the total absorption cross section for parallel (antiparallel) orientation of photon and particle spins. This sum rule, formulated in the 1960's, rests upon fundamental physics principles (for example, Lorentz invariance and gauge invariance). It gives a very important connection between ground state properties of a particle (right-hand side of eq. 3.7) and an integral property of its whole excitation spectrum (left-hand side of eq. 3.7).

Using a polarised beam, and target, the asymmetry, $\sigma_{TT\prime} = \frac{1}{2}(\sigma_{3/2} - \sigma_{1/2})$ can be measured for $K^+\Lambda$ photoproduction.

The integral over the excitation spectrum can be measured by summing over all possible photoproduction processes. A partial wave analysis based on the SAID model found the strangeness photoproduction channels to contribute $\sigma_{TT\prime} = +4\mu b$ to the photo production process [89]. An equivalent measurement using the Kaon-MAID model extracted a value of $\sigma_{TT\prime} = +2.94\mu b$ [90]. Fig. 3.22 shows $\sigma_{TT\prime}$ for $K^+\Lambda$ photoproduction with different multipole and partial wave

analysis. Clearly, experimental measurements of this parameter with a polarised beam and target would help constrain resonances in the photoproduction process. Such measurements are scheduled at Jefferson Lab and ELSA and will be possible at MAMI-C using the new technique developed in this thesis (section 6).

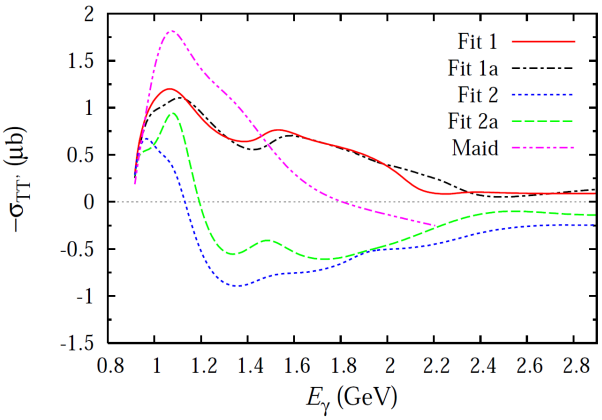

Figure 3.22: $\sigma_{TT'}$ for $K^+\Lambda$ photoproduction as function of photon beam energy. Fits 1(a) and 2(a) multipole models from [67, 68] fitting to the SAPHIR [46] and CLAS [51] respectively. Fits 1 and 2 are equivalent and further constrained by C_X and C_Z measurerments from CLAS [63]. Taken from [91].

3.4 Constraints on narrow nucleon resonances

The possible existence of particles with "exotic" combinations of quarks, such as tetraquarks or pentaquarks is an outstanding issue in hadron physics. Pentaquarks are a class of particle consisting of five valence quarks. Despite their existence not being prohibited by QCD, experimental measurements have not given consistent evidence of a pentaquark signal. For a review of experimental searches of pentaquarks, see reference [92].

Kuznetsov and Polyakov [93] argued that a pentaquark must exist in a multiplet of non-exotic three quark hadrons. The non-exotic states would consist of an isodoublet of two non-strange resonance states, N^* and an isotriplet of three

states with strangeness, $S = -1$. Fig. 3.23 is a diagram of this proposed multiplet. A chiral quark soliton model [94] was used to investigate soliton excitations beyond the observed baryon spin 1/2 octet and spin 3/2 decuplet. In the case of including three flavours (u, d, and s), it was argued that that the radial excitations could provide the baryon states to populate the proposed multiplet. The model predicted the N^* states to be P_{11}, with a mass approximately 1685 MeV and a width less than 30 MeV (assuming a pentaquark in the same multiplet with a mass of approximately 1540 MeV). The narrow N^* states were also predicted to couple much more strongly to the neutron than the proton, with the predominant decay channels being ηN, $\pi\Delta$ and $K\Lambda$ [95].

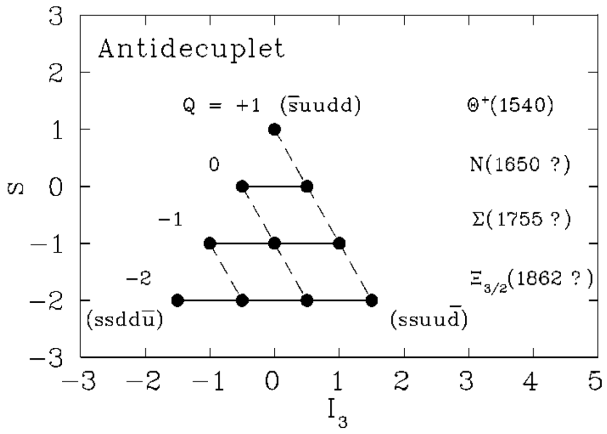

Figure 3.23: Predicted exotic decuplet with the Θ^+ pentaquark at $S = 1$ and narrow non-strange states at $S = 0$. Taken from [95].

Comparison of photoproduction cross sections from proton and neutron targets could potentially provide evidence of narrow nucleon resonances in this multiplet. η photoproduction at the GRAAL facility in 2004 [96] yielded a narrow peak in the quasi-free neutron cross section which was not observed when using a proton target. The data was confirmed at the ELSA accelerator in Bonn [97] (fig. 3.24).

An alternative explanation for the second peak in the neutron cross section was proposed by Shklyar, Lenske and Mosel [98]. They demonstrated by tuning the neutron photocoupling amplitudes, a coupled channel approach including

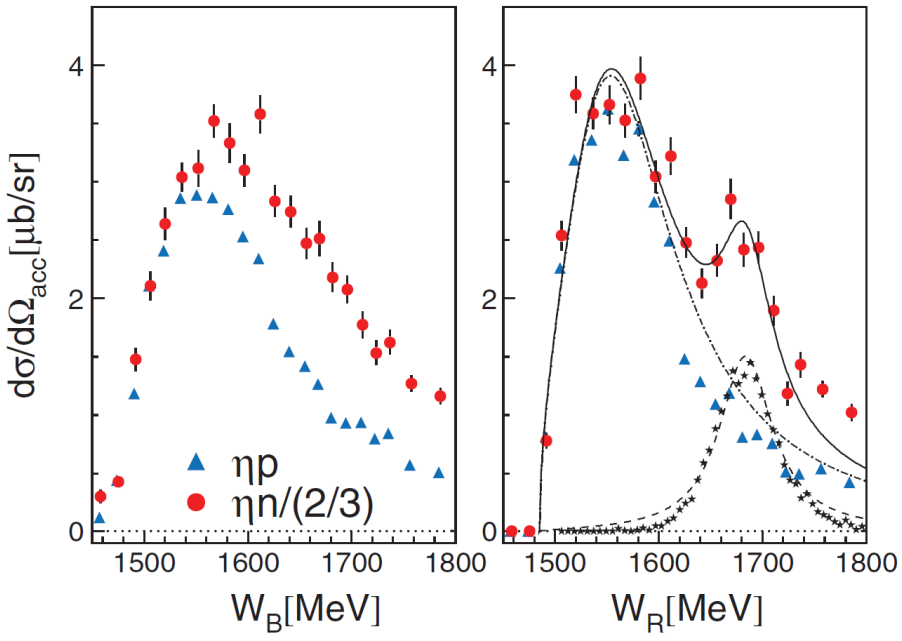

Figure 3.24: η photoproduction for centre of mass polar angles, $\cos\theta_{cm} < -0.1$ off the proton (blue points) and neutron (red points). Left panel: neutron Fermi motion uncorrected. Right panel: neutron Fermi motion corrected. Dot dashed line: Breit-Wigner curve from $S_{11}(1535)$, stars: experimental response of an inputed δ function smeared by simulated detector resolutions, solid line: sum of both fits. Taken from [97].

$S_{11}(1650)$ and $P_{11}(1710)$ resonances could create structure in the region of the observed second "peak".

Until recently, experimental facilities have not had the beam energy resolution and high statistical accuracy to measure structure below 50 MeV. Narrow structure in cross section measurements (less than 20 MeV) of $\gamma(p, K^+)\Lambda$ have therefore never been measured. The beam energy resolution of approximately 4 MeV obtained in the results from this thesis will provide the first sensitivity to narrow structure in $K\Lambda$ photoproduction.

3.5 Summary

The first accurate experimental measurements of strangeness photoproduction have only been realised in the last ten years with currently ongoing measurements of polarisation observables at world leading photon beam facilities. It is clear from partial wave analysis of the existing world data (predominantly the SAPHIR [46] and CLAS [51] data sets) however, that the world data set is currently not of sufficient extent and accuracy, and even recent measurements are inconsistent with each other. This will be addressed with future measurements and this current work. In the next three to four years, partial wave analysis will be constrained for the first time with a complete measurement of experimental observables.

As well as partial wave analysis, reaction models based on different approaches have shown some success and will also be improved with the new data to constrain. In particularly, it is apparent that the treatment of the background terms can have large effects and t-channel contributions from K^* vector mesons and u-channel hyperonic resonances can potentially lead to ambiguities in the determination of the resonance structure [73].

Threshold strangeness photoproduction also provides a unique test of χPT based effective Lagrangians. The comparatively large strange quark mass causes the chiral symmetry to be broken much more strongly than in non-strange SU(2) χPT. A dearth of data near threshold is therefore a limiting factor in the test of SU(3) χPT based effective Lagrangians.

With theoretical models suggesting a coupling of narrow resonances to $K\Lambda$, strangeness photoproduction also provides an excellent testing ground for narrow structure and evidence of pentaquarks.

Chapter 4

Experimental Details

4.1 Introduction

Experimental data for this thesis was collected during July 2007 and April 2009 over a period of 31 days (13 days in 2007 and 18 days in 2009) at the Mainz Microtron facility in Mainz, Germany. This chapter describes the facility and the detector apparatus used.

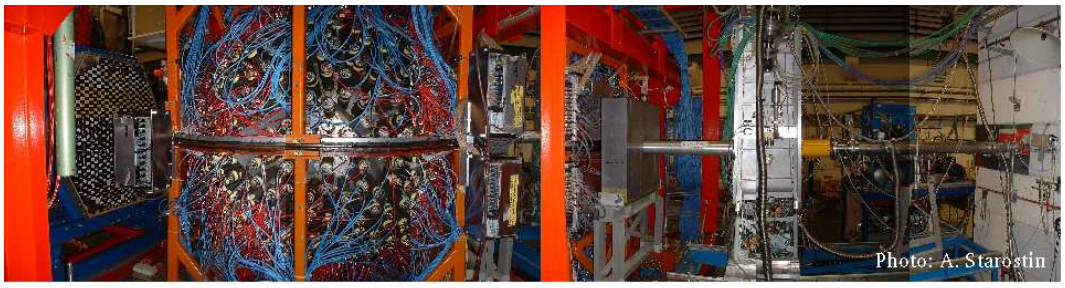

Figure 4.1: The Crystal Ball Detector. Photon beam travels from right to left, with the Glasgow photon tagger and TAPS detector at the far right and left respectively.

Fig. 4.2 is an overall schematic of the detector apparatus used in the experiment. Electrons (incident to the left of fig 4.2) were accelerated to 1.5 GeV by the Mainz Microtron and used to produce bremsstrahlung photons, which were energy tagged by the Glasgow Photon Tagger. The photons were incident upon

a liquid hydrogen target located at the centre of the Crystal Ball detector. The reaction products were detected in the Crystal Ball and TAPS (Two-Armed Photon Spectrometer[1]) segmented calorimeters. The Crystal Ball and TAPS provide nearly 4π steradian acceptance for particles produced in the target.

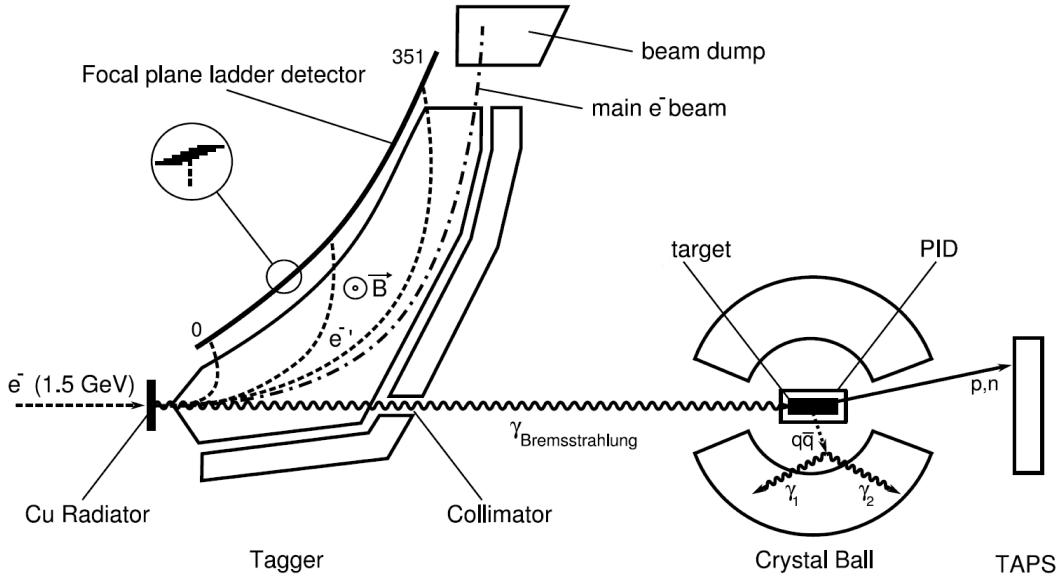

Figure 4.2: Schematic diagram of the Crystal Ball detector and apparatus. Taken from [99].

The Edinburgh Particle Identification detector (PID) was positioned between the target and the Crystal Ball, providing charged particle identification for reaction products in the Crystal Ball, while an additional segmented plastic array provided equivalent information for TAPS.

Each of the components of the experimental apparatus are described in more detail in the following sections.

[1]The "Two-Armed" name is historical, it is now just a single, forward arm but retains the name TAPS

4.2 The Mainz Microtron

4.2.1 The Mainz Microtron Design

The Mainz Microtron is based on three race-track microtrons (RTMs) and an harmonic double sided microtron (fig.4.3). In the RTMs the electrons are circulated through a series of short linacs[1] by two 180° dipole magnets of constant and uniform magnetic field, undergoing energy gain (of the order of 1 MeV/m), with each pass through the linacs. The radius of the beam orbit increases following each pass. When it reaches the energy required, the beam is extracted from the microtron.

The path through the magnetic field with each pass is carefully adjusted so that electrons arrive back in phase with the accelerating field of the rf cavities. Due to this longitudinal phase focussing, RTMs provide excellent energy resolution and low divergence. The moderate energy gains through each recirculation make this an efficient use of the rf power when compared to single linac systems, and the modest energy gains allow the rf cavities to be operated continuously without overheating.

MAMI was first developed in 1979, where a single RTM successfully accelerated an electron beam to 14 MeV. MAMI-A was built in 1983. This used two RTMs to accelerate an electron beam to 180 MeV [100]. MAMI-B started operation in 1990. This integrated a third RTM to produce beam energies up to 883 MeV [101].

By the end of the 1990s, MAMI-C was under development to produce beam energies up to 1.5 GeV. It was not possible to use another RTM to accelerate to this energy due to space constraints. The dipole magnets would have had to be of the order of 2200 tons each to produce the necessary field, compared to the previous dipole magnets of 450 tons. A double sided mictrotron was developed to

[1] A linac (linear particle accelerator) accelerates particles in a straight line through a series of drift tubes. An alternating electric field is applied to plates between each drift tube to accelerate the particles towards the next plate. As electrons pass into each drift tube, the polarity of the plates is reversed to accelerate the electron towards the next tube. Linacs are often used to provide charged particles a "kick" before they are injected into a higher energy accelerator.

overcome this (Fig. 4.3). Using an idea that was first suggested in the 1970s, this uses two sets of dipole magnets, each magnet deflecting the beam by 90°. The system still uses two linacs to accelerate the electrons, one operates at 4.90 GHz to provide a moderate energy gain per recirculation, and the other operates at 2.45 GHz to provide longitudinal stability. Field gradients are employed at each of the magnet pole faces to prevent vertical defocusing due to the 45° angle of the pole face to the beam direction. The two linac operation gave rise to the name Harmonic Double Sided Microtron (HDSM).

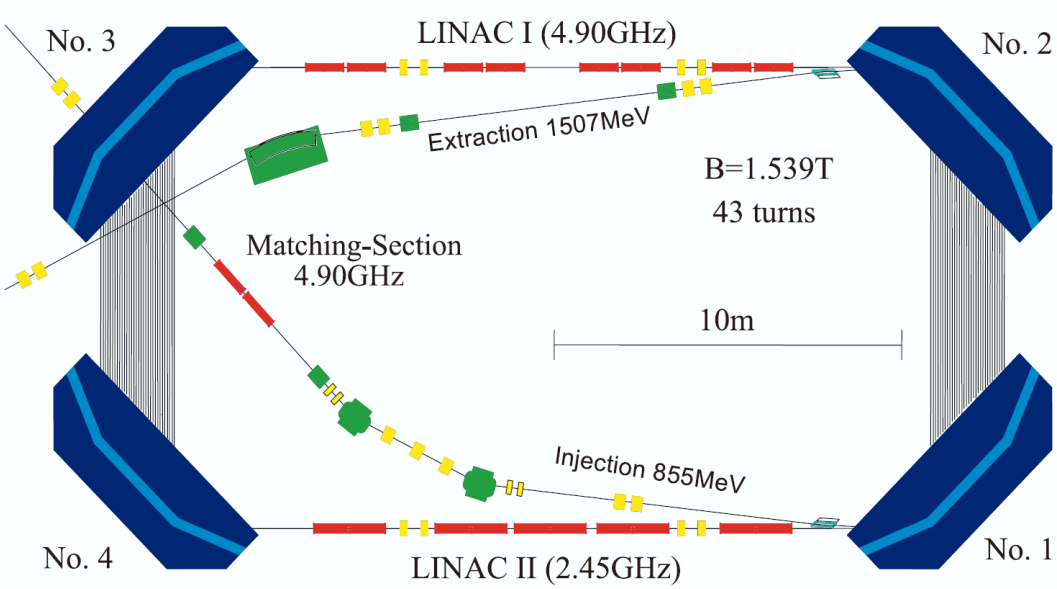

Figure 4.3: The Mainz Harmonic Double Sided Microtron. Electrons enter at 855 MeV (top left of diagram), accelerated by linacs (red) and deflected by dipole magnets (blue) into the racetrack. The electrons are ejected from the HDSM once they have an energy of 1.507 GeV. Taken from [102].

MAMI C met the design energy of 1.508 GeV in December 2006, with the first experimental data being taken in February 2007.

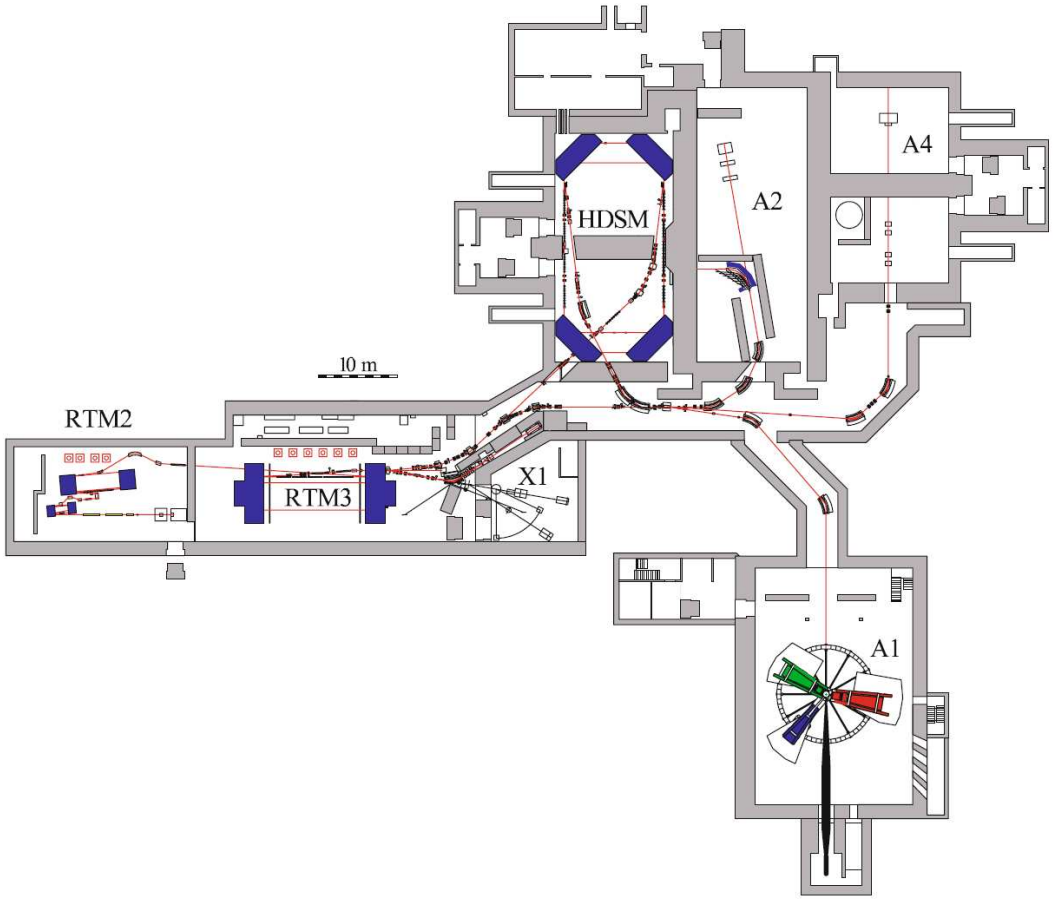

Figure 4.4: Floor plan of the MAMI facility. The Crystal Ball detector and apparatus is housed in the hall labelled A2-System. Taken from [102]

4.3 The Glasgow Photon Tagger

The Crystal Ball detector system is housed in Hall A2 at the MAMI facility (see fig. 4.4). Electrons from MAMI-C enter the hall up to an energy of 1508.0 MeV[1]. The electrons are incident upon a thin, 10 μm thick copper radiator. Bremsstrahlung radiation is produced as the electrons are decelerated in the Coulomb field of the copper nuclei in the radiator. A thin radiator is used to minimise multiple scattering processes in which the electrons undergo more than one scattering event in the radiator. The energy of the bremsstrahlung photons, E_γ, can be calculated from eq. 4.1.

$$E_\gamma = E_e - E_{e'} \tag{4.1}$$

where E_e is the energy of the electron supplied by MAMI and $E_{e'}$ is the electron energy measured in the tagger. Eq. 4.1 neglects energy transferred to the recoiling radiator nuclei, however copper has a sufficiently high mass so that a negligible amount of energy is transferred compared to the energy resolution (of the order of a few keV).

The Glasgow Photon Tagger [103, 104] (fig. 4.5) is a wide band magnetic spectrometer comprising a quadrupole and a dipole magnet. After passing the radiator, the quadrupole magnet focuses the electrons vertically before the electrons enter the dipole magnet. The dipole magnet disperses the electrons on the horizontal plane according to their momentum, with the hit position at the focal plane recorded in an array of plastic scintillator detectors (fig. 4.5). The energy of the electrons is determined by the extent of the deflection. The bremsstrahlung photons pass undeflected through a hole in the dipole magnet. The electron hit in the focal plane is correlated to the subsequent reaction products in the particle detectors by timing coincidence techniques (section 5.4.3).

[1]This is the electron beam energy for July 2007. The data set used from April 2009 had an electron beam energy of 1557.4 MeV

4.3.1 The Focal Plane Detector

The focal-plane detector consists of 353 plastic scintillators, of length 80 mm, thickness 2 mm and variable widths of 9 to 32 mm, decreasing along the focal plane to ensure a roughly constant energy resolution. The scintillators are positioned close to the focal plane of the magnetic field (fig. 4.5). The intrinsic resolution of the photon tagger arising from the uniformity of the magnetic optics is approximately 0.1 MeV. Each scintillator overlaps the adjacent one by slightly more than half of the width. An electron therefore produces a coincidence hit between two detector elements. This coincidence requirement reduces the number of low energy random events in the focal plane. The width of this overlap region corresponds to approximately 4 MeV for an incident electron beam of 1.5 GeV, and determines the channel width of the photon tagger, giving an energy resolution of approximately 2 MeV. The photon tagger is able to measure photon energies from 80 to 1401 MeV for an electron beam energy of 1508 MeV. The photon tagger tags photons with a flux up to 10^8 s^{-1}.

The material EJ200 [105] is used for the plastic scintillators as the light spectrum matches the response of the phototubes well and is not susceptible to radiation damage as much as some alternative scintillators. Each scintillator module is wrapped in aluminized mylar to avoid scintillation light transfer between neighbouring scintillators and is connected to an individual Hamamatsu R1635 photomultiplier tube (PMT) via a lucite light guide. Steel plates are fitted around the PMTS to reduce the magnetic field exposure of the PMTs which needs to be kept less than 0.01 T to avoid their performance being compromised.

4.3.2 Photon collimation and tagging efficiency

Photons from the tagger passed through a lead collimator before being incident upon the target. This keeps the beam spot size upon the target small and well defined so that the reaction vertex can be better determined. The collimator used in this experiment was 4 mm in diameter, 15 cm in length and was positioned 2.4 m from the radiator. The resulting beam spot size was 1 cm in diameter.

Without collimation, the number of photons incident upon the target could have been accurately established from the number of hits in the focal plane de-

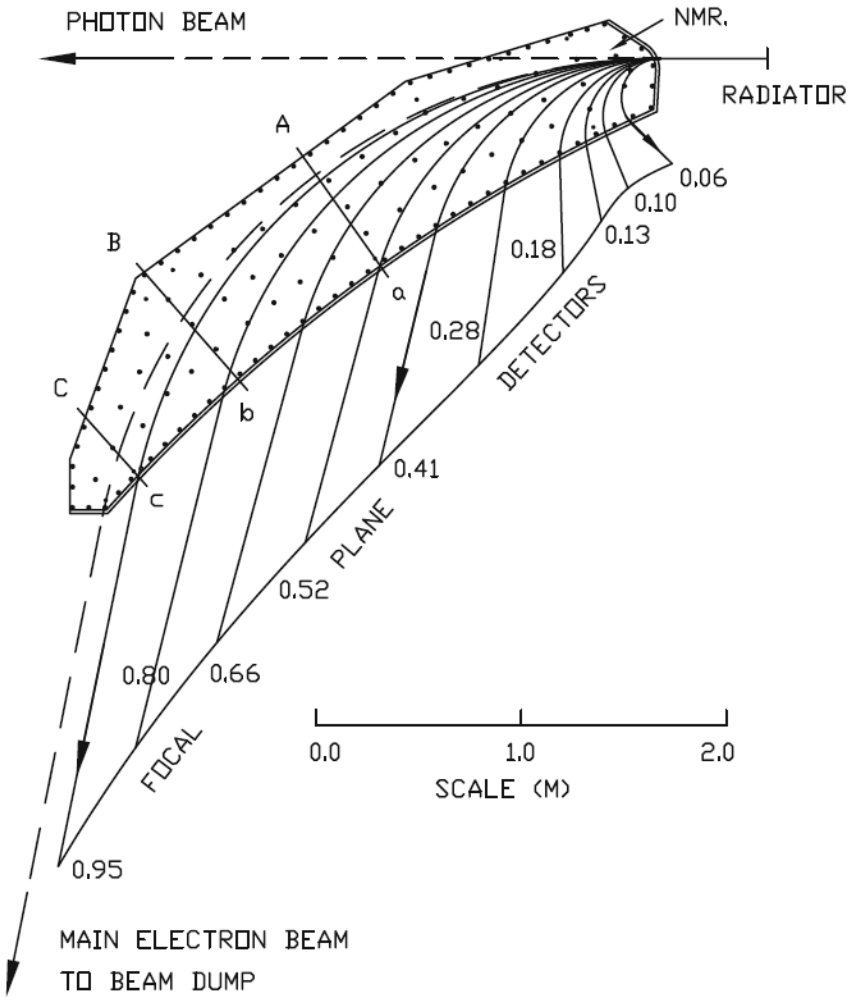

Figure 4.5: Plan drawing of the Glasgow Photon Tagger, with path of the photon beam and a range of electron trajectories included. The electron beam energy at the focal plane detector is labelled as a fraction of the incident electron beam energy. Taken from [103].

tector. Using the collimator, a correction was needed to account for the fraction of photons which did not pass through to the target. This was defined as the tagging efficiency, ϵ_{tagg}:

$$\epsilon_{tagg} = \frac{N_\gamma}{N_e} \tag{4.2}$$

where N_γ is the number photons which pass through the collimator and N_e is the number of electrons incident upon the tagger focal plane detector.

To measure the tagging efficiency, a lead glass scintillator was positioned in front of the collimated photon beam. The number of coincident hits between the lead glass detector and each individual focal plane detector were measured. The ratio of this quantity to the total number of hits in the focal plane detector during the same run period gave the tagging efficiency for each focal plane element. The tagging efficiency was performed with separate data runs to the standard beamtime and with a lower beam intensity to ensure that the the lead glass detector was not damaged by the intense beam. The lower beam intensity also ensured there were not multiple hits in the FPD elements. At the lower beam intensity, the lead glass detector had a detection efficiency close to 100%. During the standard data acquisition, a caesium iodide camera imaged and recorded the beam spot position, and an ionising chamber measured the photon beam flux to ensure that the beam was aligned correctly through the collimator.

4.4 The Crystal Ball Detector

The Crystal Ball was built in the 1970s for multi γ-ray detection at colliding beam facilities. First used at SLAC for measurements of J/ψ, the Crystal Ball has also been used at DESY and the Brookhaven National Laboratory. The Crystal Ball began work at the MAMI accelerator facility in 2002 after an extensive electronics upgrade.

4.4.1 The Crystal Ball Design

The Crystal Ball consists of 672 optically isolated NaI(Tl) crystals, arranged into the geometry of a 20 sided polyhedron called an icosahedron. This has 20 major

triangular faces, each of these with four minor triangular faces, each of which are segmented into nine actual crystal faces. (Fig.4.6).

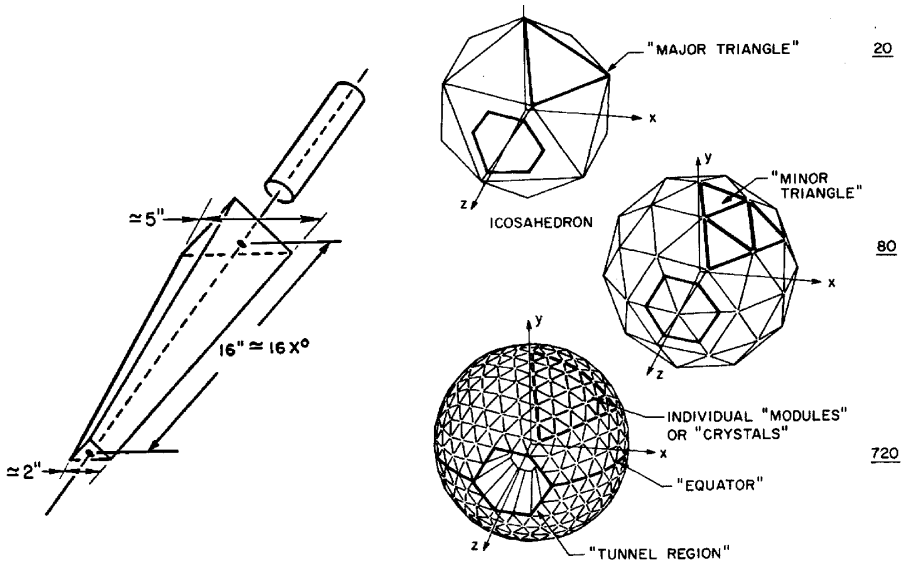

Figure 4.6: Crystal Ball geometry

Figure 4.7: The Crystal Ball photographed upstream with TAPS on the right.

Energy resolution	$\frac{\sigma_E}{E} \approx \frac{1.7\%}{E(GeV)^{0.4}}$
Time resolution	$\sigma_t \approx 2ns$
Angular resolution	$\sigma_\theta \approx 2^\circ - 3^\circ$ (polar) $\sigma_\phi \approx \frac{2^\circ}{sin\theta}$ (azimuthal)

Table 4.1: Crystal Ball parameter resolutions.

The Crystal Ball is the combination of two evacuated hemispheres containing the NaI crystals. This is essential as the crystals are hygroscopic and their optical properties deteriorate with exposure to moisture. The outer and inner radii of the hemispheres are 66.0 cm and 25.3 cm respectively. The equator region between the hemispheres is 0.8 cm thick with two stainless steel plates with a thickness of 1.5 mm each and an air gap between the plates which is adjustable, but generally set at 5 mm. The active region of the Crystal Ball covers approximately 94% of 4π steradians, with an inactive region of 1.6% around the equator and 4.4% at the beam entrance and exit regions.

NaI crystals are used due to their good energy resolution over a wide range of energies, which is an essential requirement for neutral meson detection. Table 4.1 lists the energy, timing and spatial resolutions of the detector. Each crystal is a truncated triangular pyramid, 40.6 cm high and with the sides of the triangular faces 5.1 cm and 12.7 cm at the front and rear end respectively. This length corresponds to approximately 15.7 radiation lengths. To ensure the crystals are optically isolated from each other, they are wrapped in reflector paper and aluminized mylar. Each crystal is viewed by its own SRC L50 B01 photomultiplier which is used due to its linearity over a wide energy range. These are placed outside of the Crystal Ball hemispheres, viewing the scintillation light produced in the crystal through a thick glass window and a 5 cm air gap.

4.4.2 The Liquid Hydrogen Target

The target system [106] comprised of the target, a hydrogen storage tank, a liquifier, a resevoir of liquid hydrogen and a supply line. The liquid hydrogen target (fig 4.8) was contained in a kapton cylinder with a diameter of 4.0 cm, and a length of 4.76 cm during the July 2007 data taking period, and a length of 10.03 cm during the April 2009 data taking period.

The target was kept at a constant pressure and temperature of 1080 mBar and 20.5 K respectively, which equates to an area density of 2.01×10^{23} protons per cm^2 and 4.243×10^{23} protons per cm^2 for the July 2007 and April 2009 targets respectively. The temperature and pressure was continually monitored and were maintained with the supply of liquid hydrogen, and the evapouration of liquid hydrogen by two 4W heaters. Surrounding the target was 8 μm of mylar and 2 μm of aluminium to help maintain the constant temperature.

Figure 4.8: The liquid hydrogen target

4.4.3 The Edinburgh Particle Identification Detector

The Edinburgh Particle Identification Detector (PID) consisted of 24 plastic scintillators, 500 mm long and 4 mm thick, forming a cylinder aligned parallel to the beam axis of inner radius 10.84 cm (fig. 4.9 and 4.10). The scintillators had a trapezoid cross section to minimise gaps between them when assembled into the cylindrical geometry. Each scintillator was optically isolated using thin aluminium foil and connected via lucite light guides to its own photomultiplier tube

(Hamamatsu H3164-10), which were positioned at the upstream end of the detector.

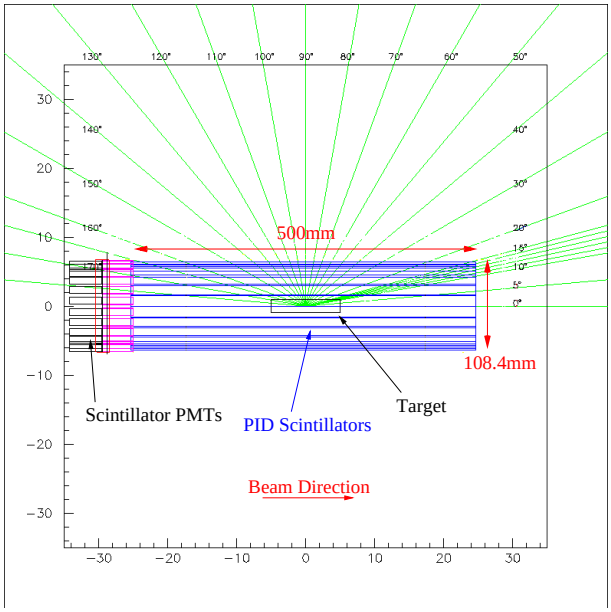

Figure 4.9: The Edinburgh PID.

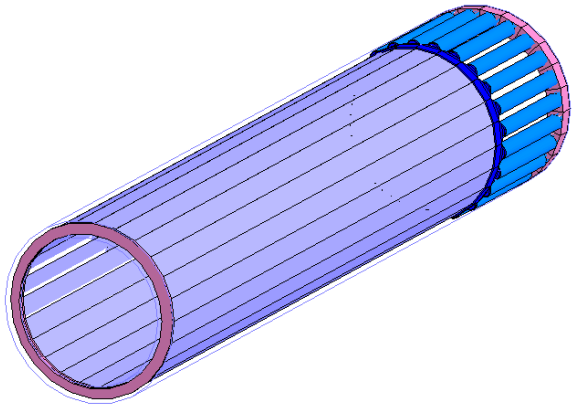

Figure 4.10: Visualisation of a Geant4 simulation of the Edinburgh PID.

Charged particle identification in the Crystal Ball was achieved by comparison of energy deposition in the PID and the Crystal Ball. A charged particle passing

through the PID deposited a fractional amount of energy before depositing the remainder of its energy in the Crystal Ball. Events in the Crystal Ball and the PID were correlated by insisting that the azimuthal angle of the Crystal Ball hit had to be within 15^0 of the centre of the PID element. Two dimensional histograms of the energy depositions yielded charactersitic loci of charged particles (fig 4.11). Two dimensional cuts were then implemented in the analysis to identify particles. This technique is referred to herein as $\Delta E - E$ analysis.

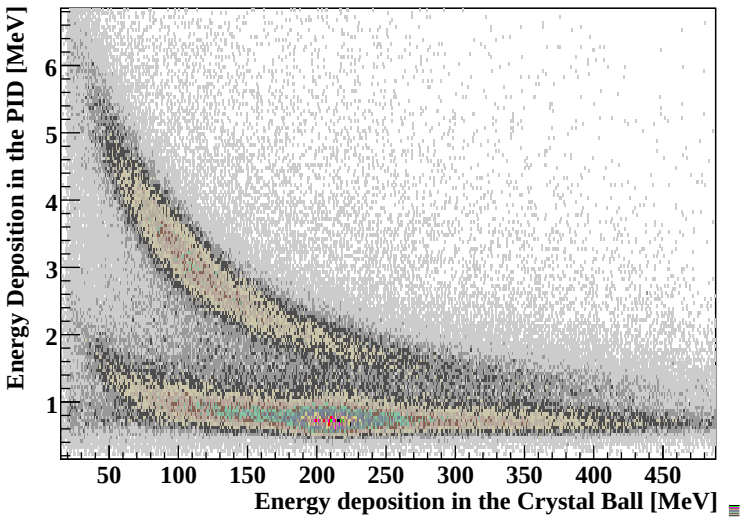

Figure 4.11: $\Delta E - E$ analysis with the PID and the Crystal Ball. Loci of protons (top) and charged pions (bottom) are apparent.

4.5 TAPS detector

The Crystal Ball had a hole at backward and forward angles (greater than 160° and smaller than 20° in polar angle) as it was designed for use in collision experiments. In fixed target experiments the reaction products are Lorentz boosted in a forward direction. This effect becomes exaggerated when the energy of the photon beam is near the threshold energy of the reaction where the reaction products have small momenta in the centre of mass frame. The TAPS detector [107] was

used as a forward wall to the Crystal Ball, covering this important forward 20^0 polar angle range.

4.5.1 TAPS Design

TAPS consisted of 384 hexagonal BaF_2 crystals which were positioned in an array 1.5 m downstream from the target (Fig. 4.13 and 4.12). Each BaF_2 crystal was 25 cm long, corresponding to 12 radiation lengths. BaF_2 has lower scintillation light output than NaI crystals (approximately 29% of NaI light output), however they have higher densities of 4.8 kg/cm^3. A desirable property of BaF_2 is the fast timing resolution of approximately 0.6 ns. This makes the crystals ideal for calorimeters using time of flight methods of particle identification. To ensure the crystals were light tight, each crystal was wrapped in 8 layers of 38 μm thick UV reflecting PTFE (Teflon) and one layer of 15 μm aluminium foil. A layer of silicon glue connected each crystal to a Hamamatsu R2059 PMT. A magnetic shield surrounded the cylindrical part of the crystal and the PMT. The energy resolution (σ) is comparable to the NaI crystals of the Crystal Ball and is shown in eq. 4.3.

$$\frac{\sigma}{E_\gamma} \approx \frac{0.59\%}{E_\gamma(GeV)^{1/2}} \tag{4.3}$$

The TAPS Veto Detector was an array of 5 mm thick plastic scintillators, each scintillator positioned directly in front of each BaF_2 crystal. Coincidence hits between the veto detector and the BaF_2 crystals distinguished between charged and neutral particles detected in TAPS and allowed $\Delta E - E$ analysis for charged particles. Each plastic scintillator was connected via an optical fibre to a Valvo XP2972 phototube.

4.5.2 TAPS Particle Identification

Particle identification in the TAPS detectors exploits three different techniques. These are described in the following sections. The analysis in this thesis only used TAPS to identify the photon from the decay: $\Sigma^0 \rightarrow \Lambda\gamma$ using time of flight techniques (TOF).

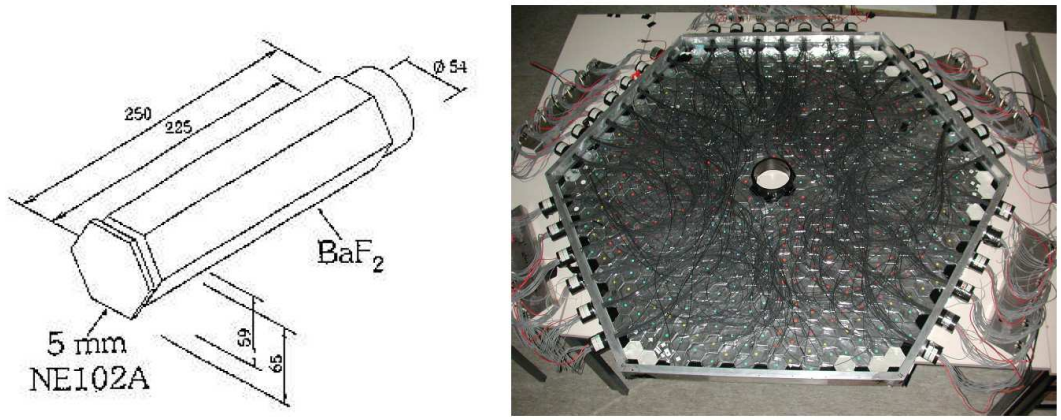

(a) (b)

Figure 4.12: Left: schematic diagram of a BaF_2 crystal. Right: Dismounted TAPS veto wall.

Pulse shape analysis

BaF_2 crystals have two scintillation components: a fast component with a decay time approximately 0.6 ns, and a slow component with a decay time of approximately 620 ns. Pulse shape analysis uses narrow and wide timing gates to enable comparison of the energy deposited from the fast and slow scintillation components. Different particle types result in different contributions in the slow and fast components. The analysis in this thesis did not use the pulse shape analysis method of particle identification and it is not discussed in detail.

Time of flight techniques (TOF)

The time of flight of particles detected in TAPS is obtained from the timing difference between the first hit in the PID and a hit in TAPS[1]. The PID timing was used as it had a better time resolution than the tagger or the Crystal Ball (approximately 1.5 ns).

[1]The method of K^+ identification required a hit in the PID to proceed (described in section 6), so only using TOF techniques in conjunction with the PID did not limit the amount of reconstructed events.

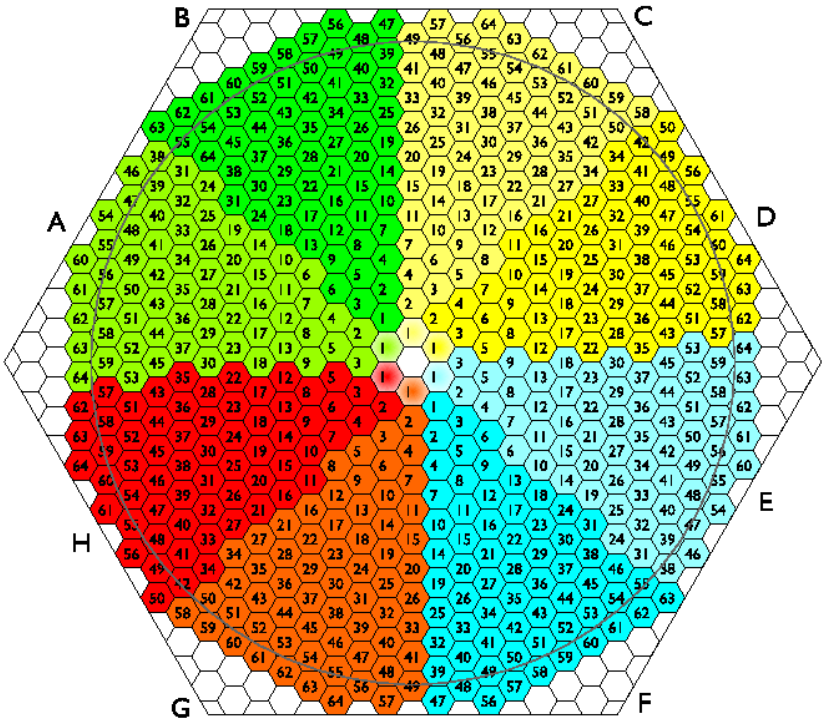

Figure 4.13: Arrangement of the BaF_2 crystals in TAPS (viewed dowstream from the target), with a hole in the centre for the beam to pass through.

Plotting the energy of the event cluster in TAPS versus the time of flight, allows protons and neutrons to be distinguished from photons, electrons and charged pions. Fig. 4.14 shows time of flight histograms for charged and neutral particles. The plastic scintillators of the veto in front of each BaF_2 allow discrimination between charged and neutral particles. Photons and particles at relativistic speeds appear at a time of zero in the time of flight plots. Protons form a ridge, with lower energy protons having a larger time of flight. the ridge is not observed for neutrons as their energy deposition does not vary linearly with their kinetic energy.

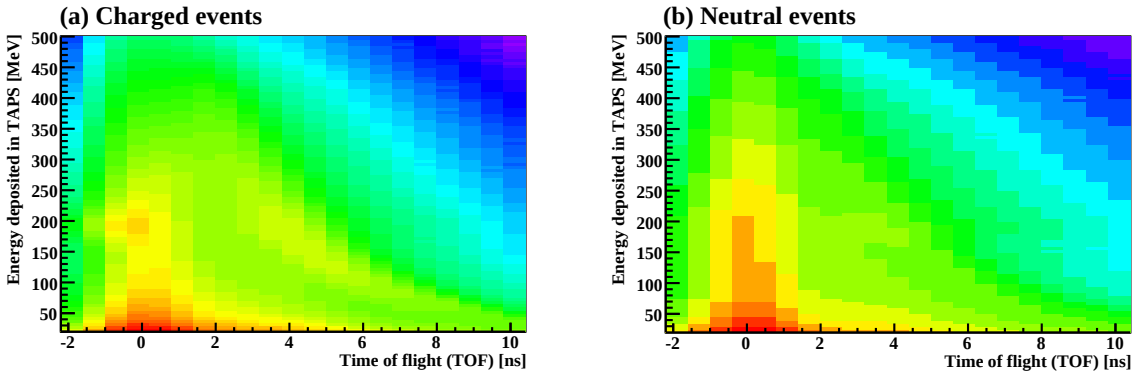

Figure 4.14: Energy deposited in TAPS versus TOF for (a) charged and (b) neutral particles.

$\Delta E - E$ analysis

The fractional energy deposited in the veto plastic scintillators and the energy deposited in the associated BaF_2 crystals enabled $\Delta E - E$ analysis to distinguish between charged particles in the same way as the Crystal Ball and the PID. A typical plot of the energy in the veto versus energy in TAPS is shown in fig. 4.15.

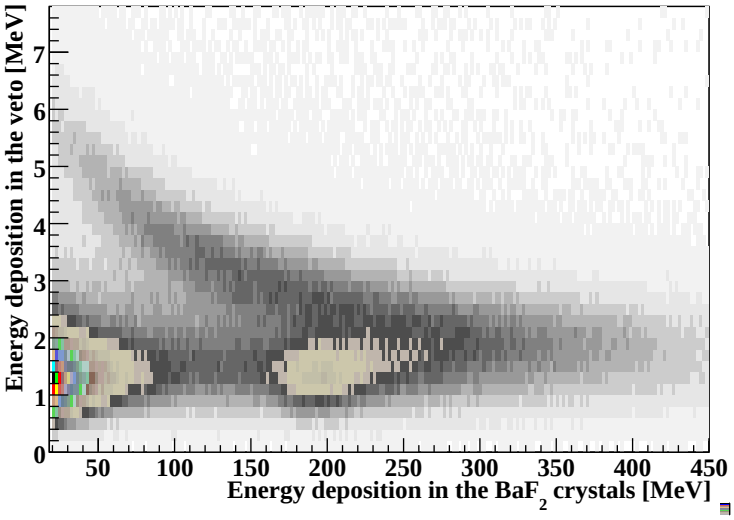

Figure 4.15: TAPS $\Delta E - E$ between the veto plastic scintillators and the BaF_2 crystals. A ridge corresponding to protons is distinguishable at the top with charged pions at 200 MeV in the BaF_2 and electrons less than 50 MeV.

4.6 Data Acquisition

All detector elements in the Crystal Ball, TAPS and Photon Tagger are read out by PMTs which produce an analogue output signal. The analogue signals from each element were analysed using charge to digital converters (QDCs), analogue to digital converters (ADCs) and time to digital converters (TDCs). QDCs and ADCs give a digital quantity to the size of the analogue signal, which in turn is proportional to the energy deposited in the element. TDCs give a digital signal relating to the time of the event. TDCs only measure the time difference between a start and stop signal, therefore they require a start signal from a logic trigger and a stop signal from the given detector element.

The electronics for the tagger, the Crystal Ball and TAPS are explained in section 4.6.1 to 4.6.3. Section 4.6.4 describes the trigger electronics used in the experiment.

The QDC and TDC signals were interfaced to a computer using the AcquDAQ software. The AcquRoot analysis converted the QDC and TDC values into phys-

ical energy and time measurements using the calibrations described in section 5. This allowed the identification of particles and momenta, and the analysis of photoproduction reactions.

4.6.1 Tagger Electronics

The energy of the recoiling electron, and therefore the energy of the bremsstrahlung photon depends on the hit position of the electron in the tagger focal plane. The hit timing is used to correlate the hits in the focal plane with events in the detectors.

If the signal from the PMT of a focal plane element passed a discriminator, a logic pulse was sent to a multihit CATCH TDC (section 4.6.2) to record the time of the hit. Additionally, a pulse from the discriminator was sent to FASTBUS scalers. The scalers provide a count of the hits in the focal plane elements and therefore a spectrum of the recoil electron energies. This was used to extract the photon beam flux for a given energy.

4.6.2 The Crystal Ball detector system electronics

The PMTs connected to each NaI crystal had a high voltage power supply of 1500 V and a currant of 50 mA. The signals from each PMT were passed to fan-out units which grouped the signals into units of 16. The analogue signal from each PMT was split into three; one branch to a Flash ADC via a delay (section 4.6.2), one to a CATCH TDC via a discriminator (section 4.6.2), and the third to triggering electronics (section 4.6.4) Fig. 4.16 is a schematic diagram of this setup.

Flash ADCs

The Flash ADCs were used to measure the integral of the pulse from each PMT by sampling the signal with a sampling rate of 40 MHz. As the large volume of sampled data from each PMT would have overloaded the DAQ, only the integral of the pulse at three different windows was recorded and output to the data stream. The first timing window was set to be behind the pulse to sample the

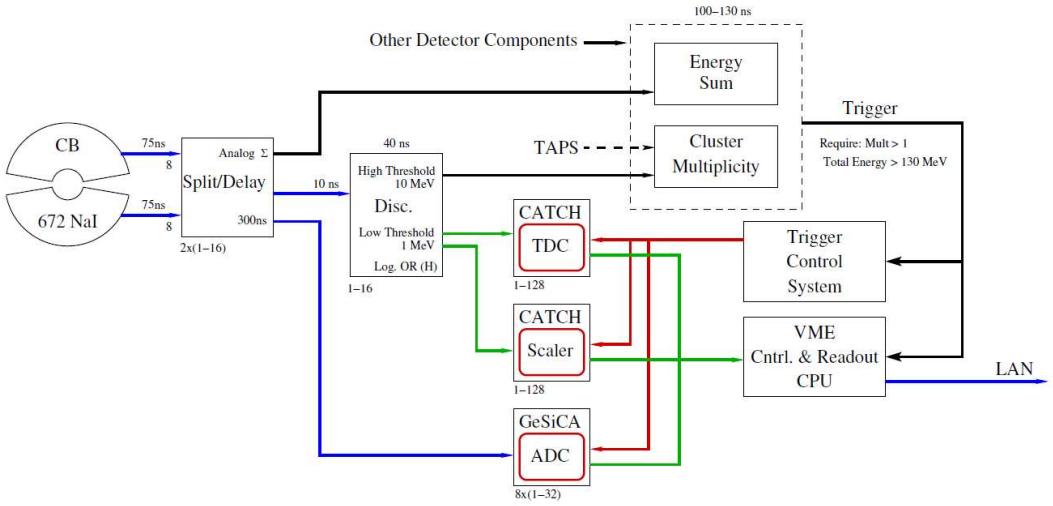

Figure 4.16: Schematic diagram of the Crystal Ball electronics. During the data taking periods for this thesis, no other detector components contributed to the energy sum trigger and TAPS did not contribute to the multiplicity trigger.

pedestal. This was the baseline signal arising from remnant light and residual charge in the PMTs. The second timing window was over the signal, and the third sampled the tail of the pulse. The pedestal was dynamically subtracted from the signal on an event by event basis, improving the achievable energy resolution from the NaI crystals.

CATCH TDCs

Standard TDCs are started by a hit in the detector and are stopped by a logic pulse from triggering hardware. CATCH (Compass Accumulation, Transfer and Control Hardware) TDCs [108], which were developed for the Compass experiment at CERN, apply a different technique to allow multiple hits in each TDC.

Each TDC was free running, using an oscillator with a frequency of approximately 10 GHz. Two Cern-Standard Trigger Control Systems (TCS) were used to synchronise signals in the TDCs. One TDC was used as a reference and was attached to the trigger. Signals in all other TDCs had the oscillator value stored in a buffer. The oscillator value from the reference TDC was subtracted from all

other TDC signals to give the channel difference, which was then converted to time with the conversion rate of 117 ps/channel.

CATCH TDCs have the advantage of allowing multiple hits, with a double hit resolution of 20 ns. This also ensures that the TDCs are not responsible for any significant dead time in the data acquisition.

4.6.3 TAPS electronics

Signals from the PMTs connected to each BaF_2 crystals were split into three branches. Two branches went via a delay to a QDC, one with an integration range of 40 ps and one with 200 ps. The ratio of these signals could then be used in the pulse shape analysis described in section 4.5.2. The third branch was passed to a constant fraction discriminator (CFD) and then to a TDC. CFDs compare the shape of the signal and send a logic pulse to the TDC to start counting when a constant fraction of the signal has passed. this differs from a standard discriminator, which sends a logic pulse once the signal has risen over a set threshold. CFDs provide more accurate timing information, which is important for the time of flight method of particle identification used with TAPS.

4.6.4 Triggering electronics

During the time taken for the DAQ to read the event, the electronics could not record any further hits in the detector system. This is known as dead time and is a limiting factor in the data taking rate during the experiment. A series of triggers were therefore used in the hardware to limit the number of events read by the DAQ. The triggers are optimised for each data taking period to only include events which are potentially useful to the physics aims of the experiment.

Two LeCroy LRS 4805 logic units were used for the triggering hardware. A first level trigger summed the energy deposited from all of the NaI crystals. The trigger required an energy deposition over 350 MeV for the event to pass (referred to as an energy sum trigger). The second level trigger grouped the NaI crystals into groups of 16. The trigger required that at least two crystals in different groups of 16 had energy depositions over 20 MeV (referred to as the multiplicity

trigger). If the event passed both of these triggers, the event was read out and the electronics were reset.

4.6.5 Software analysis code, AcquRoot

Both online and offline analysis of the data was carried out using the AcquRoot framework.

AcquRoot [109] was written in C++ and based upon the suite of libraries and software tools of ROOT [110]. AcquRoot is split into three distinct parts: AcquDAQ Data Acquisition, AcquRoot Analysis, and AcquMC Event Generation.

4.6.5.1 AcquRoot Analysis

AcquRoot was adapted and extended for the work performed in sections 6 and 7. Fig. 4.17 shows the class based structure of the software. The "TA2" prefix implies the class inherits from the TA2System utility class. TA2CrystalBall, TA2TAPS and TA2Tagger inherit from the TA2Apparatus class. Each of these contain the sub-detectors which inherit from the TA2Detector class. For instance, the TA2CrystalBall class includes the detectors "PID" and "NaI". Element positions and timing and energy calibrations are saved in ascii format and read into the analysis for each run.

Calibrations proceed in the TA2Detector classes. Particle identification and their four-momentum reconstruction occurs in the TA2Apparatus classes. More advanced analysis where information is required from multiple detectors[1], and the identification of reaction channels is performed in the TA2Physics classes.

For the method of K^+ identification described in section 6, alternative classes for the Crystal Ball and a general cluster detector class were written. New routines were created for the reconstruction of K^+ kinematics and extraction of cross

[1]For example, the identification of π^0 from the two decay photons. Occasionally one photon is detected in the Crystal Ball and the other in TAPS. The invariant mass of all combinations of two photons from all detectors is checked and compared the π^0 mass. π^0 are selected if the mass difference is smaller than a limit which is input by the user (typically 20 MeV). The same approach is adopted for η identification, which can involve up to six photons.

section measurements. The majority of the TA2TAPS class was changed to reflect the needs of this analysis, eschewing particle identification by pulse shape analysis and $\Delta E - E$ and bringing the time of flight identification procedure into the TA2Physics class.

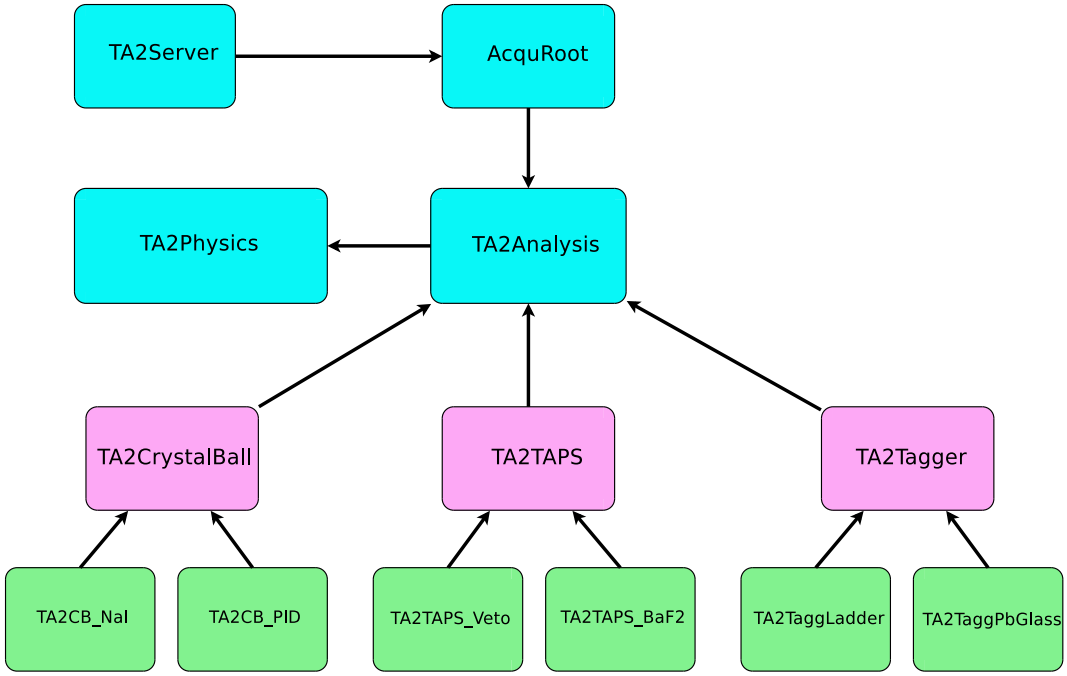

Figure 4.17: The AcquRoot Analysis class based software. Arrows dictate the flow of information. Classes which inherit from TA2Detector are in green, TA2Apparatus in magenta.

4.6.5.2 AcquMC Event Generation

AcquMC is an event generator that provided Monte Carlo particle kinematics which were used as input into the A2 Geant4 simulation. The number of events, the range of the photon beam energy, the target dimensions, and the type of particles produced were all required inputs. By default, a uniform beam energy distribution and a phase-space distribution of particle kinematics were produced.

The kinematics of the reaction could be changed to more realistically model an actual reaction process in a number of ways. The distribution of the kinematics

of the beam and any of the reaction products could follow the form of an inputted function, for example the bremsstrahlung photon beam spectrum, varying as the reciprocal of the energy. Physics models were also incorporated into the event generation. Photoproduction reactions were based upon the differential cross section data taken from SAID partial wave analysis [42, 43, 44]. The SAID data was input to multidimensional grids; the particle kinematics were fixed after the centre of mass angle and photon energy were selected from the interpolated grid distributions.

4.7 Crystal Ball Geant4 simulation

The response of the detector apparatus to particles was simulated using the A2 Geant4 simulation [111]. The A2 Geant4 simulation [111] was developed by the Edinburgh group and is based on the Geant4 suite of C++ libraries [112, 113]. Events generated with AcquMC were input into the simulation. Through the accurate reproduction of the materials and geometry of the real detector system (fig. 4.18), the identification of final state particles was realistically treated.

Geant4 treats the passage of particles as a series of steps. Each step consists of a beginning and end point, containing the particle's coordinates, energy and momentum. Between these points, "delta processes" are applied, for example the energy loss as the particle passes through the material, the time of flight between the beginning and end point, and discrete processes such as bremsstrahlung radiation in the case of electrons. All "delta processes" have a set step length which is small enough to ensure that the discretisation into steps has negligible effect upon the physical outcome. The step length for each particle is taken as the smallest step length from all included "delta processes".

The vertex of the $\gamma(p, K^+)\Lambda$ reaction was randomly generated within a volume of the beam spot size and the length of the liquid hydrogen in the target. The length of the target was changed according to the simulation of the July 2007 or April 2009 data, and any K^+ interactions within the liquid hydrogen as it passed out of the target, or the interation of any other part of the detector system was realistically treated via the discretisation of the K^+ trajectory into steps. Energy

deposits and hit times were recorded in output files which were interfaced to the same AcquRoot analysis as used for the experimental data.

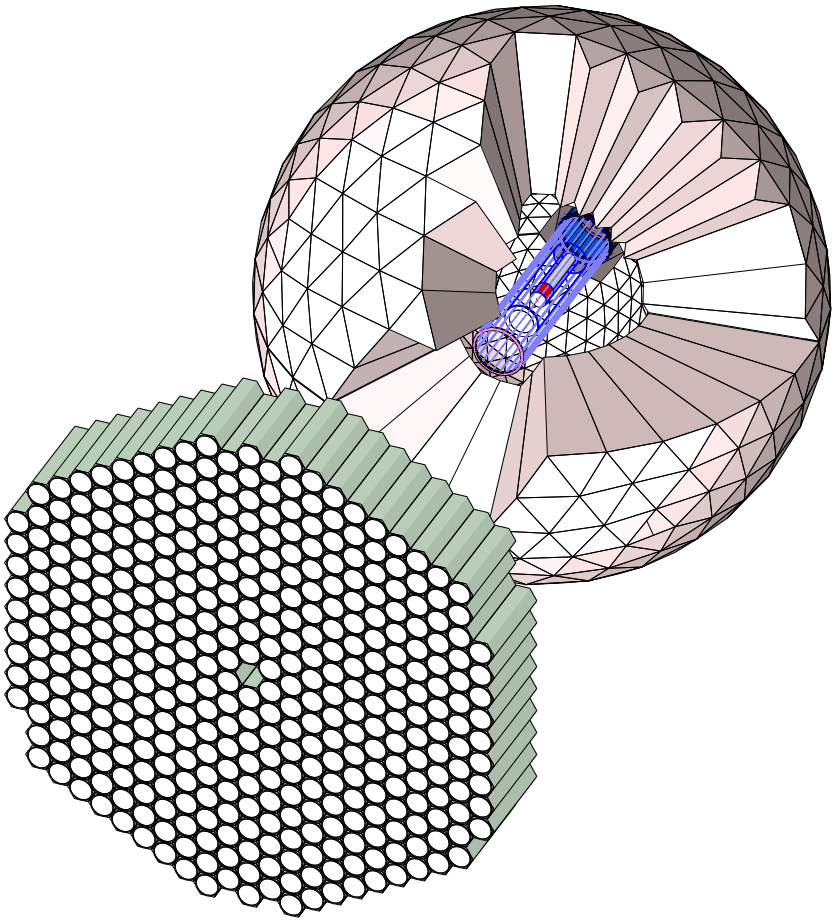

Figure 4.18: A visualisation of the detector apparatus from the A2 Geant4 simulation. The Crystal Ball has a cut-away to reveal the PID and the target.

Although the simulation gives the expected energy deposits and timing information, it does not account for the energy and timing resolution of the detector elements. The resolutions were extracted from experimental data and applied

to the simulated data at the interface to the data analysis. This analysis and a comparison with experimental data is described in detail in section 6.3.3.

The simulation provided a tool for measuring detection efficiencies of particular reaction channels and understanding systematic errors in the experimental data. Decay branching ratios and particle interaction strengths could be altered to observe the effects in the output of the analysis. The simulation was used extensively in the development of the analysis for this thesis, the applications of which are described in section 6.

Chapter 5

Detector calibrations

The calibration of the experimental apparatus is described in this chapter. The calibration first converts the raw ADC and TDC signals from the detector elements into the physical quantities of the energy deposited in the detectors and the time of the event in the detector. The timing for elements of the same detector need to be aligned. Energy calibrations require a gain factor (MeV / channel) and an offset to be applied in the software to convert the ADC channels to energy.

These energy and timing quantities are further analysed to determine the four-vectors of detected reaction products in the Crystal Ball and TAPS, and the incident photon in the Photon Tagger. Section 5.1 describes the methods used to align the timing of events in the detector system. Sections 5.4.3 to 5.4.4 describe the detector energy calibrations.

5.1 Detector timing alignments

Obtaining accurate timing for the events in the detectors is crucial for numerous aspects of the data analysis. For example, timing coincidences to correlate coincident particle events between sub-detectors, clustering algorithms for event showers in the Crystal Ball and TAPS, and time of flight methods of particle identification with TAPS. A timing alignment was done for the Crystal Ball, the PID, TAPS and the TAPS Veto in the same way, so only the Crystal Ball timing alignment is decribed here.

The TDC time spectrum for each NaI crystal in the Crystal Ball was fitted to with a Gaussian function to determine the mean value. As the spectrum was not Gaussian shaped but had a broader tail (fig.5.1(a)), only a 10 MeV range over the mean value was included in the fit. The mean extracted values were used on a crystal by crystal basis to adjust the offset in the timing calibration, and align the peak in the timing spectra (fig.5.1(b)).

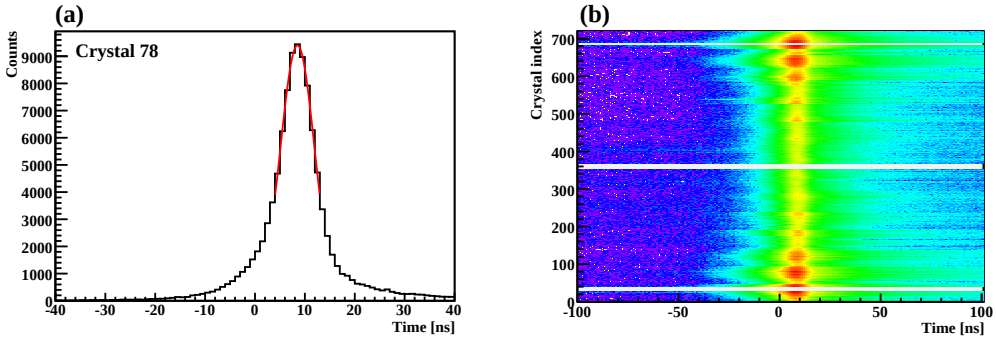

Figure 5.1: (a) Time of hits in crystal 78. A Gaussian function was fitted over a 10 ns range centred on the maximum bin. (b) The time of hits spectra for all crystals after timing alignment. The spaces are where there are no crystals due to the indexing convention.

Fig. 5.2 demonstrates the equivalent procedure to align the peak in the timing spectra of the PID elements.

5.2 Crystal Ball Time Walk Correction

Due to the slow rise time of the pulses produced from NaI crystals (approximately 250 ns), a correction is required to account for the difference in time at which a small signal reaches the discriminator threshold compared to a larger signal with the same mean value (fig 5.3). This produces a shift in timing between small pulse heights and large pulse height events in the Crystal Ball. The corrected time, T' is given in eq. 5.1, where a signal at measured time T has an amplitude

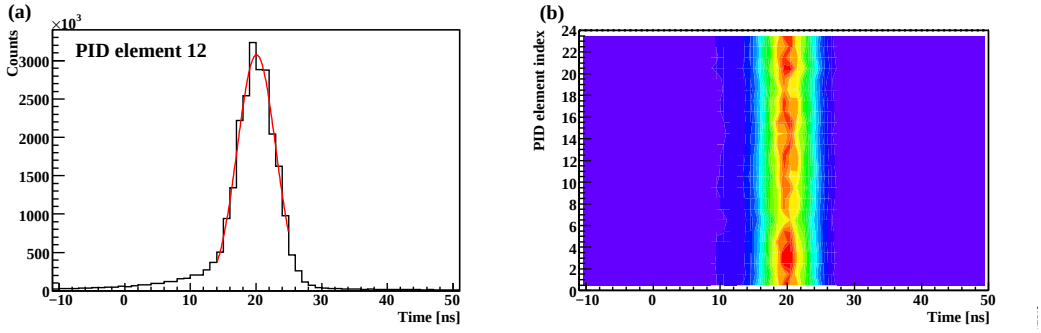

Figure 5.2: (a) Time of hits in PID elememt 12. A Gaussian function was fitted over a 10 ns range centred on the maximum bin. (b) The time of hits spectra for all PID elements after timing alignment.

a with a rise time of r and the discriminator is set at a voltage of a_0.

$$T' = T - r\sqrt{\frac{a_o}{a}} \tag{5.1}$$

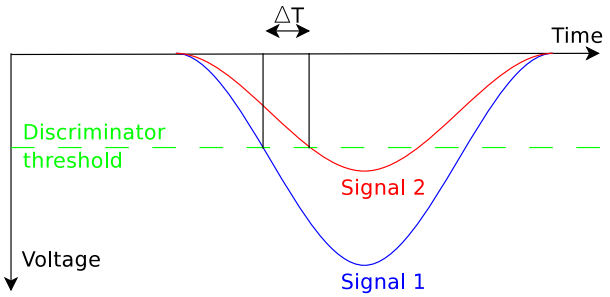

Figure 5.3: Schematic diagram demonstrating the time walk effect. Two TDC signals with equal means but different pulse heights have a measured time difference of ΔT due to the slow rise time and discriminator threshold (dotted green line).

The measured energy was plotted against time, and the parameters a_0 and r were extracted to correct for the time walk in eq. 5.1.

5.3 Photon tagger random subtraction

Not all electron hits in the scintillator elements of the tagger corresponded to the photons responsible for the measured reaction products. There was a background of hits from electrons associated with photons passing through the target with no interactions, Møller scattering in the radiator, and photons which do not pass through the collimator (so called "random hits"). A timing analysis was applied to the data to discern between the "prompt" hits in the tagger which correspond to a timing coincidence with the photon interacting in the target, and the "random" hits corresponding to the background. Random hits in the prompt timing region must be subtracted in the data analysis.

The time difference between the experimental trigger and the hit in the tagger scintillator elements was measured for all tagger hits (fig. 5.4). For scintillator hits corresponding to a photon which interacted in the target, this time difference shows a prompt peak at 100 ns in fig. 5.4. It should be noted that the prompt peak was arbitrarily aligned a common time of 100 ns for all focal plane elements using the timing alignment described in section 5.1. Fig. 5.4 only gives the timing for the first hit in each focal plane element (denoted as "M0" hits). The CATCH TDCS record multiple hits for each focal plane element (the second hit being "M1", third "M2" and so on). These second and third hits necessarily occur at a later time than the "M0" hit. Because of this timing dependence, the background therefore only gives a flat time distribution beneath the prompt peak when all multiple hits are included in the spectrum. To illustrate this effect, Fig. 5.5 shows the time difference between the experimental trigger and M1 hits in the tagger scintillator elements, where as expected, there are more hits at larger times.

Individual hits in the prompt peak region of the tagger time spectrum cannot be identified as either prompt or random on an event by event basis, but given the large number of events, a subtraction of random events can be made by sampling regions on either side of the peak. The determination of any experimental observable involving the photon energy requires a sample of random events and another sample for prompt events (blue and red respectively in fig 5.4). Subtracting the appropriately weighted sample of random events from the prompt region removes the effect of the random events in the prompt sample. To obtain good statistics,

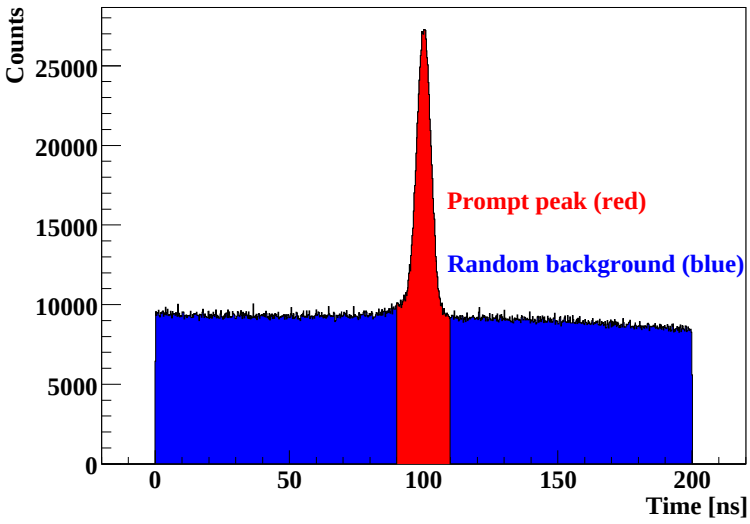

Figure 5.4: Timing of hits in the tagger scintillator elements. Red and blue shaded regions are the prompt and random event samples respectively.

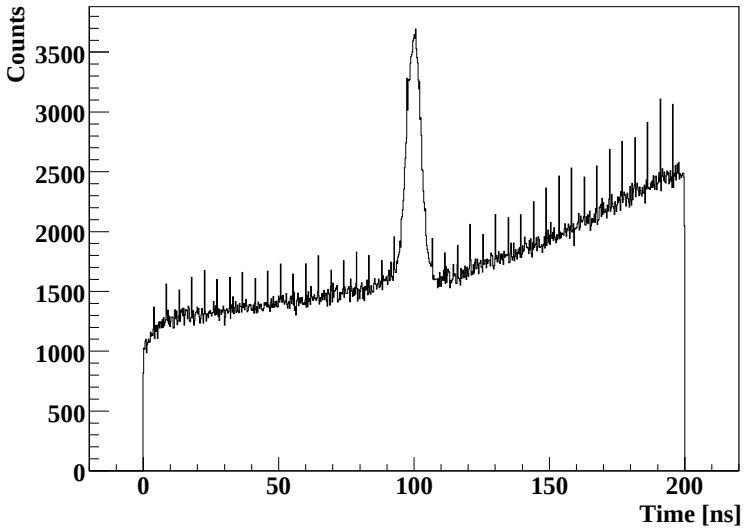

Figure 5.5: Timing of "M1" hits in the tagger scintillator elements.

the random event sample was taken over a time range as wide as possible (seven times that of the prompt region).

5.4 Detector energy calibrations

This section will describe the process of converting the ADC readout from the detector elements in the Crystal Ball and TAPS into energy.

The standard energy calibration procedures for the Crystal Ball and TAPS use photon events and are optimised for photon detection. The electromagnetic showering of the photon is accounted for in the clustering algorithm described in section 5.4.1. The extraction of the gain factors is described in section 5.4.2.

K^+ do not have produce electromagnetic showers and so the calibration was needed to be adapted to account for this. Section 6 describes the refinements required for accurate K^+ energy measurements.

5.4.1 Crystal Ball clustering algorithm

As a consequence of bremsstrahlung and pair production, photons and electrons entering the crystals of the Crystal Ball produce showers of particles. For example, an incident electron will produce bremsstrahlung photons, in turn creating electron positron pairs (pair production), both producing further bremsstrahlung photons. Due to Coulomb scattering, the shower spreads out laterally, firing a group of crystals in the detector. These group of adjacent crystals are referred to as a cluster. The analysis of experimental data therefore requires an algorithm to identify clusters, and a method to extract the position and energy of incident particles from the energies and positions of crystal hits within the cluster.

The clusters are constructed in the analysis by scanning over all of the crystal hits and selecting the crystal with the greatest energy deposition. If there is an energy deposition above 5 MeV in the neighbouring crystals, these crystals are included in the cluster. The procedure iterates for all neighbouring crystals, increasing the size of the cluster until no neighbouring crystals exceed the crystal energy threshold. The energy of the cluster is given as $E_{tot} = \sum_N E_i$, where E_i

is the energy of the ith crystal in a cluster of N crystals. For the cluster to be saved in the analysis, E_{tot} must exceed 20 MeV to suppress background.

The algorithm proceeds to scan over the remaining hits in the detector which have not been included in this cluster, repeating the process. The identification of clusters continues until there are no more crystals with energy deposits above threshold.

The position of the cluster, which determines the hit position of the incident particle is given by the weighted mean position, r_m in eq. 5.2, where E_i and r_i is the energy and position of the ith crystal in the cluster.

$$r_m = \frac{\sum_N r_i \sqrt{E_i}}{\sum_N \sqrt{E_i}} \tag{5.2}$$

5.4.2 Crystal Ball energy calibration

The Crystal Ball energy calibration was performed by colleagues at UCLA and the University of Mainz [114, 115]. The NaI crystals of the Crystal Ball were calibrated in three steps. The first step adjusted the potentiometer to the PMT voltage supplies to match the gains for low energy photons. The second step used an iterative method of calibration from the decay photons of π^0. Finally, an energy scale factor was applied to account for crystal thresholds and clustering algorithms in different analyses.

Crystal Ball gain matching at low energies

For low energies, and as an approximate first step to a complete calibration, a low energy photon was used to match the high voltage gains of the NaI crystals. An ^{241}Am/^{9}Be source was placed in the centre of the Crystal Ball. The α decay of the americium started a chain of reactions, finishing with $^{*12}\mathrm{C} \rightarrow {}^{12}\mathrm{C} + \gamma$, where the photon had an energy of 4.438 MeV. The photon was detected in each of the crystals, and the potentiometer to the base of each PMT was adjusted until the peak from the energy of the photon was in the same position on the ADC spectra for every crystal.

Crystal Ball energy calibrations using π^0 decay photons

The decay: $\pi^0 \rightarrow \gamma\gamma$ provided ideal kinematics to refine the Crystal Ball energy calibrations at energies more typical of photoproduction reactions. The invariant mass of two photons detected in the Crystal Ball was reconstructed and events were selected where the two-photon invariant mass was within 30 MeV of the π^0 mass. For the calibration procedure, these events were subject to the following selection cuts:

1. At least 70% of the energy of cluster from the photons had to have been deposited in a single crystal. As the calibration was performed on a crystal by crystal basis it was important that for every cluster, only one crystal contained most of the energy.

2. The energy difference between the two photon clusters had to be less than 25% of the total energy to ensure that the two photons had a similar energy.

3. The tagged energy of the photon beam had to be less than 180 MeV. This caused the decay photons to have an energy of 40-125 MeV. Insisting on low energy photons ensured that the opening angle between them was large, so that the sampling of the crystals in the Crystal Ball was even. Higher energies for instance would result in smaller opening angles with the majority of photons travelling forwards.

For each crystal, the invariant mass of the π^0 was reconstructed from the two decay photons. A Gaussian function was fitted, and the mean of the function, $m_{\gamma\gamma}$ was compared to the accepted π^0 mass, m_{π^0}. A new gain factor, G_{new} was extracted for each crystal according to eq. 5.3:

$$G_{new} = \frac{m_{\gamma\gamma}}{m_{\pi^0}} G_{Old} \tag{5.3}$$

where G_{Old} was the gain factor used previous to this calculation.

As the energy of the photon cluster depended not only on the central crystal but also on the other crystals in the cluster, changing the calibrations on all of the crystals only once did not give accurate results. The method was iterated until the new calibration gain factor did not differ significantly from the previous calibration gain factor. This took four iterations.

Energy scale factor

The energy of the incident photons is not necessarily equal to the energy of the cluster, E_{tot}, due to individual crystal energy thresholds and the extent of showering. It was necessary to apply a global energy scale to the energy calibration to extract the correct incident photon energy. This was set by the reconstruction of the π^0 mass from the two decay photons. Fig. 5.6 shows the invariant mass peak, after an energy scale factor of 1.073 was applied to the data to ensure the mean is at the correct mass of 135 MeV.

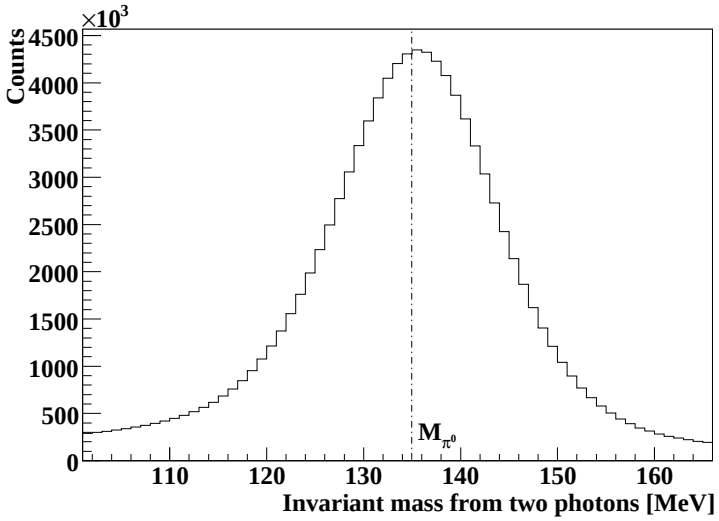

Figure 5.6: The invariant mass of two photons detected in the Crystal Ball. The energy scale factor was set at 1.073 to ensure the correct π^0 invariant mass was reconstructed (135.0 MeV).

5.4.3 Glasgow Photon Tagger energy calibrations

The Photon Tagger calibrations were performed by colleagues at the The University of Glasgow [103].

Electron beams were extracted from MAMI-C at seven different energies, ranging from 195.3 MeV to 1307.8 MeV. The uncertainty in the measured electron energy was 140 keV [102], so the beams provided an accurate tool to calibrate

the photon tagger. Two NMR probes were used to measure the magnetic field strength over the range of the tagger. For each electron energy, varying the magnetic field by up to 5% allowed the electrons to be scanned over the overlapping regions of the focal plane detectors. This gave a hit position with an accuracy of approximately ±0.05 channel. To calibrate the focal plane channel to the electron energy, a linear interpolation between the seven different energies was used.

A small correction was applied to account for the difference in the magnetic field strength across the tagger. The uncertainty in the calibration was estimated as ±0.5 MeV due to non-uniformity in the magnetic field, with a further ±0.2 MeV due to dips in the magnetic field close to the screws fixing the pole shims.

5.4.4 TAPS calibrations

Energy calibrations for the BaF_2 crystals and plastic vetos were performed by colleagues at the University of Giessen [116, 117]. This section describes the methods used.

BaF_2 Energy Calibration

The supply voltage to each of the BaF_2 PMTs was set from the detection of cosmic rays. The minimum ionising peak from relativistic muons is at 37.7 MeV. The potentiometer to each PMT based was adjusted until this peak was at the same ADC position for all BaF_2 crystals.

Due to the small angular coverage of TAPS, a final stand alone calibration was not possible, and so the calibration of TAPS was completed after the Crystal Ball calibration. The calibration proceded by the same method as the Crystal Ball, but insisted on one π^0 decay photon detected in the Crystal Ball and one in TAPS. For a detailed description see [116].

Plastic veto energy Calibration

The ADC channel hits in the veto were plotted against the energy deposited in the BaF_2 crystals. The A2 Geant4 simulation was used with a Monte Carlo generation of protons. The mean of the proton peak in the veto was compared between

experimental and simulated data for different energy ranges in the BaF_2 crystals, and a linear fit for the calibration was extracted. For a detailed description see [117].

5.5 PID Calibrations

5.5.1 PID Azimuthal Alignment

The azimuthal angle of the PID with respect to the Crystal Ball needed to be accurately known to identify angular correlations between hits in the PID elements and hits in the Crystal Ball. The PID is often taken out of the Crystal Ball when targets are replaced, so the azimuthal alignment of the PID had to be repeated for each data taking period. The procedure to accurately establish the azimuthal alignment of the PID is described below.

The first stage was to select events where there was only one crystal fired in a cluster in the Crystal Ball. This ensured the hits included in the calibration had well defined angles and reduced the probability of mis-identifiying photons which typically had larger cluster sizes than events from charged particles. Of these events, a smaller set were selected which had only one hit in the PID to avoid background from events with multiple charged particles in the final state.

The azimuthal angle of Crystal Ball hits were plotted for a coincidence hit in each of the PID elements. This gave a peak over the azimuthal range each PID element occupied. There was also a smaller peak 180° apart due to reactions with two, back to back particles in the final state, where only one particle was charged. A Gaussian function was fitted to the larger of the peaks, and the means of the fits were plotted against the PID element indices (fig. 5.7). Each PID element occupied 15° over the azimuthal range, so a linear fit was used where the gradient was fixed to change the angle by 15° per element.

5.5.2 PID energy calibration

The PID energy for each element was calibrated from the $\Delta E - E$ plots described in Section 4.4.3. The raw ADC signal from each PID element was plotted on a

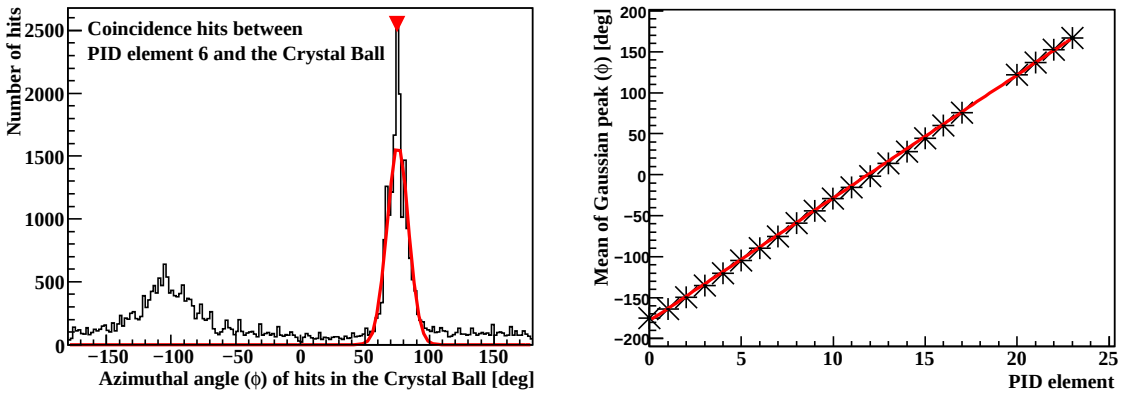

Figure 5.7: Left: Azimuthal angle of hits in the Crystal Ball which have a coincidence hit in PID element 6. A Gaussian function fitted to the larger peak gives the mean azimuthal angle of the PID element. Right: The mean of the Gaussian fit for element plotted against element index. A linear fit gives the azimuthal alignment for the PID.

two dimensional histogram against the energy deposition in the Crystal Ball. For each PID element, the characteristic loci from the ridge of protons was compared to the Geant4 simulated data described in Section 4.7.

$\Delta E - E$ plots from the experimental data were divided into 10 MeV regions along the x-axis (energy deposited in the Crystal Ball) and each of these projected onto the y-axis (energy deposited in the PID). From the prominent loci of protons and pions in the $\Delta E - E$ plots, two corresponding peaks were seen in each of the projections of the raw ADC signal in the PID. The peak from the proton contribution was identified and a Gaussian function was fitted over a range of 200 channels to extract the mean position of the proton peak (fig. 5.8, bottom right panel).

Equivalent plots were used to find peak positions in the simulated data (fig. 5.8, top right panel). The main charged reaction products expected in the energy range of the experiment were $p\pi^0$, $n\pi^+$, and $n\pi^0\pi^+$. A phase space generation of these channels (300 000 events each) were input into the A2 Geant4 simulation.

For each PID element, the mean position of the fits to the proton loci were

plotted against the equivalent fitted projections from the Geant4 simulation and a linear fit used to extract the gain and offset for the calibration (fig. 5.8, bottom left panel). An additional correction for the light attenuation for protons in the NaI crystals was applied [118]. Light attenuation was not described by the simulation and the correction was therefore required to extract linear fits for the PID energy calibrations.

Performing the calibrations in this manner ensured that the $\Delta E - E$ plots for each PID element were matched and allowed the application of uniform particle selection cuts.

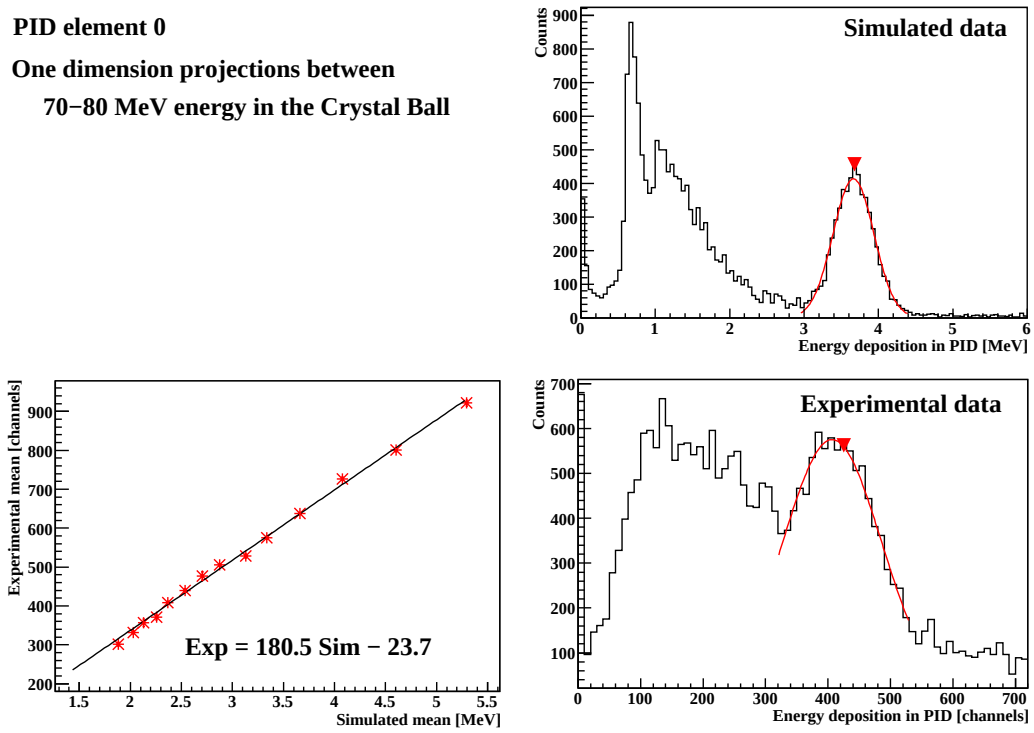

Figure 5.8: Energy calibration for PID element 0. Top and bottom right: Energy deposition in the PID for energy between 70-80 MeV in the Crystal Ball. The proton ridge was identified and a Gaussian function fitted. Bottom left: The mean of Gaussian functions for experimental and simulated data plotted against each other. The linear fit (parameters inset) was used to calibrate the energy deposition in PID element 0.

Chapter 6

K^+ identification with the Crystal Ball

6.1 Introduction

The cross section of strangeness photoproduction channels are of the order ten to one hundred times smaller than non-strange production channels (for example $\gamma p \to p\pi^0$ and $\gamma p \to p\pi^+\pi^-$). It is therefore essential to use a rigorous method of K^+ identification to eliminate other reaction channels from the analysis. This section explains the new method of K^+ detection with the Crystal Ball that was developed for this thesis.

Two different methods of K^+ detection have been employed in recent measurements with photon beams of the order of 1 GeV (section 3). The CLAS detector at Jefferson Lab used large magnetic spectrometers and time of flight detectors to reconstruct particle momenta and energy [51]. This allowed the determination of particle charge and mass and had sufficient resolution to seperate K^+ from protons and π^+. The SAPHIR detector at ELSA used drift detectors to reconstruct the detached Λ decay vertex to tag the associated production of K^+ [46].

Neither method was possible with the Crystal Ball. The short path length to the crystals of the Crystal Ball prevented useful TOF information and the absence of a magnetic field prevented accurately resolving particle momentum in

this manner. Initial attempts to identify K^+ in the data were made using $\Delta E - E$ analysis with an energy measurement from the PID and the Crystal Ball.

This method of K^+ identification proved insufficient due to the large background of protons and charged pions in the same region of the $\Delta E - E$ histogram as the K^+. Additionally, the energy of the decay products of the K^+ deposited in the Crystal Ball spoiled the $\Delta E - E$ signature (fig. 6.1). It was realised that the signature of the decay products could be used to identify K^+, and this led to the development a new K^+ detection technique, exploiting the timing and energy correlations from the weak decay of the K^+ as a means of identification.

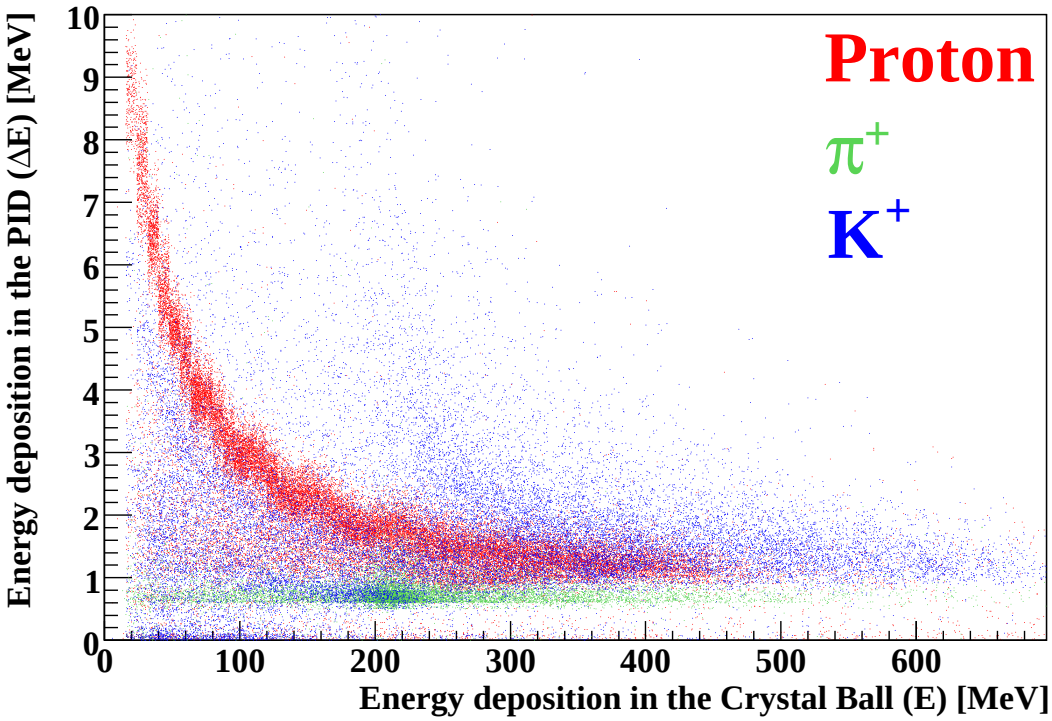

Figure 6.1: $\Delta E - E$ analysis of simulated data, tracking protons (red), π^+ (green) and K^+ (blue).

6.2 Identification Technique

The K^+ has a mean life time of approximately 12 ns and decays weakly. Its predominant decay modes are listed in table 6.1. The identification technique involved separating the cluster produced by the K^+ into the crystals involved in stopping the K^+ (incident sub-cluster) and the crystals fired by the decay products in the subsequent weak decay of the K^+ (decay sub-cluster). Fig. 6.2 is a schematic showing a typical hit distribution for a K^+ in the Crystal Ball.

K^+ mean life $\tau = 12.380 \pm 0.021$ns

Main K^+ decay modes	Branching ratio
Predominant Leptonic and semileptonic modes	
$K^+ \rightarrow \mu^+\nu_\mu$	$(63.54 \pm 0.14)\%$
$K^+ \rightarrow \pi^0 e^+\nu_e$	$(5.08 \pm 0.05)\%$
$K^+ \rightarrow \pi^0\mu^+\nu_\mu$	$(3.35 \pm 0.04)\%$
Predominant Hadronic modes	
$K^+ \rightarrow \pi^+\pi^0$	$(20.68 \pm 0.13)\%$
$K^+ \rightarrow \pi^+\pi^0\pi^0$	$(1.761 \pm 0.022)\%$
$K^+ \rightarrow \pi^+\pi^+\pi^-$	$(5.59 \pm 0.04)\%$

Table 6.1: K^+ decay modes.

Only the two predominant decay modes; the "muonic decay mode" ($K^+ \rightarrow \mu^+\nu_\mu$), and the "pionic decay mode" ($K^+ \rightarrow \pi^+\pi^0$) are discussed in the description of the technique, however it should be noted that all processes were included in the simulated data and were present in the experimental data. Combined, the dominant modes account for approximately 84% of all K^+ decays. The decay sub-clusters from these dominant decay modes have different decay characteristics.

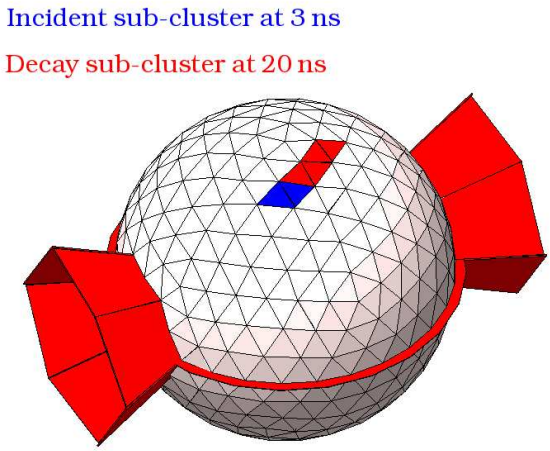

Figure 6.2: Schematic diagram of K^+ detection in the Crystal Ball. An initial cluster is split into an incident sub-cluster from the stopped K^+ with a mean time less than 3 ns between the crystal hits (blue crystals), and a decay sub-cluster (red crystals) with a mean time of 20 ns from the decay of the K^+.

For a K^+ decaying from rest via the muonic mode, the μ^+ has a kinetic energy of 152 MeV which is deposited in the Crystal Ball in the decay sub-cluster. In NaI, this corresponds to a path length of approximately 25 cm, or the width of five crystals. The neutrino will not be detected.

For the case of the pionic decay, the π^0 kinetic energy (110 MeV) and mass will be released in the two photon decay, and the π^+ will add its kinetic energy of 109 MeV, producing a decay sub-cluster in the Crystal Ball. This gives a total energy deposition of up to 360 MeV in the pionic decay sub-cluster.

6.2.1 K^+ identification algorithm

The K^+ identification proceeded as follows.

1. An initial grouping of crystal hits in the Crystal Ball were made using the iterative cluster algorithm (section 5.4.1), including all neighbouring crystal hits.

2. If crystal hits in the cluster were within 8 ns of each other, they were grouped together into smaller sub-clusters.

3. The first sub-cluster in time was assumed to be the incident K^+ and the second, later sub-cluster to be the decay sub-cluster.

4. The incident sub-cluster was required to have an energy over 25 MeV and the decay sub-cluster was required to have an energy over 75 MeV (fig. 6.4(a)).

5. Only events with incident sub-cluster sizes below three crystals were accepted. This improved the K^+ angle and momentum reconstruction.

6. Events had to have at least four crystals in the decay sub-cluster (fig. 6.3(a)).

7. The furthest distance between each crystal in the decay sub-cluster from the incident sub-cluster had to exceed 11 cm (fig. 6.3(b)). The distances were calculated from the distance of the midpoint of the crystals.

8. The time difference between the incident and decay sub-clusters had to be between 10 to 45 ns (fig. 6.3(c)). The upper time limit was imposed due to an artefact from the CATCH TDCs at approximately 50 ns. The timing associated with each sub-cluster was taken as the mean of the times of each crystal in that sub-cluster.

9. Events were only included in the analysis if the $\Delta E - E$ correlation between the PID hit and the energy of the incident cluster was consistent with the loci of the K^+. A two dimensional cut was used to remove background in random coincidence at low Crystal Ball and PID energies (Fig. 6.3(c)).

Fig. 6.4 shows four spectra illustrating various aspects of K^+ identification in the Crystal Ball. The energy of the decay sub-cluster (fig. 6.4(a)), shows a peak at the muonic decay energy (152 MeV) and a broad shoulder over the region expected to be populated following pionic decay (150 to 350 MeV). The time difference between the average time of the incident and decay sub-clusters would be expected to reflect the lifetime of the K^+. Fitting an exponential

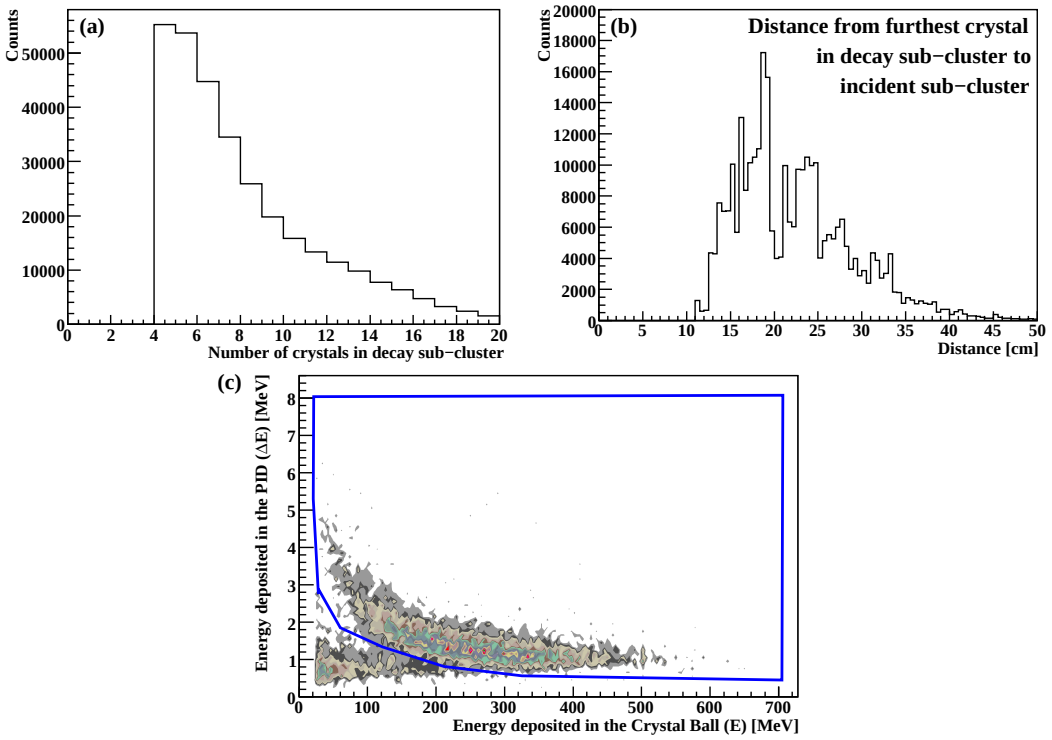

Figure 6.3: (a) The number of crystals in the decay cluster. (b) The length of the decay cluster. (c) $\Delta E - E$ analysis for events with an incident and decay cluster. The blue cut removes background from electrons and charged pions.

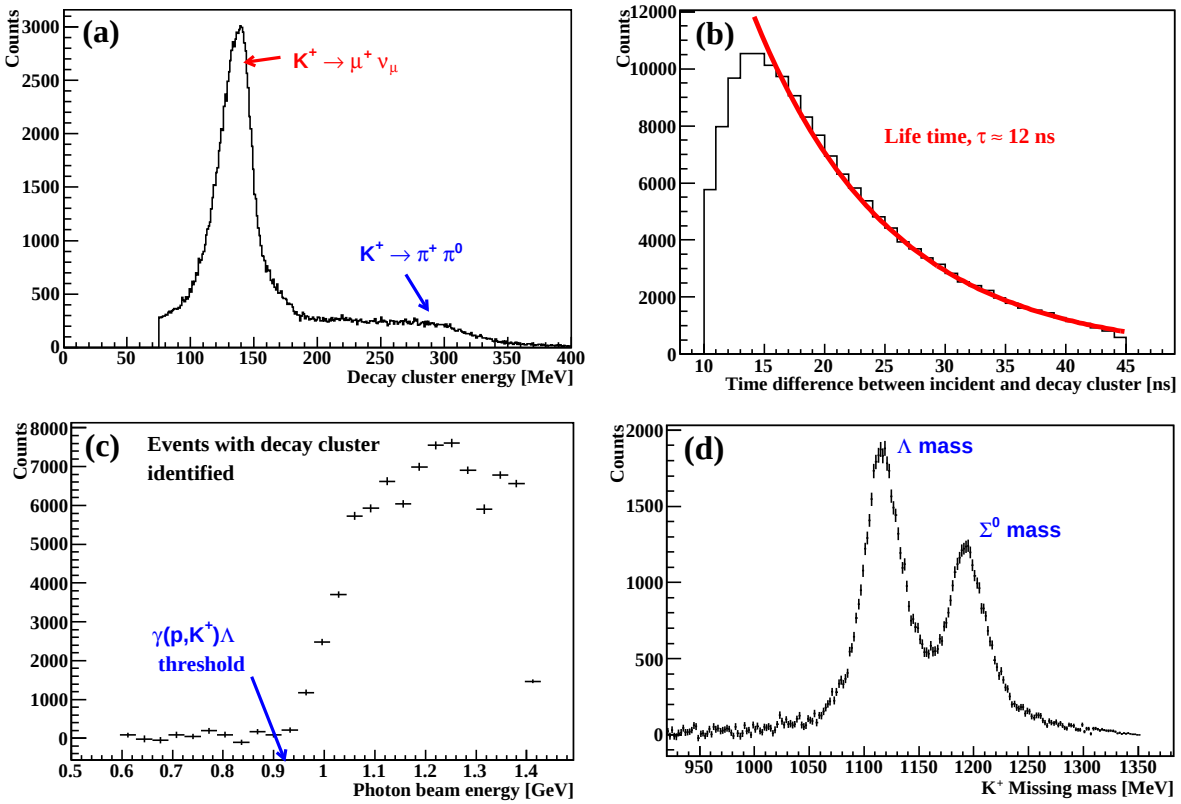

Figure 6.4: (a) Energy of the decay cluster. (b) Time difference between incident and decay cluster. (c) Photon beam energy for events with incident and decay clusters. (d) Reconstructed missing mass from K^+ detection.

function to the time difference between the incident and decay sub-clusters yields the expected K^+ lifetime of approximately 12 ns (fig. 6.4(b)). Fig. 6.4(c) is a histogram showing the yield of K^+ events versus the photon beam energy. There is a sharp rise in the yield at the $\gamma(p, K^+)\Lambda$ energy threshold of 911 MeV, as would be expected for a good sample of K^+ events. Fig. 6.4(d) is the missing mass from the reconstructed K^+ momenta and incident photon energy. The two peaks are over the Λ and Σ^0 masses of 1115.7 and 1192.6 MeV respectively.

All of the plots illustrate the success of the new technique in isolating K^+ reaction channels from background reactions and enabling a reliable determination of its energy.

The efficiency of K^+ detection was determined using the A2 Geant4 simulation (section 6.3). The detection efficiency was obtained from the ratio of the number of detected K^+ to the number input into the simulation. Varying with K^+ polar angle and beam energy, the detection efficiency was up to a maximum of 14%. The simulation was also used to measure the amount of other reaction channels that were misidentified as K^+ events. A negligible amount of non-strange reaction channels are misidentified (of the order of 10^{-3}%)[1].

6.2.2 K^+ energy corrections

To identify the $K^+\Lambda$ final state and to measure the centre of mass polar angle of the event, the energy of the K^+ at the reaction vertex must be determined. Three corrections to the measured energy of the K^+ were required: a material energy loss correction, a remnant energy correction to account for the residual decay product energy in the incident sub-cluster, and a final energy scaling.

6.2.2.1 Material energy loss correction

The material energy loss correction accounted for kinetic energy lost as the K^+ passed from the target to the crystals in the detector. As this depended upon the geometry and composition of the detector and associated apparati, an energy loss

[1]This is discussed in section 7.6.2, where the simulation of other reaction channels was partly used to estimate systematic errors in $\gamma(p, K^+)\Lambda$ cross-section measurements.

correction as a function of the measured K^+ energy was needed for each detector crystal.

Two million simulated single K^+ events were used with the A2 Geant4 simulation to extract the material energy loss correction factors. The K^+ were generated over an energy range of 25 to 340 MeV, corresponding to the range of kinetic energies of K^+ detected in the Crystal Ball. These events were generated over the Crystal Ball polar angle range of 20^0 to 160^0 and over all azimuthal angles. The process to extract the correction factors is described below.

For each generated K^+, the difference between the actual energy and the K^+ energy measured in the Crystal Ball was calculated. This was divided by the measured energy to give a fractional energy loss. The decay of the K^+ was "switched off" in the simulation process to ensure that the energy measured was only due to the K^+ kinetic energy and not the K^+ decay. Detected events were only kept in the analysis if the K^+ cluster consisted of only one crystal. Histograms of K^+ fractional energy loss were created for every 10 MeV increment in measured energy and for every crystal. A Landau function was fitted to these energy loss spectra. Fig. 6.5 is an example of energy loss spectra in a single crystal. Fig. 6.5(a) shows the fractional energy difference for measured K^+ energies between 40 to 50 MeV. The mean of each Landau function was plotted against the measured K^+ energy and this was fitted with the sum of a linear and exponential function (Fig. 6.5(b)).

To correct the K^+ energy in subsequent data analysis, the index of the crystal in the incident sub-cluster with the largest energy deposition was identified and the parameters of the fit for that crystal were read into the analysis to correct the energy. As was stated in the K^+ identification algorithm, K^+ events were kept with incident sub-cluster sizes of up to two crystals. As the fit parameters did not differ significantly between neighbouring crystals (of the order of 0.1%), the difference in energy correction for clusters of two crystals was negligible.

Fig. 6.6 is the K^+ energy difference for all crystals before and after the energy loss correction. After the correction, the spectrum has narrowed with the most probable value on zero as expected.

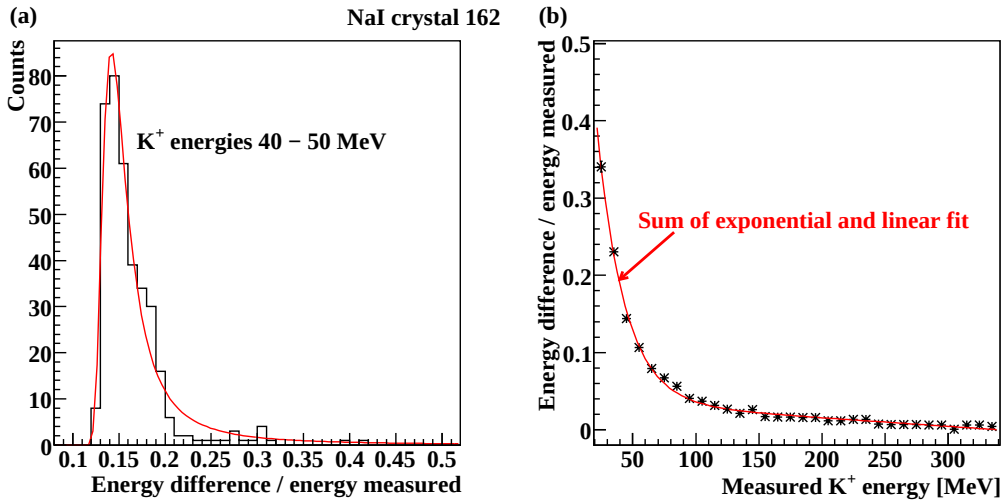

Figure 6.5: Energy loss corrections for crystal 162: (a) Energy difference / measured energy for K^+ energies 40-50 MeV with a Landau function fitted. (b) Energy loss for K^+ measured energies 20 to 340 MeV. The red line is a sum of an exponential and a linear fit.

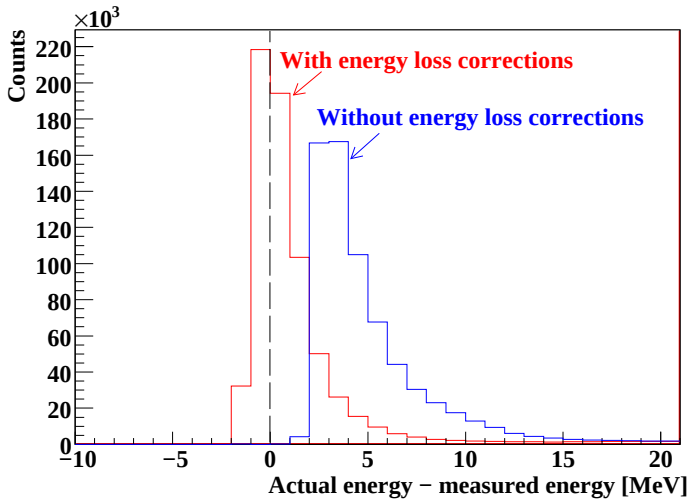

Figure 6.6: Simulated K^+ energy difference between generated and measured energies, with and without energy loss correction.

6.2.2.2 Remnant energy correction

For every K^+ event, a fraction of the energy from the K^+ decay products were left in the incident sub-cluster. As this did not derive from the incident energy of the K^+ it needed to be subtracted to optimise the energy resolution for the detected particle. The remnant energy correction could not be parameterised in terms of crystal index and measured K^+ energy like the material energy loss correction, as it depended on the decay mode, direction of the decay products from the K^+ and the geometry of the neighbouring detector crystals. To proceed, the decay mode of the K^+ was identified and each mode treated separately.

The energy deposition characteristics of the decay sub-cluster were used to identify the decay mode. During the muonic decay ($K^+ \rightarrow \mu^+\nu_\mu$), only the μ^+ was detected in the Crystal Ball. As the μ^+ moved through the crystals, energy was deposited in a straight line from the incident sub-cluster with the majority of the energy deposited in the further most crystals as the μ^+ decelerated (the Bragg peak). During the pionic decay ($K^+ \rightarrow \pi^0(\gamma\gamma)\pi^+$), the Crystal Ball detected all three decay particles. The energy deposition therefore did not form a straight line from the incident sub-cluster and was more uniformly spread across the decay sub-cluster crystals.

To assess the characteristics of the two decay processes, two million phase space generated K^+ were input to the A2 Geant4 simulation. An angle from the incident sub-cluster to the crystal in the decay sub-cluster with the highest energy deposition was extracted. The difference in angle between this crystal and similar angles from all other crystals in the decay sub-cluster was calculated and a mean value obtained (fig. 6.7). This value was defined as the "linearity" of the decay cluster. A small value suggested the decay sub-cluster was close to a straight line from the incident sub-cluster, a large value suggested it was spread around the incident sub-cluster.

The other parameter used in the analysis of the cluster was the fractional energy, E_{frac}. The energy of the crystal in the decay sub-cluster furthest from the incident sub-cluster was measured. This was divided by the total energy of the decay sub-cluster to give E_{frac} (fig. 6.7). A fractional energy approaching

unity suggested the majority of the energy of the decay sub-cluster was in the crystal furthest from the incident sub-cluster.

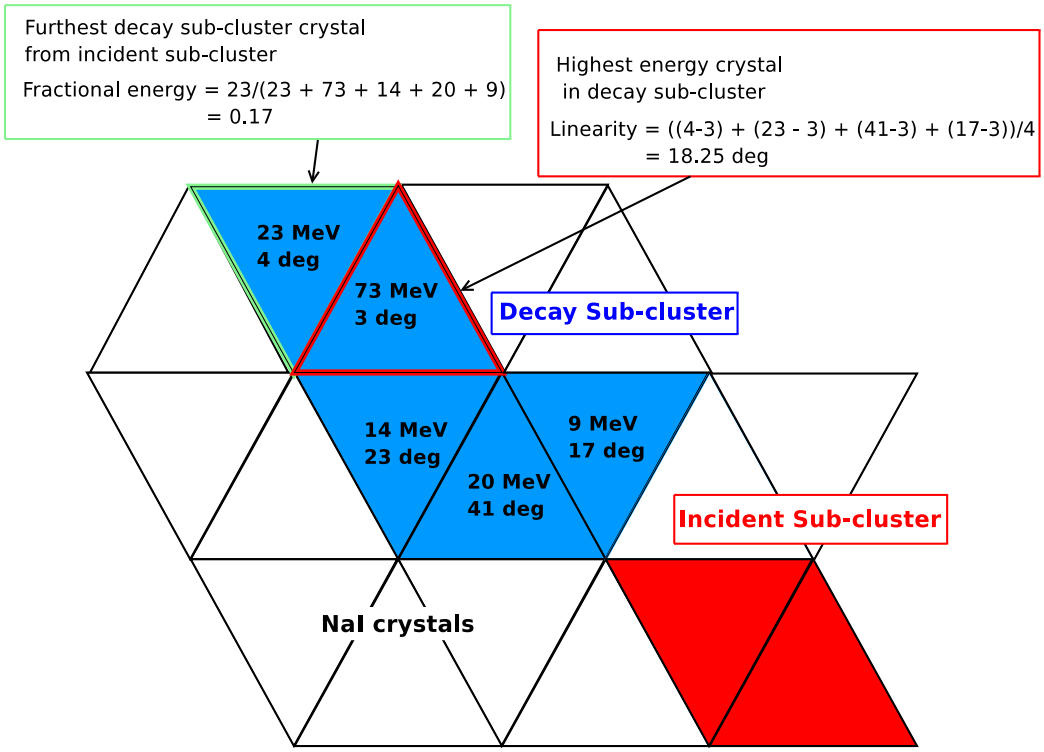

Figure 6.7: Schematic diagram of the incident and decay sub-clusters in the crystals of the Crystal Ball (red and blue respectively). Each crystal in the decay sub-cluster is labelled with the energy deposition and angle to incident cluster. An example calculation of the fractional energy, E_{frac}, and the linearity is included.

Fig. 6.8 is the linearity versus the fractional energy. For simulated events, the muonic and pionic K^+ decay modes can be seperated. These are plotted on separate histograms in fig 6.8. The same histogram is also plotted for experimental data. The superimposed cuts split the experimental data into the two predominant decay modes. Fig 6.9 is the energy of the decay sub-cluster for experimental data. All events are in black with the muonic and pionic events in red and blue respectively. Approximately 80% of the total yield from each event type fall into either cut. Excellent agreement between the experimental and simulated data is observed giving further confidence in the description of the process

by the A2 Geant4 simulation. Events which missed both cuts were assigned as either muonic or pionic events if the decay cluster energy was below or above 180 MeV respectively. The remnant energy correction then proceeded for pionic and muonic events seperately.

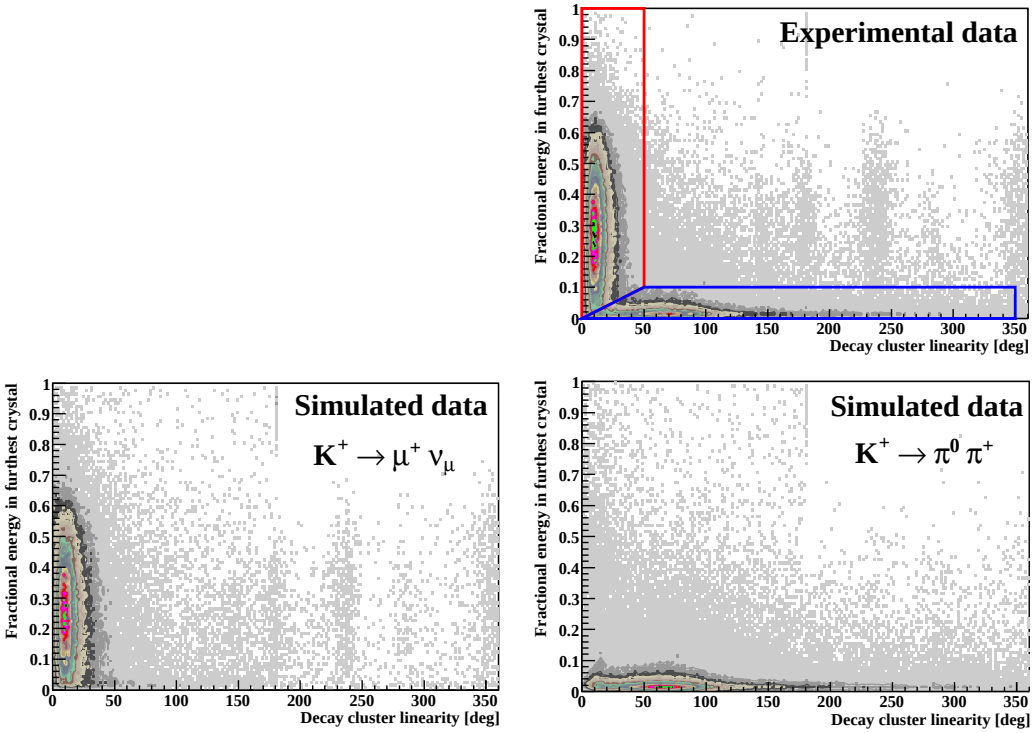

Figure 6.8: The fractional energy deposited in the furthest decay cluster crystal versus linearity for experimental data (top right), simulated data only allowing the muonic decay (bottom left) and simulated data only allowing the pionic decay (bottom right). The red and blue cuts on the experimental data select muonic or pionic decays respectively.

The fractional remnant energy correction, E_{rem}, for each decay mode is defined as:

$$E_{rem} = \frac{E_{K^+} - E_{meas}}{E_{meas}} \tag{6.1}$$

where E_{K^+} is the actual K^+ energy and E_{meas} is the measured energy from the incident sub-cluster, with the material energy loss correction applied. E_{rem} was

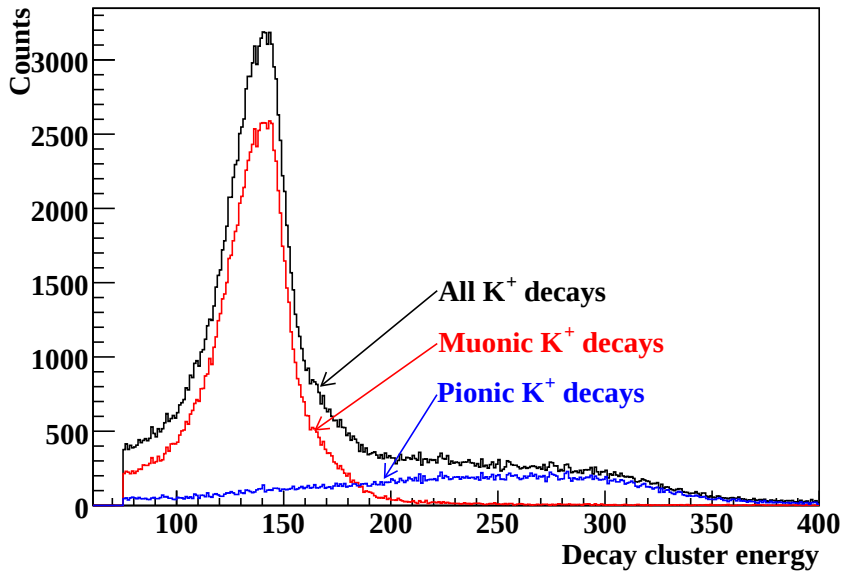

Figure 6.9: Decay cluster energy split into muonic and pionic decay modes (red and blue lines respectively). The black line is for all events. Events which did not pass either cut, but were assigned pionic or muonic depending upon the decay sub-cluster energy have not been included.

plotted for measured energy increments of 30 MeV (fig. 6.10). The mean of each spectra was then plotted against the measured K^+ energy. E_{rem} did not vary by more than 5% with measured energy and so a horizontal line was fitted and a constant correction factor extracted. This factor differed depending on the decay mode reflecting the different energy deposition characteristics. Pionic decay events required the measured K^+ energy to be scaled by 0.81, muonic decay events required the K^+ energy to be scaled by 0.95.

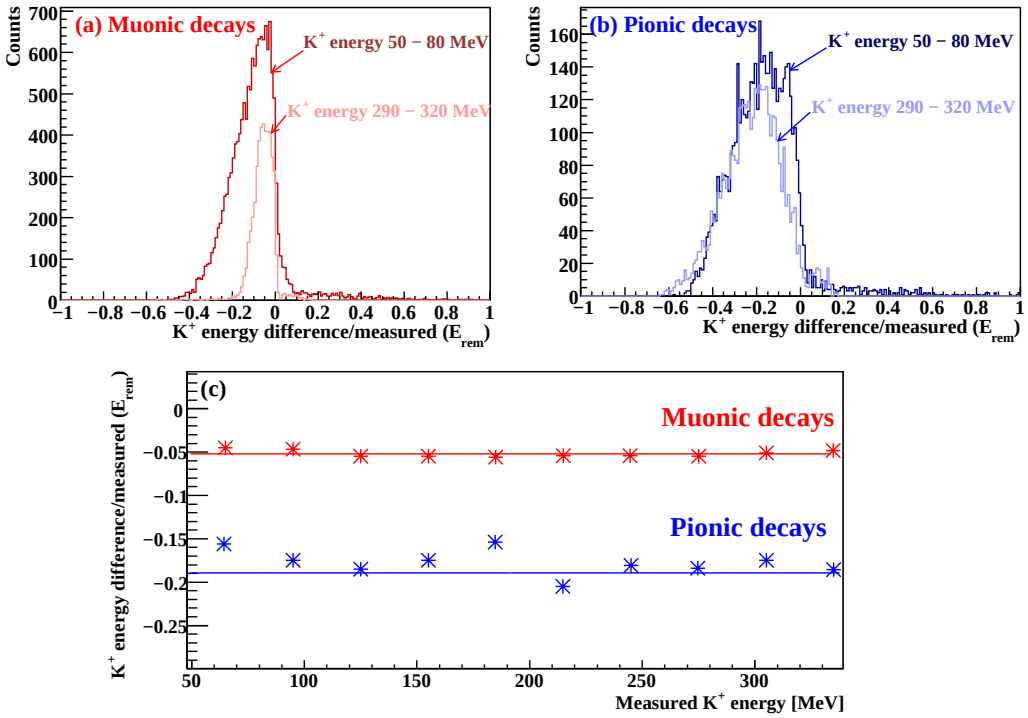

Figure 6.10: Fractional energy difference between measured and real K^+ energy. (a) Muonic decays and (b) pionic decays at low and high K^+ energy. (c) Energy difference plotted against measured K^+ energy. Correction factors were extracted from the fits to the data.

6.2.2.3 K^+ energy scaling factors

The scaling factor described in section 5.4.2 was set by measuring the mean of the π^0 mass peak. This gave a correction for the electromagnetic shower not

contained by the crystals and crystal threshold effects. The K^+ deposits all of its energy in the crystals after energy losses are accounted for, and so the energy scaling factor for K^+ detection was changed to ensure the missing mass peaks reconstructed from the K^+ and incident photon were centred over the Λ and Σ^0 masses. Scaling factors of 0.88 and 0.95 for muonic and pionic decaying K^+ were used respectively. The small difference in the energy scale improved the resolution of the two peaks in the missing mass spectrum.

6.2.2.4 Results of material energy loss and remnant energy corrections

Fig. 6.11 is the missing mass for K^+ events before and after the energy corrections. The widths of the peaks over the Λ and Σ^0 masses are narrower after the corrections. Fig. 6.12 shows the missing mass with the pionic and muonic events separated.

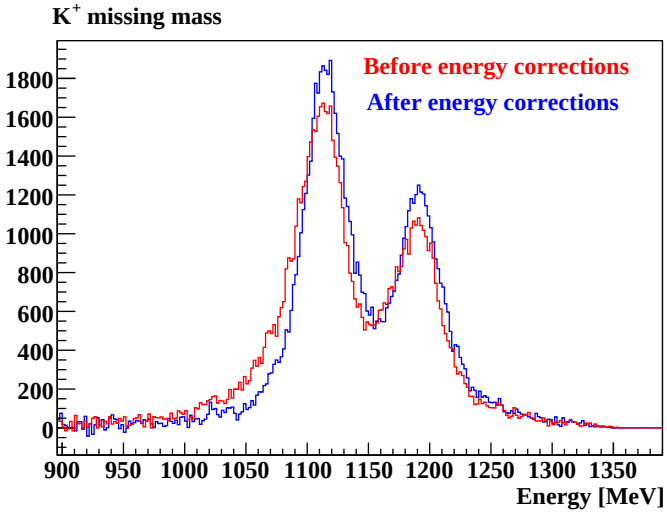

Figure 6.11: K^+ missing mass, before and after K^+ energy corrections (red and blue lines respectively).

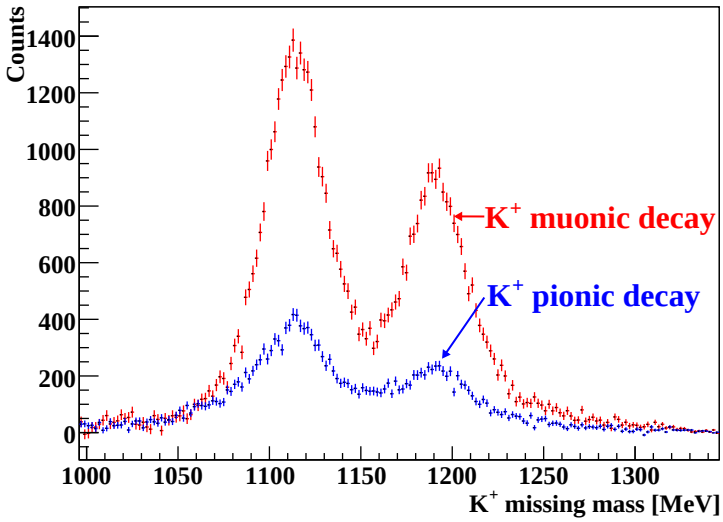

Figure 6.12: K^+ missing mass for K^+ muonic and pionic decays (red and blue lines respectively).

6.3 Extraction of K^+ detection efficiency

To show the detection processes were well understood it was necessary to perform consistency checks between simulated and real data. Once verified and tuned, it was then possible to use the simulation to provide the detection efficiencies required to extract the cross sections. This section describes the simulation and the steps taken to ensure the experimental and simulated data were consistent.

6.3.1 Monte Carlo procedure

The software AcquMC, described in section 4.6.5, was used to generate thirty million $\gamma(p, K^+)\Lambda$ events. The kinematics were generated using distributions from the Kaon-MAID [41] partial wave analysis solution using the existing world data. This was folded with the bremsstrahlung shape of the incident photon beam distribution, ensuring the distribution of kinematics matched that of the experimental data as closely as possible.

The generated events were input to the A2 Geant4 simulation described in section 4.7. The output from the simulation was then read into the AcquRoot

data acquisition (section 4.6.5). To ensure the analysis of the simulated data was identical to the experimental data, the energy and timing resolution inherent in the hardware of the detector system needed to be incorporated into the simulated data. Also, additional timing cuts were required to reflect the integration range of the ADCs. These procedures are described in the following sections.

6.3.2 Integration time of the Crystal Ball readout

To match the integration time of the ADCs in the experiment, a timing cut was imposed in the A2 simulation. The ADC integration range for the Crystal Ball in the experimental data was from -400 to 600 ns, with the prompt timing of the Crystal Ball crystals set to 0 ns. As the time for particles to travel from the target to the NaI crystals was of the order of 1 ns, the timing cut in the simulation was set to 600 ns.

6.3.3 Simulation of energy resolution

Beam energy resolution

The photon tagger energy resolution was determined by the width of the scintillators in the tagger focal plane and their corresponding momentum tagging range. For every simulated event at a known incident photon energy, the focal plane element which would have detected the bremsstrahlung electron was identified. A random number generated uniformly over the energy width of the tagger channel was used to smear the beam energy.

Crystal Ball energy resolution

To establish the energy resolution of the Crystal Ball, a comparison of simulated and experimental data for a two body reaction channel was used. To select the channel: $\gamma(p,p)\pi^0$, the analysis insisted upon identifying one proton using $\Delta E - E$ analysis and two photons in the Crystal Ball. The four-momentum of the two photons was summed to give the four-momentum of a potential π^0. The analysis insisted that the invariant mass of the summed four-momentum was within 30 MeV of the accepted π^0 mass of 135 MeV. Reconstructing the missing

mass from the π^0, incident photon and target four-momentum gave a peak in the missing mass spectrum over the proton mass of 938 MeV.

The width of the missing mass peak was compared between the experimental and simulated data (fig. 6.13). Events were only included for a π^0 polar lab angle of $80° - 100°$ and photon beam energies 700-750 MeV. The selection of a narrow kinematic range ensured that there were no differences in the kinematic distributions between experimental and simulated data. To include the energy resolution in the simulation, the measured energy in the crystals was smeared by the distribution given in eq. 6.2.

$$E_{res} = E + N_{rand} E^{0.75} \tag{6.2}$$

where E and E_{res} is the energy before and after the energy resolution had been implemented, and N_{rand} is a random number sampled from a Gaussian distribution. This follows the formula which has been shown to describe the Crystal Ball energy resolution (table 4.1).

Fig. 6.13 shows the experimental and the simulated data with different energy resolutions. The best match between simulated and experimental data was obtained when the width of the Gaussian from which N_{rand} was sampled from was set to 0.125.

6.3.3.1 Timing resolution

The timing resolution of the Crystal Ball detector was set by comparing the timing of crystals in the same cluster. Only clusters from decay photons of π^0 were selected to ensure that all crystals in the cluster came from the same electromagnetic shower and were therefore hit at the same time. The time difference between the first crystal to be hit compared to all other crystals in the same cluster was plotted for simulated and experimental data (fig. 6.14). Smearing the timing by a random number sampled from a Gaussian function allowed the simulated and experimental distributions to be matched. A Gaussian function with a width of 1.9 ns gave the best match between simulated and experimental data. This is consistent with previous estimates (table 4.1).

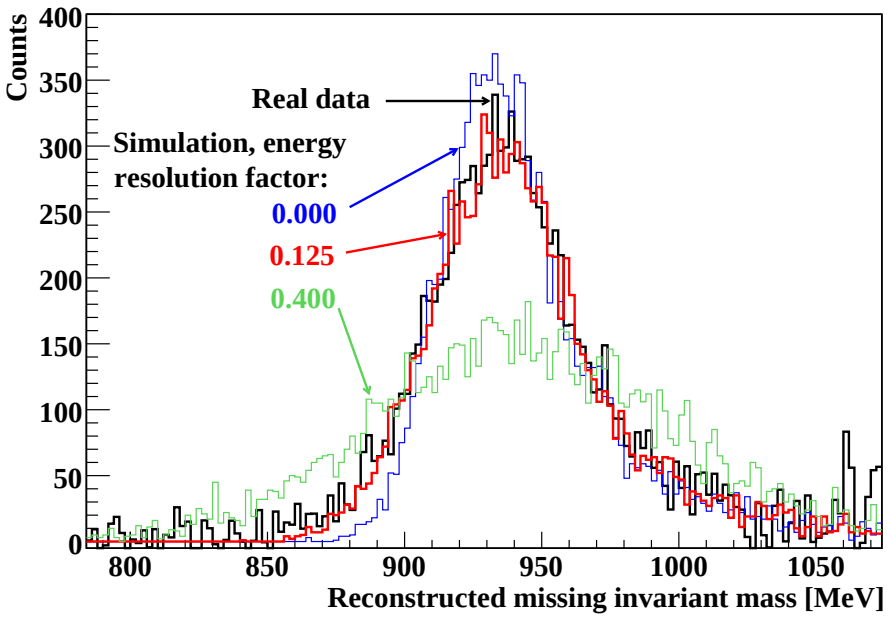

Figure 6.13: π^0 missing mass. The analysis insisted upon identifying a proton with the $\Delta E - E$ analysis and the two π^0 decay photons in the Crystal Ball. The width of the peak over the proton mass matches between simulated and real data (black line) with a resolution factor, N_{rand} sampled from Gaussian with width 0.125.

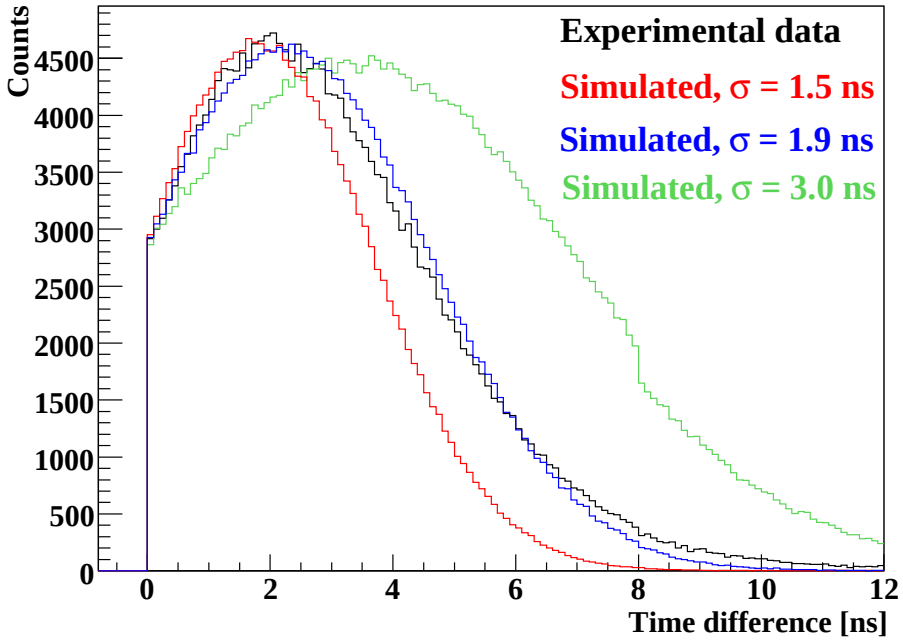

Figure 6.14: Time difference between crystals in the same cluster from π^0 decay photons. A simulated time resolution of 1.9 ns (blue line) matches the real data well (black line).

To check whether the time resolution depended upon the energy deposited, the above procedure was repeated for crystals with less than 20 MeV energy deposited and crystals with more than 100 MeV deposited. The experimental and simulated data matched for all energies.

6.3.4 K^+ decay sub-cluster energy scaling

A separate energy scaling was required to align the muon decay peaks in the decay sub-cluster energy spectra for real and simulated data. The peak moved with the measured K^+ energy by approximately 15 MeV and the calibration required a different energy scale at low K^+ energy to high K^+ in the real data. This was expected as at low energies, K^+ stop earlier in the crystal and further from the PMT. A greater proportion of the energy of the decay will therefore be lost due to light attenuation. In the simulated data the peak did not move with K^+ energy as the light attenuation in the crystals was not described by the simulation.

The mean of the peak in the decay sub-cluster was identified from fitting a Gaussian function to a 20 MeV energy range surrounding the bin with the highest number of counts. Fig. 6.15 shows the mean of the muon decay peak as a function of measured K^+ energy. The two energy scales of 1.15 and 1.12 (blue and red points) match the real and simulated data at low and high energy K^+ respectively but neither match well over the entire energy range. The energy scale which was used varied linearly with the measured K^+ energy and was an interpolation of these two scales (green points).

6.3.5 Simulation of hardware triggers

The Crystal Ball energy triggers described in section 5.4.1 were modelled and included in the analysis of the simulated data.

Multiplicity trigger

The multiplicity trigger in the hardware electronics for the experimental data (section 4.6.4) was checked by measuring the energy of crystals when three clusters were identified. For an M3 trigger, this required at least one crystal from each

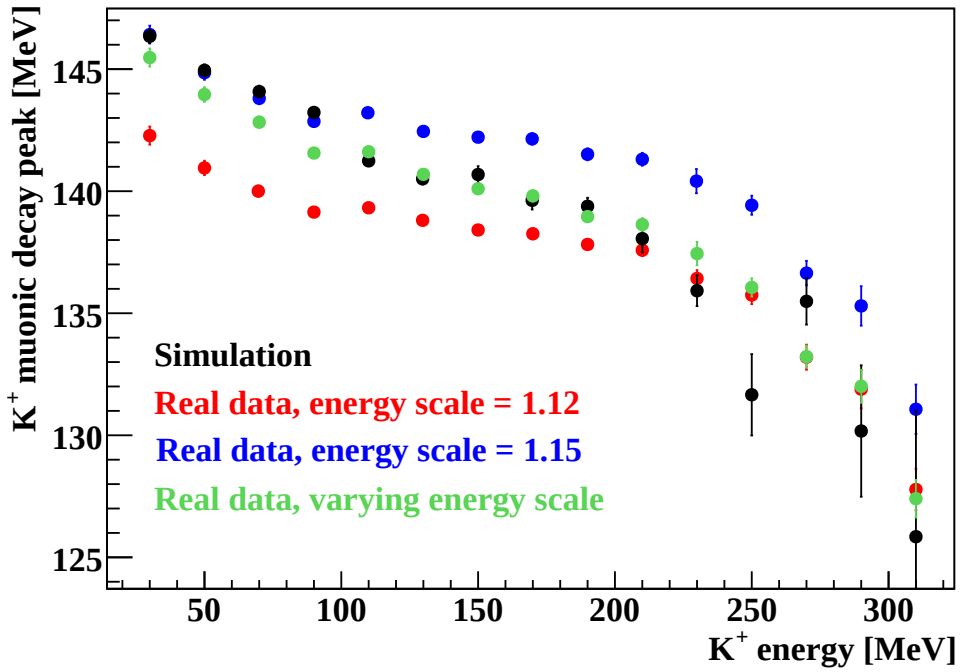

Figure 6.15: Mean of the muonic decay peak for the decay cluster energies as a function of measured K^+ energy. Black points are from simulation, blue and red are real data with an energy scaling of 1.15 and 1.12 respectively. The green points are real data with a varying energy scale: a linear interpolation of the scales 1.15 and 1.12 at low and high K^+ energies respectively.

cluster to exceed the threshold applied by the discriminators in the hardware. Fig 6.16 shows the energy deposited in the highest energy crystal in each cluster when three clusters are identified. It is clear there is a sharp drop in counts at 20 MeV.

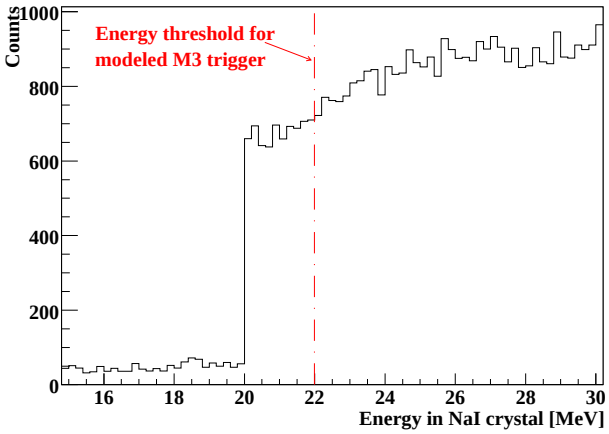

Figure 6.16: The energy deposited in the most energetic crystal for each cluster when three clusters were identified in the Crystal Ball. The energy threshold for the multiplicity trigger prevented the highest energy crystals having less than approximately 20 MeV. The simulated multiplicity trigger used a threshold value of 22 MeV (dotted red line).

To model the multiplicity trigger for the simulated data, the crystals were split into the same 45 units of 16 as the real detector system (section 4.6.1). For every event, the crystal with the most energy in each section was identified. At least three sections had to contain a crystal with an energy of at least 22 MeV for the event to pass. This model was applied to the real data as well as the simulated data. By demanding a threshold approximately 2 MeV greater than the experimental multiplicity trigger ensured there were no differences between the selection of experimental and simulated events.

Crystal Ball energy sum

The energy sum of the Crystal Ball was formed from a discriminator applied to the OR signal of the entire detector (section 4.6.1). This was prior to an

accurate calibration of the Crystal Ball, and depended upon the gains applied to the PMTs (section 5.4.2). Consequently, to accurately model the energy sum, the experimental data needed to be compared to simulated data without the energy sum applied.

The $\gamma(p, K^+)\Lambda$ reaction channel was identified by the selection cuts described in section 6.2 in both the experimental and simulated data. Of these events, a further cut rejected events above the $\gamma(p, K^+)\Sigma^0$ beam energy threshold of 1050 MeV to ensure there was no contamination from this channel. The energy sum trigger in the experimental data was applied before any energy scaling or corrections were applied in the analysis of the data. Therefore no corrections to the energy deposition were applied, to leave the original energy calibration described in section 5.4.2. Fig. 6.17 (left panel) shows the total energy deposition for experimental and simulated data. The yields have been scaled to make comparisons easier. The yield from the empty target data (green data points) has been scaled according to the number of hits in the focal plane detector and subtracted from the experimental data.

It is apparent that above 450 MeV, the simulated data matches the experimental data very well. The experimental data rises quickly between 300 to 450 MeV at the threshold of the energy sum, whereas the simulated data with no energy sum has total energy depositions as low as 200 MeV.

To simulate the energy sum, the experimental data was divided by the simulated data (fig 6.17, right panel). This gave a distribution with an "S" shaped rise over the region of the energy sum threshold, to a flat distribution beyond 450 MeV where the experimental and simulated data agreed. A cumulative distribution (CDF) was fitted to the data (red line in fig 6.17, right panel):

$$f(E_{Tot}) = \frac{h}{1 - e^{\frac{\overline{x} - E_{Tot}}{\sigma}}} \tag{6.3}$$

where E_{Tot} is the total energy deposition, h is the height as $E_{Tot} \rightarrow \infty$, $\overline{x} = E_{Tot}$ when $f(E_{Tot}) = h/2$ and σ is the width of the function.

To model the energy sum in subsequent analysis of simulated data, a random number was generated between zero and one. For each event, the total energy

deposition was used with the parameters from the CDF fit in fig 6.17 to give a value for the CDF function, $f(E_{Tot})$. If the random number was greater than $f(E_{Tot})$, the event passed the energy sum cut, if the random number was smaller than $f(E_{Tot})$, the event was rejected. The black data points in fig 6.17, left panel, are the simulated data with the simulated energy sum. The agreement between simulated and experimental distributions was checked over different polar angle regions of the Crystal Ball and found to be consistent for all angles.

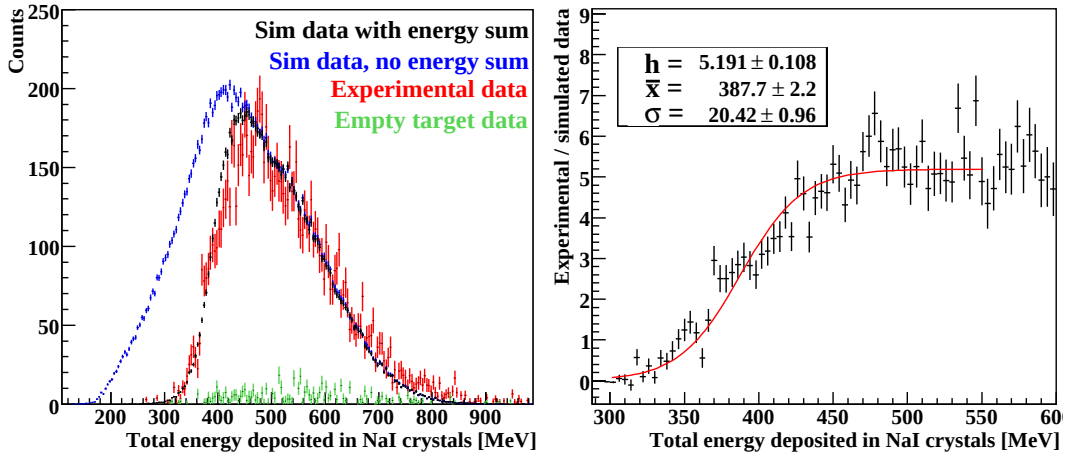

Figure 6.17: Left panel: Total energy depositions in the Crystal Ball for experimental, empty target, and simulated data (before and after simulating the energy sum trigger). The simulated data was scaled to the experimental data to aid comparison. Right panel: the ratio of energy deposition for experimental and simulated data. A CDF (eq 6.3) was fitted over the energy sum threshold region of 310 to 500 MeV (red line). Fit parameters are inset.

6.4 Comparison between real and simulated data

Fig. 6.18 compares experimental and simulated data for characteristic plots in the detection of K^+ decay. To aid comparison, the integral of the simulated data has been normalised to the integral of the experimental data. It is clear that the distribution of the energy of the K^+ decay sub-cluster is in very close agreement

between simulated and experimental data. Both data sets exhibit a broadening of the peak from the muonic decay with increased K^+ energy. Higher energy K^+ pass further into the NaI crystals, where the width of the crystals are larger, reducing the effectiveness of seperating the energy from stopping the K^+ and the K^+ decay.

The time difference between decay and incident sub-clusters is also plotted for simulated and experimental data. The spectra have excellent agreement, and fitting with exponential functions reproduces the K^+ lifetime within the errors of the fit parameters using either data sets.

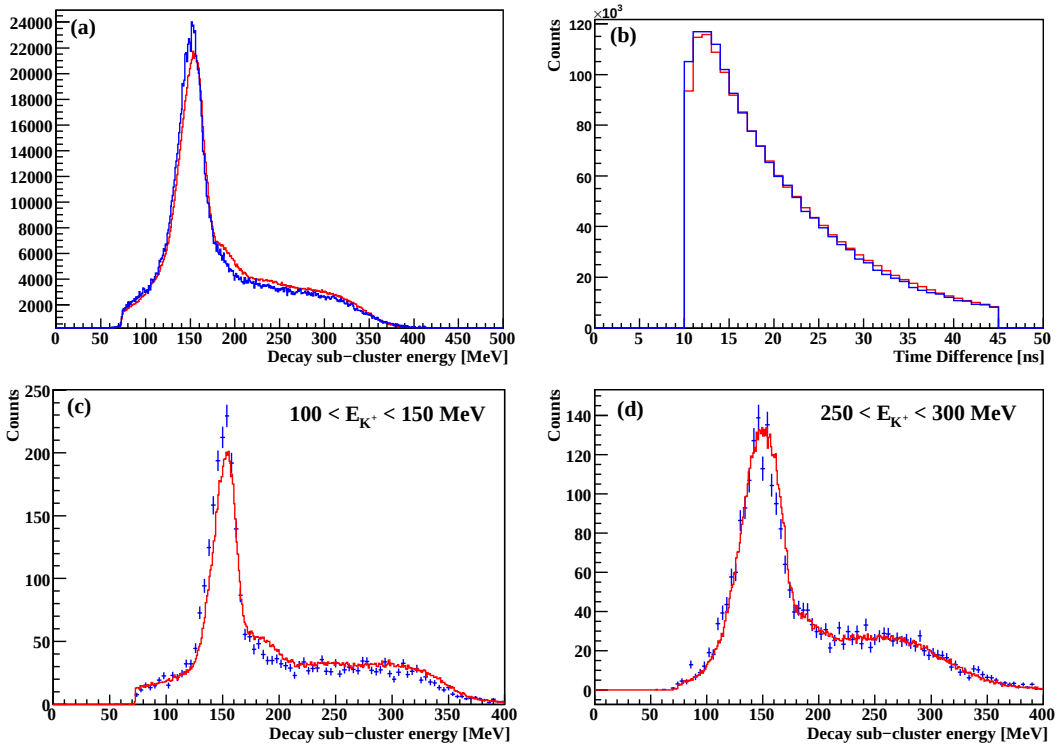

Figure 6.18: Comparison between simulated and experimental identification of K^+ (red and blue data respectively). (a) Decay sub-cluster energy. (b) Time difference between decay and incident sub-clusters. (c) Decay sub-cluster energy for K^+ with measured energy 100-150 MeV. (d) Decay sub-cluster energy for K^+ with measured energy 250-300 MeV. The simulated spectrum is scaled to the integral of the experimental spectrum.

Fig. 6.19 compares K^+ missing mass plots for different photon beam energy ranges, E_γ, and centre of mass polar angles, θ_{cm}. The lab-frame polar angle of K^+ detection is shown in the right column.

The widths and mean of the Λ and Σ^0 mass peaks agree between simulated and experimental data. For the kinematic range $1.0 < E_\gamma < 1.1$ GeV and $0.35 < \cos\theta_{cm} < 0.45$ (bottom panel), the lab-frame angle of detection is at the very front of the Crystal Ball (just over 20^0). The lack of acceptance at more forward angles prevents the detection of $K^+\Sigma^0$ in this bin (For a given E_γ and θ_{cm} range, $K^+\Sigma^0$ events are detected at more forward lab frame angles than $K^+\Lambda$). This is observed in the K^+ missing mass plot, where only the low energy tail of the Σ^0 mass peak is observed in the simulated and experimental data.

The excellent comparison between simulated and experimental spectra demonstrates the reliability of the simulation to extract accurate detection efficiencies.

6.5 K^+ identification with TAPS

The same method of K^+ identification was investigated with the TAPS detector at angles forward of 20^0. Fig. 6.20 shows simulated data of the energy of the decay sub-cluster and the time difference between incident and decay sub-clusters. Fitting an exponential function gave the K^+ lifetime of 12 ns.

Attempts to identify K^+ in TAPS in the experimental data were made, however the large Crystal Ball energy sum of approximately 350 MeV severely limited the yield in TAPS. Fig 6.20 shows the lab frame polar angle of K^+ detection. TAPS covers the polar angle range from 0^0 to 20^0. It is apparent that increasing the simulated energy sum from 100 to 330 MeV loses nearly all events in TAPS.

The simulation of K^+ identification in TAPS demonstrates that the detection technique could in principle work with other segmented calorimeters. For this thesis, K^+ identification was limited to the angular acceptance of the Crystal Ball. It should be noted that the beam times were originally optimised for η' cross section measurements, which benefitted from the high energy sum threshold. Now that the technique is established, modifications are being made to the experimental trigger to make K^+ detection in TAPS possible in future measurements.

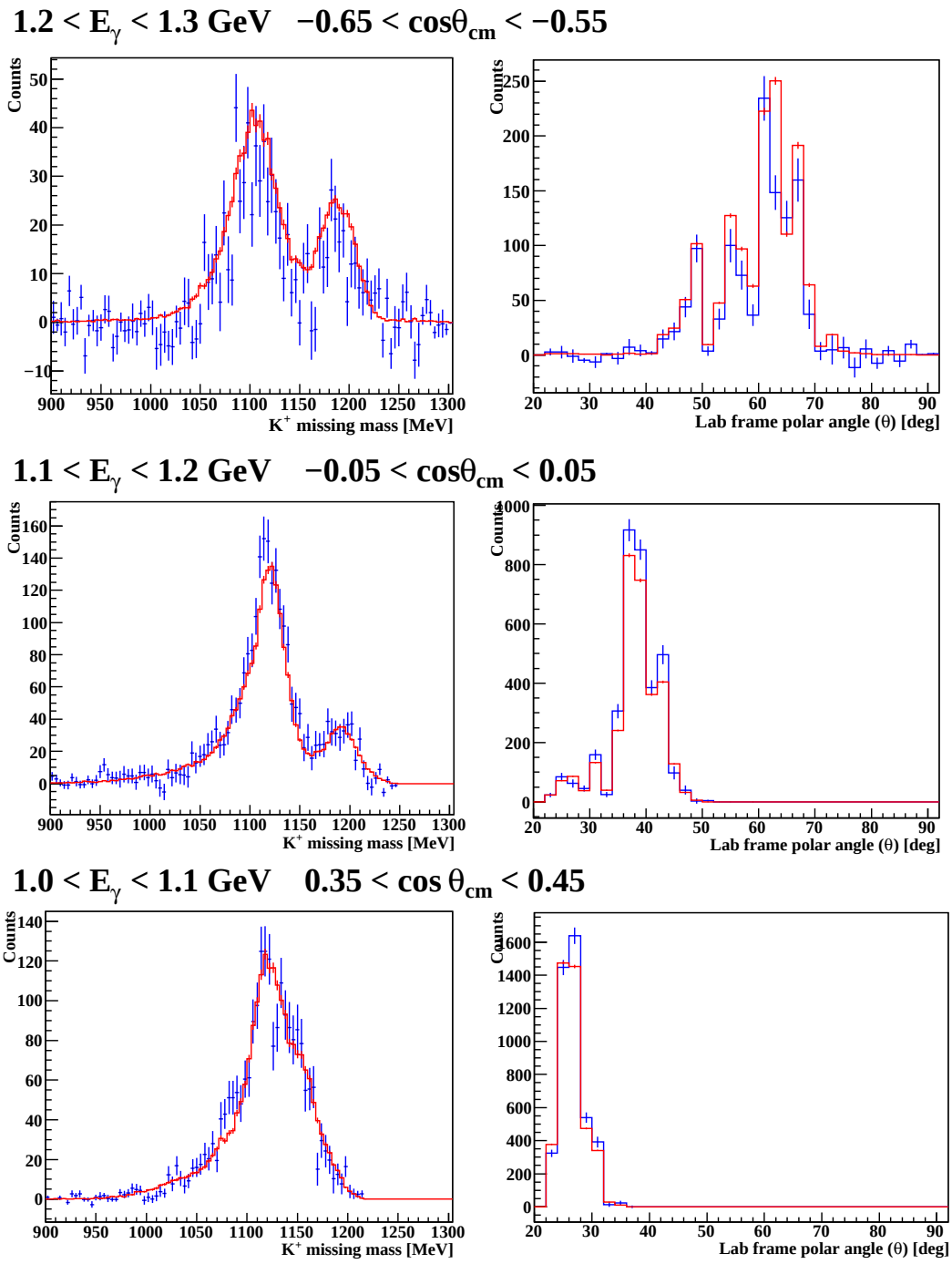

Figure 6.19: K^+ missing mass and lab frame polar angle of detection for three different ranges of photon beam energy, E_γ, and centre of mass polar angle, θ_{cm} (ranges inset). Simulated data is in red, experimental data is in blue.

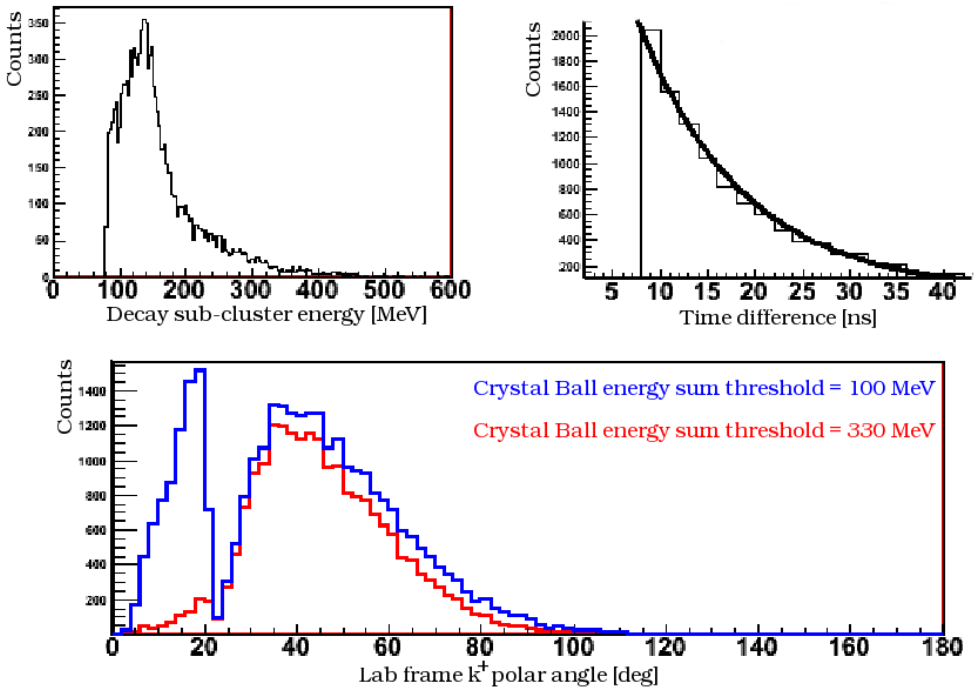

Figure 6.20: Simulated K^+ identification in the TAPS detector. Top left: energy of the decay subcluster. Top right: Time difference between incident and decay sub-cluster. Bottom: lab frame polar angle of detection of K^+, with high and low Crystal Ball energy sum thresholds applied. TAPS acceptance range is below 20^0.

Chapter 7

Extraction of $\gamma(p, K^+)\Lambda$ Cross sections

This chapter describes how the cross section for $\gamma(p, K^+)\Lambda$ was extracted from the yield of K^+ identified by the methods described in section 6. The cross section formalism is described in chapter 7.1 and the determination of the variables required to extract the cross section are outlined in sections 7.2 to 7.4. Statistical and systematic uncertainties of the measurement are then explained in section 7.6.

7.1 Cross section formulism

In simplified terms, the cross section of a reaction is a measure of the probability of the reaction occurring. For a reaction $A(a, b)B$, the total cross section, σ is given as:

$$\sigma = \frac{N_b}{N_a N_A} \tag{7.1}$$

where N_b is the number of particles emitted, N_a is the number of particles per unit area of the target as seen by the beam, and N_A is the total flux of incident particles.

In this experiment, N_b was the yield of K^+ corrected by the detection efficiency (section 7.4). N_A was the number of hits in the tagger focal plane detector,

corrected by the tagging efficiency (section 7.3.3), and N_a was the area density of protons in the target cell as seen by the beam. The angular differential cross section at fixed photon beam energy, E_γ, and centre of mass polar angle, θ_{cm}, can then be written as:

$$\frac{d\sigma}{d\Omega} = \frac{N_{K^+}}{N_s \epsilon_{tagg}\, \epsilon_{det}\, \rho\, \Omega} \tag{7.2}$$

where:
N_{K^+} is the yield of K^+ in the energy bin E_γ and angle bin θ_{cm},
N_s is the number of photon tagger hits in the energy bin E_γ,
ϵ_{tagg} is the tagging efficiency in the energy bin E_γ,
ϵ_{det} is the K^+ detection efficiency in the energy bin E_γ and angular bin θ_{cm},
ρ is the target density (the number of protons per unit area),
$\Omega = \int_{\phi_1}^{\phi_2} d\phi_{cm} \int_{\theta_1}^{\theta_2} \sin\theta\, d\theta_{cm}$ (the solid angle of detection in steradians).

In the remainder of the thesis, the energy of the incident photon beam is referred to as E_γ, and the centre of mass polar angle of K^+ detection as θ_{cm}. θ_{cm} is often binned into intervals of $\cos\theta_{cm}$ so that each bin has a constant solid angle. The range θ_{cm} = 0 to 180^0 therefore corresponds to the range $\cos\theta_{cm}$ = -1.0 to 1.0. The intervals of E_γ measured in the experiment correspond to intervals set by the size of the focal plane elements in the Photon Tagger. The widths are not constant, but vary slightly from 2 MeV to 4 MeV.

7.2 Extraction of $\gamma(p, K^+)\Lambda$ yield

The $\gamma(p, K^+)\Lambda$ yield was extracted from an integration under the K^+ missing mass spectra for a given E_γ and θ_{cm} bin.

For the kinematics of the experiment there were two possible reactions contributing to the yield of K^+: $\gamma(p, K^+)\Lambda$ and $\gamma(p, K^+)\Sigma^0$. To extract the Λ production yield, the Σ^0 events were first suppressed through the detection of the photon in the $\Sigma^0 \rightarrow \Lambda\gamma$ decay. This is discussed in section 7.2.1. After this procedure, two separate procedures were used to extract the Λ yield; a simultaneous fit to the Λ and Σ^0 contributions in K^+ missing mass spectra (section 7.2.3), and a complete subtraction of the Σ^0 yield using the decay γ as a tag (section 7.2.4).

7.2.1 Identification of the photon from Σ^0 decay

To differentiate between $\gamma(p, K^+)\Lambda$ and $\gamma(p, K^+)\Sigma^0$ channels, the photon from the decay: $\Sigma^0 \rightarrow \gamma\Lambda$ was analysed in the Crystal Ball and TAPS. The first step of this analysis was to differentiate between the decay photon and other detected neutral particles. For events with a K^+ identified, additional sources of neutral particles were photons from the $\pi \rightarrow \gamma\gamma$ decay, and the neutron from the $\Lambda \rightarrow n\pi^0$ decay.

The A2 Geant4 simulation was used to study the kinematics of these neutral particles. The simulation was run three times, with each run only allowing one of the neutral particles from the entire reaction process to be tracked. Fig. 7.1 shows the lab frame polar angle versus detected energy in the Crystal Ball and TAPS for neutrons, π^0 decay photons, and the Σ^0 decay photon. It is clear that the Σ^0 decay photons occupy a definite loci, unlike the other neutral particles. The two-dimensional cut superimposed upon the histogram was used as a preliminary method to select the Σ^0 decay photons.

A further step was required to remove the remaining neutrons and π^0 decay photons. The momentum of the hyperon, P_{hyp} (either Λ or Σ^0) was reconstructed from the K^+ and incident photon momentum:

$$P_{Hyp} = P_{beam} + P_{target} - P_{K^+} \tag{7.3}$$

The four-momenta of decay photon candidates which passed the two dimensional cut were Lorentz boosted into the rest frame of the hyperon and the energy calculated. For the decay of a Σ^0 from rest, the energy of the decay photon is equal to the $\Sigma^0 - \Lambda$ mass difference of 76.9 MeV. Fig. 7.2 shows the particle energy in the hyperon rest frame plotted for experimental and simulated data. There is a peak over the hyperon mass difference in the experimental data. In the simulated data, there is a small amount of background from the $\gamma(p, K^+)\Lambda$ channel (from mis-identified neutrons and π^0 decay photons) and a large peak over the mass difference for the $\gamma(p, K^+)\Sigma^0$ channel. For events with multiple neutral particles passing the initial two dimensional locus cut[1], the energy of

[1] neutrons and π^0 decay photons were also detected from $K^+\Sigma^0$ events after the decay of the Σ^0 to Λ, and Λ to $n\pi^0$.

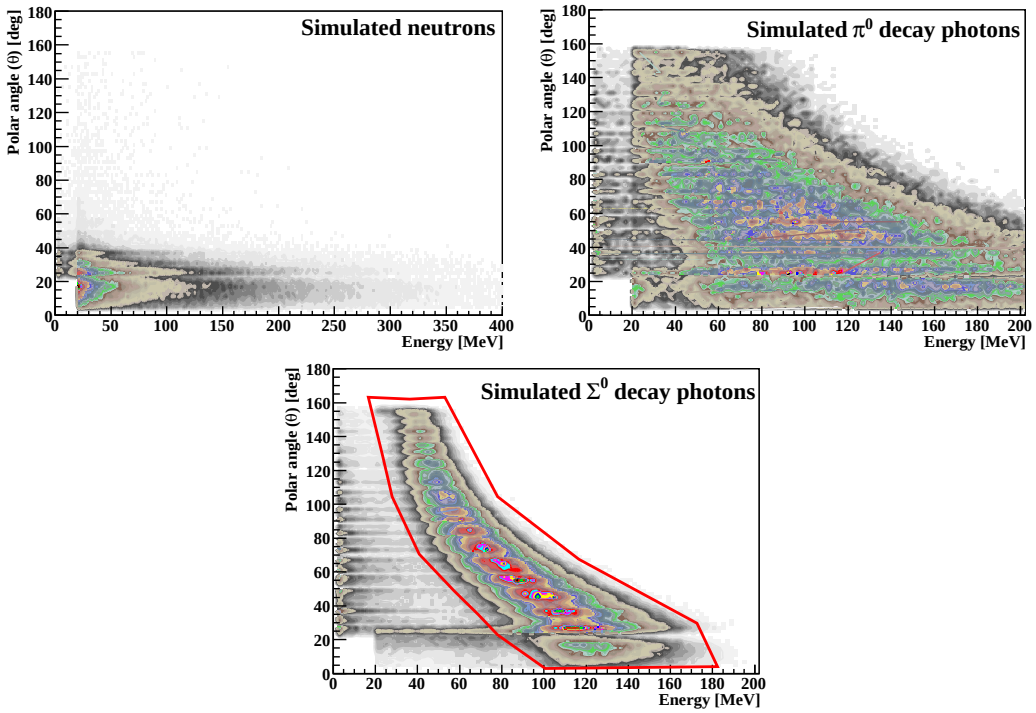

Figure 7.1: Simulated data, tracking only neutrons (top left), π^0 decay photons (top right) and Σ^0 decay photons (bottom). The red selection cut on the Σ^0 decay photons provides an initial means of selection.

all neutral particles were measured in the hyperon rest frame and the particle with the closest energy to the $\Sigma^0 - \Lambda$ mass difference was selected. These events were identified as $\gamma(p, K^+)\Sigma^0$ when the neutral particle energy was between 55 - 95 MeV.

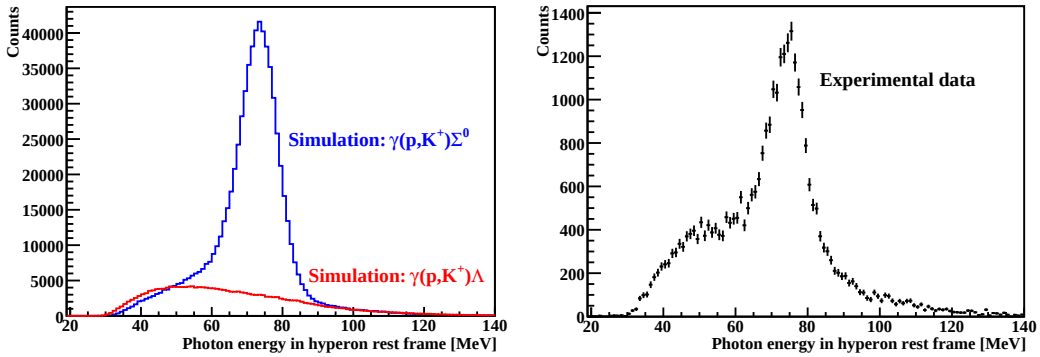

Figure 7.2: The energy of decay photon candidates which pass the two dimensional cut in fig. 7.1 boosted into the hyperon rest frame. Left: simulated data of $\gamma(p, K^+)\Lambda$ and $\gamma(p, K^+)\Sigma^0$ (red and blue respectively, 30 million events each), Right: experimental data.

Using simulated data, where the detection efficiency of the Σ^0 decay photon could be measured, this method of discrimination between $\gamma(p, K^+)\Lambda$ and $\gamma(p, K^+)\Sigma^0$ correctly identified 50-60% of $K^+\Sigma^0$, only misidentifying 5-10% of $K^+\Lambda$ events. Fig 7.3 is the K^+ missing mass spectrum before and after the subtraction of K^+ events with the Σ^0 decay photon identified.

7.2.2 Rejection of punch through K^+

K^+ with kinetic energies over 340 MeV had sufficient energy to "punch through" the back of the NaI crystals in the Crystal Ball (this was tested with simulation). Whilst the majority of the punch through K^+ were not detected as the identification method required a stopped K^+ to decay, a small amount of K^+ punched through and decayed immediately outside the crystal, passing selection cuts in the identification procedure. As the entirety of the kinetic energy of the K^+ was not contained in the crystal, the energy of the K^+ was underestimated. As the

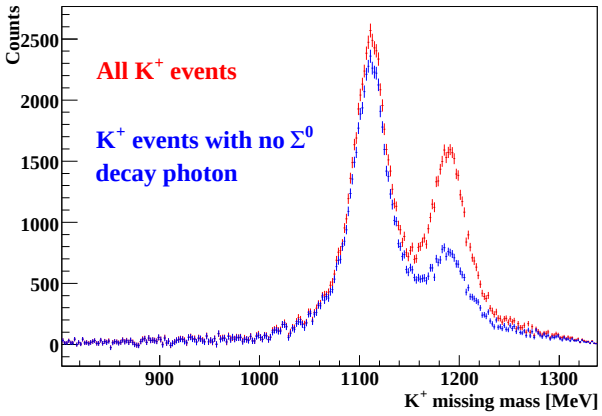

Figure 7.3: K^+ missing mass spectrum for all K^+ (red) and for events with no Σ^0 decay photon identified (blue).

centre of mass polar angle, θ_{cm} depended on the K^+ momentum, this would be calculated incorrectly for punch through K^+.

To reject punch through K^+, the kinetic energy of the K^+ (E_{K^+}) was reconstucted from the two-body kinematics of the reaction using the momentum of the incident photon (P_γ) and the K^+ lab frame polar angle (θ) (eq. 7.4). K^+ events were rejected if the reconstructed energy was greater than 340 MeV.

The derivation of eqn. 7.4 can be found in reference [119]. The equation assumes that every event is a $K^+\Lambda$ event. For $K^+\Sigma^0$ photoproduction, the reconstructed energy of the K^+ was larger than the actual energy, reducing the contribution from $K^+\Sigma^0$.

$$E_{K^+} = \frac{AE_T + P_\gamma \cos\theta \sqrt{A^2 - 4M_{K^+}^2(E_T^2 - P_\gamma^2 \cos^2\theta)}}{2(E_T^2 - P_\gamma^2 \cos^2\theta)} - M_{K^+} \qquad (7.4)$$

where:
M_{K^+} = the K^+ mass.
E_T = the total energy of the system ($E_T = M_p + E_\gamma$).
$A = E_T^2 + M_{K^+}^2 - P_\gamma^2 - M_\Lambda$, where M_Λ = the Λ mass.

7.2.3 Fitting to K^+ missing mass spectra

To subtract the remaining $K^+\Sigma^0$ yield from the total for each E_γ and θ_{cm} bin, fits were applied to the K^+ missing mass spectra. The contribution from $K^+\Sigma^0$ was measured from the fit and subtracted from the yield. This section explains the procedure.

7.2.3.1 The fitting algorithm

From the simulated data of $\gamma(p, K^+)\Lambda$, it was found that the peak in the K^+ missing mass spectrum was not symmetric, and so a simple Gaussian distribution defined by its mean, width and area did not describe the spectrum well. Instead, the sum of two Gaussian functions was required; one tall and narrow, centred on the Λ mass in the missing mass spectrum, and one low and wide with the centre offset from the tall Gaussian to account for the asymmetry of the spectrum. The same situation was found for simulated $\gamma(p, K^+)\Sigma^0$ events.

To extract the $K^+\Lambda$ yield in the experimental data, four Gaussian functions were fitted to the missing mass spectra (two Gaussian functions to describe the contribution from each reaction channel). The contributing fit to the $K^+\Sigma^0$ was subtracted from the missing mass spectra to leave only the $K^+\Lambda$ contribution. The $K^+\Lambda$ yields were then extracted from an integration over the subtracted spectra.

With the experimental data, where there were fewer statistics than the simulated data, and with the contributions from $K^+\Lambda$ and $K^+\Sigma^0$ overlapping each other, it was necessary to "train" the fit parameters by constraining the relative mean positions and widths to values acquired from the simulated data. This procedure was non trivial; using simulated data it was found that the shape of the spectra changed with E_γ and θ_{cm}, with a very narrow structure near threshold for example, becoming much broader at higher energies. Eq. 7.5 defines the parameters for fitting to both hyperon masses in the missing mass spectra, where the fit parameters of the shorter Gaussian are described as a fraction of the equivalent parameter of the taller Gaussian. For example, the height and width parameters may be given as $h_S = 0.2$ and $\sigma_S = 3.0$, so that the shorter Gaussian is always one fifth as tall and three times as wide as the taller Gaussian function.

$$
\begin{aligned}
y(x) &= h_T^{\Lambda}\Big[e^{-\frac{1}{2}\left(\frac{x-X_T^{\Lambda}}{\sigma_T^{\Lambda}}\right)^2} + h_S^{\Lambda} e^{-\frac{1}{2}\left(\frac{x-X_T^{\Lambda}X_S^{\Lambda}}{\sigma_T^{\Lambda}\sigma_S^{\Lambda}}\right)^2}\Big] \\
&+ h_T^{\Sigma^0}\Big[e^{-\frac{1}{2}\left(\frac{x-X_T^{\Sigma^0}}{\sigma_T^{\Sigma^0}}\right)^2} + h_S^{\Sigma^0} e^{-\frac{1}{2}\left(\frac{x-X_T^{\Sigma^0}X_S^{\Sigma^0}}{\sigma_T^{\Sigma^0}\sigma_S^{\Sigma^0}}\right)^2}\Big]
\end{aligned}
\tag{7.5}
$$

where:
h_T = height of the taller Gaussian,
X_T = mean of the taller Gaussian,
σ_T = width of the taller Gaussian,
h_S = fractional height of the shorter Gaussian,
X_S = fractional mean of the shorter Gaussian,
σ_S = fractional width of the shorter Gaussian,
and the superscript Λ or Σ^0 denotes which of the hyperon mass peaks the parameter describes.

30 million simulated $\gamma(p, K^+)\Lambda$ were used to constrain the fitting parameters. To aid the fitting to the simulated data, initial parameters were extracted from the overall spectra. The procedure also demanded that the height of both Gaussian functions were greater than zero.

This fitting procedure was implemented for 25 MeV intervals in E_γ, from threshold to 1.4 GeV, and intervals in $\cos\theta_{cm}$ of 0.1, covering all polar angles. To train the fitting procedure for each $\cos\theta_{cm}$ interval, the values of the fitting parameters plotted against E_γ were fitted with a polynomial of up to fourth order. This was done one at a time, the parameters of the polynomials being used to fix each fitting parameter. The fitting procedure was repeated, with each iteration fixing a further parameter, until all parameters were fixed except for h_T which determined the height and the integral of the fitting function. Fig. 7.4 shows the parameters before and after they had been fixed for a specific $\cos\theta_{cm}$ bin. The same procedure was repeated for $\gamma(p, K^+)\Sigma^0$ for all $\cos\theta_{cm}$ bins.

With all of the parameters from eq. 7.5 fixed apart from the heights of the $K^+\Lambda$ and $K^+\Sigma^0$ contributions (h_T^{Λ} and $h_T^{\Sigma^0}$ respectively), the fitting function was applied to the experimental data.

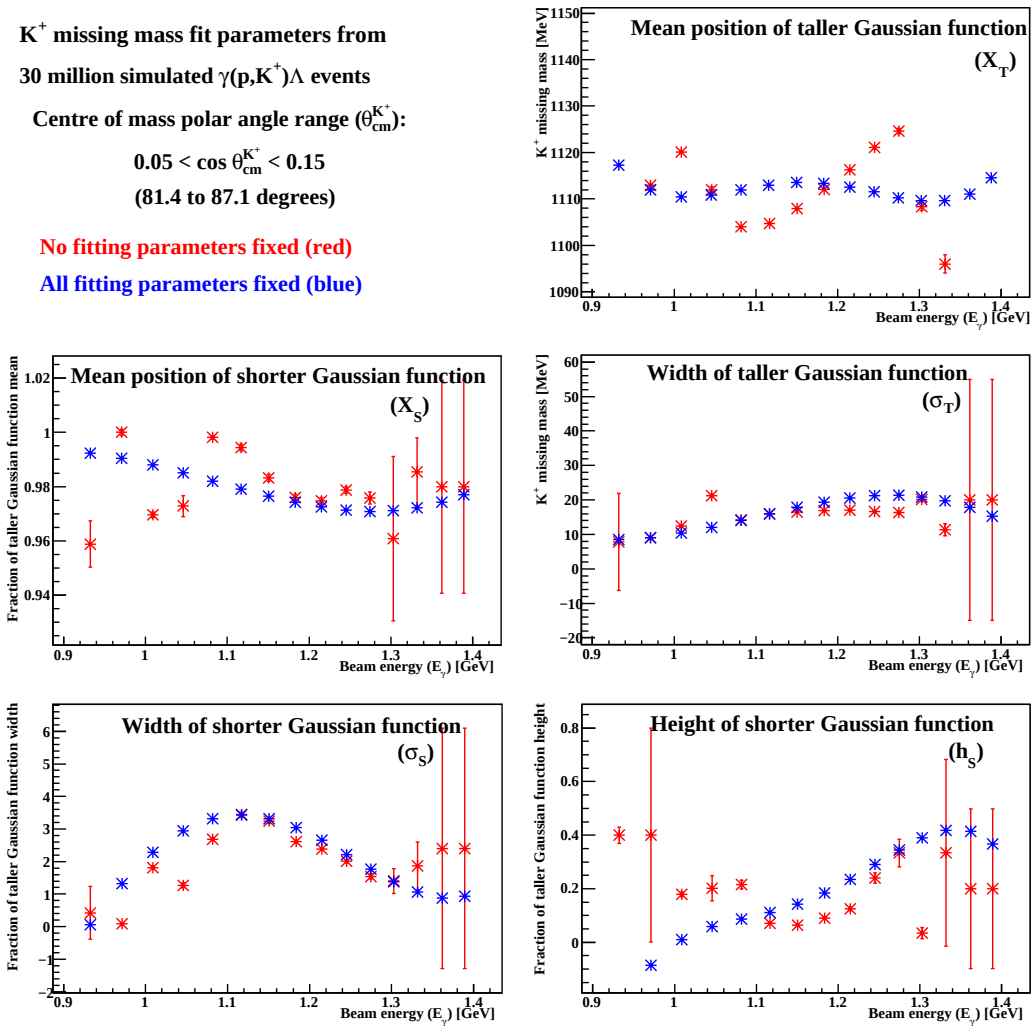

Figure 7.4: Missing mass fit parameters as a function of beam energy before and after constraining with polynomial fits (red and blue respectively)

The calibration of the K^+ energy gave good agreement between experimental and simulated data, however it was decided that fixing the mean of the Gaussian functions was too restrictive. Instead, the difference in the means of the fits between the $K^+\Lambda$ and $K^+\Sigma^0$ (X_T^{Λ} and $X_T^{\Sigma^0}$ respectively) contributions was fixed. Fig. 7.5 is an example of the fit to experimental and simulated data. Simulated data for both reaction channels has also been included and fit to with the contributing fit to that channel.

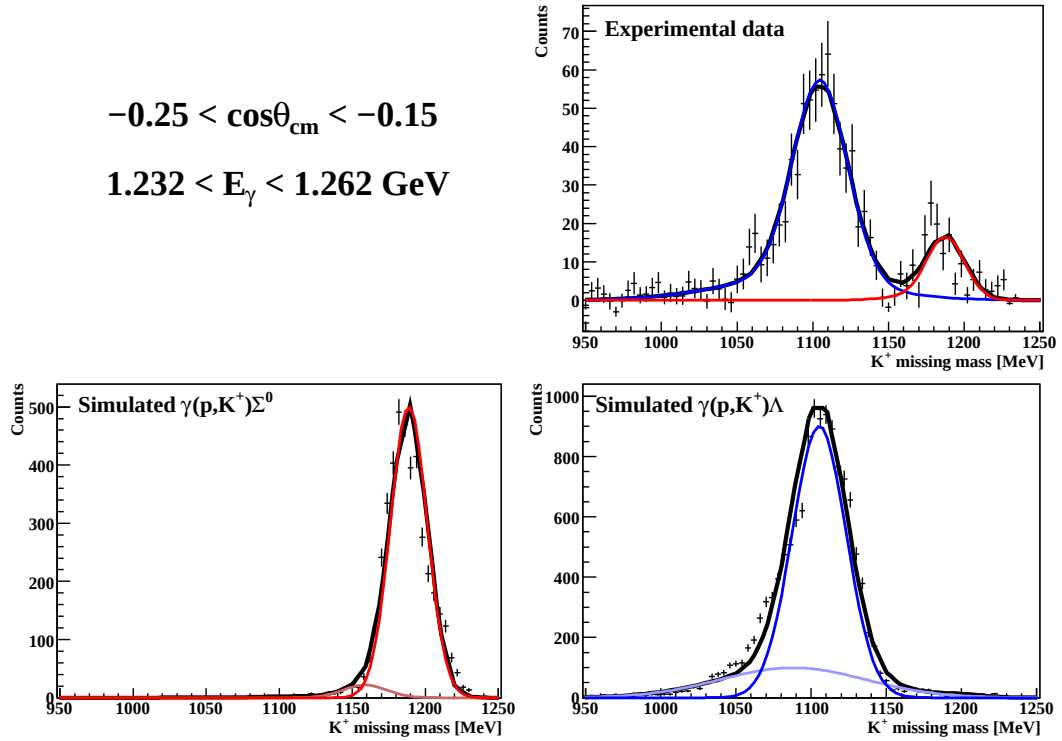

Figure 7.5: Fitting to K^+ missing mass spectra ($\cos\theta_{cm}$ and E_γ ranges inset). Top: Experimental data with eq. 7.5 fitted. Contributions from $K^+\Lambda$ and $K^+\Sigma$ have been superimposed in red and blue respectively. Bottom: Fits to simulated data, where only the $K^+\Sigma^0$ or $K^+\Lambda$ contributions have been fitted to. The two Gaussian functions which are summed for each fit have been superimposed (black line).

7.2.4 Decay photon tagging method of yield extraction

A second method of $K^+\Lambda$ yield extraction was used which did not rely upon fitting to the missing mass spectra. As well as providing an important systematic check on the fitting algorithm in section 7.2.3.1 and yield extraction, it enabled the extraction of $K^+\Lambda$ in kinematic regions where it was difficult to discern between $K^+\Lambda$ and $K^+\Sigma^0$ contributions in the missing mass spectra. This method gave the most benefit at high beam energies, particularly from data with the 10.03 cm long target (April 2009 data set), where the angular resolution of the K^+ was poorer. The method proceeds as follows.

For every E_γ and θ_{cm} bin, two histograms were filled; one for events where a decay photon was identified, and one where no decay photon was identified. The total number of $K^+\Lambda$ and $K^+\Sigma^0$ events were distributed into the two missing mass spectra according to the detection efficiency of the Σ^0 decay photon.

To extract the Σ^0 decay detection efficiency, a Kaon-MAID [41] distribution of 30 million $K^+\Sigma^0$ were input into the A2 simulation. The ratio of the number of counts in each missing mass spectrum for each E_γ bin provided a detection efficiency, $\epsilon_\gamma(E_\gamma)$ of the decay photon, given the detection of a K^+. ϵ_γ was found not to vary with θ_{cm}. Fig 7.6 shows this detection efficiency as a function of E_γ. A linear fit was used to calculate the detection efficiency for any given E_γ bin.

The simulated Σ^0 decay detection efficiency, ϵ_γ, was subsequently used in the analysis of the experimental data. The missing mass spectra where a decay photon was identified was adjusted by the detection efficiency so that the integral was scaled to the number of $K^+\Sigma^0$ events where the decay photon was not identified. This scaled spectrum was then subtracted from the spectrum where no decay photon was identified. The resulting spectrum then only contained $K^+\Lambda$ events. Fig. 7.7 demonstrates this method of $K^+\Lambda$ yield extraction.

This method reduced the detection efficiency of $K^+\Lambda$ as it was unavoidable to not subtract a small proportion of $K^+\Lambda$ which were misidentified (5-10%).

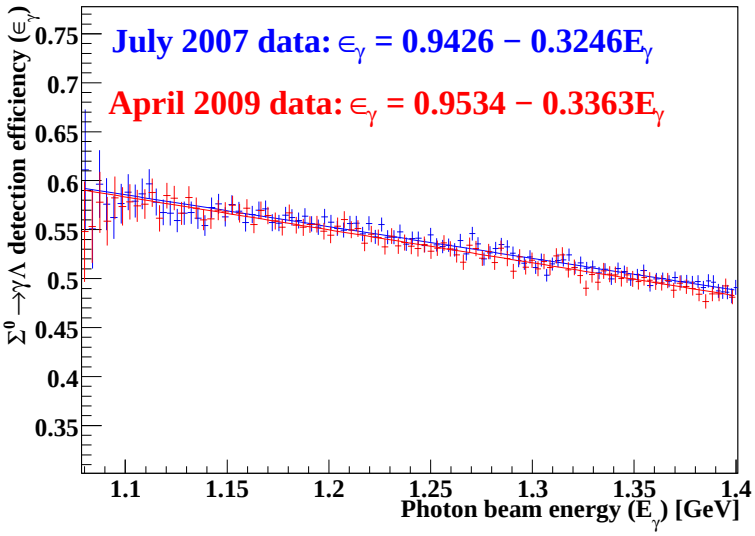

Figure 7.6: Detection efficiency of Σ^0 decay photons for July 2007 (blue data) and April 2009 (red data), each with a linear fit (equations inset).

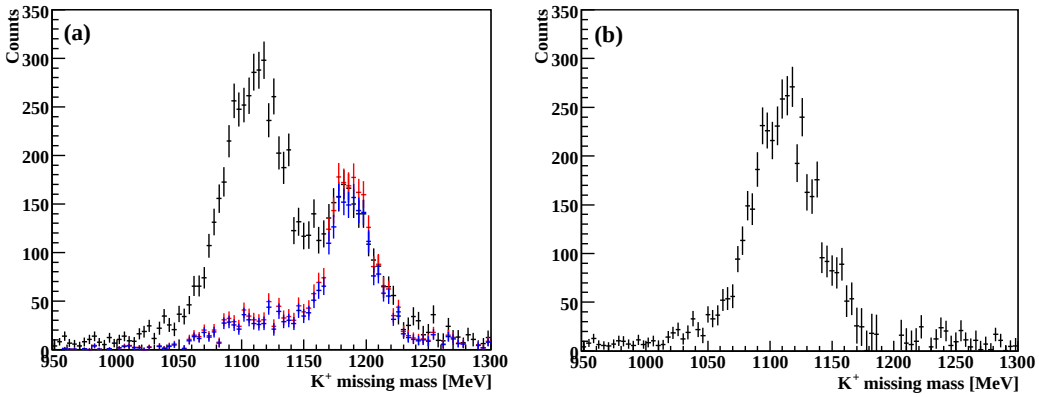

Figure 7.7: Subtraction of $K^+\Sigma^0$ from identifying the decay: $\Sigma^0 \to \Lambda\gamma$. Left: (a) K^+ missing mass plots for when no decay γ is identified (black), when it is identified (red), and after being scaled by the detection efficiency (blue). Right: (b) K^+ missing mass spectrum after the subtraction of the $K^+\Sigma^0$ contribution. $\cos\theta_{cm}$ range -0.25 to -0.15, and E_γ range 1.1 to 1.4 GeV.

7.2.5 Rejection of K^+ with poor momentum reconstruction

To ensure an event sample as clean as possible, a further restriction on the energy of the K^+ was applied. Fig. 7.8 shows the difference in measured and reconstructed K^+ energies. The reconstructed energy was calculated from the photon beam energy and polar angle of the K^+ momentum, assuming a $K^+\Lambda$ reaction in eq. 7.4. Real $K^+\Lambda$ events form a peak centred on zero. This peak is evident in the experimental and simulated data. Events which did arise from $K^+\Lambda$ have different distributions centred away from this region, as indicated by the $K^+\Sigma^0$ simulated events in the figure. Additionally, background channels, such as $\gamma(p, p)\pi^+\pi^-$ form a background in this spectrum (discussed in section 7.6.2). To reduce their contribution, a restriction on events consistent with $K^+\Lambda$ kinematics was applied. Events where the energy difference was greater than 60 MeV were rejected.

There was a small deviation between reconstructed and measured energy at high K^+ energy. For K^+ with an energy of 300 MeV, this deviation was of the order of 10 MeV. This was consistent between simulated and experimental data, however a small correction was required if the reconstructed energy was to be used as a selection cut.

To perform this correction, K^+ were divided into 10 MeV energy ranges. the peak from the energy difference was fitted with a Gaussian function. The mean of each fit was plotted against K^+ energy and a third order polynomial fitted. The parameters from the polynomial were input into subsequent analysis to correct the K^+ energy to equal the reconstructed energy.

The selection cut on the K^+ energy difference rejected approximately 87% of remaining $K^+\Sigma^0$ contribution to the yield. The change in the missing mass spectrum is shown in fig. 7.9. Due to the change in shape of the spectra, the remaining $K^+\Sigma^0$ yield could not be subtracted using the fitting method described in section 7.2.3. The cross section measurements presented in the next section therefore only used the Σ^0 decay tag method of yield extraction to subtract the remaining $K^+\Sigma^0$ contribution. Implementing the K^+ energy difference selection cut reduced the detection efficiency of Σ^0 decay photon by approximately 10%.

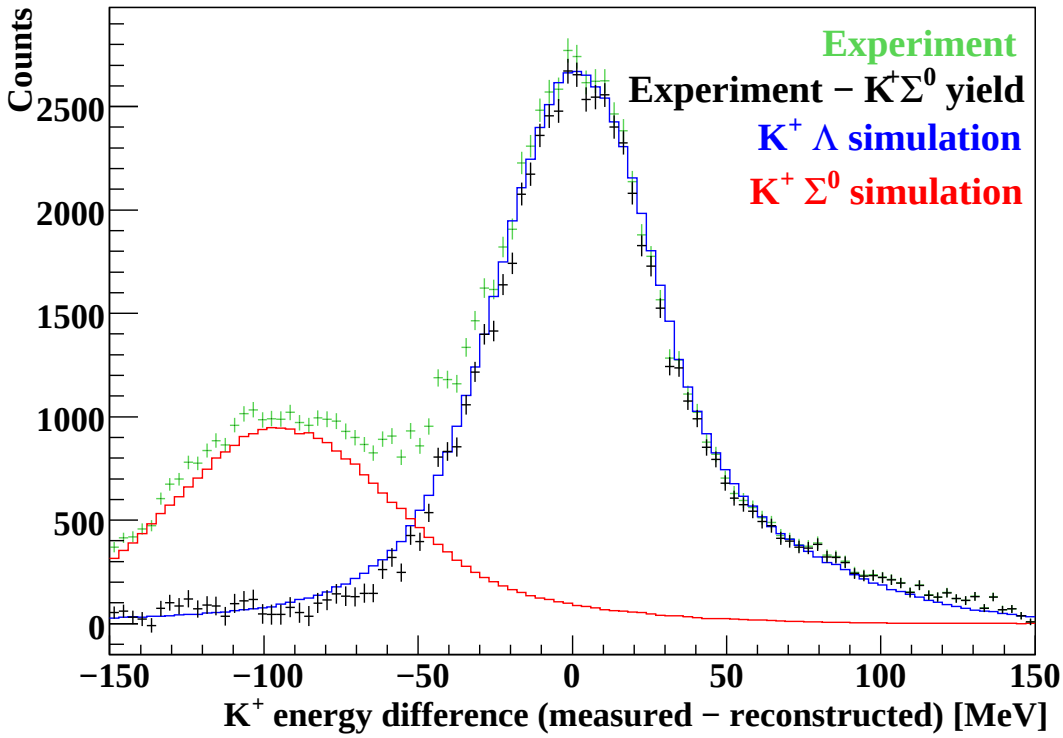

Figure 7.8: The K^+ energy difference between measured and reconstructed energies. Simulated data was scaled to the experimental data. The yield from $K^+\Sigma^0$ was estimated and subtracted from the experimental data. Legend inset.

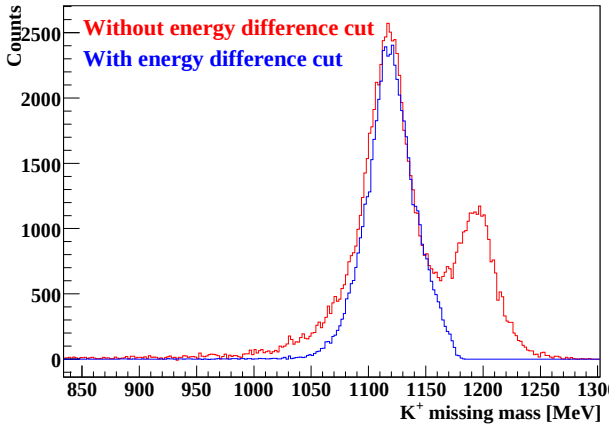

Figure 7.9: Experimental data showing K^+ missing mass before and after the K^+ energy difference selection cut (red and blue lines respectively).

7.3 Measurement of the incident photon flux

To extract the cross section it was necessary to know the tagged photon flux on the target, $N_\gamma = N_S \epsilon_{tagg}$ (see eq. 7.2), where N_S is the total number of electrons hitting the contributing tagger channels and ϵ_{tagg} is the tagging efficiency. N_S was measured by a scaler module which counted the number of hits in each focal plane channel and was read out every 20 seconds by the data acquisition (section 4.6.1). The summed spectrum tagger hits for the July 2007 data set is shown in fig. 7.10. The slope reflects the $1/E_\gamma$ bremsstrahlung spectrum. The non-smooth variation between channels is due to variations in the electron detection efficiency of the individual channels. The two noisy channels at approximately channel 30 were rejected from the analysis.

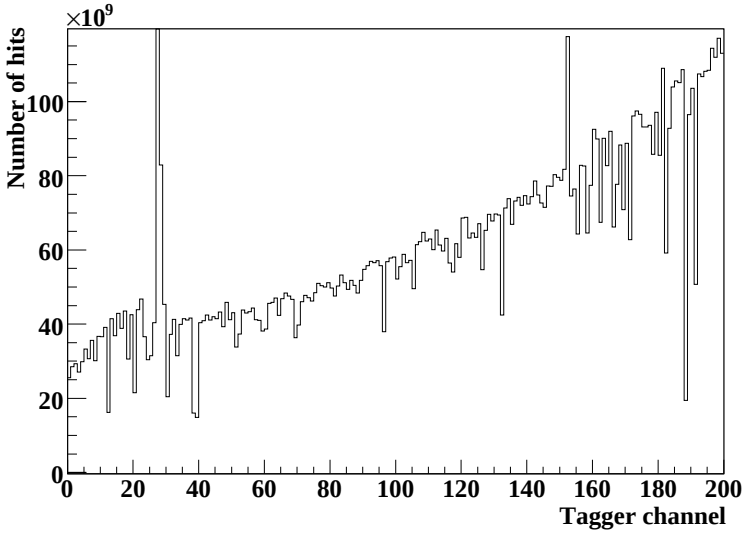

Figure 7.10: The number of electron hits in the Tagger focal plane elements. Channels 20 and 190 correspond to photon energies 1.402 GeV and 75 MeV respectively.

7.3.1 Addition of Tagger M1 data

Nearly all of the measured yield of K^+ events derived from a single hit in the scintillator elements of the photon tagger. If a random electron had given an

earlier signal, the multihit CATCH TDCs (section 4.6.1) recorded signals for multiple hits in the scintillator elements. For a correct measurement of the photon flux, events derived from the second, "M1" hits were also included in the measured yield (the first hit was labelled "M0"). The analysis procedure was therefore performed twice, once with M0, and once with M1 hits included in the event sample. The M1 events were then added to the M0. The addition of the M1 events accounted for approximately 3% of the total K^+ yield.

7.3.2 Dead time correction

The Crystal Ball data acqisition was slower than that of the tagger, and impeded the speed of the data acquisition due to the "dead time" during the read out of the event. As the tagger scalers were only gated by the dead-time of the tagger electronics read out, a correction to the tagger scalers was required. To do this, the live-time ratios of the Tagger and Crystal Ball were extracted from two scalers: one which was continually counting, and a scaler which only counted whilst the data acquisition was enabled. The ratio of these live-time ratios gave a correction factor to the Tagger scaler counts of approximately 0.77.

7.3.3 Extraction of the tagging efficiency

The Tagging efficiency described in section 4.3.2 was measured, to give the ratio of the number of photons passing the collimator to the number of hits in the focal plane detector of the photon tagger. This was measured once per day over the data taking periods. Fig. 7.11 shows the tagging efficiencies for the two data runs, taken from an average of these measurements.

7.4 Detection efficiency measurements with Geant4

The detection efficiency was extracted from the A2 Geant4 simulation by taking the ratio of number of $\gamma(p, K^+)\Lambda$ events detected, to the amount that were input into the A2 simulation for each E_γ and θ_{cm} bin. 30 million $\gamma(p, K^+)\Lambda$ events

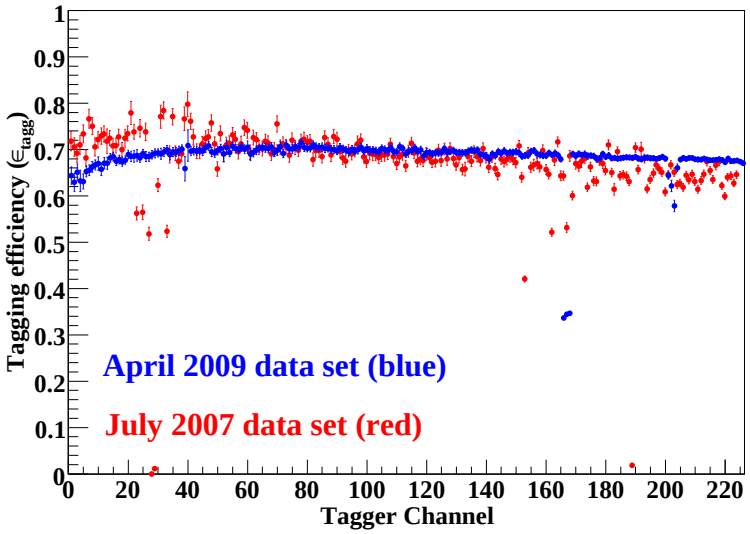

Figure 7.11: The tagging efficiency for the July 2007 and April 2009 data sets (blue and red respectively). Channels 20 and 190 correspond to photon beam energies 1.402 GeV and 75 MeV for the July 2007 data set and 1.392 GeV and 78 MeV for the April 2009 data set .

following a realistic distribution from the Kaon-MAID partial wave analysis [41] were used as the simulation input. Using a Kaon-MAID distribution ensured that the comparitive statistics between experimental and simulated yields was roughly constant for each bin. Using the Σ^0 decay photon tag procedure in section 7.2.4 to extract the $K^+\Lambda$ yields, fig. 7.12 and fig. 7.13 show the detection efficiencies versus photon beam energy (E_γ) for each $\cos\theta_{cm}$ bin.

The detection efficiencies for the April 2009 data was less than that of the July 2007 data due to the larger target reducing the angular resolution. The final selection cut on the energy difference between reconstructed and measured K^+ energy also rejected a larger proportion of $K^+\Lambda$ events in the April 2009 data set.

7.5 Subtraction of empty target data

The contribution of $K^+\Lambda$ from reactions in the mylar windows of the target cell and residual nuclei in the air of the "evacuated" beam pipe needed to be

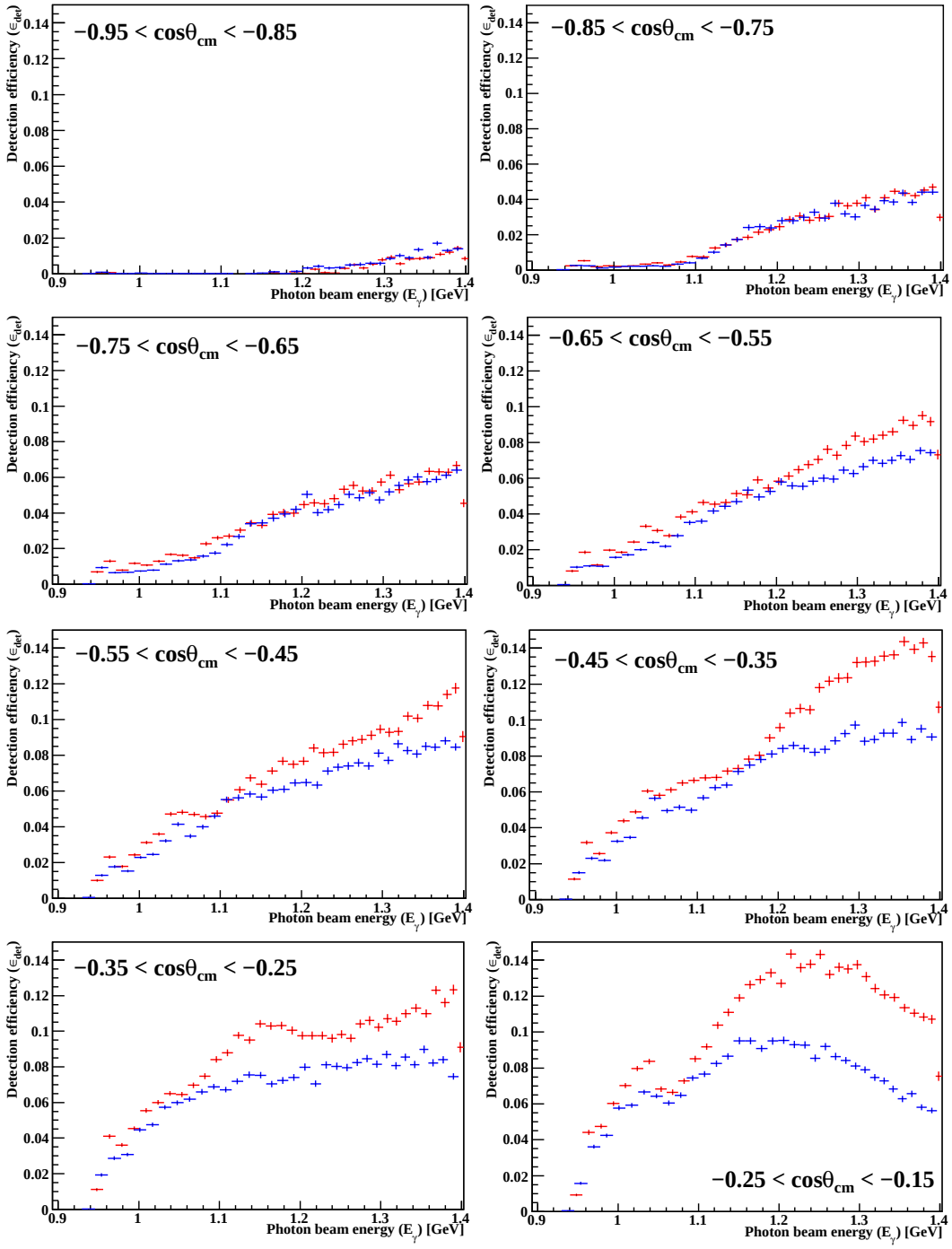

Figure 7.12: $K^+\Lambda$ detection efficiencies for backwards centre of mass angles (θ_{cm}). Red and blue data points are the detection efficiencies for the July 2007 and April 2009 beam times respectively.

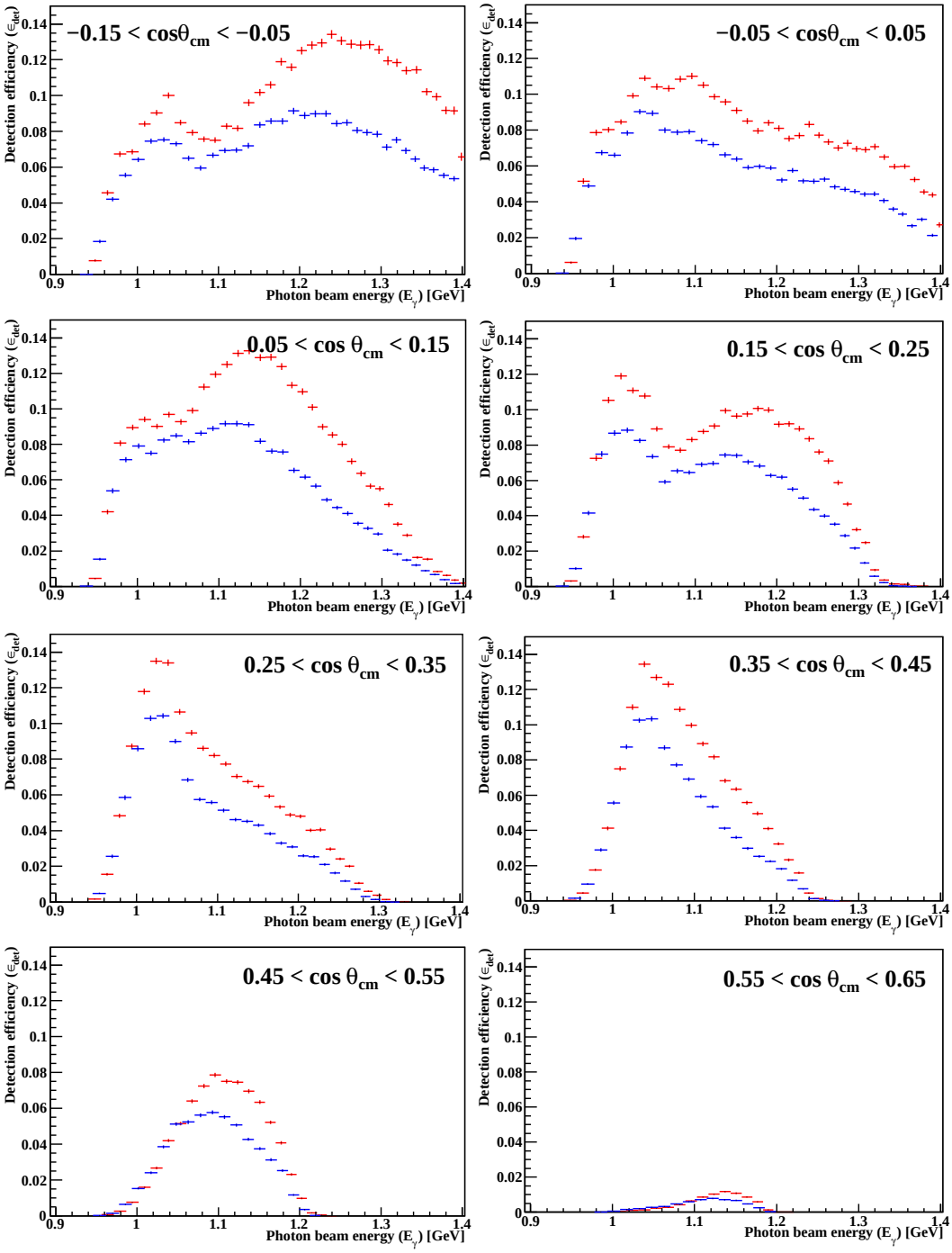

Figure 7.13: $K^+\Lambda$ detection efficiencies for forward centre of mass angles (θ_{cm}). Red and blue data points are the detection efficiencies for the July 2007 and April 2009 beam times respectively.

subtracted from the cross section. Separate data runs with an empty target cell were used, with the K^+ yield extracted in the same manner as for the full target. The yield was normalised by dividing out the number of tagger scaler hits and tagging efficiency for the empty target runs, before subtracting from the full target yield. Fig. 7.14 is an example of the full and empty target yields, the empty target yield typically accounted for 10% of the full target yield in the July 2007 data set. The April 2009 empty target yield only accounted for 4-5% of the total yield as the target was approximately double the July 2007 target length.

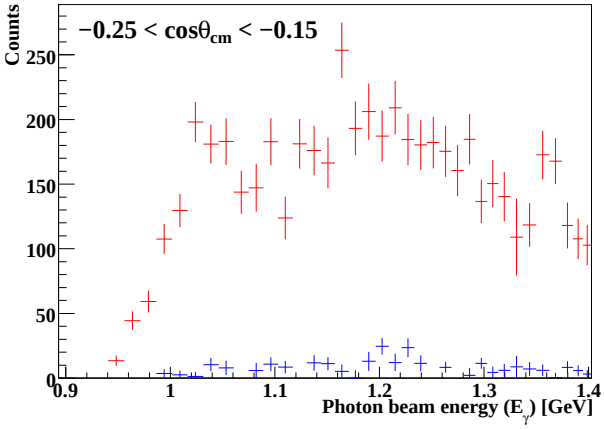

Figure 7.14: $K^+\Lambda$ yield for full and empty target (red and blue points respectively). The empty target data was scaled according to the difference in tagger scalers. θ_{cm} range inset.

7.6 Experimental uncertainties

This section discusses the statistical and systematic uncertainties in the cross section measurements.

7.6.1 Statistical uncertainty

Statistical uncertainties followed a Poisson distribution and arose from:

1. The measured K^+ yield for each E_γ and θ_{cm} bin.

2. $K^+\Lambda$ detection efficiency. Statistical uncertainties were generated both from the yield of reconstructed events, and the number of generated events which were input into the simulation. These were typically 3% and 1% respectively.

3. Tagging efficiency measurements. This was approximately 2% for each tagger channel

4. The detection efficiency of the Σ^0 decay photon. The error from the linear fit in fig. 7.6 was approximately 0.5% and was carried into the scaling of the missing mass spectrum where the decay photon was identified.

5. The number of scalers from the tagger focal plane elements. This was of the order of 10^{-5}% for each tagger channel.

7.6.2 Systematic uncertainties

Dominant systematic errors are estimated in the following sections, and are summarised in section 7.6.2.7.

7.6.2.1 Contamination from other reaction channels

To measure how effective the selection cuts were at isolating the $\gamma(p, K^+)\Lambda$ channel, Monte Carlo generations of other reaction channels were input to the A2 simulation. Table 7.1 lists the approximate percentage which pass the selection cuts and were included in the $K^+\Lambda$ yield. The percentage for $K^+\Lambda$ is approximately three times lower than the detection efficiencies in fig. 7.12 and 7.13 as it includes the generation of K^+ which were out of the acceptance region of the Crystal Ball.

From table 7.1, it is apparent that the selection cuts were excellent at isolating the $K^+\Lambda$ channel, however strangeness cross sections are between 30 to 50 times less than the non strange reaction cross sections which are listed above. To properly understand the contamination from these reaction channels, the yield needed to be scaled by the difference in cross section. The background from $p\pi^+\pi^-$ is an order of magnitude larger than other channels, and the cross section is

Reaction channel	Percentage passing selection cuts [%]
$K^+\Lambda$	3.52
$p\pi^0$	4.78 $\times 10^{-4}$
$n\pi^+$	0.00
$n\pi^+\pi^0$	0.00
$p\pi^+\pi^-$	6.40 $\times 10^{-3}$

Table 7.1: Percentage yield of reaction channels passing selection cuts. Due to the low statistics of some reaction channels, the values are only approximate.

also larger over the energy range of 0.9 to 1.4 GeV. Only this channel was therefore used to estimate systematic uncertainty from background contamination. Fig 7.15 is the ratio of the total cross section for $\gamma(p, p)\pi^+\pi^-$ to the total cross section for $\gamma(p, K^+)\Lambda$.

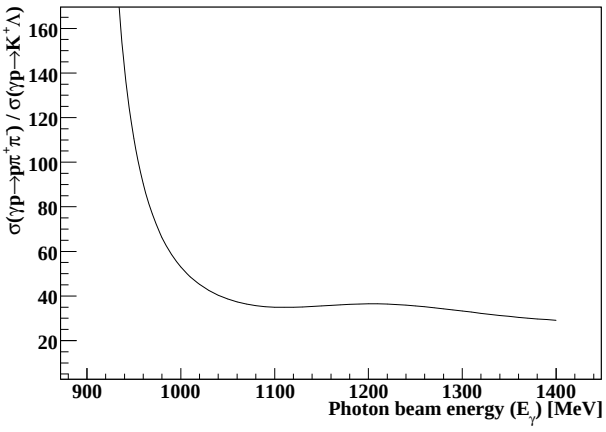

Figure 7.15: Ratio of the total cross sections for $\gamma(p, p)\pi^+\pi^-$ compared to $\gamma(p, K^+)\Lambda$. Cross section data taken from references [120] and [44] respectively, with a smooth line fitted.

Fig. 7.16 shows the simulated $K^+\Lambda$ and $p\pi^+\pi^-$ yields for two $\cos\theta_{cm}$ bins. The $p\pi^+\pi^-$ yield has been scaled by the difference in total cross section. The $p\pi^+\pi^-$ yield was then divided by the sum of both yields. This gave the fraction

of background contamination in $K^+\Lambda$ yields which were extracted from experimental data. The bottom panels of fig 7.16 show these as percentages. The achievable statistics of the $p\pi^+\pi^-$ channel prevent an estimation of this quantity on a bin by bin basis, and so a linear fit was been used to estimate the background contamination as a function of beam energy, E_γ for each $\cos\theta_{cm}$ bin.

The contribution from background was estimated to be of the order of 1-2% over most E_γ and θ_{cm}, increasing to approximately 5% at forward angles and photon beam energies beyond 1.2 GeV.

The measured cross sections were corrected to remove the contribution from the background contamination. A conservative estimation of the systematic error in this procedure was made. The magnitude was taken as being 50% of the estimated background contamination.

7.6.2.2 PID detection efficiency

The method of K^+ detection described in section 6 applied a two dimensional cut to the $\Delta E - E$ analysis between the Crystal Ball and the PID. Inefficiencies in the detection of K^+ in the PID which are not described in the simulation would therefore lower the measured cross section.

As the energy deposition of K^+ in the PID is similar to that of protons, the PID detection efficiency was measured using the $\gamma(p,p)\pi^0$ reaction. To select the $\gamma(p,p)\pi^0$ reaction channel, π^0 were identified in the Crystal Ball from the invariant mass of the two decay photons (fig. 7.17(a)), and then the missing mass of the π^0 was extracted. Events were selected if they were within 30 MeV of the proton mass (fig. 7.17(b)). From these events, the momentum of the proton was reconstructed from the beam and π^0 momenta. The angle between this momentum and all hits in the Crystal Ball was measured, and the hit which gave the smallest angle difference was selected as being the best candidate for the proton. A cut rejected any events where this angle difference was greater than 20° (fig. 7.17(c)). The events which passed all of these selection cuts were grouped into two categories: events where there was a coincidence hit in the PID, and events where there was no coincidence hit in the PID. A coincidence hit is

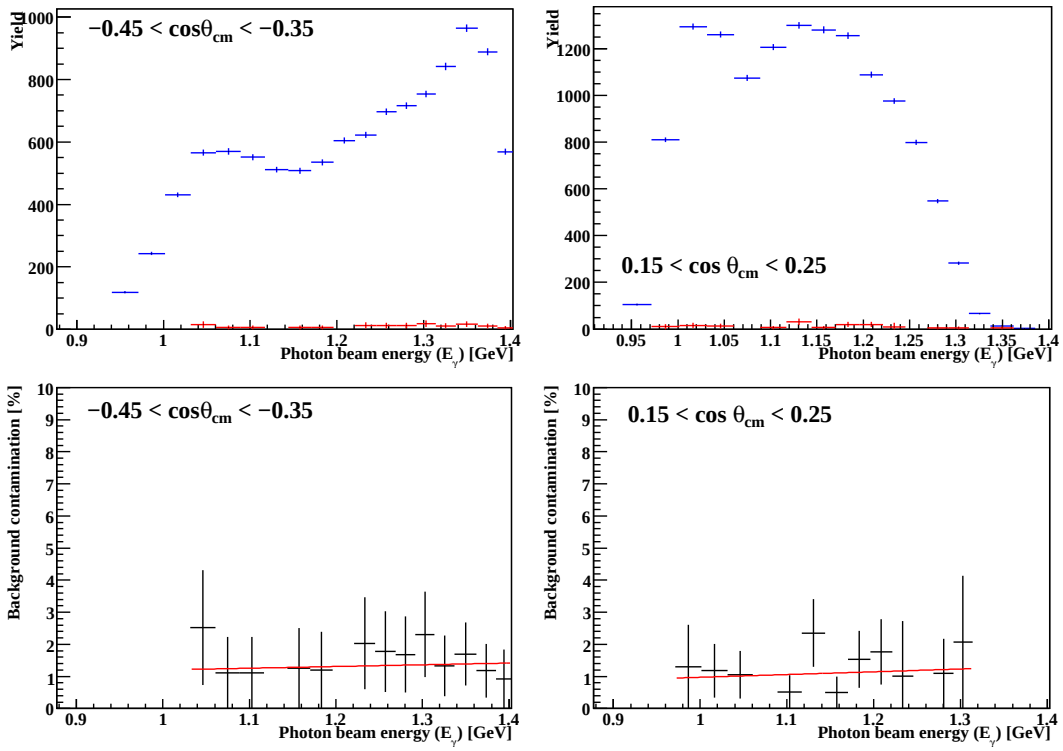

Figure 7.16: Top panels: Simulated $K^+\Lambda$ yield and contamination from $p\pi^+\pi^-$ for two θ_{cm} ranges (blue and red points respectively). Bottom panels: Percentage of contamination of $p\pi^+\pi^-$ of the total yield, with a linear fit (the same θ_{cm} range as the above plot).

defined as a hit in the Crystal Ball within 15° azimuthal angle to the centre of the hit PID element.

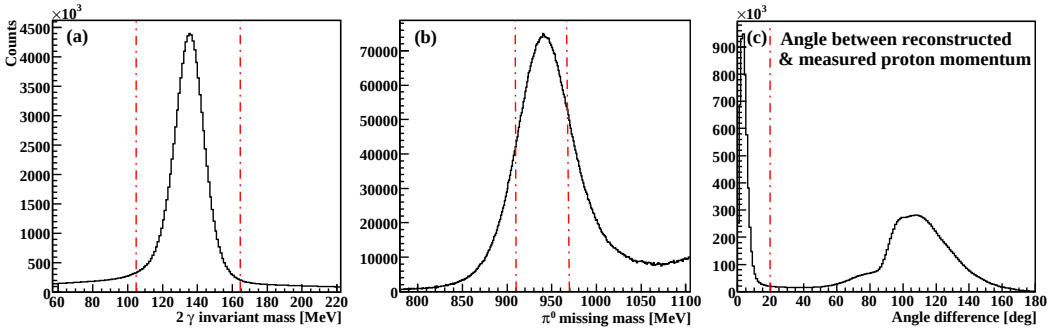

Figure 7.17: Selection cuts to identify the $\gamma(p,p)\pi^0$ reaction. (a) the invariant mass of two photons in the Crystal Ball, with a peak at the π^0 mass. (b) π^0 missing mass, with a peak at the proton mass. (c) Angle difference between reconstructed proton angle and measured angle in the Crystal Ball. Dotted red lines indicate cuts imposed to the data set.

Fig. 7.18 shows the azimuthal distributions with and without coincidence PID hits for simulated data and experimental data. The reduction of counts at 0° and 180° is due to a gap in acceptance at the junction of the Crystal Ball hemispheres. Fig. 7.19 is the PID detection efficiency, defined as the number of events with coincidence PID hits divided by the total number of events. The simulated data does not exhibit 100% detection efficiency due to gaps between the scintillator elements in the PID and the dependence on the Crystal Ball angular and energy resolution for the reconstruction of the $\gamma(p,p)\pi^0$ channel. Fig 7.19 shows the detection efficiency plotted against measured proton energy for simulated and experimental data. The detection efficiency for the July experimental data is less than the simulated data by approximately 1%.

The cross sections were therefore scaled by a factor of 1.01, with a conservative estimation of systematic uncertainties in this procedure of ± 50% of this correction.

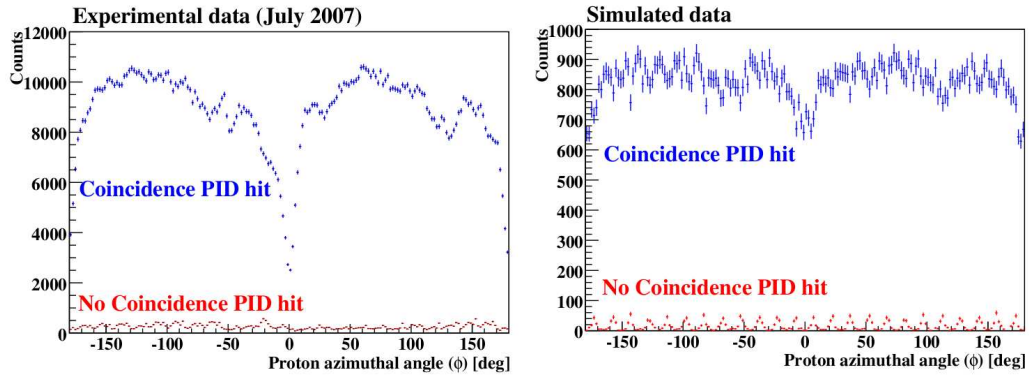

Figure 7.18: Coincidence and non-coincidence hits in the PID and the Crystal Ball for experimental and simulated data (left and right respectively).

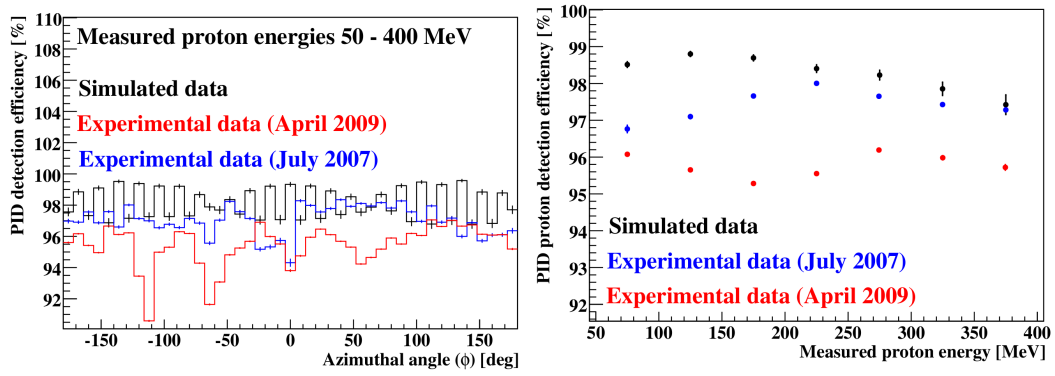

Figure 7.19: Left: PID detection efficiencies for experimental and simulated data. Proton energy range inset. Right: Detection efficiency versus measured proton energy for experimental and simulated data.

7.6.2.3 Separation of $\gamma(p, K^+)\Lambda$ and $\gamma(p, K^+)\Sigma^0$ yields

To understand uncertainties in the Σ^0 decay photon identification, the $K^+\Lambda$ yield extraction was compared to the fitting method described in section 7.2.3.1. As the methods are independent of each other, it was judged that discrepancies between cross section measurements using either method gave a good estimation of systematic uncertainties. To use the fitting method of yield extraction, the final selection cut on the energy difference between reconstructed and measured K^+ was removed (section 7.2.5).

Results from a representative E_γ and $\cos\theta_{cm}$ range, fig. 7.20 show the two methods of yield extraction for experimental and simulated data.

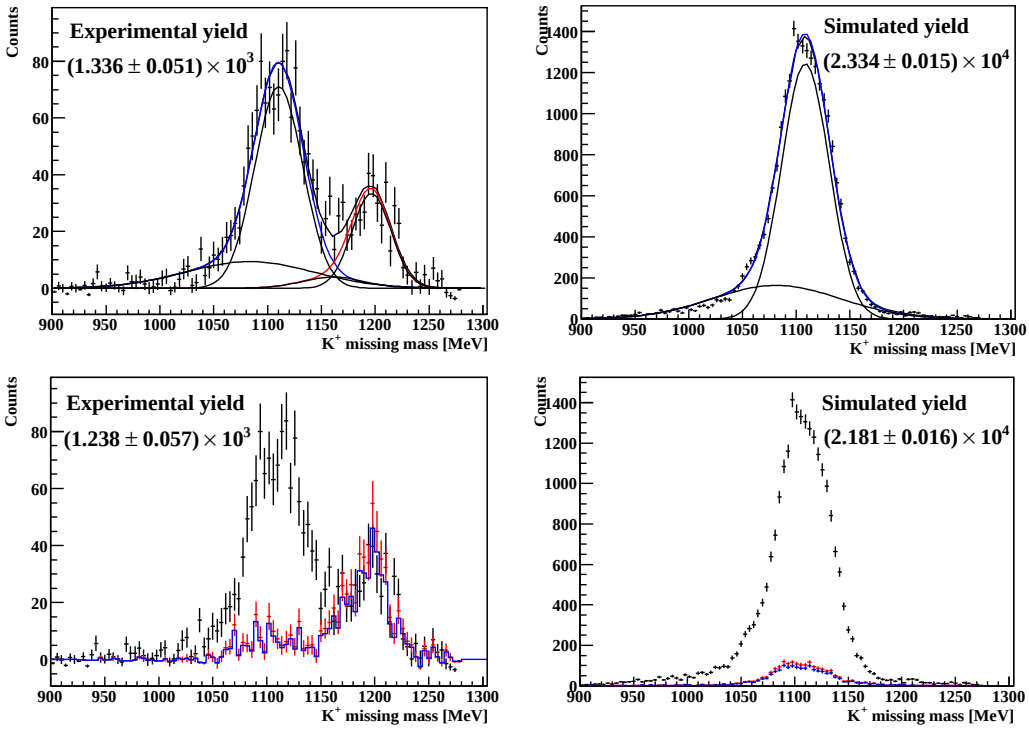

Figure 7.20: K^+ missing mass spectra for $E_\gamma = 1.201$ to 1.262 GeV and $\cos\theta_{cm} =$ -0.25 to -0.15. Top panels: Fitting method used to calculate $K^+\Lambda$ yields for experimental and simulated data. Bottom panels: Σ^0 decay tag method of $K^+\Lambda$ yield extraction.

Table 7.2 lists the ratio of the experimental to simulated yields using the two methods of extraction for four different E_γ and θ_{cm} ranges. Only kinematic ranges where both Λ and Σ^0 missing mass peaks could be fitted to were included.

E_γ [GeV]	$\cos\theta_{cm}$	$R_{Fit} \times 10^{-2}$	$R_{\Sigma^0} \times 10^{-2}$
1.201 - 1.262	-0.55 - -0.45	5.418 ± 0.325	5.285 ± 0.405
1.136 - 1.169	0.05 - 0.15	6.586 ± 0.261	7.119 ± 0.287
1.101 - 1.136	0.15 - 0.25	6.295 ± 0.288	6.354 ± 0.304
1.201 - 1.262	-0.25 - -0.15	5.710 ± 0.221	5.679 ± 0.266

Table 7.2: Systematic uncertainty for $K^+\Lambda$ yield extraction. For each E_γ and $\cos\theta_{cm}$ range, the ratio of the experimental to simulated yield is given as R_{Fit} and R_{Σ^0} for the fitting method and Σ^0 decay tag method respectively.

The agreement in the methods of extraction demonstrates the reliability of the method of identifying the Σ^0 decay. The systematic uncertainty in the $K^+\Lambda$ yield extraction is taken as the average difference of the measurements, which is approximately 3%.

7.6.2.4 Modelling of hardware triggers in simulated data

The modelling of the energy sum threshold and the multiplicity threshold in the simulated data could both potentially give systematic uncertainty. A number of tests were made to asses this and are described in this section.

Changing the multiplicity trigger to M2 made no significant difference to the yield in the simulated data (less than 0.5%), demonstrating that the simulated data was not sensitive to this. It was judged that the multiplicity trigger did not produce any significant systematic uncertainties.

To estimate systematic uncertainties arising from modelling the energy sum in the simulation, the mean value of the cumulative distribution function (section 6.3.5) was varied. The statistical error in the fit used to extract the mean energy sum threshold, $\overline{x}$ was 5 MeV. Fig. 7.21 shows the simulated yield for two $\cos\theta_{cm}$ ranges, using $\overline{x}$ for the modelled energy sum (386 MeV), and increasing and decreasing this by 5 MeV. The lower panel of fig. 7.21 shows the ratio of the yields from the high and low energy sum mean, divided by the yield from the

accepted mean. It is clear that the differences in the yields are small (less than 4%), decreasing as the photon beam energy, E_γ increases. The uncertainty is greater at backward angles where the cross section is more sensitive to the energy sum. A linear fit was fitted to the each θ_{cm} to estimate the systematic uncertainty as a function of photon beam energy, E_γ.

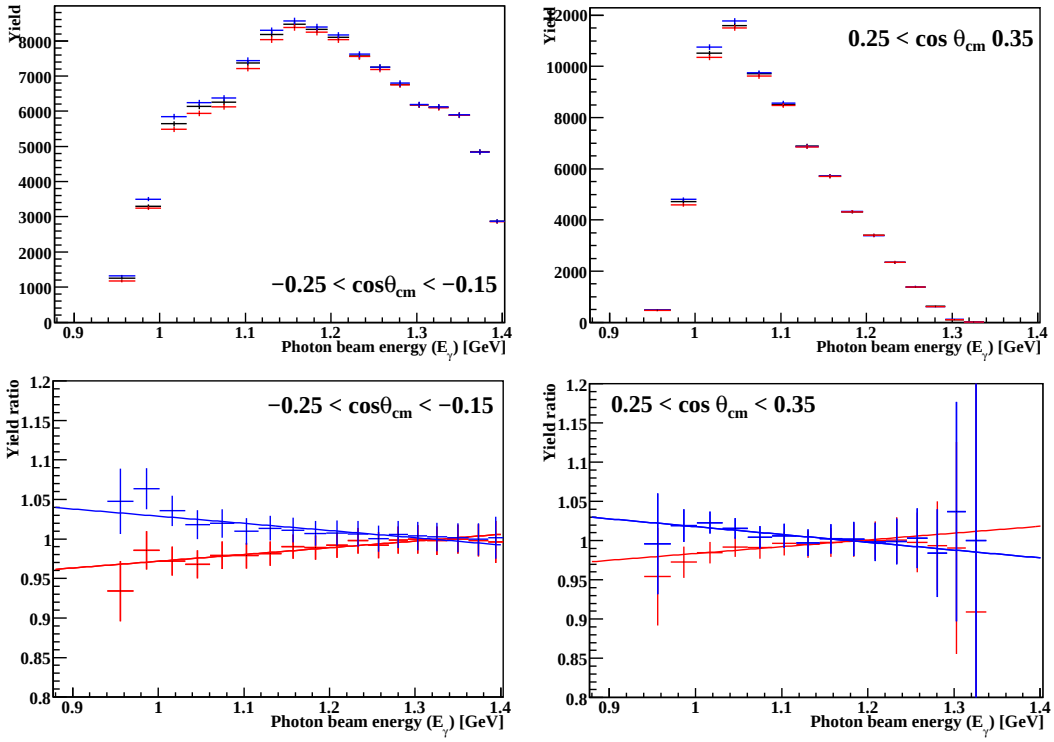

Figure 7.21: Top panels: simulated $K^+\Lambda$ yields for two θ_{cm} ranges. Black points: standard energy sum model (mean at 186 MeV), red points: high energy sum (mean at 191 MeV), blue points: low energy sum points (181 MeV). Low panels: Ratio of the low energy sum yield to the standard energy sum yield (blue) and high energy sum yield to the standard energy sum yield (red points). Linear fits estimate systematic uncertainties.

7.6.2.5 K^+ hadronic interactions

As K^+ identification depended on the detection of the weak decay, if the K^+ interacted strongly with a nucleon in the NaI crystals, the K^+ was not detected. The modelling of the K^+ strong interaction in the A2 simulation could therefore change the detection efficiency and the extracted cross sections.

The modelling of K^+ nuclear interactions in Geant4 [121] uses tabulated data, interpolating between data points and applying isospin and strangeness conservation to calculate cross sections where there is no tabulated data. At present, the propagation of K^+ through the nucleus relies on a hard-sphere potential which was developed for the propagation of pions. Nucleon-nucleon correlations are also not included. For these reasons, a systematic check of the effect of the K^+ strong interaction on the cross section measurements was needed.

The distance the K^+ propagated through the NaI crystal, and therefore the probability of a strong interaction occurring, depended on the K^+ energy. If the strong interaction had not been modelled correctly in Geant4, the discrepancies would therefore be more apparent for high energy K^+. Fig. 7.22 and 7.23 show the K^+ energy for each centre of mass angle bin for the experimental and simulated data with and without hadronic interactions "switched on". The experimental data has had empty target data subtracted and scaled to match the simulated data according to the ratio of the integrals. It is clear there is excellent agreement of the distribution of K^+ energies between experimental and simulated data. As expected, the yield is greater when the strong interaction is switched off in the simulation and the effect is largest at high energies.

To obtain a maximum limit of the effect of K^+ hadronic interactions on the cross section, the yield of $K^+\Lambda$ was extracted for simulated data with and without the hadronic interactions switched on. Fig. 7.24 shows the yield for the data with hadronic interactions divided by the data without the hadronic interactions. If the hadronic interactions were not included, near threshold, the cross section would reduce by 10%, and beyond 1.2 GeV, the extracted cross section would reduce by 20-25%.

It is obvious that this is an overestimation, as the hadronic interaction has been included in the detection efficiency measurements. Assuming the K^+ hadronic

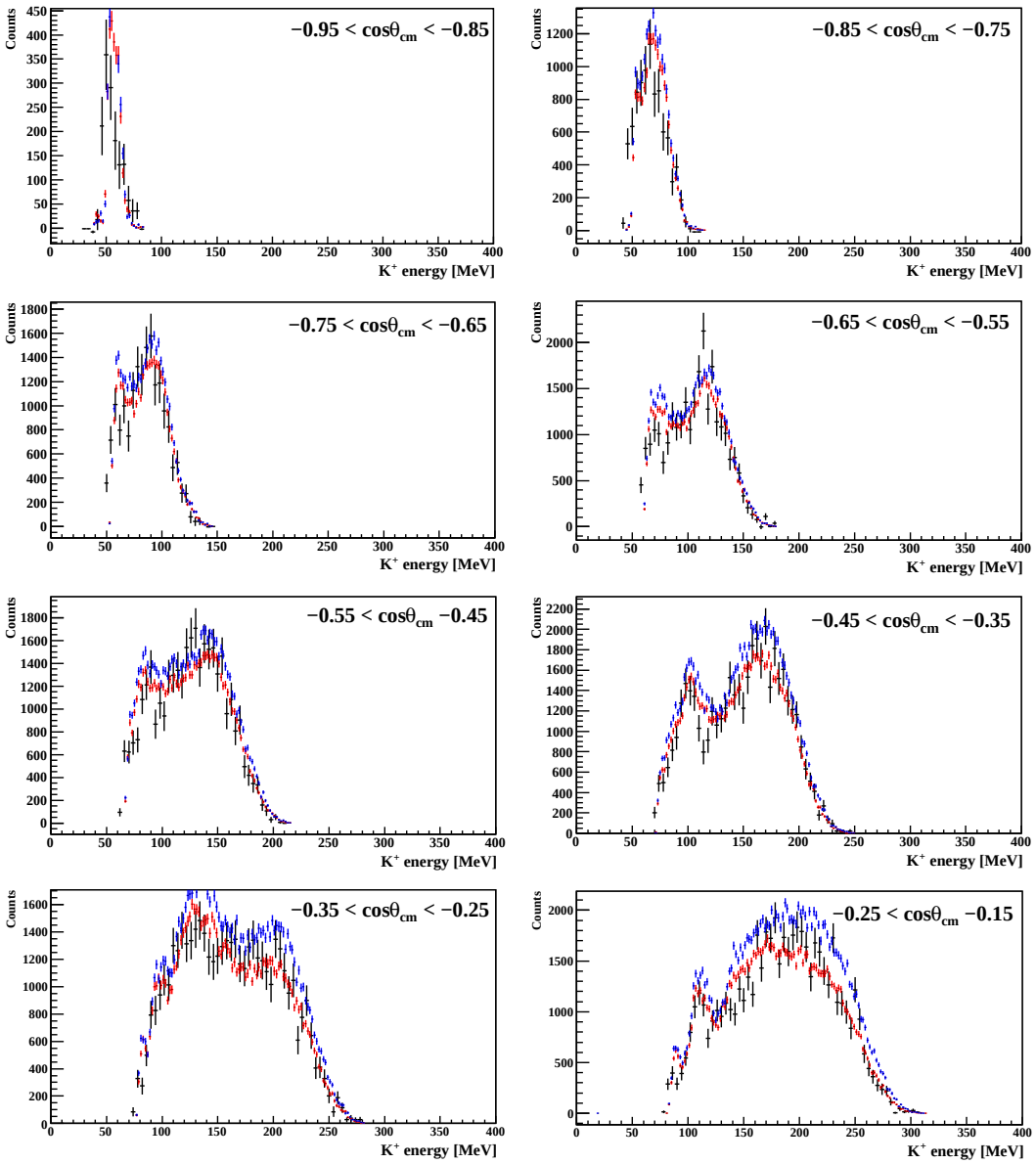

Figure 7.22: K^+ energy distributions for backward centre of mass angle bins. Black data points are the experimental data with empty target subtracted, red is the simulated data and blue is the simulated data with the K^+ hadronic interactions switched off. The integral of the experimental data is normalised to the simulated data.

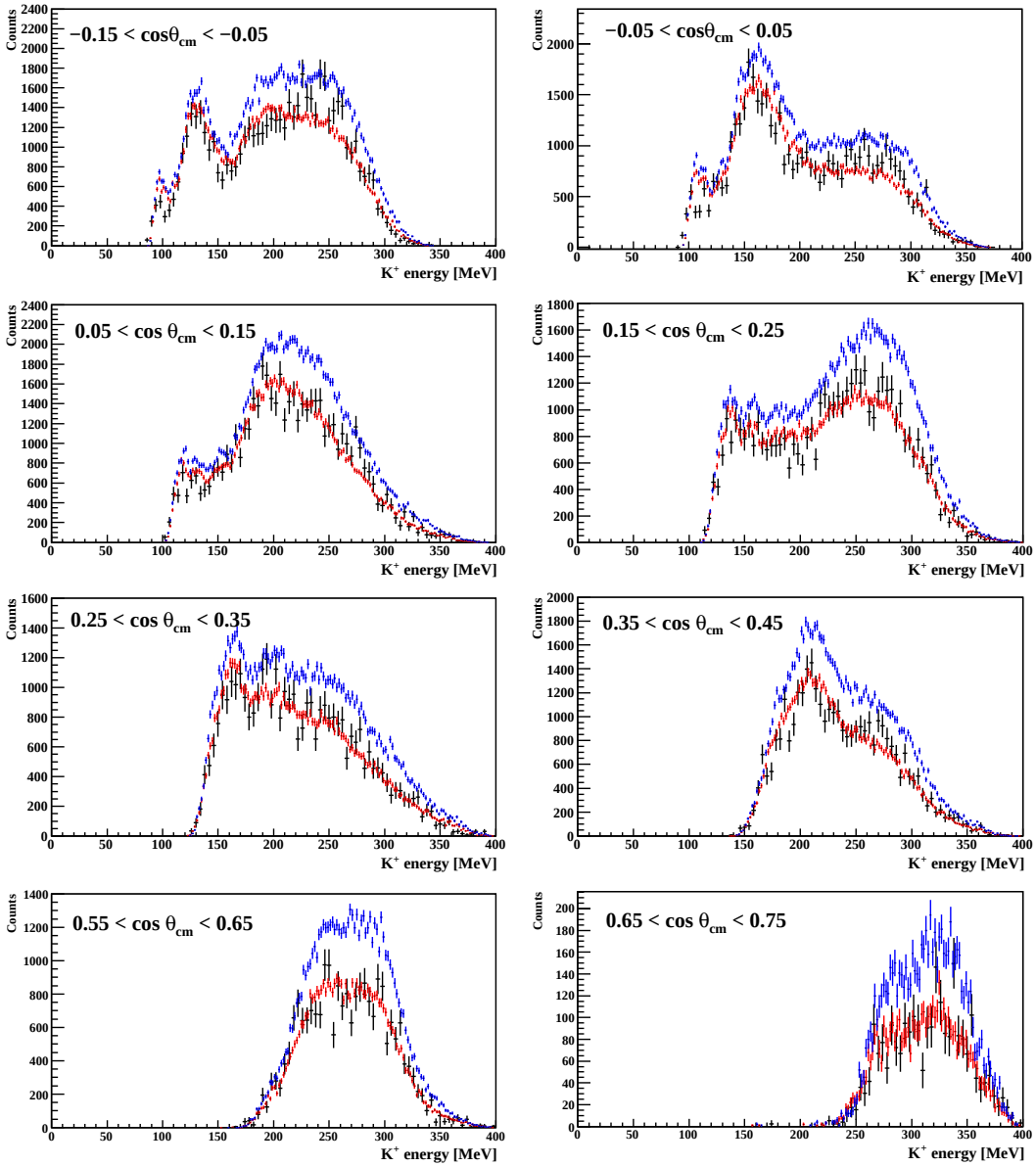

Figure 7.23: K^+ energy distributions for forward centre of mass angle bins. Black data points are the experimental data with empty target subtracted, red is the simulated data and blue is the simulated data with the K^+ hadronic interactions switched off. The integral of the experimental data is normalised to the simulated data.

cross section to be modelled accurately to within 20% results in a systematic uncertainty of 4% at 1.15 GeV (20% of a 20% discrepancy with no hadronic interactions included), decreasing near threshold.

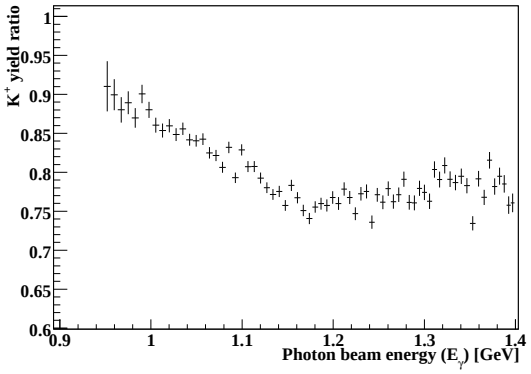

Figure 7.24: $K^+\Lambda$ yield from simulated data. Data without K^+ hadronic interactions was divided by data with K^+ hadronic interactions.

7.6.2.6 Target parameters

The target length was measured as 4.76 ± 0.30 cm and 10.03 ± 0.30 cm for the July 2007 and April 2009 respectively. The main source of uncertainty was due to the deformation of the entrance window. This gave a systematic uncertainty to the cross sections of 0.63% and 0.30% for the July 2007 and April 2009 data sets respectively.

7.6.2.7 Summary

For a given source of systematic uncertainty, the magnitude was compared between the July 2007 and April 2009 data sets. The larger magnitude was selected (although the magnitudes were always very similar), and summed linearly with the other major sources of systematic uncertainty. Table 7.3 is an example of the contributing systematic uncertainties for two E_γ and $\cos\theta_{cm}$ intervals.

Fig. 7.25 and 7.26 plot the total systematic uncertainties versus E_γ for all $\cos\theta_{cm}$ intervals. Below photon beam energies of 1.1 GeV, the predominant uncertainty is due to the simulated energy sum model. Above 1.1 GeV, uncertainty

Source of systematic uncertainty	Example 1 [%]	Example 2 [%]
Hadronic interactions	±2.42	±4.69
Background reaction channels	±0.94	±1.48
Target length	±0.50	±0.50
PID detection efficiency	±1.00	±1.00
Simulated energy sum	+4.27 -5.28	+0.51 -0.61
$K^+\Sigma^0$ contribution	±0.00	±3.00
Total	+9.13 -10.14	+11.18 -11.28

Table 7.3: Examples of contributing systematic uncertainties for two E_γ and $\cos\theta_{cm}$ intervals. Example 1: $E_\gamma = 1.0$ GeV and $-0.65 < \cos\theta_{cm} < -0.55$. Example 2: $E_\gamma = 1.2$ GeV and $-0.05 < \cos\theta_{cm} < +0.05$.

from the hadronic interactions and background contributions dominate. The increase at 1.1 GeV is due to the seperation of the $K^+\Lambda$ and $K^+\Sigma^0$ channel. Although the threshold for $K^+\Sigma^0$ is at 1.05 GeV, the yield of this channel below 1.1 GeV was negligible.

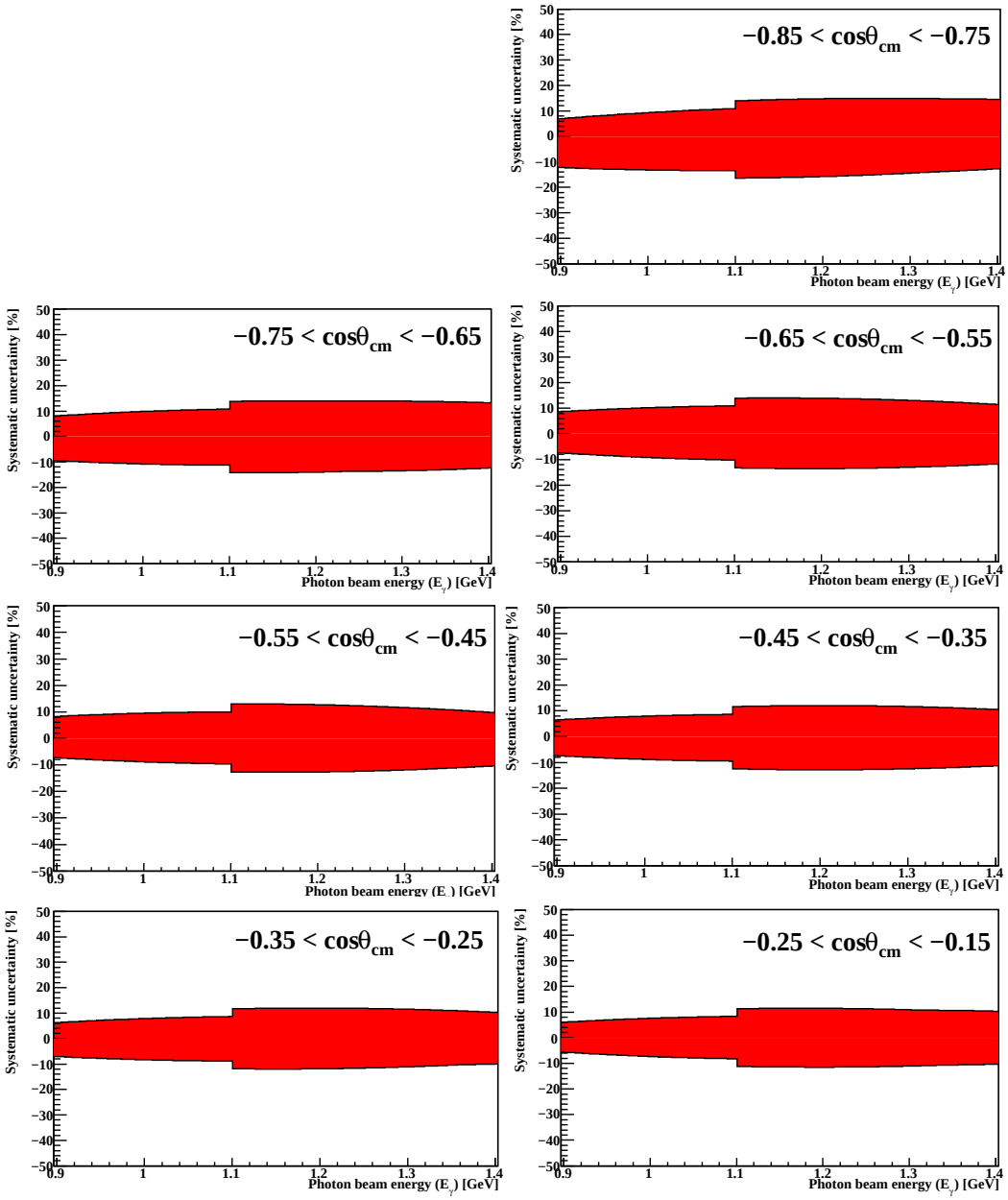

Figure 7.25: Total systematic uncertainties as a fraction of the measured differential cross sections (selecting the larger source of systematic uncertainties from both data sets). $\cos\theta_{cm}$ ranges inset.

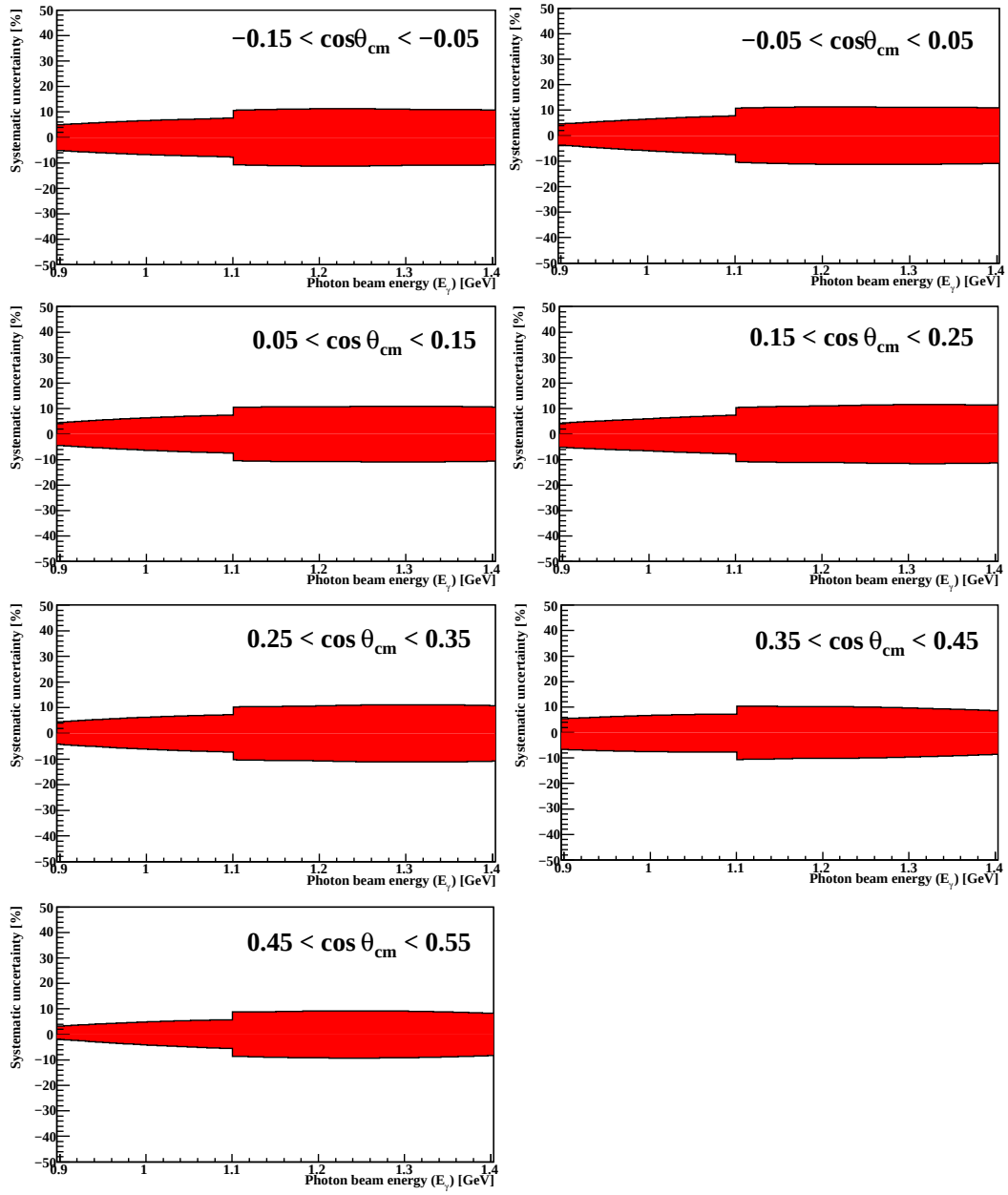

Figure 7.26: Total systematic uncertainties as a fraction of the measured differential cross sections (selecting the larger source of systematic uncertainties from both data sets). $\cos\theta_{cm}$ ranges inset.

Chapter 8

Results and discussion

This chapter presents the new $\gamma(p, K^+)\Lambda$ differential cross section measurements and compares the results to previous measurements and model predictions. The error bars of data presented herein only include the statistical uncertainty, not the systematic uncertainty. As shown in section 7.6.2, the systematic uncertainty is approximately 10% over most of the kinematic range, reducing to approximately 6% at forward centre of mass angles and photon beam energies less than 1.1 GeV. $K^+\Sigma^0$ contributions have been subtracted using the Σ^0 decay photon tag method (section 7.2.4).

8.1 Comparison and discussion of data sets

Fig. 8.1 and 8.2 show new $\gamma(p, K^+)\Lambda$ differential cross sections versus the photon beam energy, E_γ, extracted from the July 2007 and April 2009 data sets. The July 2007 data has been binned into energy intervals corresponding to the tagging range of four focal plane detector elements, and the April 2009 data into three focal plane detector elements. At angles smaller than $\cos\theta_{cm} = -0.85$ (corresponding to angles in degrees larger than 164.7^0), there was insufficient statistics in either data set to extract cross section measurements. At forward angles, the data does not extend to 1.4 GeV as the K^+ travels forward, outside of the acceptance region of the Crystal Ball. The contribution from $K^+\Sigma^0$ was subtracted from each E_γ and $\cos\theta_{cm}$ interval using the Σ^0 decay photon tag method (section 7.2.4).

Events were also rejected at forward angles and at high energies if there was any ambiguity whether the K^+ "punched through" the NaI crystals. In principle, with detailed systematic checks of the modelling of the materials outside the Crystal Ball (steel cladding, windows, PMTs and cables for example) more high energy events can be retained with future analysis. To reduce systematic uncertainties, a conservative cut was applied to remove K^+ events punching through or stopping near to the outside edge of the NaI crystals. The position of this cut was extracted using simulated data, where the actual energy of the K^+ was known. K^+ kinetic energy was plotted against incident photon beam energy, E_γ for each $\cos\theta_{cm}$ interval. Fig. 8.3 is an example, where it is apparent that rejecting events where E_γ is greater than 1.23 GeV safely removes K^+ events approaching the "punch through" energy.

The longer target in the April 2009 data compared to the July 2007 data set led to somewhat poorer angular momentum resolution for the K^+. This necessitated the rejection of potential "punch through" K^+ at a lower photon beam energy than the July 2007 data (by approximately 70 MeV).

It is clear that the agreement between the two data sets (fig. 8.1 and 8.2) is good over a wide range of E_γ and θ_{cm}. Given the difference in target size, electron beam energy, calibrations (of all the detectors), and the triggering electronics, this agreement indicates the systematic uncertainties are largely under control (the only major systematic uncertainty which is identical for both data sets is the modelling of the K^+ hadronic interactions).

The remainder of this chapter presents the weighted average of both data sets. This was non-trivial due to the variable bin widths of the incident photon energy and different photon energy ranges for each data set. Appendix A explains this procedure. The data presented herein is rebinned by a factor of three (corresponding to three focal plane elements in the April 2009 data). This energy range varies, but is approximately 10 MeV.

Three different theoretical models have been superimposed on the cross section graphs: The Regge-Plus-Resonance model of Corthals *et al.* [87] (section 3.3.5), the model of Borasoy *et al.* based upon a chiral effective Lagrangian [38] (section 3.3.4) and the Kaon-MAID partial wave solution [41] (section 2.5.3). As

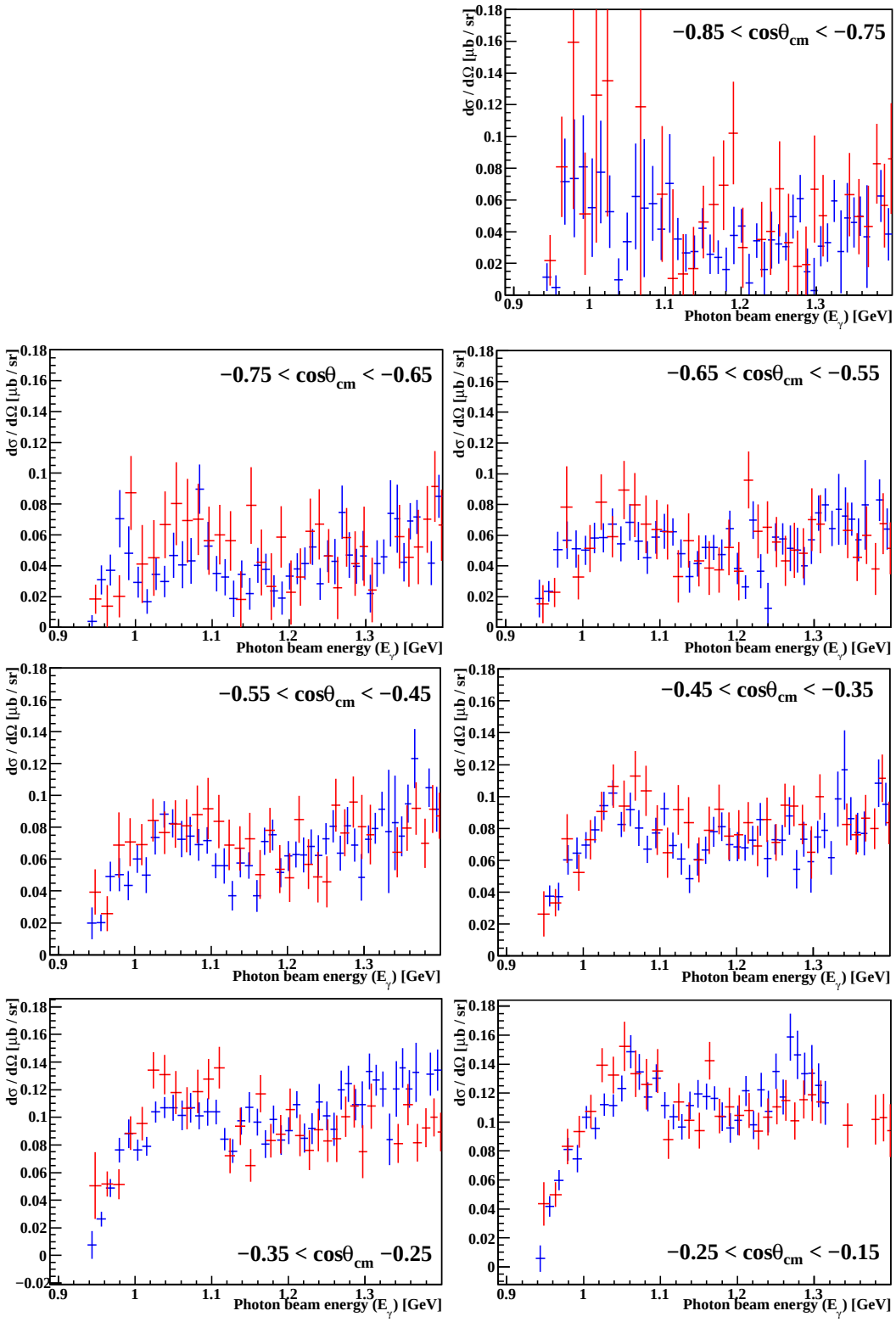

Figure 8.1: Differential cross sections versus E_γ. Red and blue data points are from July 2007 and April 2009 data sets respectively. $\cos\theta_{cm}$ intervals inset. Error bars correspond to the statistical error only

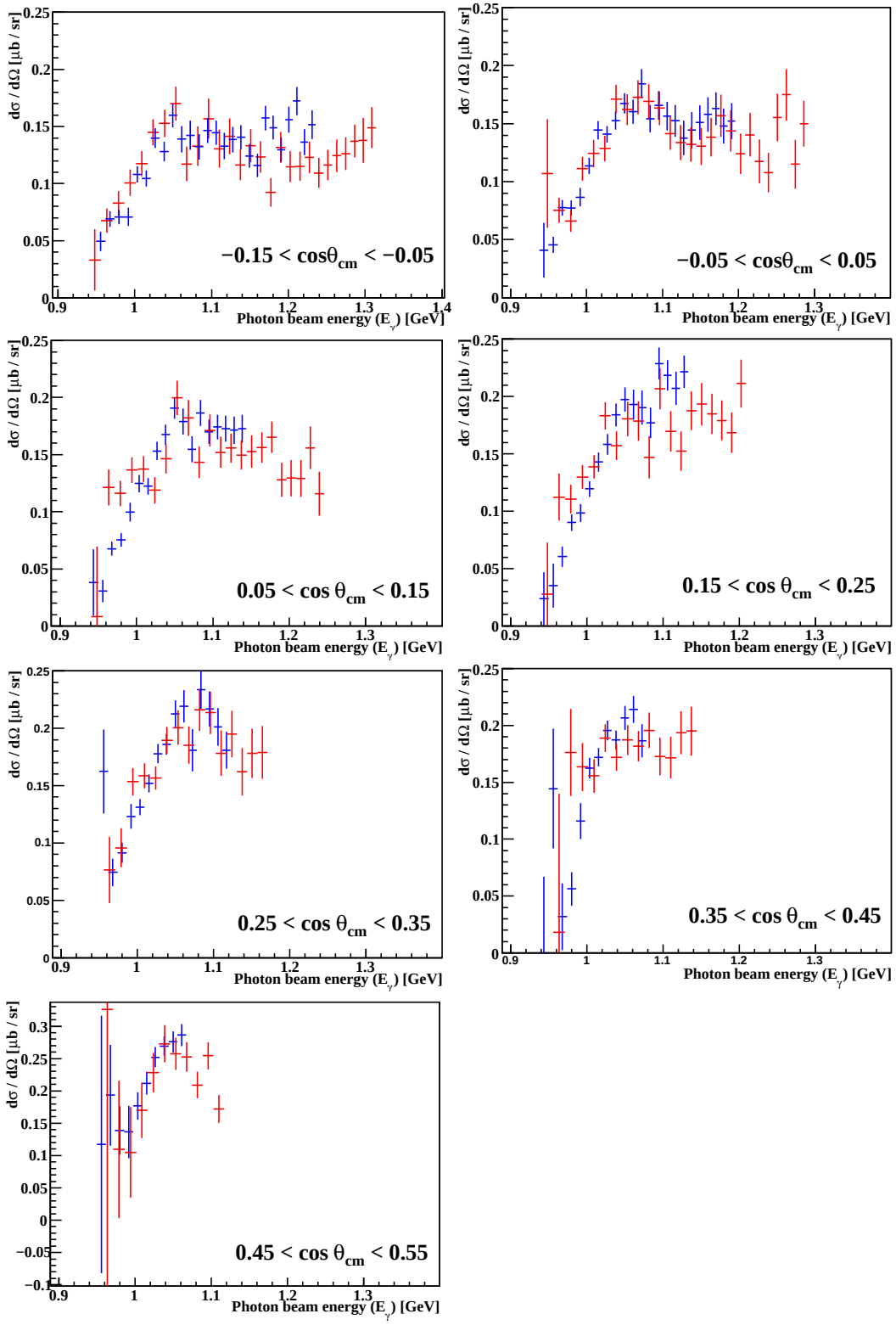

Figure 8.2: Differential cross sections versus E_γ. Red and blue data points are from July 2007 and April 2009 data sets respectively. $\cos\theta_{cm}$ intervals inset. Error bars correspond to the statistical error only

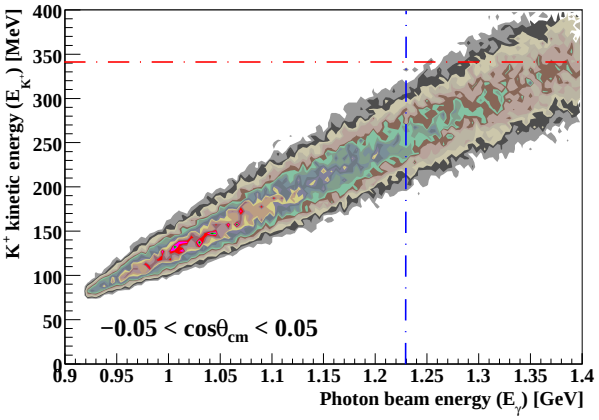

Figure 8.3: K^+ kinetic energy (E_{K^+}) versus photon beam energy (E_γ) for a given $\cos\theta_{cm}$ interval (inset). The approximate energy at which a K^+ punches through the back of the NaI crystals has been drawn as a dotted red line. Cross section measurements for beam energies beyond the dotted blue line were excluded.

a reminder, the Kaon-MAID solution splits the transmission matrix into seperate background and resonance terms. The resonance terms are expanded as a series of partial waves and constrained by fits to experimental data. The current Kaon-MAID solution includes the resonances $S_{11}(1650)$, $P_{11}(1710)$, $P_{13}(1720)$ and $D_{13}(1900)$, and is constrained by fits to the SAPHIR data from Glander *et al.* [46].

8.2 $\gamma(p, K^+)\Lambda$ differential cross sections versus energy

Fig. 8.4 and 8.6 show the differential cross sections as a function of the invariant mass of the system, W. This is derived from the photon beam energy, E_γ and target mass, m_p (proton mass):

$$W = \sqrt{m_p(2E_\gamma + m_p)} \tag{8.1}$$

Plotting the cross section as a function of W is more appropriate when studying resonance structure, with W being the mass of contributing resonances[1].

[1]This is the same quantity defined from the Mandelstamm variable, s in section 2.5.

The threshold for $K^+\Lambda$ and $K^+\Sigma^0$ photoproduction in W are 1.609 GeV and 1.686 GeV respectively. The tagged photon beam gives access to W up to 1.87 GeV for reactions off a proton target.

The statistics of the differential cross section measurements generally exceed previous measurements. At backward angles, the new data is approximately 20 % lower than previous measurements, and approximately 5-6% outside of the combined systematic error of this data and the SAPHIR [46] data[1]. At forward angles, the data agrees well with the SAPHIR data. Both CLAS data sets [54, 51] exhibit consistently higher cross sections than this data or the SAPHIR data. In particular, the large peak in the cross section data at approximately 1.68 GeV is not reproduced in this data or the SAPHIR data set. Moreover, there is a sizeable discrepancy between the two CLAS data sets in this region. This was discussed in reference [54], but the source of the discrepancy was not found.

The data gives broad general agreement with the superimposed Kaon-MAID analysis [41]. This calculation has been fit to the SAPHIR data. The generally good agreement between the Kaon-MAID calculations and this new data therefore support the overall agreement between this data and the SAPHIR data. It has already been proposed to perform an independent partial wave analysis with this new data set [122] and this will form part of a future publication. The improved statistical accuracy of the new data will give more stringent constraints on these partial wave analyses.

As an indication of the contributing resonances, fig. 8.7 shows for two $\cos\theta_{cm}$ intervals, the Kaon-MAID calculation separated according to the contribution from each of the resonances. The current solution suggests the cross section is dominated by the $S_{11}(1650)$ resonance, with destructive interference from the other resonances lowering the cross section at backward angles. The effect of hyperon and meson resonances on the cross section mechanism, particularly at backwards angles is currently being discussed [123], and the new Crystal Ball data over these kinematic ranges will help to constrain these aspects in a new partial wave analyses. It should be remarked that superimposing each resonance contribution as in fig. 8.7 can be misleading; if the partial wave analysis was to be

[1] for each $\cos\theta_{cm}$ interval, the SAPHIR data is over a $\cos\theta_{cm}$ range backwards by 0.05.

repeated, but for example without the inclusion of the $D_{13}(1900)$, the constraints to the data would change the coupling to all of the other resonances.

The Regge-Plus-Resonance (RPR) model [87, 124] (section 3.3.5), does not describe the data well at backward angles where it predicts a cross section approximately twice the measured value. At forward angles it agrees closely with the CLAS data. This agreement at forward angles may be expected, as the fit parameters were only constrained to data at small angles, where $\cos\theta_{cm} < 0.35$. This was done as the Regge parameterisation is only valid at forward angles where the momentum exchange is small and t-channels dominate. A revised model is currently being worked on to improve the comparison to experimental data at backward angles, where the new data will be a valuable constraint [125].

8.3 $\gamma(p, K^+)\Lambda$ differential cross sections versus angle

Fig. 8.8, 8.9, 8.10 and 8.11 show differential cross sections versus $\cos\theta_{cm}$. Due to the improved statistics of this data, previous data sets are not available for comparison at all presented intervals of W. Each interval in W is between 5-7 MeV, and previous data is presented if its mean energy was inside the interval of W.

Near threshold, the statistics of the new data are far superior to previous data sets. This will provide a very important constriant on χPT based effective field theories. The chiral effective Lagrangian model of Borasoy *et al.* [38] is superimposed where available[1]. Despite parameters being constrained by fits to the SAPHIR and CLAS data, the model generally gives a better description of this new data near threshold (below $W = 1.688$ GeV) than observed with previous data. The model prediction is expected to be accurate at these energies, where s-waves dominate, and so an accurate constraint at these energies is necessary to reliably extend and test the model at higher energies (for example, including higher order partial waves to describe photoproduction data further from threshold). Near threshold, the Kaon-MAID calculation does not agree with this

[1]Extracted from reference [38] .

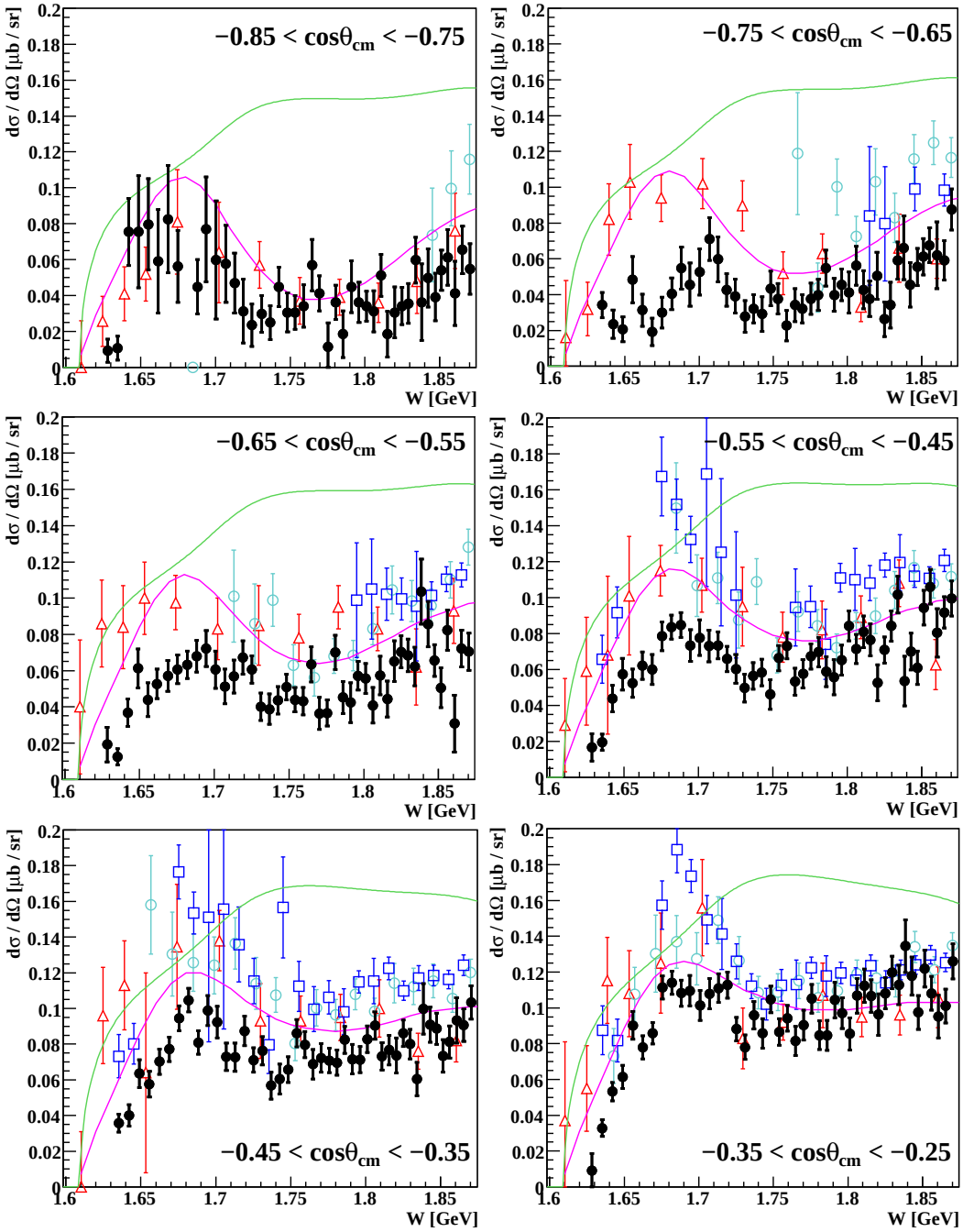

Figure 8.4: Differential cross sections versus centre of mass energy, W. This data (black, filled circles, error bars correspond to the statistical error only), SAPHIR [46] (red, open triangles), CLAS [51] (light blue, open circles) and [54] (dark blue, open squares), Kaon-MAID [41] (magenta line), and a Regge-Plus-Resonance (RPR) parameterisation [87, 124] (green line). The SAPHIR angle range is backwards by $\cos\theta_{cm} = -0.05$ for each interval.

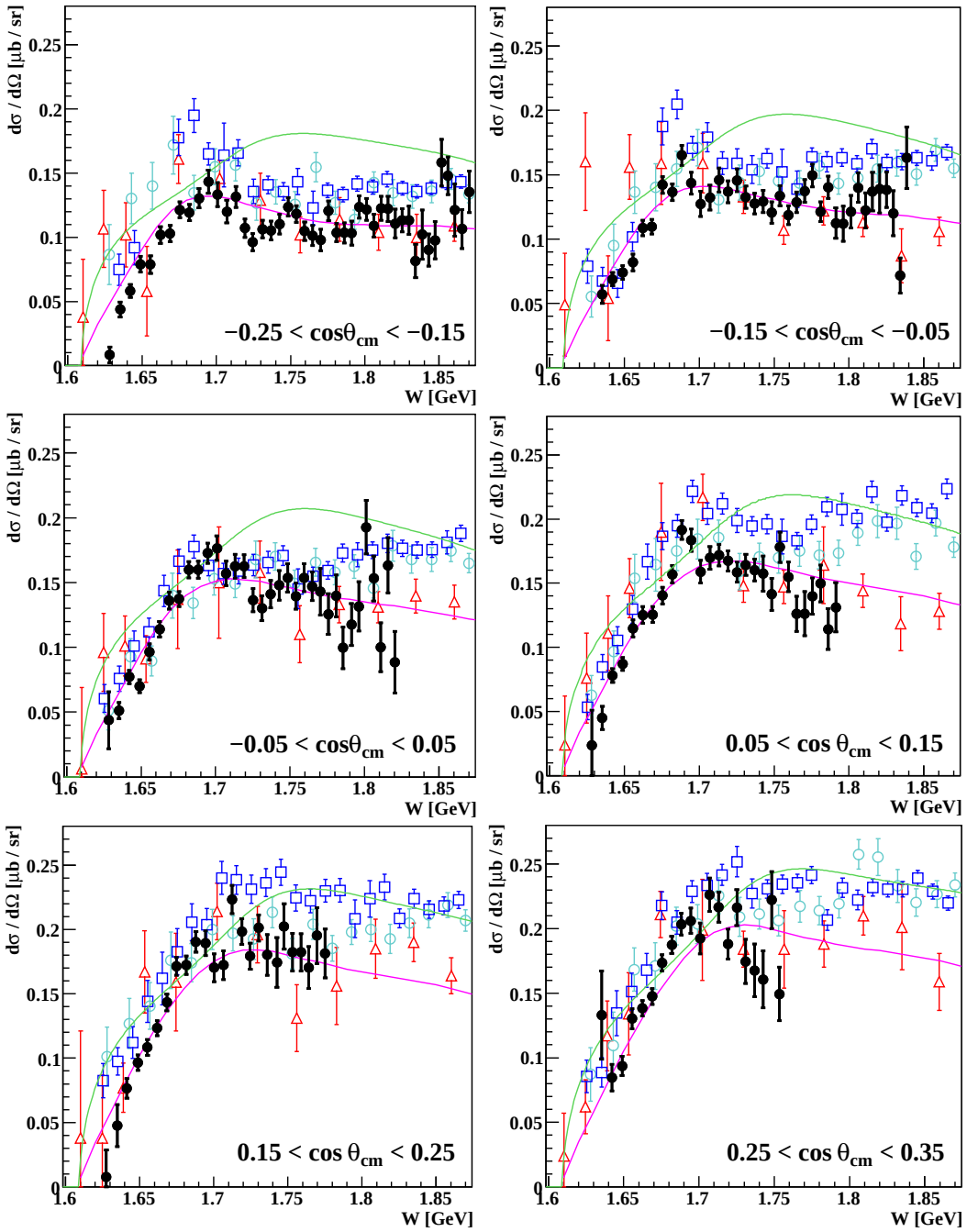

Figure 8.5: Differential cross sections versus centre of mass energy, W. This data (black, filled circles, error bars correspond to the statistical error only), SAPHIR [46] (red, open triangles), CLAS [51] (light blue, open circles) and [54] (dark blue, open squares), Kaon-MAID [41] (magenta line), and a Regge-Plus-Resonance (RPR) parameterisation [87, 124] (green line). The SAPHIR angle range is backwards by $\cos\theta_{cm} = -0.05$ for each interval.

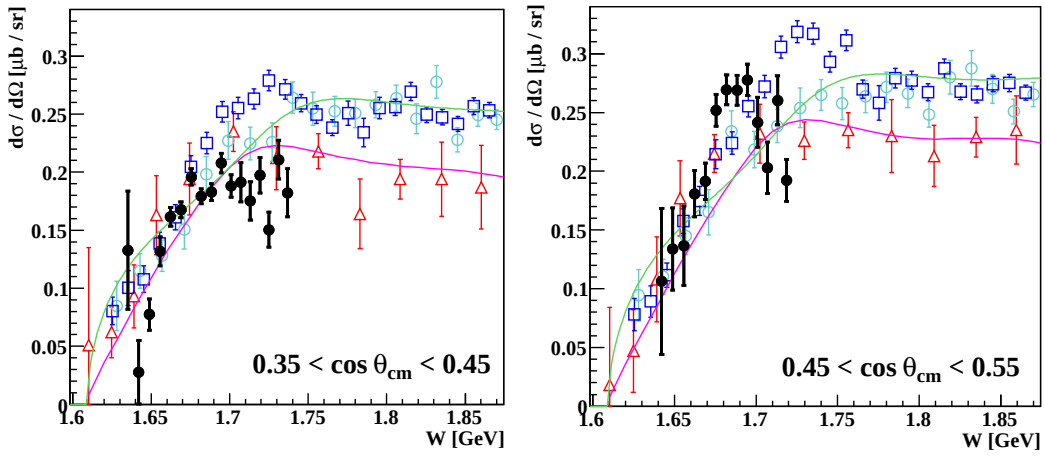

Figure 8.6: Differential cross sections versus centre of mass energy, W. This data (black, filled circles, error bars correspond to the statistical error only), SAPHIR [46] (red, open triangles), CLAS [51] (light blue, open circles) and [54] (dark blue, open squares), Kaon-MAID [41] (magenta line), and a Regge-Plus-Resonance (RPR) parameterisation [87, 124] (green line). The SAPHIR angle range is backwards by $\cos\theta_{cm} = -0.05$ for each interval.

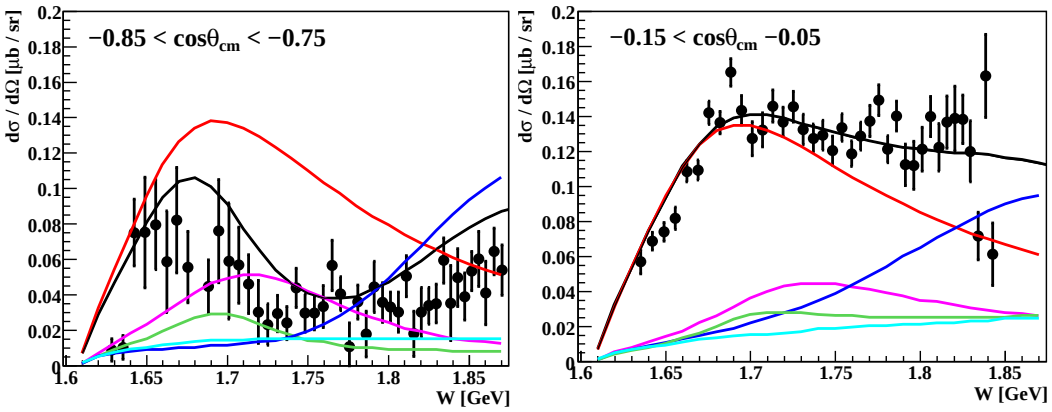

Figure 8.7: Kaon-MAID [41] resonance contributions for two $\cos\theta_{cm}$ intervals (inset). Coloured legend explains the contribution from each resonance. The background terms are the Born terms and the $K^*(893)$ and $K_1(1270)$ meson resonances.

new data set, however the calculation is constrained by the SAPHIR data with comparatively large statistical error. This new data set will therefore provide an important new constraint on partial wave analysis near threshold.

Above invariant mass energies of 1.7 GeV, this data is consistent with the previous data sets and the Kaon-MAID prediction.

8.4 A search for narrow resonances

Fig. 8.12 shows differential cross sections for the large polar angle range: $-0.65 < \theta_{cm} < 0.05$. This is a similar range used when the narrow peak was observed in η photoproduction off the neutron [97] (section 3.4), and rejects data at the extremities of the kinematic acceptance where the statistics are poor. Cross section measurements are plotted for both of the data sets as well as the weighted average.

This is the first cross section measurement of $\gamma(p, K^+)\Lambda$ at an energy resolution of approximately 4 MeV and sets the first constraint on theories of narrow resonance structure in this channnel (for example reference [93] in section 3.4). There does not appear to be any structure as striking as the peak which was observed in η photoproduction between 1650-1700 GeV. This indicates that if such a state exists, its $K\Lambda$ decay branch or the electromagnetic coupling to the proton is too small to give significant effects in the cross section.

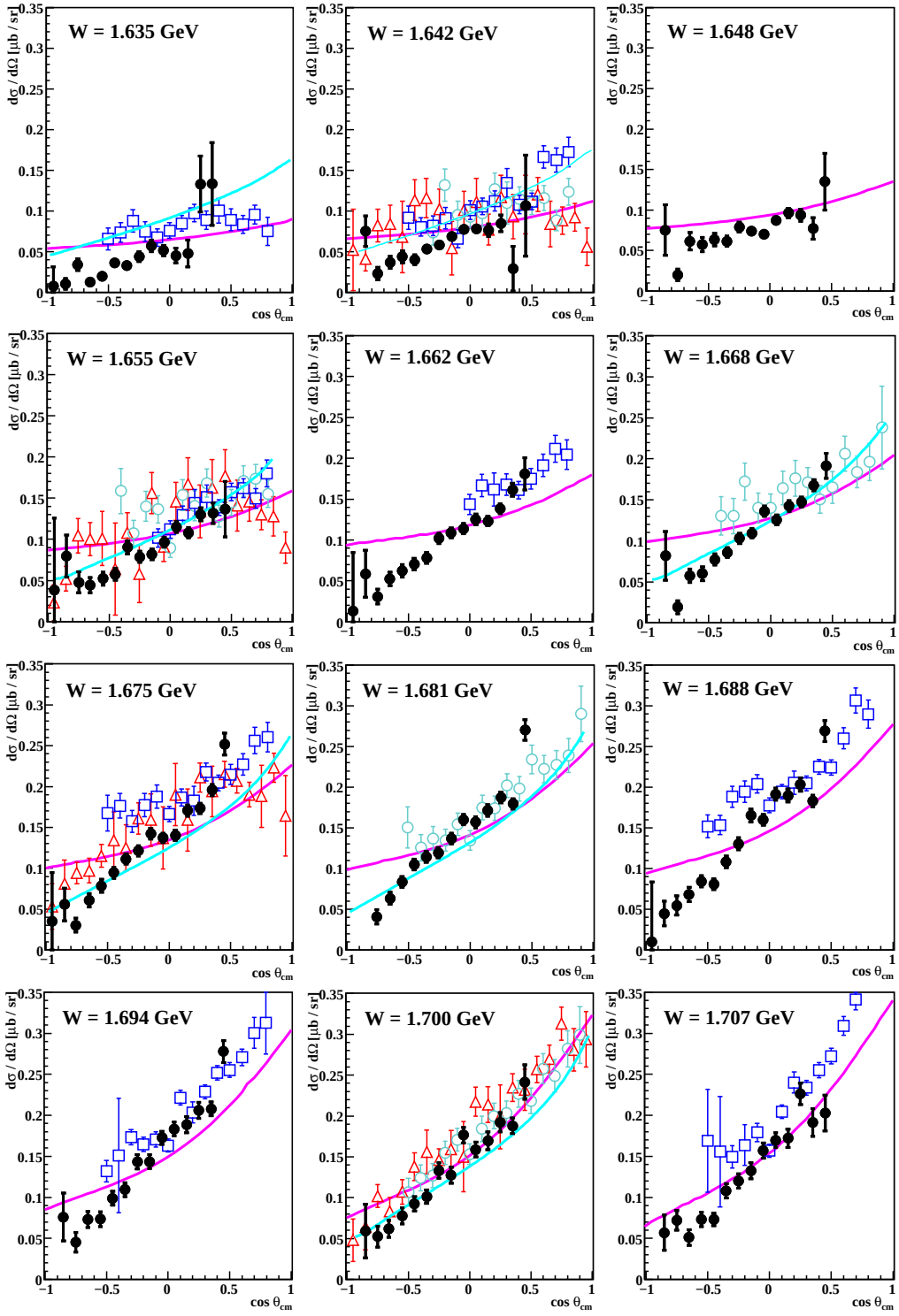

Figure 8.8: Differential cross sections versus $\cos\theta_{cm}$. This data (black, filled circles, error bars correspond to the statistical error only), SAPHIR [46] (red, open triangles), CLAS [51] (light blue, open circles) and [54] (dark blue, open squares), Kaon-MAID [41] (magenta line), and a gauge invariant chiral unitary parameterisation [38] (cyan line).

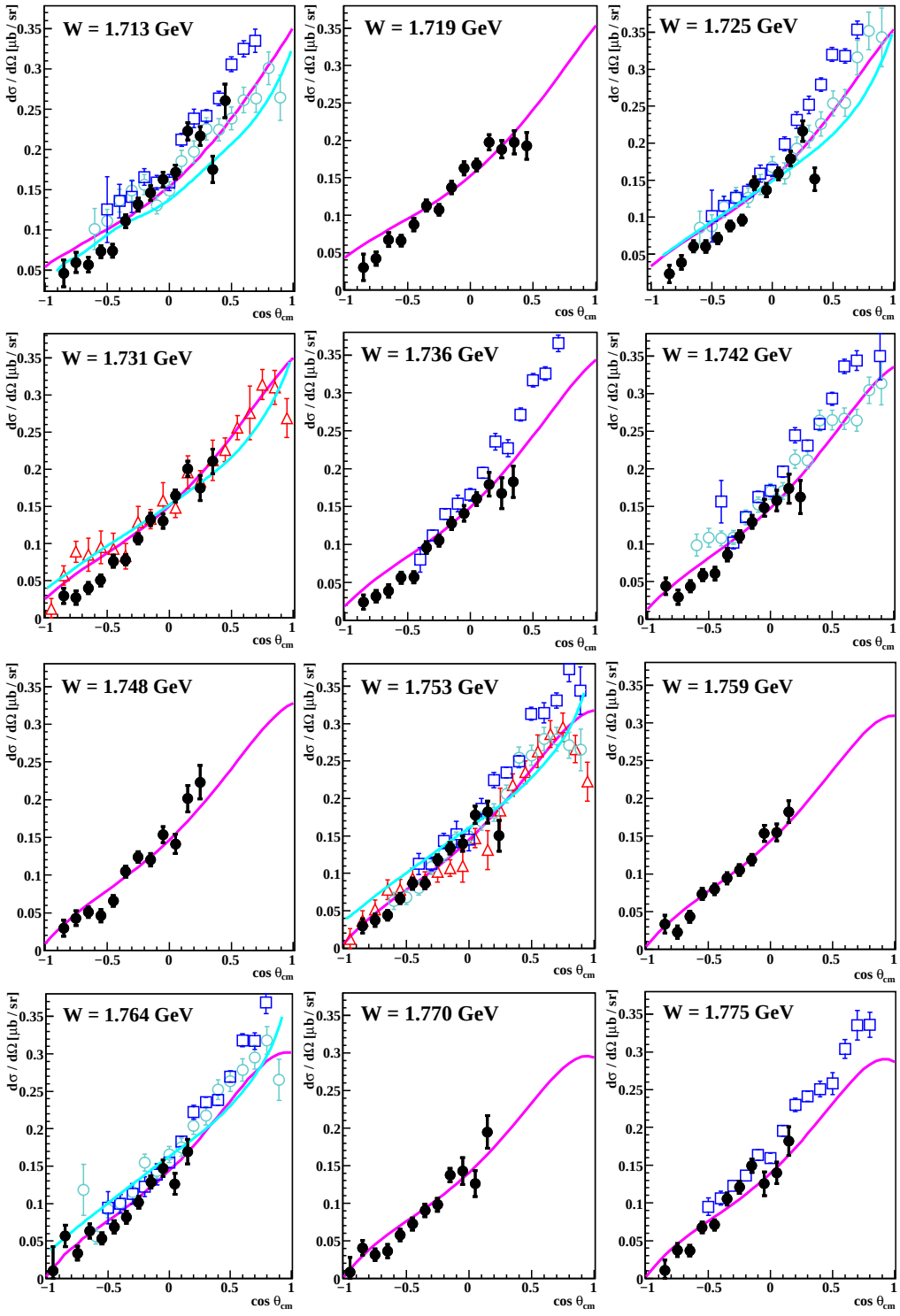

Figure 8.9: Differential cross sections versus $\cos\theta_{cm}$. This data (black, filled circles, error bars correspond to the statistical error only), SAPHIR [46] (red, open triangles), CLAS [51] (light blue, open circles) and [54] (dark blue, open squares), Kaon-MAID [41] (magenta line), and a gauge invariant chiral unitary parameterisation [38] (cyan line).

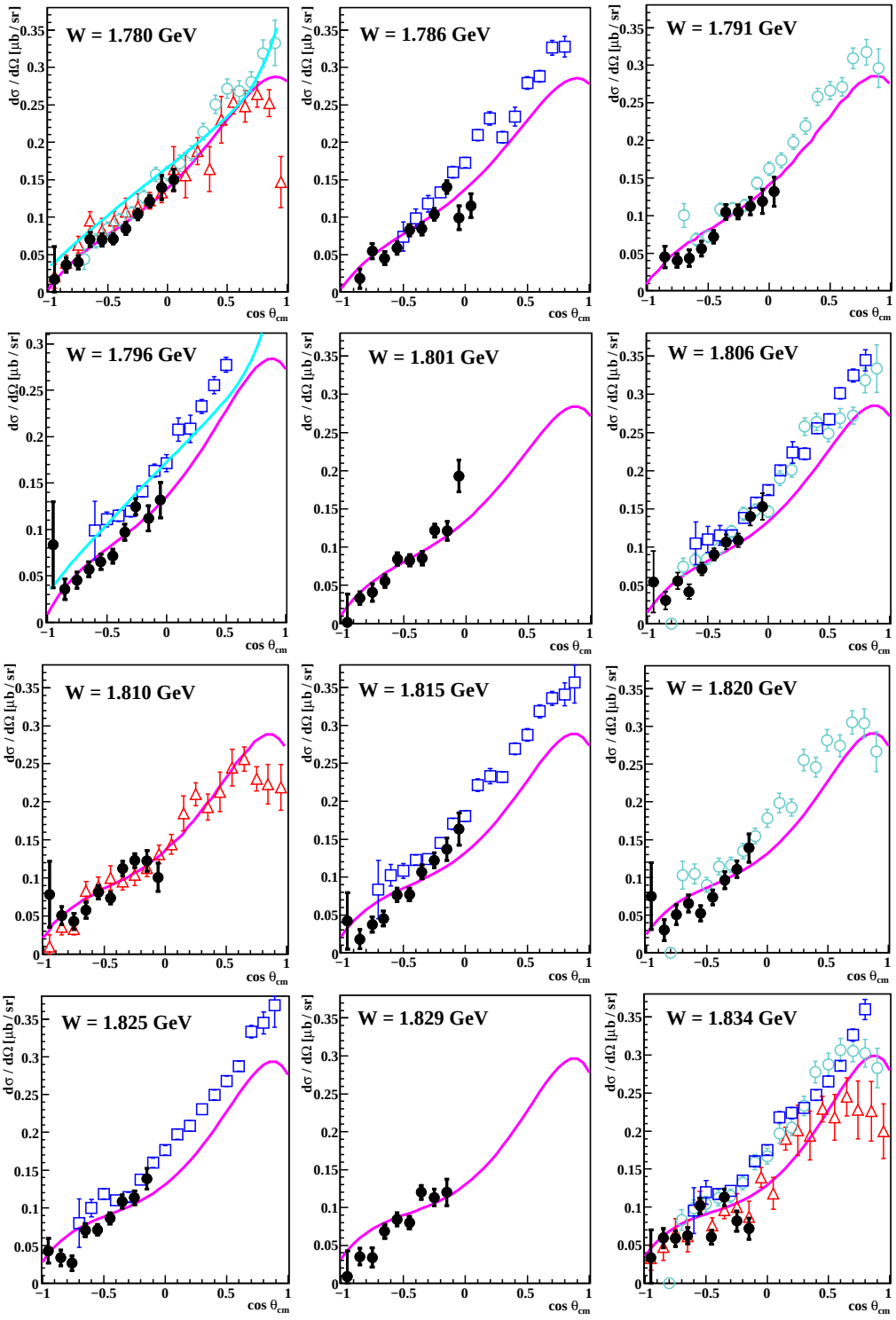

Figure 8.10: Differential cross sections versus $\cos\theta_{cm}$. This data (black, filled circles, error bars correspond to the statistical error only), SAPHIR [46] (red, open triangles), CLAS [51] (light blue, open circles) and [54] (dark blue, open squares), Kaon-MAID [41] (magenta line), and a gauge invariant chiral unitary parameterisation [38] (cyan line).

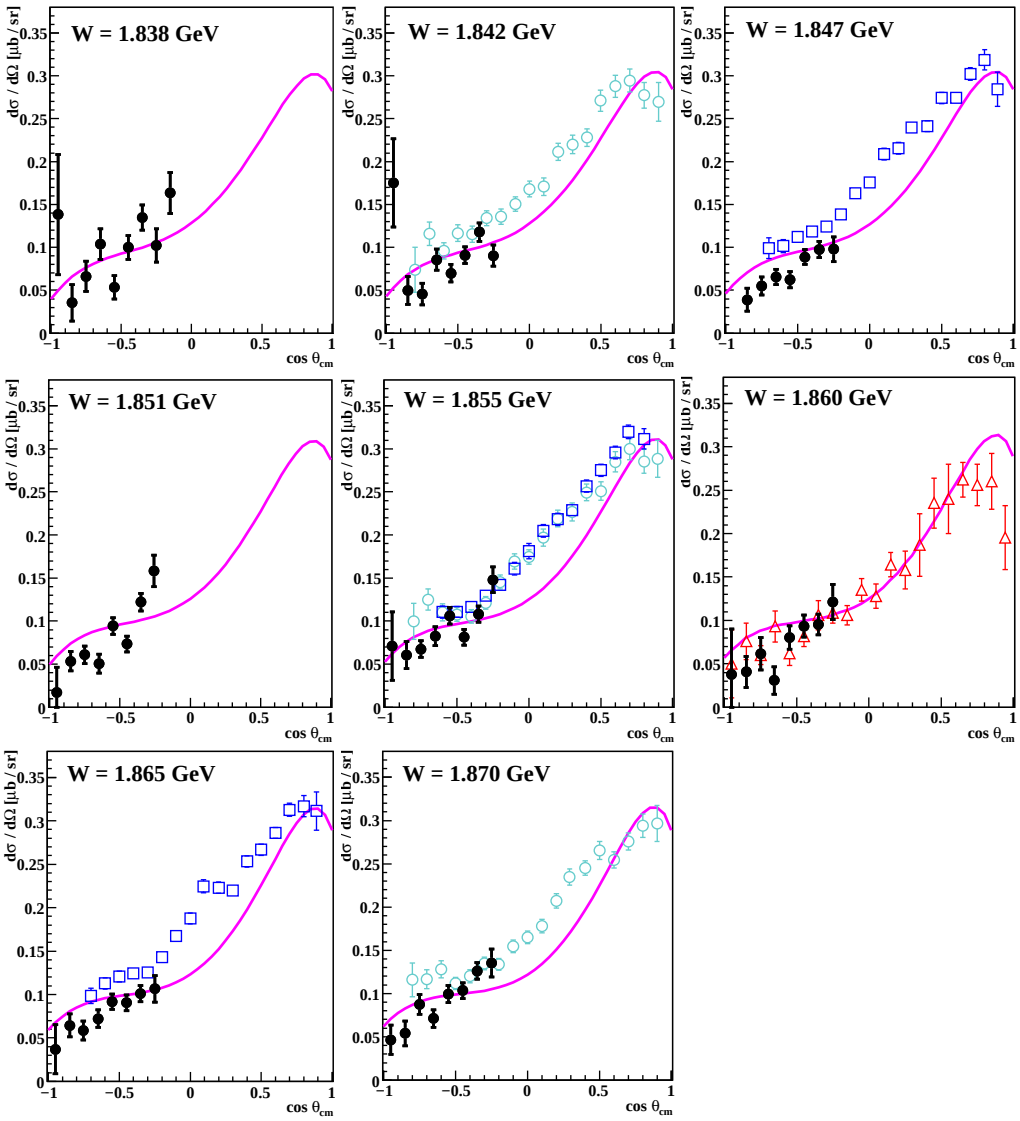

Figure 8.11: Differential cross sections versus $\cos\theta_{cm}$. This data (black, filled circles, error bars correspond to the statistical error only), SAPHIR [46] (red, open triangles), CLAS [51] (light blue, open circles) and [54] (dark blue, open squares), and Kaon-MAID [41] (magenta line).

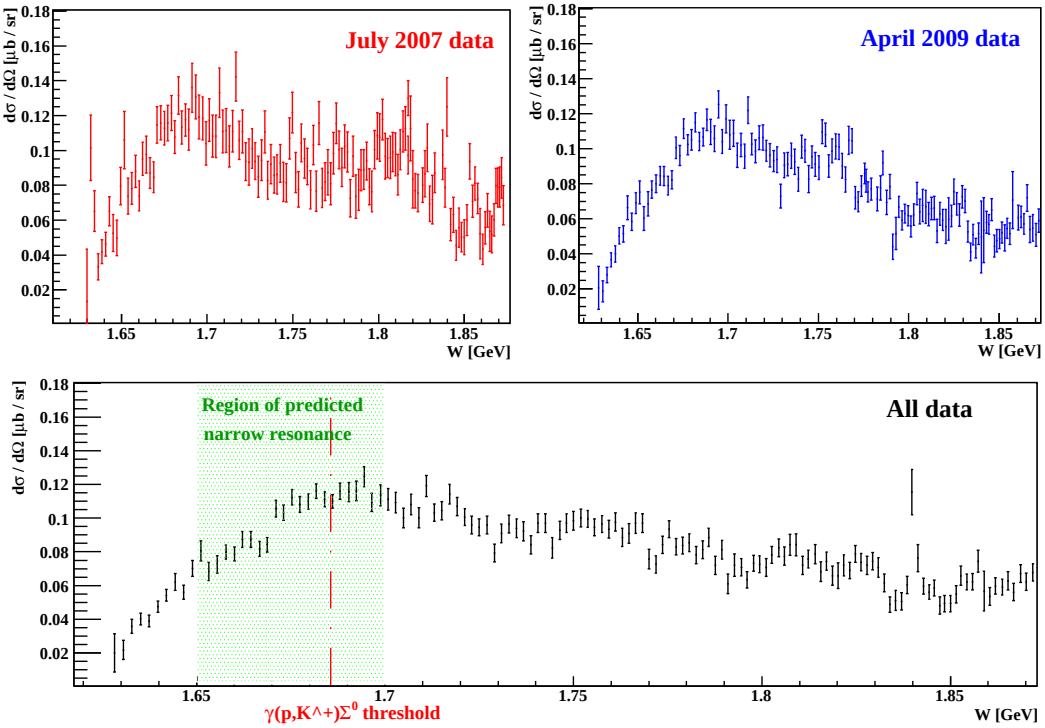

Figure 8.12: $\gamma(p, K^+)\Lambda$ differential cross sections for the polar angle range $-0.65 < \cos\theta_{cm} < 0.05$. Top panel: July 2007 and April 2009 data sets, bottom panel: weighted average of both data sets. The threshold energy for $K^+\Sigma^0$ photoproduction is indicated with a dotted red line and the region of the proposed narrow resonance is shaded in green. Error bars correspond to the statistical error only.

Chapter 9

Conclusions and outlook

This thesis presents $\gamma(p, K^+)\Lambda$ differential cross sections from threshold to a photon beam energy of 1.4 GeV, measured using the Crystal Ball detector at MAMI-C.

The analysis pioneered a new method of K^+ detection, in which the K^+ was identified by its weak decay signatures within the crystals of a segmented calorimeter. The new technique proved excellent at isolating K^+ mesons, and created an opportunity to measure properties of strangeness photoproduction channels with the Crystal Ball. Comparison of simulated and calibrated experimental data demonstrated that the method was described well in Geant4.

Novel methods to separate the different strangeness photoproduction channels were also investigated and developed. The identification of the Σ^0 decay photon enabled a new method to separate $\gamma(p, K^+)\Lambda$ and $\gamma(p, K^+)\Sigma^0$. The method took advantage of the large angular coverage and excellent energy resolution for detected photons in the Crystal Ball; features which were not available with detectors used in previous measurements.

The intense photon beam with the Crystal Ball at MAMI-C provided high statistics for $\gamma(p, K^+)\Lambda$ differential cross section measurements. The addition of this data set to the existing world data provides valuable new constraints to theoretical models of the process. Improvements in the data near the reaction threshold will challenge effective Lagrangians based upon the chiral symmetry of QCD (for example, the model of Borasoy *et al.* [38]). The new data is in better agreement with these models than previous data sets.

Models which implicitly include the nucleon resonance structure, such as isobar, and resonance-plus-Regge models have been limited by the range, accuracy and inconsistency of the world data set. The Crystal Ball measurement provides new data in these discrepant regions, with particularly high statistics at backward K^+ centre of mass polar angles. This region is particularly important to constrain contributions from meson and hyperon resonances. The RPR model of Corthals *et al.* [87, 124] is already planned to be revised and extended to backward angles where this new data set will provide an important constraint [125].

The new data will be an important component of the current world programme for a "complete measurement" of observables in the $\gamma(p, K^+)\Lambda$ reaction. This aims to achieve an almost model independent partial wave extraction of the four basic reaction amplitudes, and is a high profile programme at all major photon beam laboratories (Jefferson Lab, ELSA, GRAAL, SPring8 and MAMI). Achieving such an aim will elucidate the resonance structure and resolve current ambiguities, such as the existence of "missing" nucleon resonances, for example the D_{13} with a mass of approximately 1900 MeV. The addition of this new data set is an important advance to address serious discrepancies in previous data sets and is one step closer to completing this global programme of experiments. The new data set broadly agrees with the current Kaon-MAID [41] solution over most of the kinematic range although the present solution is higher than our data near threshold at backward angles. A new partial wave analysis will be carried out using this new data set in the coming months [122].

This data set is the first to extract $\gamma(p, K^+)\Lambda$ differential cross sections at an incident photon energy resolution as high as 4 MeV (previous measurements were of the order of 20 MeV). This is an important new constraint on predictions of narrow resonances (the soliton model reference [96] for example) which are predicted to couple to $K\Lambda$. No strong signals of such states were observed.

Now established, the K^+ detection technique can be further refined in future work. An immediate extension is to recover the high energy K^+ which may punch through the NaI crystals of the Crystal Ball. This will involve detailed tests of the simulation of the material on the outside of the Crystal Ball. It is judged that this will provide differential cross section measurements at higher energies at forward angles, where discrepancies in the world data set are even more marked.

Preliminary investigations into extracting $\gamma(p, K^+)\Sigma^0$ differential cross section measurements have been carried out and the procedure looks feasible. The identification of this channel using the Σ^0 decay photon will suppress background contributions from other reaction channels even more than that of $K^+\Lambda$.

Beam-recoil polarisation observables, C_X and C_Z can also be extracted infuture work. (section 3.2). First measurements of these have recently been obtained using the CLAS detector [63] and led to the surprising result of almost complete transfer of polarisation to the Λ over all measured kinematic ranges. Future work with the Crystal Ball can confirm this observation and extend the measurements down to threshold. The polarisation of the Λ can be extracted from both possible decays ($\Lambda \rightarrow p\pi^-$ and $\Lambda \rightarrow n\pi^0$), whereas the CLAS measurement was limited to $\Lambda \rightarrow p\pi^-$.

The new technique of K^+ identification has application with other segmented calorimeters where K^+ identification using magnetic fields or drift chambers is not feasible. It is already planned to use the technique with the BGO-open dipole experiment which is being constructed at the ELSA accelerator in Bonn [126].

Appendix A

Addition of cross section data with different binning

The width of each energy bin, E_γ corresponded to the photon energy range each focal plane element in the Photon Tagger was associated with. This varied from approximately 2-4 MeV. As the electron beam energy was different between the July 2007 and April 2009 data sets, the calibration of the Photon Tagger was different, and so the energy binning was not the same. To combine the cross section data from both data sets, the cross sections from each data set had to calculated independently due to the different detector calibrations. The E_γ intervals for the July 2007 were then changed to the intervals of the April 2009 cross section measurements. The combined cross sections were the statistical error weighted mean of both data sets.

This appendix decribes the method of rebinning and calculating the new statistical errors for the July 2007 data set. It should be stressed that the rebinning is different to rebinning a histogram of a yield. For example, doubling the width of two equal width cross section bins would give a bin with a height of the mean of the two previous bins, whereas the equivalent procedure for the yield of K^+ would give the height as the sum total of the previous two bins.

Fig. A.1 depicts an example of two sets of bins from two different histograms.

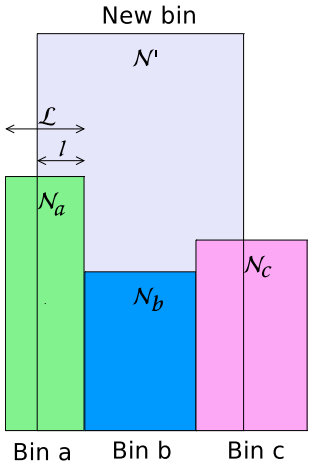

Figure A.1: Three bins (a,b and c) with bin content N_a, N_b and N_c. A new histogram has a bin with content N'.

For each of the bins in the new histogram, some or all of the contents of the old bins needs to be included. The old histogram bin, a overlaps the new bin by a width ℓ. The fraction of bin a which overlaps is therefore: $\delta_a = \frac{\ell}{L}$. The contents of the new bin, N' should therefore contain a δ_a fraction of the contents of bin a. The total contents of the new bin, N_T, from the overlapping bins a, b and c is therefore given as:

$$N_T = \delta_a N_a + \delta_b N_b + \delta_c N_c \tag{A.1}$$

It is clear that bin b is completely contained within the new bin and so δ_b will be unity.

The contents of the new bin has to be scaled according to the amount of old bins which were included. For example, if exactly three bins have been included, the new bin content has to be scaled by 1/3 to account for the different bin widths. In the example in fig. A.1, the number of bins overlapping is: $\delta_a + \delta_b + \delta_c$.

Generally, the contents of a bin in the new histogram is given as:

$$N' = \frac{N_T}{\sum_i \delta_i} = \frac{\sum_i N_i \delta_i}{\sum_i \delta_i} \tag{A.2}$$

where i is summed over all of the bins in the old histogram.

The satistical error of bins a, b, and c are ΔN_a, ΔN_b, and ΔN_c respectively. The error of the contents of bin a which is included in the new bin is $\sqrt{\delta_a}\Delta N_a$. The total error in the new bin is therefore:

$$\Delta N' = \sqrt{\delta_a \Delta N_a^2 + \delta_b \Delta N_b^2 + \delta_c \Delta N_c^2} \tag{A.3}$$

Scaling this according to the number of old bins into the new bin gives:

$$\Delta N' = \frac{\sqrt{\sum_i \delta_i \Delta N_i^2}}{\sum_i \delta_i} \tag{A.4}$$

where i is summed over all of the bins in the old histogram.

It is necessary to justify why the error of the contents of bin a included in the new bin is $\sqrt{\delta_a}\Delta N_a$ and not $\delta_a \Delta N_a$. Consider a cross section which is uniform and has a value of $C \pm \sqrt{C}$ for all energies and angles. The measurement of the cross section was performed over uniform energy intervals, with each data point measuring over 4 MeV for example. Now imagine shifting these data points so that each one covered an energy range 2 MeV greater than previously. It would be expected for the content and error for each data point to be the same as the previous data point. The contents and error of these shifted measurements can be calculated using eq. A.2 and A.4. Each new shifted bin contains half of two old bins. The new contents is then given as:

$$N' = \frac{\sum_i N_i \delta_i}{\sum_i \delta_i} = \frac{0.5C + 0.5C}{0.5 + 0.5} = C \tag{A.5}$$

The error of the new shifted bin is then given as:

$$\Delta N' = \frac{\sqrt{\sum_i \delta_i \Delta N_i^2}}{\sum_i \delta_i} = \frac{\sqrt{0.5C + 0.5C}}{0.5 + 0.5} = \sqrt{C} \tag{A.6}$$

If the error included in the new bin was given as $\delta_a \Delta N_a$ instead of $\sqrt{\delta_a}\Delta N_a$, making the necessary adjustments to the above equation yields an error for each new bin of approximately $0.7\sqrt{C}$, so that the shifting of the data points would reduce the error by approximately 30%. Furthermore, the error would change according the extent of the shift of the new data points to the old. If the data points were shifted forward by one third of the width of each point, the new error

would be calculated as approximately $0.75\sqrt{C}$. This change in the extracted error clearly demonstrates that this is not a valid method of error propagation in these circumstances.

References

[1] M. Gell-Mann and Y. Neeman. *The Eightfold way.* Benjamin, 1984.

[2] W. Heisenberg. Uber den Bau der Atomkerne. *Zeitschrift fr Physik*, 77:1–11, 1932.

[3] J. Steinberger. *Learning about particles - 50 priviledged years.* Springer-Berin-Heidelberg, 2005.

[4] A. Pais. Some remarks on the V particles. *Phys. Rev.*, 86:663, 1952.

[5] T. D. Lee and C. N. Yang. Question of Parity in Weak Interactions. *Phys. Rev.*, 104:254, 1956.

[6] V. E. Barnes et al. Observation of a Hyperon with Strangeness Number Three. *Phys. Rev. Lett.*, 12:204, 1964.

[7] K. G. Wilson. Confinement of Quarks. *Phys. Rev. D*, 10:2445, 1974.

[8] M. Creutz, L. Jacobs and C. Rebbi. Monte Carlo study of Abelian lattice gauge theories. *Phys. Rev. D*, 20, 1979.

[9] S. Durr, *et al.* Ab Initio Determination of Light Hadron Masses. *Science*, 322:1224–1227, 2008.

[10] J. W. Negele C. Alexandrou, G. Koutsou and A. Tsapalis. Nucleon electromagnetic form factors from lattice QCD. *Phys. Rev. D*, 74:034508, 2006.

[11] S. Basak, *et al.* Group-theoretical construction of extended baryon operators in lattice qcd. *Phys. Rev. D*, 72:094506, 2005.

[12] J. F. Donoghue. Chiral symmetry as an experimental science. *CERN-TH-5667-90*, 1990.

[13] V. Bernard and U. G. Meissner. Chiral perturbation theory. *arXiv:hep-ph/0611231v1*, 2006.

[14] S. Weinberg. Phenomenological Lagrangians. *Physica. A*, 96:327, 1979.

[15] S. Adler and R. Dashen. *Current Algebras and Applications to Particle Physics*. Benjamin, 1968.

[16] N. Bianchi *et al.* Total hadronic photoabsorption cross section on nuclei in the nucleon resonance region. *Phys. Rev. C*, 54:1688–1699, 1996.

[17] C. Amsler *et al.* [Particle Data Group]. Review of Particle Physics. *Phys. Lett. B*, 667:1, 2008.

[18] E. Klempt. Baryon Spectroscopy. *arXiv:0901.2055v2*, 2009.

[19] D. Faiman and A. W. Hendry. Harmonic-oscillator model for baryons. *Phys. Rev*, 173:1720–1729, 1968.

[20] R. Koniuk and N. Isgur. Baryon decays in a quark model with chromodynamics. *Phys. Rev. D*, 21:1868–1886, 1980.

[21] L. Ya. Glozman and D. O. Riska. The spectrum of the nucleons and the strange hyperons and chiral dynamics. *Phys. Rept.*, 268:263–303, 1995.

[22] S. Theberge and A. W. Thomas. Pionic corrections to the MIT bag model: The (3,3) resonance. *Phys. Rev. D*, 22:2838–2852, 1980.

[23] S. Capstick and R. Roberts. Quark models of baryon masses and decays. *Prog. Part. Nucl. Phys.*, 45:s241–s331, 2000.

[24] T. H. R. Skyrme. A Unified Field Theory of Mesons and Baryons. *Nucl. Phys.*, 556:31, 1962.

[25] E. Guadaginini. Baryons as solitons and mass formulae. *Nucl. Phys. B*, 236:35, 1984.

[26] M. Anselmino, *et al.* Diquarks. *Rev. Mod. Phys*, 65:1199–1233, 1993.

[27] E. Santopinto. Interacting quark-diquark model of baryons. *Phys. Rev. C*, 72:022201, 2005.

[28] D. B. Leinweber. Do quarks really form diquark clusters in the nucleon? *Phys. Rev. D*, 47:5096–5103, 1993.

[29] C. P. Forsyth. Evidence against diquarks from baryon resonance decays. *Nucl. Phys. B*, 178:35–44, 1981.

[30] S. Capstick and W. Roberts. Strange decays of nonstrange baryons. *Phys. Rev. D*, 58:074011, 1998.

[31] S. Capstick and W. Roberts. Quasi-two-body decays of nonstrange baryons. *Phys. Rev. D*, 49:4570–4586, 1994.

[32] Bjorken and Drell. *Relativistic Quantum Mechanics.* McGraw-Hill, New York, first edition edition, 1964.

[33] G. F. Chew, M. L. Goldberger, F. E. Low and Y. Nambu. Relativistic dispersion relation approach to photomeson production. *Phys. Rev.*, 106:1345–1355, 1957.

[34] K. M. Watson. The hypothesis of charge independence for nuclear phenomena. *Phys. Rev.*, 85:852–857, 1952.

[35] I. S. Barker and A. Donnachie. Complete experiments in pseuodoscalar photoproduction. *Nuc. Phys. B*, 95:347–356, 1975.

[36] T. Mart and C. Bennhold. Evidence for a missing nucleon resonance in kaon photoproduction. *Phys. Rev. C*, 61:012201, 1999.

[37] B. Julia-Diaz, B. Saghai, T. S. H. Lee and F. Tabakin. Dynamical coupled-channels approach to hadronic and electromagnetic kaon-hyperon production on the proton. *Phys. Rev. C*, 73:055204, 2006.

[38] B. Borasoy, P. C. Bruns, U. G. Meissner and R. Nissler. A gauge invariant chiral unitary framework for the kaon photo- and electroproduction on the proton. *Eur. Phys. J. A*, 34:161–183, 2007.

[39] Close, Donnachie and Shaw. *Electromagnetic Interactions and Hadronic Structure*. Cambridge University Press, Cambridge, UK, first edition edition, 2007.

[40] F. X. Lee, T. Mart, C. Bennhold, H. Haberzettl and L. E. Wright. Quaifree kaon photoproduction on the nuclei. *Nucl. Phys. A*, 695:237–272, 2001.

[41] T. Mart, C. Bennhold, H. Haberzettl and L. Tiator. An effective Lagrangian Model for Kaon Photo- and Electroproduction on the Nucleon. *wwwkph.kph.uni-mainz.de/MAID//kaon/*, 2010.

[42] R. A. Arndt, W. J. Briscoe, I. I. Strakovsky and R. L. Workman. Extended partial-wave analysis of π N scattering data. *Phys. Rev. C*, 74:045205, 2006.

[43] R. A. Arndt, R. L. Workman, Z. Li and D. L. Roper. Partial-wave analysis of pion photoproduction. *Phys. Rev. C*, 42:1853–1863, 1990.

[44] R. A. Arndt, W. J. Briscoe, I. I. Strakovsky and R. L. Workman. SAID Partial-Wave Analysis Facility. *gwdac.phys.gwu.edu*, 2010.

[45] R. A. Adelseck and B. Saghai. Kaon photoproduction: Data consistency, coupling constants and polarization observables. *Phys. Rev. C*, 42:180, 1990.

[46] K. H. Glander, *et al.* Measurement of $\gamma p \rightarrow K^+\Lambda$ and $\gamma p \rightarrow K^+\Sigma^0$ at photon energies up to 2.6 GeV. *Eur. Phys. J. A*, 19:251–273, 2004.

[47] D. Husmann and W. D. Schwille. *Phys. B1.*, 44:40, 1988.

[48] W. J. Schwille *et. al.* Design and construction of the SAPHIR detector. *Nucl. Instrum. Methods A*, 344:470–486, 1994.

[49] Glenn F. Knoll. *Radiation Detection and Measurement*. John Wiley Sons, NewYork, second edition, 1989.

[50] W. R. Leo. *Techniques for Nuclear and Particle Physics Experiments.* Springer-Verlag, Berlin, second revised edition, 1994.

[51] R. Bradford, R. A. Schumacher, *et. al.* [CLAS Collaboration]. Differential cross sections for $\gamma + p \rightarrow K^+ + Y$ for Λ and Σ^0 hyperons. *Phys. Rev. C*, 73:035202, 2006.

[52] B. A. Mecking, *et. al.* [CLAS Collaboration]. The CEBAF large acceptance spectrometer (CLAS). *Nucl. Instrum. Methods A*, 503:513, 2003.

[53] R. A. Arndt and W. J. Briscoe and I. I. Strakovsky and R. L. Workman. Analysis of pion photoproduction data. *Phys. Rev. C*, 66:055213, 2002.

[54] M. E. McCracken. Differential cross section and recoil polarization measurements for the $\gamma p \rightarrow K^+\Lambda$ reaction using CLAS at Jefferson Lab. *Phys. Rev. C*, 81:025201, 2010.

[55] M. Q. Tran *et al.* Measurement of $\gamma p \rightarrow K^+\Lambda$ and $\gamma p \rightarrow K^+\Sigma^0$ at photon energies up to 2 GeV. *Phys. Rev. Lett. B*, 445:20–26, 1998.

[56] M. Guidal, J. M. Laget, and M. Vanderhaeghen. Pion and kaon photoproduction at high energies: forward and intermediate angles. *Nucl. Phys. A*, 627:645–678, 1997.

[57] M. Guidal, J. M. Laget, and M. Vanderhaeghen. Electroproduction of strangeness above the resonance region. *Phys. Rev. C*, 61:025204, 2000.

[58] J. C. David, C. Fayard, G. H. Lamot and B. Saghai. Electromagnetic production of associated strangeness. *Phys. Rev. C*, 53:2613–2637, 1995.

[59] M. Sumihama *et. al.* [LEPS Collaboration]. The $\overline{\gamma}p \rightarrow K^+\Lambda$ and $\overline{\gamma}p \rightarrow K^+\Sigma^0$ reactions at forward angles with photon energies from 1.5 to 2.4 GeV. *Phys. Rev. C*, 73:035214, 2006.

[60] O. Bartalini, *et al.* Measurement of π^0 photoproduction on the proton from 550 to 1500 GeV. *Eur. Phys. J. A*, 26:399, 2005.

[61] A. Lleres, *et al.* Polarization observable measurement for $\gamma p \rightarrow K^+\Lambda$. *Eur. Phys. J. A*, 31:79–93, 2007.

[62] D. I. Glazier. Recoil Polarisation Measurements in Meson Photoproduction. *International workshop on partial wave analysis, Bad Honnef, Germany*, 2009.

[63] R. Bradford *et. al.* [CLAS Collaboration]. First measurement of beam-recoil observables C_X and C_Z in hyperon photoproduction. *Phys. Rev. C*, 75:035205, 2007.

[64] A. V. Saranstev, V. A. Nikonov, A. V. Anisovich, E. Klempt and U. Thoma. Decays of baryon resonances into ΛK^+, $\Sigma^0 K^+$, and $\Sigma^+ K^0$. *Eur. Phys. J. A*, 25:441–453, 2005.

[65] R. Schumacher. Polarization in hyperon photo- and electro-production. *Eur. Phys. J. A*, 35:299–305, 2008.

[66] C. A. Paterson, The University of Glasgow. PhD thesis, 2008.

[67] T. Mart and A. Sulaksono. Kaon photoproduction in a multipole approach. *Phys. Rev. C*, 74:055203, 2006.

[68] T. Mart and A. Sulaksono. Multipole approach for photo- and electro-production of kaons. *Proceedings of the IX international conference on hypernuclear and strange particle physics*, pages 345–348, 2007.

[69] R. Nelson and T. Mart. Kaon photoproduction on the nucleon with constrained parameters. *Mod. Phys. Lett. A*, 24:964–967, 2009.

[70] H. Thom. Phenomenological analysis of $K^+\Lambda$ photoproduction. *Phys. Rev.*, 151:1322, 1966.

[71] T. Feuster and U. Mosel. Unitary model for meson-nucleon scattering. *Phys. Rev. C*, 58:457, 1998.

[72] B. Saghai. From known to undiscovered resonances. *arXiv:nucl-th/0105001v1*, 2001.

[73] S. Janssen *et al.* Kaon photoproduction: Background contributions, form factors, and missing resonances. *Phys. Rev. C*, 65:015201, 2001.

[74] W. T. Chiang and F. Tabakin. Coupled-channel study of $\gamma p \to K^+\Lambda$. *arXiv:nucl-th/0104052v2*, 2001.

[75] R. A. Williams, C. R. Ji and S. R. Cotanch. Hyperon electroproduction in a crossing and duality constrained model. *Phys. Rev. C*, 46:1617–1635, 1992.

[76] R. A. Arndt, I. I. Strakosky, R. L. Workman and M. M. Pavan. Updated analysis of πN elastic scattering data to 2.1 GeV: The baryon spectrum. *Phys. Rev. C*, 52:2120–2130, 1995.

[77] R. A. Arndt, I. I. Strakovsky and R. L. Workman. Updated resonance photodecay amplitudes to 2 GeV. *Phys. Rev. C*, 53:430, 1996.

[78] A. Usov and O. Scholten. $K\Lambda$ and $K\Sigma$ photoproduction in a coupled-channels framework. *Phys. Rev. C*, 72:025205, 2005.

[79] J. W. C. McNabb *et al.* Hyperon photoproduction in the nucleon resonance region. *Phys. Rev. C*, 69:042201, 2004.

[80] Z. Li and B. Saghai. *Nucl. Phys. A*, 644:345, 1998.

[81] B. Saghai and Z. Li. *Eur. Phys. J. A*, 11:217, 2001.

[82] K. Hagiwara *et al.* Particle Data Group. *Phys. Rev. D*, 66:010001, 2002.

[83] E. E. Salpeter and H. A. Bethe. A relativistic equation for bound state problems. *Phys. Rev.*, 84:1232–1242, 1951.

[84] T. Regge. *Il Nuovo Cimento*, 14:951, 1959.

[85] V. N. Gribov and I. Ya. Pomeranchuk. Regge poles and Landau singularities. *Phys. Rev. Lett.*, 9:238–242, 1962.

[86] Donnachie, Dosch, Landshoff, Nachtman. *Pomeron Physics and QCD.* Cambridge University Press, Cambridge, UK, first edition, 2002.

[87] T. Corthals, J. Ryckebush and T. Van Cauteren. Forward-angle $K^+\Lambda$ photoproduction in a Regge-plus-resonance approach. *Phys. Rev. C*, 73:045207, 2006.

[88] S. D. Drell and A. C. Hearn. Exact sum rule for nucleon magnetic moments. *Phys. Rev. Lett.*, 16:908–911, 1966.

[89] D. Drechsel, S. S. Kamalov and L. Tiator. Gerasimov-Drell-Hearn sum rule and related integrals. *Phys. Rev. D*, 63:114010, 2001.

[90] T. Mart. Kaon contributions to the Gerasimov-Drell-Hearn integrals on the proton. *Int. J. Mod. Phys.*, 23:599–612, 2008.

[91] T. Mart. Gerasimov-Drell-Hearn Sum Rule and the Discrepancy between the New ClAS asnd SAPHIR Data. *Few-Body Systems*, 42:125–138, 2008.

[92] F. Close. Vanishing pentaquarks. *Nature*, 435:287, 2005.

[93] V. Kuznetsov and M.V. Polyakov. New Narrow Nucleon N*(1685). *JETP Lett.*, 88:347–350, 2008.

[94] D. Diakonov, V. Petrov and M.V. Polyakov. Exotic Anti-Decuplet of Baryons: Prediction from Chiral Solitons. *Z. Phys. A*, 18:305, 1997.

[95] R. A. Arndt, Y. I. Azimov, M. V. Polyakov, *et al.* Nonstrange and other flavor partners of the exotic Θ^+ baryon. *Phys. Rev. C*, 69:035208, 2004.

[96] V. Kuznetsov *et al.* Evidence for a narrow structure at $W \approx 1.68$ GeV in η photoproduction off the neutron. *Phys. Lett. B*, 647:23, 2004.

[97] I. Jaegle *et al.* Quasi-free Photoproduction of η mesons off the Neutron. *Phys. Rev. Lett.*, 100:252002, 2008.

[98] V. Shklyar, H. Lenske and U. Mosel. η photoproduction in the resonance region. *Phys. Lett. B*, 650:172, 2007.

[99] D. Werthmuller. Investigation of the anomaly in η-photoproduction off the neutron. *Chinese Phys. C*, 33:1345–1348, 2009.

[100] H. Herminghaus *et al.* Status report on the normal conducting CW race-track microtron cascade "MAMI". *IEEE Trans. Nucl. Sci.*, 30:3274, 1983.

[101] H. Herminghaus *et al.* First Operation of the 850 MeV CW Electron Accelerator MAMI. *Proc Conf. LINAC 90*, 12004-C:362, 1990.

[102] A. Jankowiak. The Mainz Microtron MAMI - Past and future. *Eur. Phys. J. A*, s01:149–160, 2006.

[103] J C. McGeorge, J. D. Kellie, *et al.* Upgrade of the Glasgow photon tagger spectrometer for Mainz MAMI-C. *Eur. Phys. J. A*, 37:129–137, 2008.

[104] I. Antony *et al.* Design of a tagged photon spectrometer for use with the Mainz 840 MeV microtron. *Nucl. Instr. Meth. A*, 301:230, 1991.

[105] Z. Li, *et al.* Properties of plastic scintillators after irradiation. *Nucl. Instr. and Meth. A*, 552:449–455, 2005.

[106] A. Thomas. Crystal Ball Hydrogen (Deuterium) Target manual. http://wwwa2.kph.uni-mainz.de/A2/, 2007.

[107] R. Novotny. The BaF_2 spectrometer TAPS. *IEEE Trans. Nucl. Sci.*, 38:2, 1991.

[108] G. Braun *et al.* TDC Chip and Readout Driver Developments for COMPASS and LHC-Experiments. *arXiv:hep-ex/9810048*, 1998.

[109] J. R. M. Annand. Data Analysis within an AcquRoot Framework. nuclear.gla.ac.uk/ãcqusys/doc/AcquRoot.11.08.pdf, 2008.

[110] R. Brun. Root manual. root.cern.ch.

[111] D. I. Glazier. http://www2.ph.ed.ac.uk/nuclear/G4/.

[112] S. Agostinelli, *et al.* Geant4 - a simulation toolkit. *Nucl. Instr. and Meth. A*, 506:250–303, 2003.

[113] J. Allison, *et al.* Geant4 developments and applications. *IEEE Trans. on Nucl. Sci.*, 53:270–278, 2006.

[114] M. Unverzagt, The University of Mainz. PhD thesis, 2008.

[115] J. Brudvik, The University of California, Los Angeles. PhD thesis, 2007.

[116] B. Lemmer, Justus-Liebig- Universitat, Giessen. Diploma thesis, 2007.

[117] T. Gessler, Justus-Liebig- Universitat, Giessen. Bachelor thesis, 2008.

[118] J. Robinson. Proton energy loss corrections. Private communication, 2009.

[119] N. Harrington, The University of Edinburgh. PhD thesis, 2005.

[120] A. Braghieri, L. Y. Murphy, *et al.* Total cross section measurement for the three double pion photoproduction channels on the proton. *Phys. Rev. B*, 363:46–50, 1995.

[121] D. H. Wright and A. Heikkinen. Adding kaons to the Bertini cascade model. *CERN Document Server (http://cdsweb.cern.ch)*, 2004.

[122] I. Strakovsky. Private communication, 2009.

[123] T. Mart. Private communication, 2010.

[124] T. Corthals, Universiteit Gent. PhD thesis, 2007.

[125] P. Vancraeyveld. Private communication, 2009.

[126] H. Schmieden. Private communication, 2010.